Inversion régionale des sources de poussières désertiques

Jerónimo Escribano

Jerónimo Escribano. Inversion régionale des sources de poussières désertiques. Environmental Engineering. Université Pierre et Marie Curie - Paris VI, 2017. English. NNT : 2017PA066023 . tel-01585908

HAL Id: tel-01585908
https://theses.hal.science/tel-01585908v1

Submitted on 12 Sep 2017

THÈSE DE DOCTORAT
DE L'UNIVERSITÉ PIERRE ET MARIE CURIE

Spécialité : Modélisation et méthodes numériques pour l'étude du système climatique

École doctorale : Sciences de l'environnement d'Île de France (ED 129)

réalisée au

Laboratoire de Météorologie Dynamique

présentée par

Jerónimo ESCRIBANO

pour obtenir le grade de :

DOCTEUR DE L'UNIVERSITÉ PIERRE ET MARIE CURIE

Sujet de la thèse :

Inversion régionale des sources de poussières désertiques

soutenue le 9 mars 2017

devant le jury composé de :

M.	Carlos Pérez	Rapporteur
M.	Vincent-Henri Peuch	Rapporteur
Mme	Béatrice Marticorena	Examinateur
M.	Cyrille Flamant	Examinateur
M.	Olivier Boucher	Directeur de thèse
M.	Frédéric Chevallier	Co-directeur de thèse

Acknowledgements

I would like to thank to all the people that were involved in this thesis, but name them all would impossible.

In the first place I would sincerely like to thank my advisor, Oliver Boucher. I deeply appreciate all his help, advice and suggestions during these years. I would also like to thank to my co-advisor Frédéric Chevallier, who helped me to carry out this work with his always well-pointed questions and comments. To Nicolás Huneeus for his inter-hemispheric support and help.

To the members of the jury of the thesis, Béatrice Marticorena and Cyrille Flamant, and especially to Vincent-Henri Peuch and Carlos Pérez for accepting to be the rapporteurs of my work.

To the members of the LMD and to the LMDZ development team, in particular to Frédéric Hourdin, who was always available to answer my questions about the model. I acknowledge L. Menut for providing his version of the dust code implementation.

I would like to give a huge thanks to Lluis (good luck in the south!), Mikel and Fuxing. And finally, to Karla, who has been with me all these years, muchísimas gracias.

This work was possible thanks to the funding from the OSIRIS project, from the MEDDE (now MEEM) via the CNRS-INSU; the funding provided by the France-Chile ECOS project C14U01 and by the Copernicus Atmospheric Monitoring Service, implemented by the ECMWF on behalf of the European Commission. I acknowledge the computing time provided by the GENCI projects t2014012201, t2015012201 and t2016012201 at the TGCC.

Résumé

Dans cette thèse, nous concevons et appliquons un système d'assimilation de données pour l'estimation des sources de poussières désertiques à l'échelle régionale. Nous assimilons des données d'épaisseur optique des aérosols à partir de produits satellitaires dans une configuration régionale d'un modèle de circulation générale, couplé à un modèle d'aérosol et à un module de production de poussières. Le vecteur de contrôle dans le système d'assimilation est composé des facteurs de correction pour les émissions obtenues par l'ébauche du module de production de poussières. Nous concentrons nos inversions sur l'Afrique du Nord et la péninsule arabique pour une période d'un an. Nous décrivons le module de production de poussières et le système d'assimilation. Les résultats de l'inversion et la validation par rapport à des mesures indépendantes sont ensuite présentés en détail. Nous poursuivons cette thèse en mettant l'accent sur la sensibilité des émissions de poussières au jeu de données d'observation. Pour cela, nous avons assimilé cinq produits différents d'épaisseur optique d'aérosols dans notre système d'assimilation de données. Nous avons identifié des erreurs systématiques dans le modèle et dans les observations, ainsi que les limites et les avantages de notre approche. Nous avons accordé une attention particulière à la définition des statistiques d'erreur et à la procédure numérique pour calculer les analyses. Nous proposons et mettons en oeuvre un schéma de correction de biais dans l'espace des observations, et nous évaluons sa performance.

Abstract

In this thesis we design and apply a data assimilation system for the estimation of mineral dust emission fluxes at the regional scale. We assimilate aerosol optical depth retrievals from satellite-borned instruments in a regional configuration of a general circulation model, coupled to an aerosol model and to a dust production module. The control variable in the assimilation system are correction factors for the prior emissions of the dust production module. We focus our inversions over North Africa and the Arabian Peninsula for a one-year period. We describe the dust production module and the assimilation system. The inversion results and the validation against independent measurements is presented in detail. We continue this thesis with a focus on the sensitivity of the inferred dust emissions with respect to the observational dataset assimilated. For this purpose, we have assimilated five different aerosol optical depth retrievals in our data assimilation system. We have identified systematic errors in the model, in the observations and limitations and advantages of our approach. We have given special attention to the definition of the error statistics and the numerical procedure to compute the analyses. We propose and implement a bias correction scheme in the observational space, and we evaluate its performance.

Contents

Chapter 1

Introduction

1.1 Atmospheric aerosols (with an emphasis on dust)

1.1.1 Definitions and interest

Aerosols are solid or liquid particles suspended in a gaseous medium. The gas itself is part of the aerosol, but for the sake of clarity in this work we follow the common usage of excluding both hydrometeors and gas from the definition of atmospheric aerosols. Aerosol physical and chemical properties are diverse and can vary considerably in space and time. An aerosol population is a collection of aerosols that usually share similar physical or chemical characteristics.

Aerosol size can range from a few nanometres of diameter to several tens of microns. It is common to group aerosol populations in size *modes* with the usual terminology of (from smaller to larger): nucleation mode, Aitken mode, accumulation mode, coarse mode and super-coarse mode. It is usual to represent an aerosol population with several modes that can overlap with each other.

Aerosol morphology varies between simple and regular geometrical forms (such as spheres or spheroids) to more complex non-regular shapes. As an illustrative example, particles resulting from high-temperature combustion processes can be described as aggregates of smaller particles formed from unburned or uncompletely burned material; aerosols resulting from the condensation of gaseous chemical species are usually spherical; asbestos particles usually have a cylindrical shape and (dry) sea salt particles may be roughly described by a parallelepiped shape. More complex morphologies can be found, for example, in biogenic particles (e.g. pollen) or aggregates of heterogeneous smaller particles. Dust particles are highly non-spherical and their shape depends on the composition and mixture of the particle. Figure 1.1 shows dust particles collected during the SAMUM I (Saharan Mineral Dust Experiment I) campaign.

In terms of aerosol formation process, two types of aerosol are commonly described; *primary* aerosols are directly emitted into the atmosphere, while *secondary* aerosols are formed by conden-

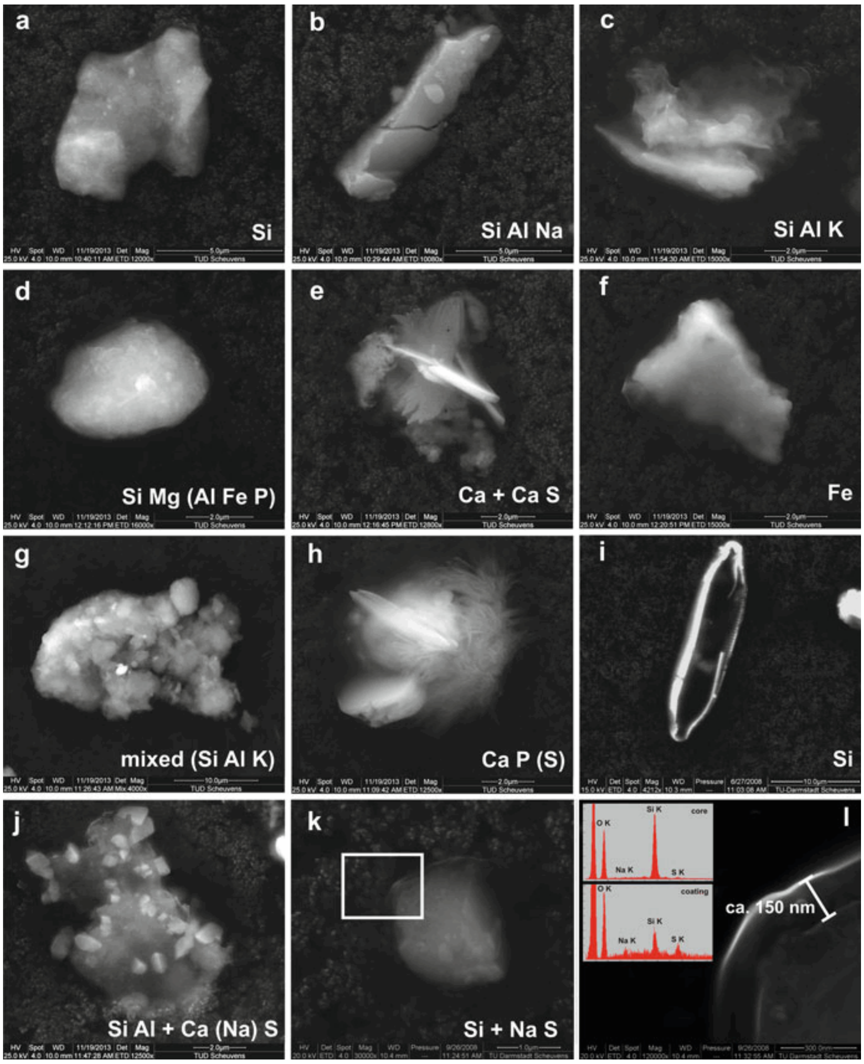

Figure 1.1: Images of dust particles collected during the SAMUM I campaign. The composition of each particle is indicated at the bottom of the panels. Figure extracted from Knippertz and Stuut (Ch. 2, 2014) with the following caption: *Secondary electron images of typical dust particles of northern Africa collected during the SAMUM I campaign in Morocco. At the bottom of the images, the major elements analyzed by energy-dispersive X-ray technique (EDX) are labelled. In the following, common atmospheric minerals with the specified composition (and matching the morphology of the particle) are given in parenthesis. (a) Si-rich particle (quartz), (b) Na-bearing aluminosilicate (albite), (c) K-bearing aluminosilicate (illite), (d) Mg-dominated silicate (palygorskite), (e) Ca sulfate and Ca-dominated mineral (gypsum on calcite), (f) Fe-dominated mineral (iron oxide or iron hydroxide), (g) complex internally mixed aluminosilicate with individual Fe-dominated phase (bright spot in center), (h) Ca-P-S-bearing particle (biological?), (i) Si-dominated particle (opaline diatom), (j) aluminosilicate (kaolin group?) with Ca(Na) sulfate (gypsum, thenardite, glauberite?), and (k) Si-rich particle (quartz) with sulfate coating (overview). (l) Detail of coating with EDX spectra for rim and core of the particle.*

sation of gases (such as sulphuric acid, nitric acid, and low-volatility organic compounds) in the atmosphere. By source, aerosols can be differentiated if they are emitted by a natural (e.g. marine, vegetation fire, desert) or by an anthropogenic (e.g. industrial, urban, agricultural) source. By chemical composition, it is common to identify inorganic aerosols (e.g., sulphate, nitrate, ammonium, sea salt as a major component of sea spray), organic aerosols (whether primary or secondary, also called carbonaceous aerosols) and mineral aerosols among others. The degree of mixture between the different chemical compounds in an aerosol population could range between an external mixture and an internal mixture, including special cases like coated particles or chain particles consisting of aggregates of smaller aerosols.

Aerosol populations can be described using different criteria either by the physical and chemical characteristics of the aerosol itself or by the capability of the aerosol population to interact with the environment in relevant atmospheric processes. For instance aerosols can be hydrophilic or hydrophobic depending on their ability to grow in size with relative humidity, and their degree of hygroscopicity is a key property. In relation to their hygroscopicity, aerosols can be grouped by their efficiency to act as cloud condensation nuclei (CCN) or ice nuclei (IN). Finally they can also be characterised by their efficiency in absorbing or scattering radiation for a given part of the electromagnetic spectrum (e.g. visible, infrared). Here the absorbing or non-absorbing character of the aerosols is quite important.

Aerosols present in the lower part of the atmosphere, the troposphere, are called tropospheric aerosols, while in the stratosphere are called stratospheric aerosols. Most of the aerosol descriptions above are inter-related, and a general classification for the purpose of aerosol climate effects can be done as in Boucher et al. (2013) by distinguishing sulphate, nitrate, black carbon, organic aerosol, mineral dust and sea spray aerosols. While such a classification may be too simple in light of observed aerosol degree of mixture, it is useful at least from a modelling perspective.

In the atmosphere, aerosols play a crucial role in radiation and cloud processes, which are key processes for weather and climate. Aerosols also impact the whole climate system through their interactions with atmospheric chemistry (e.g., actinic fluxes, heterogeneous chemistry, formation of polar clouds), or with their interaction with the biosphere (e.g., fertilization effect in the Amazon forest because of phosphorus deposition) or with the cryosphere (e.g., through deposition of black carbon in the Artic).

At the moment, there is a large uncertainty in the quantification of aerosol impact in weather and climate (e.g. Boucher et al., 2013). Along with the current lack of knowledge in some of the physical and biogeochemical processes involving aerosols; the quantification of the global aerosol mass balance is still highly uncertain. In terms of global aerosol mass, natural emissions provide the largest source of aerosol, and within them, sea spray over ocean and mineral dust over continent are the most important contributors to the global burden. It is worthy to note that both sea spray and mineral dust emissions, are driven by near surface wind speed (depending on the local atmospheric conditions) along with local surface characteristics complexifying the study and understanding of both processes of emissions, which results in a large uncertainty of their respective contributions at global and local scales.

Linked with the uncertainties in the sources, transport, transformations and sink processes of aerosols in the atmosphere are still not well characterized. All these factors together pose difficulties in estimating the lifetime of aerosols in the atmosphere (see Huneeus et al. (2011) for a comparison of dust lifetime in different models). In fact, the lifetime (τ) of aerosols in the atmosphere can be defined by

$$\tau = \frac{B}{S} = \frac{B}{R} \quad ,$$

where B is the aerosol burden, that is, the column integrated mass of aerosols, S is the source flux (in terms of mass per time) and R is the sink flux (in the same unit). When all the sink and/or source processes are included in the S and R terms of the previous equation, τ is often called *residence* time. For aerosols, the sink term includes wet and dry deposition. The latter includes the dry deposition for small aerosols (mainly driven by brownian motion) and sedimentation for coarser particles (mainly driven by gravitational settling). For coarser aerosols as mineral dust or sea spray, the sedimentation rate is highly dependent on the size of the particles. Thus the residence time of these coarser aerosols depends on the cutoff size considered (larger aerosols will have shorter residence time).

Radiative forcing and radiative effect are important concepts to describe and quantify perturbations to the climate system, as they diagnose changes in the energy balance in the system, which then impact on the climate system. Conceptually, the aerosol-radiation radiative forcing (RF) can be decomposed into four terms (Schulz et al., 2006), as is shown in Equation (1.1.1) below:

$$\mathrm{RF} = \underbrace{\frac{\mathrm{RF}}{\mathrm{AOD}}}_{\text{(A)}} \times \underbrace{\frac{\mathrm{AOD}}{\mathrm{BURDEN}}}_{\text{(B)}} \times \underbrace{\frac{\mathrm{BURDEN}}{\mathrm{EMISSIONS}}}_{\text{(C)}} \times \underbrace{\mathrm{EMISSIONS}}_{\text{(D)}} \quad . \tag{1.1.1}$$

The first term (A) is the radiative efficiency of the aerosol; the second (B) is related to the aerosol microphysics (mass extinction efficiency). Aerosol residence time can be identified in term C of Equation (1.1.1), while the emission rate represents term D. The aerosol chemical composition is important for terms A, B (by their optical properties) and C (by their chemical reactions). The size distribution is crucial for the aerosol residence time (C) and for term B of Equation (1.1.1). Emissions are directly related to the aerosol residence time and to the RF. Radiative forcing due to aerosol-cloud interactions is also sensitive to these parameters. In brief, uncertainties in sources and sinks of aerosols propagate to all aerosol radiative forcing and radiative effect calculations due to its high sensitivity of this quantity to the aerosol size distribution, spatial distribution and composition (among others). Therefore, increasing the accuracy of aerosol emission estimates is a necessary step to improve the current knowledge on the effects and interactions of aerosols in the climate system.

As was mentioned before, the largest contributor to continental aerosols is mineral dust, but their emission flux remains highly uncertain at the global scale. This work will focus on the largest mineral dust emission region of the world, Africa, with the aim of narrowing uncertainties

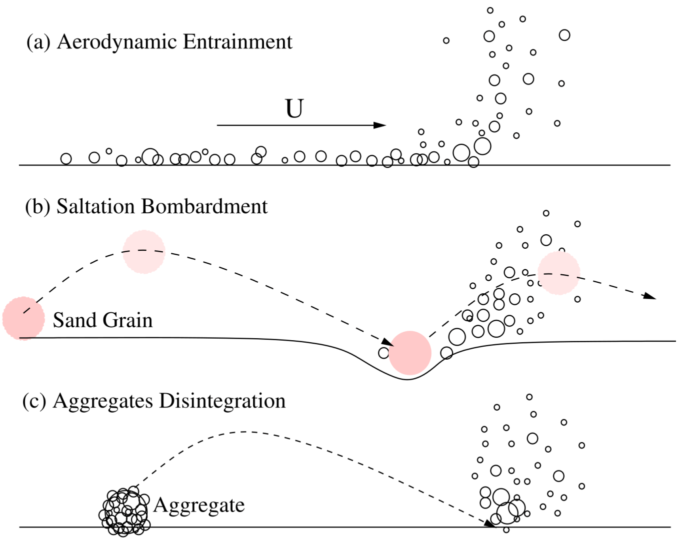

Figure 1.2: Representation of dust emission process. Panel (a) for direct emission from the saltation process, panel (b) for the saltation (pink circles) and panels (b) (white circles) and (c) for the sandblasting process. Figure from Shao et al. (2011).

in flux estimates.

1.1.2 Dust and African dust

As mentioned above, mineral dust is mostly emitted by natural processes (Ginoux et al., 2012). Aeolian erosion of arid and semi-arid soils can produce mineral dust emissions, depending on several factors including the wind speed, soil texture, soil moisture, the presence of available erodible material, etc. Conceptually, mineral dust is the result of three main physical processes (Ch. 5 from Knippertz and Stuut, 2014). First, the aeolian erosion is only reached when the wind momentum is strong enough to lift particles from the soil. This threshold is usually defined by a minimum friction velocity, which may depend on the size distribution of soil particles, the crusting effects, soil moisture and the surface roughness. Secondly, the so called creeping and saltation processes take place when the particles moves close to the ground either by “rolling” on the surface or by making small jumps, impacting other particles in the soil. The fraction of particles injected into the boundary layer through the saltation processes is estimated to be small (Ch. 5 from Knippertz and Stuut, 2014), but the impact of the saltation on the soil can release more particles available for this process, or break the binding energies of soil particles themselves into smaller ones that can be injected into the boundary layer. This last process is called sandblasting. Figure 1.2 shows a schematic representation of these processes. A detailed description of the dust production module used in this work which includes the three aforementioned processes can be found in Section 2.1.3.

Figure 1.3 shows picture of a *haboob*, a dust storm generated by a strong downward flux of air related to convective activity. A satellite view of a dust outbreak is also shown in Figure 1.4. In this figure the dust plume can be noticed over the Atlantic Ocean.

Figure 1.3: *Haboob* picture captured during the AMMA (Analyses Multidisciplinaires de la Mousson Africaine) campaign at Hombori, Mali. (© Françoise Guichard/Laurent Kergoat/CNRS Photothèque).

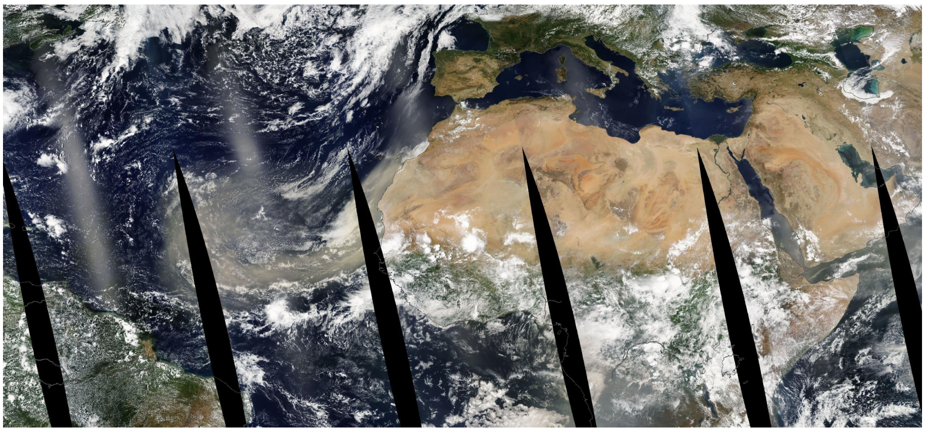

Figure 1.4: Dust outbreak captured by the MODIS/Aqua instrument on 31 July 2013. Satellite image obtained from the ICARE service (`http://www.icare.univ-lille1.fr/`).

Region	Emission
North Africa	792
Middle East	128
Asia	137
South America	9.8
South Africa	11.8
Australia	30.7
North America	2.0

Table 1.1: Median of mineral dust emission rate for the models shown in Huneeus et al. (2011). Values are in teragrams per year (Tg yr^{-1}). Obtained from Huneeus et al. (2011).

It is worthy to note that dust emission is a process that primarily occurs on a very local scale (of the order of centimetres to meters). Due to the large variability of surface conditions, the estimation of global or regional emission flux is therefore a difficult task. On the regional scale, satellite-based observational studies have been successful in estimating the frequency of dust events (over an emission threshold) (e.g. Schepanski et al., 2007) or directly estimating regional dust emissions flux from satellite and model data as in Evan et al. (2014). For the first approach, satellite imagery was used to track all recognizable dust plumes to the source pixel. The work by Schepanski et al. (2007) is a good example on how to determine dust emission regions and their frequency of emission, but it is only valid for dust that can be manually identified from satellite images, which implicitly sets a threshold on the emission rate. With this methodology, it is not possible to directly estimate the emitted flux. Evan et al. (2014) use dust emissions and aerosol burden from models with aerosol burden estimated from satellite optical depth measurements. This valuable first order approximation cannot well distinguish contributions of dust and sea spray aerosols in the observationally-estimated dust burden.

Modelling studies have also been used to estimate emissions (Huneeus et al., 2011). Estimates of dust emission over North Africa can range between hundreds to thousands of teragrams per year (Tg yr^{-1}), depending on the estimation methodology and tools used. Figure 1.5 shows the estimated annual average dust emission flux over the globe by Ginoux et al. (2012). In the work by Ginoux et al. (2012) they derived a preferential dust source map using AOD retrievals from MODIS Deep Blue, and then they computed the emissions using the dust emission model proposed in Ginoux et al. (2001). Despite the fact that the use of MODIS Deep Blue could be less accurate than other methods (Schepanski et al. (2012) show that the afternoon sampling of the MODIS/Aqua satellite impacts negatively the geographical identification of dust emission sources with this method), Figure 1.5 shows that the largest region of mineral dust emission is the Sahara Desert. However, non-negligible dust sources can be identified in Asia, North America, South America and Australia. Table 1.1 shows the total dust emissions for the median of the models analysed in Huneeus et al. (2011).

The importance of North Africa and the Arabian Peninsula in the global balance. can be inferred from Table 1.1 and Figure 1.5. Additionally, the impact of the dust emitted in these

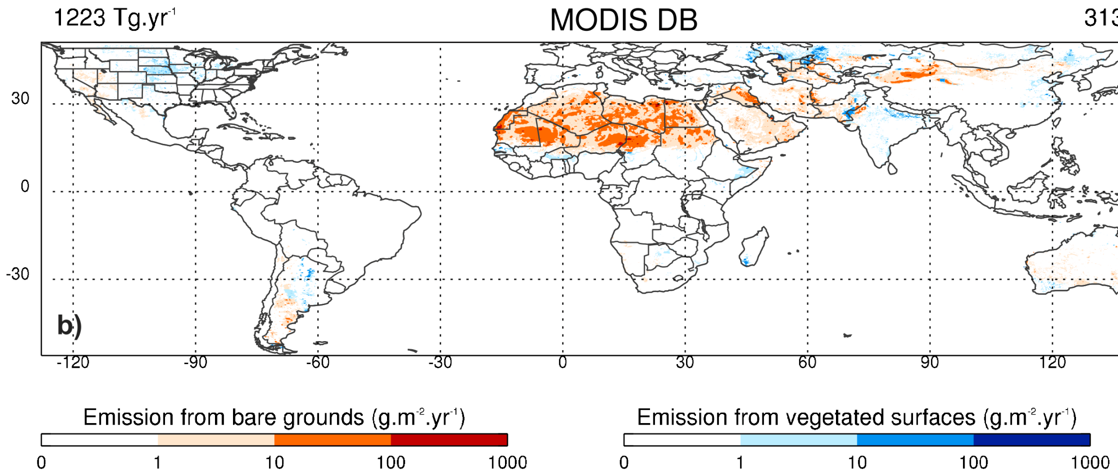

Figure 1.5: Global emission fluxes from Ginoux et al. (2012). Dust flux is calculated using a preferential source map derived from MODIS Deep Blue retrievals. Figure from Ginoux et al. (2012).

regions on the climate puts forward the need of improving our understanding and knowledge on this topic.

Despite our incomplete knowledge on some key physical processes affecting mineral dust, it has been shown that mineral dust plays an active role in the Earth system. Feldespar-rich mineral dust is one of the most effective aerosols that could serve as ice nuclei (IN) (Atkinson et al., 2013). Deposition of dust containing soluble iron over the ocean can be a limiting factor in the marine productivity, with impacts in the oceanic biogeochemical cycles and potential impacts in the climate system (Jickells et al., 2005). Mineral dust deposited over the Amazon rainforest provides phosphorus to the vegetation (Yu et al., 2015). Yu et al. (2015) propose that the Saharan dust deposition over the rainforest is necessary to avoid the depletion of phosphorus in tropical ecosystems in the long term. Dust interactions with short-wave and long-wave radiation have effects on the surface temperature and the vertical profile of temperature which could modulate a large range of atmospheric variables (e.g., evaporation, vegetation, atmospheric stability, winds, etc.), impacting clouds and the global radiative budget.

On the human dimension, dust can affect agriculture by the erosion of soils (removing fine particles and nutrients from the soil) when dust is emitted and by the abrasion and deposition of dust over crops and natural vegetation (Goudie and Middleton, 2006). Airborne dust reduce the shortwave solar radiation flux at the surface, which decreases the production of electricity of solar power plants. Dust particles, like other aerosols, also have an impact on human health, which is potentially important for local African populations. Inhalation and ingestion of dust are the most important routes of entrance of aerosols into the human body. Once deposited in the human body, they can react with fluids and tissues (Knippertz and Stuut, 2014). Dust increases the incidence of respiratory disease, eye infections, and cardiovascular mortality (Morman and Plumlee, 2013); and has been associated to deadly epidemics of meningococcal meningitis in the African Sahel (Martiny and Chiapello, 2013; Pérez García-Pando et al., 2014) and to coccidioidomycosis (*valley fever*) in North America (e.g. Kirkland and Fierer, 1996; Goudie, 2014).

In the previous paragraph we have spoken about aerosols and dust in the atmosphere, giving the rationale and the interest of the dust emission estimation problem. We will continue this chapter with a second topic, more related to the methodology that we have applied, and which is present throughout all this thesis: data assimilation in atmospheric sciences.

1.2 Data assimilation and numerical models of the atmosphere

Numerical weather prediction models are numerical implementations of the equations governing the dynamics and the physics of the atmosphere. The equations themselves represent approximations of atmospheric processes and are therefore an integral part of such models. Atmospheric models aim to solve, at least, the most important equations from fluid dynamics applied to the atmosphere. These are the momentum equation, the continuity equation and thermodynamics equations, where the variables are the so-called “state” or prognostic variables (i.e., wind field, temperature, surface pressure) and mixing ratio of some important atmospheric trace gases or particles (e.g., water vapour) among others. Numerically it is usual to split the process of solving the (discretized) equations into the “dynamics” (momentum and continuity equations) and the “physics” parts of the model, the latter consisting of radiative transfer, boundary layer and surface exchange, convection and other cloud processes.

Atmospheric observations consist of in situ and remote sensing measurements of the atmosphere. Typically atmospheric remote sensing rely on measuring radiative quantities which can be translated into relevant atmospheric variables (e.g., temperature) through a “retrieval scheme” that is based on fundamental physical laws. If the source of the electromagnetic radiation employed by the sensor is a natural source (e.g., radiation emitted by the sun or terrestrial radiation emitted by the Earth system), then the remote sensing is called *passive*. This is, for example, the case of sunphotometers and of a range of passive satellite-borne (spectro)radiometers. When the emitted source is artificial, then the retrieval technique is called *active*. Lidars and radars are examples of this type of instruments (Liou, 2002). Information about the state or the composition of the atmosphere can be retrieved by using remote sensing. In this case, the electromagnetic spectrum is sampled depending on the variables of interest. For example, the visible and infrared parts of the spectrum are commonly used in cloud detection, the ultraviolet is useful to determine ozone concentrations. Aerosols are usually retrieved by using the visible part of the electromagnetic spectrum, but infrared radiation can also be useful to detect coarse mode aerosols such as dust. Operational products developed for dust detection rely on visible (e.g., Levy et al., 2013) or infrared (e.g., Peyridieu et al., 2013) electromagnetic radiation. In particular, infrared dust retrievals can give information about dust size distribution and the height of the dust layer (Peyridieu et al., 2013). We will describe the observations used in this thesis in Chapter 2.

Observations typically provide discrete information on the state of the atmosphere, while models try to provide a comprehensive and almost continuous view of the state of the atmosphere. To achieve realistic forecast, models need observations. Weather and chemical weather forecasting is modelled as a partial differential equation system, which includes the equation themselves, the domain where the variables needs to be solved, the initial conditions and the boundary conditions. Boundary conditions at the surface can be artificially imposed or they can be extracted from observations, land and ocean models (also driven by observations) or a combination of both. At the top of the atmosphere, the solar radiation is the most important boundary condition, which is typically acquired from astronomical knowledge. For realistic forecasts, the initial conditions have to be close to the real state of the atmosphere, and thus the incorporation of observations of the atmosphere is fundamental.

Models are not perfect, and observations neither. How can we estimate the real state of the atmosphere taking into account model and observational errors in a physically consistent estimate? That is the principal subject of study of data assimilation, which we now discuss.

Data assimilation techniques have been developed since the pioneering works of Panofsky (1949) and Cressman (1959). They have proven very successful to estimate the fundamental variables of the atmosphere (temperature, pressure, ...) as shown by the accuracy of weather forecasts (e.g., Buizza et al., 2005) and the quality of atmospheric reanalyses (e.g. Saha et al., 2010; Dee et al., 2011). In the last decades data assimilation techniques have been used to estimate the chemical state of the atmosphere (e.g. Bocquet et al., 2015, for a review). In this work, we will focus on the variational approach.

In data assimilation (DA) the real state is unknown, but it can be approximated by a prior (or first guess) and by the observations. The aim is to find the best estimate of the real state, using these two approximations and descriptions of their statistical errors. To this effect, in variational DA, a variable called *control vector* (or *state vector*) is controlled in the model domain, and the best estimate of the state of the atmosphere is determined by the result of the minimization of a *cost function.*

The formulation of a DA problem relies on two different spaces. The control vector is defined in a subspace of $\mathbb{R}^n$, i.e., it is a vector of n components corresponding to n model variables, while the observation vector $\mathbf{y}$ is defined in $\mathbb{R}^p$ where p is the number of observations. In a typical 6-hour window of a numerical weather prediction assimilation, the number of model variables is $O(10^7 - 10^8)$ and the observations are $O(10^5 - 10^6)$ (Nichols, 2010).

If $\overline{\mathbf{x}}$ is the true continuous state of the atmosphere, we will denote by $\mathbf{x}^t$ the projection of $\overline{\mathbf{x}}$ into the space of the control vector $\mathbf{x}$ through a projection operator Π, that is, $\mathbf{x}^t = \Pi(\overline{\mathbf{x}})$. The *prior* (or *background*) represents the a priori information and it is denoted by $\mathbf{x}^b$ (with $\mathbf{x}^b \in \mathbb{R}^n$). The prior is assumed unbiased and can be expressed as $\mathbf{x}^b = \mathbf{x}^t + \varepsilon^b$, with ε^b a random variable with mathematical expectancy equal to zero ($E(\varepsilon^b) = 0$). The assumption that the prior is unbiased is an important one, which we will come back to later in this work. The covariance matrix of ε^b is denoted by $\mathbf{B}$.

Observations $\mathbf{y}$ have an *instrumental error* denoted by ε^i. In other words, there exists a map h such that $\mathbf{y} = h(\overline{\mathbf{x}}) + \varepsilon^i$ (Bocquet, 2014). Elements in the control vector space are compared with the observations using an *observation operator* $H : \mathbb{R}^n \to \mathbb{R}^p$. The observations $\mathbf{y}$ can be written as $\mathbf{y} = H(\mathbf{x}^t) + \varepsilon^o$. The error ε^o is called the *observational error*, it is also assumed unbiased with covariance matrix $\mathbf{R}$, and it can be written as the sum of two errors: the instrumental error ε^i and the *representativeness error* ε^r as in Bocquet (2014):

$$\varepsilon^o = \varepsilon^i + \varepsilon^r \quad ,$$

with $\varepsilon^r = h(\overline{\mathbf{x}}) - H(\mathbf{x}^t) = (h - H \circ \Pi)(\overline{\mathbf{x}})$.

The representativeness error includes the discretization errors of the observations (e.g., sampling and model grid approximation) and errors of the observation operator (e.g., errors or unresolved physical processes in the model) while the instrumental error basically corresponds to the measurement and retrieval errors.

Non-diagonal terms of $\mathbf{R}$ are the covariances between the different elements of the observational error, while non-diagonal terms of $\mathbf{B}$ are the covariances between the different elements of background error. It is usual to assume independence between the observational and background errors probability density functions. In this work we will implicitly use this assumption. In data assimilation, one of the main challenges is to properly estimate the covariance matrices $\mathbf{B}$ and $\mathbf{R}$, including their non-diagonal terms. Later in this thesis we will work on this topic, for both covariance matrices.

With the definitions above, it is possible to define the cost function J as:

$$J(\mathbf{x}) = \frac{1}{2}(\mathbf{x} - \mathbf{x}^b)^T \mathbf{B}^{-1} (\mathbf{x} - \mathbf{x}^b) + \frac{1}{2}(\mathbf{y} - H(\mathbf{x}))^T \mathbf{R}^{-1} (\mathbf{y} - H(\mathbf{x})) \quad . \tag{1.2.1}$$

The solution of the minimization of Equation (1.2.1) over a feasible domain of $\mathbf{x}$ is called the *analysis* and it is denoted by $\mathbf{x}^a$. The analysis is the best estimate of the state of the system, but only under well defined assumptions such as unbiased errors and well defined error covariance matrices.

In this work, we will perform the data assimilation minimizing Equation (1.2.1) in Chapter 4 and Chapter 5.

1.3 Aerosol data assimilation

Measurements of the amount of aerosols in the atmosphere can be assimilated into models through filtering or variational approaches. Observational information of the amount of aerosols may come from ground-based, airborne or spaceborne instruments.

Ground-based observations include direct measurements, such as surface aerosol mixing ratios, and indirect (remote-sensing) measurements, such as the Aerosol Optical Depth (AOD) from sunphotometers which represent the column aerosol amount, or vertically- resolved aerosol extinction coefficients retrieved from lidar systems.

Passive instruments on board satellites can measure the reflection of solar radiation by the atmosphere and the surface at several wavelengths. Qualitative retrievals of the amount of aerosol in the atmospheric are, for example, the aerosol index (AI) from the satellite-borne instruments Total Ozone Mapping Spectrometer (TOMS) and Ozone Monitoring Instrument (OMI). Aerosol optical depth is a quantitative measure of the aerosol burden and it can be retrieved by satellite-borne instruments as the Moderate Resolution Imaging Spectroradiometer (MODIS), the Multiangle Imaging Spectroradiometer (MISR), the Advanced Infrared Radiation Sounder (AIRS), the Infrared Atmospheric Sounder Interferometer (IASI), the Polarization and Directionality of the Earth's Reflectances instrument (POLDER) among others. Spaceborne active instruments can also retrieve aerosol vertical profiles (e.g., Cloud-Aerosol Lidar with Orthogonal Polarization,CALIOP) but the current state of play makes it difficult to invert a consistent AOD given the characteristics of current spaceborne lidars.

The aforementioned instruments are on-board low earth orbit (LEO) satellites with sub-synchronous polar orbits. Instruments on-board LEO satellites typically cross the equator at the same local time everyday, and thus they visit a point in the equator at most one time per day and other at night. Depending on the instrument swath, a global coverage can be done in a few days (one day for Visible/Infrared Imaging Radiometer Suite, VIIRS, 2 days for MODIS, 9 days for MISR, etc.). AOD can be also derived from measurements of instruments onboard geostationary satellites, for example from the Spinning Enhanced Visible and Infrared Imager (SEVIRI) instrument onboard Meteosat Second Generation (MSG) and the Advanced Himawari Imager (AHI) onboard the Japanese geostationary meteorological satellite Himawari-8. These measurements can be done at a high temporal frequency (15 minutes) but only cover a fixed portion of the globe.

At the current state, AODs derived from satellite measurements are the most widely used products in aerosol data assimilation. It can be assimilated at several wavelengths or from several instruments simultaneously. Although AOD is a column integrated piece of information with relatively large uncertainty at the pixel level, the large temporal and spatial coverage of satellite retrievals can counteract these disadvantages. On the contrary, aerosol concentration measurements at surface level can report a more detailed and accurate measurements than AOD including, for example, size distribution or aerosol composition (but only at surface level). The local nature of these measurements hampers their use in large scale studies, unless there exists a dense observational network. Such measurements have been assimilated in chemical transport models as well.

Instead of assimilating AOD, it is possible to directly assimilate the measured radiances. This implies including the retrieval process in the observation operator, and consequently lessening the possible inconsistencies between the aerosol model (in the observation operator) and the retrieval algorithm. This approach also needs a more complex radiative transfer code, because the measured radiances at the top of the atmosphere are also influenced by gases, clouds, surface properties and viewing angles. Additionally and depending on the instrument, the radiative transfer code should be able to handle polarized radiances at the top of the atmosphere (e.g., POLDER) or radiances measured in several viewing angles and wavelengths (e.g., MISR).

Such observational aerosol information can be assimilated in models at the global or regional scale. Depending on the choice of the control vector, aerosol data assimilation can be used to improve initial conditions in chemical weather forecast, improve modelled aerosol concentrations for observed states ("reanalysis") or estimate emissions using a top-down approach.

The control vector can be either the aerosol concentrations or aerosol emissions, or both. In the former case, the size of the control vector is usually large (the order of magnitude of the number of gridboxes in the model). In the case of AOD assimilation, it is necessary to make assumptions on the aerosol vertical profile and the aerosol composition in the observation operator. In this thesis, we will assimilate AOD by defining a control vector related to the aerosol emissions. More precisely, we will use correction factors of the prior emissions for all the aerosols and gaseous precursors simulated by the model.

1.4 Inversion of dust fluxes

The overall emission rate of mineral dust is estimated to range from hundreds to thousands of teragrams per year (e.g. Huneeus et al., 2011), with a large associated uncertainty. As we stated in previous sections, the knowledge about the amount of atmospheric aerosols in the climate system is required for a better understanding of our environment. The estimation of these emissions is not an easy task. Direct measurements of emissions are unpractical in large source regions, so an indirect estimation has to be done.

Additionally, emissions of natural aerosols have a large temporal variability, and are modulated on time scales from seconds to decades. There are several factors at different time and spatial scales affecting dust production. The dust emission process itself has a scale of seconds, and can be triggered by wind gusts and turbulence close to the surface. Diurnal cycle of winds and boundary layer stability, with temporal scale from minutes to hours, are important for the characteristics of near surface winds. Soil moisture is a variable that can decrease the soil capacity to produce dust, with a variability from hours to months. It also influence the presence and growing of vegetation in semi-arid or transition regions, having impacts on dust emissions from the seasonal to the inter-annual scale. Meteorological conditions at the synoptic and seasonal scales also have an impact onto the dust emission flux, through precipitation and near surface winds. Finally, long-term changes in the climate system affects the meteorology and thus the ensemble of variables mentioned below.

A large amount of observations is therefore needed to capture the sporadic nature of emissions of natural emissions. If the aerosol is measured downwind of its source region, other aerosol related processes (such as transport or deposition) that are driven by complex physical mechanisms need to be accounted for when estimating the source strength.

In this work we intend to tackle the issue of dust aerosol source in a systematic way, using tools from data assimilation and thus including a large amount of satellite observations. We have deliberately reduced the degrees of freedom of the problem by controlling regional emissions. To this end, we have defined appropriate regions, in which an improved model of dust emissions provides prior emission fields.

The main aim of this work is to perform dust inversions, giving new estimates of mineral dust fluxes. However another aim is to study the quality of the assimilation system and the scope of our estimates. Some work has been performed to compare the quality of the different satellite retrievals of AOD and the feasibility to use them for aerosol data assimilation purposes, with a special attention on their potential biases. We illustrate our methodology for dust source inversion, but the methodology that we present here can easily be applied to a more general assimilation framework with other aerosol species and for other regions.

1.5 Outline of this thesis

This thesis comes in 7 chapters. Chapter 2 describe the main tools used in this thesis: the assimilated observations and the most important aspects of the observation operator, i.e., the dust emissions, aerosol and meteorological model. Chapter 3 describes the choice of control vector and the data assimilation system.

A first dust source inversion is shown in Chapter 4 and the sensitivity of the dust fluxes inversion to the assimilated observation is discussed in Chapter 5. A proposed and implemented bias correction scheme is shown in Chapter 6. Final conclusions and remarks follow in Chapter 7.

Chapter 2

Observation operator and observations

This Chapter presents two main pieces of the inversion system: the observation operator (H in Equation (1.2.1)) and the assimilated observations ($\mathbf{y}$ in Equation (1.2.1)).

2.1 Observation operator

The observation operator is the function that maps elements of the control vector space into the observational space. In our case, it maps the correction factors of dust emissions into simulated AOD. Details about the control vector (emission correction factors) are given in Chapter 3.

The observation operator mainly relies on the combination of three coupled models: the dust emission model, the aerosol model and the meteorological model. These are described in the next three subsections. Technically speaking the observation operator also samples the simulated AOD field according to the spatial and temporal coverage achieved by the AOD-measuring satellite instrument.

2.1.1 LMDZ model

The general circulation model of the Laboratoire de Météorologie Dynamique (LMDZ, Hourdin et al., 2013) is a hydrostatic model with a hybrid vertical coordinate and a stretchable latitude-longitude horizontal grid. The model resolves a finite difference discretization of the equations of motion, thermodynamics and mass conservation. The model also numerically solves the advection equations on a three dimensional grid (the so-called *dynamics*). Sub-grid scale processes, including radiative transfer, cloud, convection, precipitation and boundary layer processes, are parameterized as part of the *physics* part of the model. A detailed description of the model can be found in Hourdin et al. (2013, and references therein). The aerosol model described in the next section is coupled to the LMDZ model and is embedded in the *physics* part of the model.

Giving initial and boundary conditions, the global LMDZ model develops its own solution which diverges from the observed one given the chaotic nature of the atmospheric dynamics. To avoid a large mismatch with the observations that would be due to the simulated meteorology, the model can be run in "nudged" mode. This is achieved by adding additional terms in some of the model prognostic equations in order to relax some of the model variables towards the observations. According to Hourdin et al. (2015), a prognostic equation for a model variable X (e.g. zonal wind, meridional wind, temperature, humidity) with the nudging term reads:

$$\frac{\partial X(t)}{\partial t} = F(X(t)) + \frac{X^a(t) - X(t)}{\tau} \quad ,$$

where F represents the model physics and dynamics, t references the time, X^a is the (observed) variable that X is nudged to and τ is the timescale of the nudging. Variable X^a is usually taken from a reanalysis dataset (e.g., ERA-interim in our case, Dee et al. (2011)). A large timescale τ would imply a weaker forcing. In the LMDZ model the nudging can be deactivated in the planetary boundary layer.

We take advantage of the zoom capability of the model to simulate dust emission, transport and deposition over North Africa and the Arabian Peninsula by defining an appropriate model grid. The LMDZ model has been configured with 39 vertical levels and a horizontal grid shown in Figure 4.2. In the latitude dimension, the grid has 88 gridpoints while in longitude it has 128 gridpoints. Over the Saharan desert, the mean gridbox size horizontal resolution is close to 1°. Hourdin et al. (2015) perform dust simulations for a zoomed grid and model version similar to the grid used in this work. Following their results, we use the same nudging parameters used in Hourdin et al. (2015). In this thesis, we nudge the model using ERA-Interim (Dee et al., 2011) zonal and meridional winds. ERA-Interim reanalysis are linearly interpolated to the model grid prior the nudging. Nudging inside the planetary boundary layer is deactivated. Outside the zoom, the nudging timescale parameter is set to 3 hours and inside the zoom is set to 48 hours.

2.1.2 SPLA model

The SimPLified Aerosol model (SPLA) is an aerosol model of intermediate complexity, which in its original version of fully described in Huneeus et al. (2009). The version presented in Huneeus et al. (2009) was coupled to version 4 of the LMDZ model (through offline coupling). In this work, we have used the LMDZ model to its 5B version, and have incorporated the SPLA model with an online coupling.

The model presented in Huneeus et al. (2009) had four tracers: gaseous precursors of aerosols, coarse mode sea salt (with diameters between 1 and 40 μm), fine mode aerosols (including fine mode dust) and coarse mode dust. In the present work, mineral dust aerosols are distributed in three bins that represent super-coarse dust (between 6 and 30 μm of diameter), coarse mode dust (between 1 and 6 μm of diameter), and fine mode dust (with diameter smaller than 1 μm). After emission, fine mode dust is included in the fine mode aerosols tracer (which also includes black carbon, particulate organic matter and sulphate aerosols), so in practice the SPLA model now has five tracers.

SPLA had been designed for data assimilation purposes, meaning that the current computational capability is an important factor to be considered that limits the level of detail that can be implemented in a model. With this aim, the number of tracers represents a compromise between computational capability (or practical feasibility of the assimilation) and expected performance of the model. Huneeus et al. (2009) compare the four-tracer SPLA model with a more complex model, with satisfactory results in terms of monthly variation and magnitude of AOD fields. They also validate the linear and adjoint SPLA model, and evaluate the model performance with respect to AOD observations.

The SPLA model presented in Huneeus et al. (2009) included the following processes:

- Emissions of dust, coarse sea salt, fine mode aerosols, and gaseous precursors
- Dry deposition
- Boundary layer mixing
- Sedimentation of coarse mode aerosols
- Gas to particle conversion
- In cloud scavenging:
    - from large scale precipitation
    - from convective precipitation
- Below-cloud scavenging
    - from large scale precipitation
    - from convective precipitation
- Convective transport

The updated version of the SPLA model has four major changes. One of them is the number of tracers –already mentioned above– splitting the original coarse dust mode into a coarse and a super-coarse dust mode. This is done in this work because we are focused on dust emissions at a regional scale while Huneeus et al. (2009) performed global aerosol inversions, for all types of aerosols described in the model. Hence more detail on atmospheric dust is desirable. In particular, as we have seen in the introduction, one of the most important characteristics of an aerosol population is it size distribution, which, in the case of mineral dust of homogeneous composition and shape, determines its optical properties and its lifetime in the atmosphere. On the one hand, the optical properties of dust will directly impact the aerosol optical depth assimilation and on the other hand, the large-scale transport of dust makes the aerosol lifetime a key parameter in the modelling. In this work, the parametrization of dust sedimentation and optical parameters have been changed accordingly to the new aerosol discretization parameters.

These changes are associated to the redefinition of the dust bins and they will be explained later in this section.

A second major change is the inclusion in SPLA of a scheme that simultaneously calculates the convective transport and scavenging of aerosols, initially developed and implemented in the LMDZ model by Pilon et al. (2015). Following the latest developments of the LMDZ model, the parameterization of thermals in the boundary layer (Hourdin et al., 2015) has also been included in SPLA. For the convective scavenging of aerosols, we kept the same parameters of aerosol solubility from Huneeus et al. (2009).

Finally, the dust emission module used in Menut et al. (2013) (see Section 2.1.3) has been coupled to the SPLA model. To achieve a successful coupling of the dust module, a large number of tests have been done using low and high model resolutions, in conjunction with correction of errors in the original code, and the selection of some model parameters. We will describe some of improvements in Section 2.1.3.

The updated version of SPLA include the following processes:

- Emissions of dust (fine mode, coarse mode, supercoarse mode), coarse sea salt, fine mode aerosols, gaseous precursors
- Dry deposition
- Boundary layer mixing
- Mixing by thermals
- Sedimentation of coarse mode aerosols
- Gas to particle conversion
- Coupled convective transport and convective wet deposition
- Large scale scavenging

Because of the coupling of the dust emission model (described in the next section), parameters determining the optical properties and sedimentation velocity of dust have been updated in SPLA. Both parameters depend on the underlying dust size distribution and they are calculated for each of the three dust bins assuming that the dust size distribution in the atmosphere within each bin is the same as at the emission point. The dust size distribution at the emission point is calculated by the dust emission module averaging the dust distribution over the domain over a one-year period. Figure 2.1 shows the assumed dust size distribution.

Sedimentation velocity of coarse mode particles (sea salt, coarse and super- coarse dust) in SPLA depends on the particle size. For a set of given atmospheric conditions, the sedimentation velocity is shown in Figure 2.2. It is calculated online in SPLA and it is parameterized as a function of the Mass Median Diameter (MMD) of the underlying size distribution. For each of the two dust bins, the MMD used in SPLA does not follow the strict definition of MMD. In fact, the MMD parameter in SPLA is such that the mass-weighted sedimentation velocity of

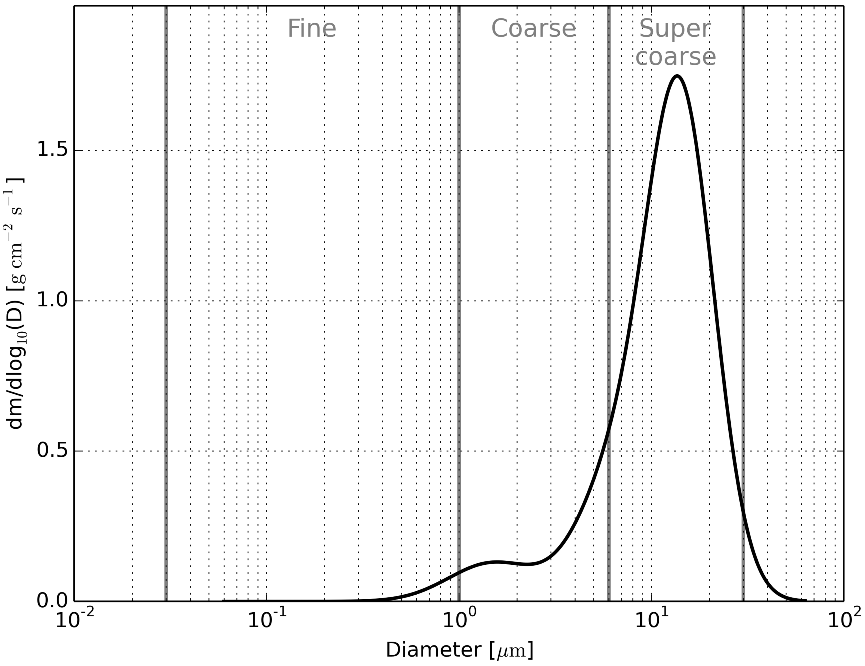

Figure 2.1: Dust mass size distribution at the emission point. The flux is normalized to 1 g cm^{-2} s^{-1}. Cut-off diameters for the SPLA dust bins are indicated in gray. Please note the logarithmic scale on the x-axis.

the underlying distribution (of each bin) matches the sedimentation velocity calculated with the MMD. In summary, for the coarse dust (between 1 and 6 µm of diameter), the MMD for the sedimentation is equal to 3.9 µm and for the super-coarse dust (between 6 and 30 µm of diameter) it is 15.1 µm.

As stated above, sedimentation velocity and mass extinction coefficients are model parameters which depend on the underlying aerosol size distribution. In the next paragraph we will describe the model update regarding the mass extinction coefficient.

Aerosols interact with solar radiation through the processes of scattering and absorption. For a single particle in the atmosphere illuminated by a monochromatic irradiance beam F_λ (units of W m^{-2} = J s^{-1} m^{-2}) with wavelength λ, the absorption (C^a_λ) and scattering (C^s_λ) cross sections are defined as (Bohren and Clothiaux, 2006):

$$C^a_\lambda = \frac{U^a_\lambda}{F_\lambda} \quad , \qquad\qquad C^s_\lambda = \frac{U^s_\lambda}{F_\lambda} \quad ,$$

with U^a_λ and U^s_λ the energy absorbed and scattered by the particle per unit of time (units of W=J s^{-1}). The cross sections can be interpreted as the effective area that interact with the radiation in a plane perpendicular to the beam direction and they have units of m^2. Related to these quantities, the effective cross section is the normalization of the cross section by the

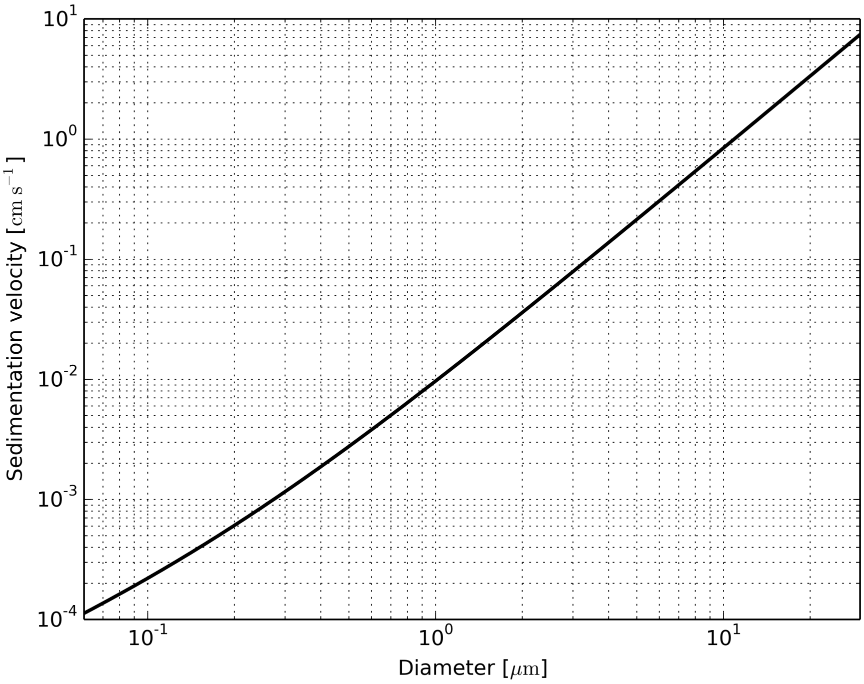

Figure 2.2: Sedimentation velocity of a single spherical particle as a function of aerosol diameter. Particle density is assumed to be 2.61 g cm^{-3}. Please note the logarithmic scale on both axis.

geometric area of the particle (perpendicular to the beam, A), denoted by Q^a_λ and Q^s_λ:

$$Q^a_\lambda = \frac{C^a_\lambda}{A} \quad , \qquad\qquad Q^s_\lambda = \frac{C^s_\lambda}{A} \quad .$$

These quantities are also termed absorption and scattering efficiencies. The extinction is defined by the sum of the absorption and scattering, that is,

$$C^e_\lambda = C^a_\lambda + C^s_\lambda \quad , \qquad\qquad Q^e_\lambda = Q^a_\lambda + Q^s_\lambda \quad .$$

For an aerosol population of spherical particles with number size distribution noted $n(r)$ (in radius), the integrated quantities of scattering, absorption and extinction coefficients are:

$$\begin{aligned} \sigma^e_\lambda &= \int_0^\infty \pi\, r^2\, Q^e_\lambda(r)\, n(r)\, dr \quad , \\ \sigma^a_\lambda &= \int_0^\infty \pi\, r^2\, Q^a_\lambda(r)\, n(r)\, dr \quad , \\ \sigma^s_\lambda &= \int_0^\infty \pi\, r^2\, Q^s_\lambda(r)\, n(r)\, dr \quad , \end{aligned}$$

with units of m^{-1}. The normalized quantities by the mass concentration of the particle size distribution are called the mass extinction, absorption and scattering efficiencies (in $\mathrm{m}^2\ \mathrm{g}^{-1}$) by:

$$\begin{aligned}
\sigma^e_{m,\lambda} &= \frac{\sigma^e_\lambda}{\displaystyle\int_0^\infty \frac{4}{3}\,\pi\, r^3\, n(r)\, \rho_p\, dr} \quad , \\
\sigma^a_{m,\lambda} &= \frac{\sigma^a_\lambda}{\displaystyle\int_0^\infty \frac{4}{3}\,\pi\, r^3\, n(r)\, \rho_p\, dr} \quad , \\
\sigma^s_{m,\lambda} &= \frac{\sigma^s_\lambda}{\displaystyle\int_0^\infty \frac{4}{3}\,\pi\, r^3\, n(r)\, \rho_p\, dr} \quad ,
\end{aligned}$$

where ρ_p is the density of the particle. In the SPLA model, the mass extinction efficiency is prescribed. In this work, the mineral dust is considered hydrophobic, so the mass extinction efficiency for coarse and super-coarse dust is a fixed parameter. For sea spray and fine mode aerosols, the mass extinction efficiency is a function of the ambient relative humidity. More details on the dependency of the mass extinction efficiency due to water uptake can be found in Huneeus et al. (2009).

The aerosol optical thickness (AOT) is the integral of the extinction coefficient between the surface and the top of the atmosphere. If the integration path is oriented vertically, this quantity has no unit, it is called aerosol optical depth (AOD or τ_λ) and can be calculated by:

$$\tau_\lambda = \int_{z_{\min}}^{z_{\max}} \sigma^e_\lambda(\xi)\, d\xi \quad ,$$

where $z_{\min}$ is the height of the surface and $z_{\max}$ is the so-called top of the atmosphere (TOA).

Assuming a given refractive index and spherical particles, the mass extinction efficiency is calculated using Mie theory through the calculation of Q^e and the underlying dust size distribution (Figure 2.1). The Mie calculation is done for a number of wavelengths for which the refractive index of dust is available. These wavelengths are not the same as in the original SPLA wavelength, so the mass extinction efficiency is interpolated using the Ångström coefficient of the closest wavelengths. If λ_1 and λ_2 are two wavelengths close to λ, the Ångström coefficient is calculated by:

$$\alpha = -\frac{\ln(\sigma^e_{m,\lambda_1}/\sigma^e_{m,\lambda_2})}{\ln(\lambda_1/\lambda_2)} \quad ,$$

and the mass extinction efficiency is interpolated by

$$\sigma^e_{m,\lambda} = \sigma^e_{m,\lambda_1} \left(\frac{\lambda}{\lambda_1}\right)^{-\alpha} \quad .$$

Values of the complex refractive index and the calculated mass extinction efficiencies are shown in Table 2.1. We have included in this table the calculated mass extinction efficiency for fine dust (which is not used in this work).

Wavelength (λ)	Refractive index	$\sigma_{m,\lambda}$ [m^2 g^{-1}]		
		Fine dust	Coarse dust	Super-coarse dust
545 nm	1.494 - 0.00225 *i*	2.899	0.4851	0.10012
550 nm		2.897	**0.4868**	**0.10021**
605 nm	1.493 - 0.00225 *i*	2.876	0.5051	0.10039
665 nm	1.491 - 0.00174 *i*	2.748	0.5292	0.10110
670 nm		2.730	**0.5318**	**0.10110**
720 nm	1.487 - 0.00140 *i*	2.565	0.5573	0.10108
825 nm	1.487 - 0.000699 *i*	2.217	0.5936	0.10231
865 nm		2.066	**0.6057**	**0.10234**
935 nm	1.487 - 0.000408 *i*	1.839	0.6269	0.10238

Table 2.1: Mass extinction efficiency in m^2 g^{-1} for coarse and super-coarse dust used in SPLA model (in bold) and refractive index of the known wavelengths used to interpolate SPLA extinction coefficients.

2.1.3 Dust emission model

There are two dust emission schemes implemented in SPLA. Outside the Sahara desert and the Arabian Peninsula the dust emission scheme is the same as in Huneeus et al. (2009) and is described in Schulz et al. (1998) and Guelle et al. (2000). Dust emissions are calculated offline using 10-meter wind speed from the ERA-interim reanalyses. The emissions are computed on the ERA-interim grid (regular latitude-longitude of 1.125 degrees of resolution) which is itself interpolated from the original ERA-interim grid. Then the emissions are interpolated to the LMDZ model grid. This emission scheme combines the saltation scheme from Marticorena and Bergametti (1995) and a semi-empirical scheme for emissions, which is useful for global studies. However, to better represent the diurnal cycle and the spatial variability of dust emissions at the regional scale, a more sophisticated dust emission scheme has been included in the model, which is based on the physics on dust emission. This more sophisticated scheme is activated over the region where the input data for this scheme are available. Hereafter our focus will be on this scheme which is used for the North African and Arabian Peninsula regions.

The dust emission scheme (or Dust Production Module, DPM) was adapted from the LMDZ implementation (Hourdin et al., 2015) of the CHIMERE-DUST emission module (Menut et al., 2013). Emission fluxes are calculated online using the LMDZ near-surface (i.e., 10-meter) wind. This allows to have consistency between the dust emissions and the local meteorological conditions.

The DPM is composed essentially of a saltation flux scheme from Marticorena and Bergametti (1995) and a sandblasting model from Alfaro and Gomes (2001). In principle, the components of the DPM used in this work are fully described in Marticorena and Bergametti (1995), Marticorena et al. (1997), Shao and Lu (2000), Alfaro and Gomes (2001), Menut et al. (2013) and Hourdin et al. (2015). In this section we will describe the complete DPM using a consistent notation and we will highlight our modifications to the code.

The relevant input parameters to the DPM are the soil type, the soil size distribution, the surface roughness length, the near-surface (i.e., 10-meter) wind and the proportion of erodible elements per unit area. The soil properties over the Sahara desert and the Arabian Peninsula are taken from the Laboratoire Interuniversitaire des Systèmes Atmosphériques (LISA) database (available at `http://www.lisa.univ-paris12.fr/mod/data/index.php`).

2.1.3.1 Soil texture and size distribution

The LISA input files have spatially-distributed information of the five predominant soil types in each gridbox with a resolution of one by one degree over the Sahara and the Arabian Peninsula. In other words, for each gridbox, from the 18 predefined soil types (Laurent et al., 2008) only the five predominant soil types are reported in the LISA input file. All the soil categories are shown in Table 2.2.

The input data from LISA database contains an map of 1° by 1° of resolution for the following variables:

- SOL: soil label for soil type (ST, from Table 2.2)
- P: fraction of the gridbox covered by SOL
- Z_{0s}: smooth roughness length
- Z_{01}: aerodynamic roughness length
- Z_{02}: aerodynamic roughness length
- D: distance between two roughness elements
- A: erodible fraction of the surface

Some of these variables (SOL, P, A, Z_{01} and Z_{0s}) are shown in Figure 2.3.

The soil size distribution is discretized in bins between 0.0001 and 0.2 cm, equally spaced in a logarithmic scale. In our implementation of the DPM, the width of the bin (in log space) is equal to:

$$\Delta \ln(D_p^i) \;=\; \ln(D_p^{i+1/2}) - \ln(D_p^{i-1/2}) \;=\; 0.0005 \quad ,$$

where i indicates the bin number, D_p^1 is the smallest diameter and D_p^N the largest one. With $\Delta \ln(D_p^i) = 0.0005$, the total number of bins used is $N = 15201$. For each discretized diameter D_p^i we will notate by $\underline{D_p^i}$ and by $\overline{D_p^i}$ the boundaries of the i-th bin, noting that $\overline{D_p^i} = \underline{D_p^{i+1}}$. For the continuous representation of the size distribution, the particle diameter is written as D_p. Using the notation from Seinfeld and Pandis (2012), the mass distribution of soil particles for each mode and soil type is:

$$n_m^e(\ln D_p) \;=\; \frac{\mathrm{d}M}{\mathrm{d}(\ln D_p)} = \frac{M_p}{\sqrt{2\pi}\,(\ln\sigma)} \exp\left(-\frac{1}{2}\frac{(\ln D_p - \ln D_{\mathrm{med}})^2}{(\ln\sigma)^2}\right) \quad , \tag{2.1.1}$$

Label	Soil Type (ST)	Mode 1			Mode 2			Mode 3		
		D_{med}	σ	p	D_{med}	σ	p	D_{med}	σ	p
1	silty fine sand (SFS)	0.021	1.8	0.625	0.0125	1.6	0.375	0	0	0
2	medium sand (MS)	0.021	1.8	0.2	0.069	1.6	0.8	0	0	0
3	coarse sand (CS)	0	0	0	0.069	1.6	1	0	0	0
4	coarse medium sand (CMS)	0.021	1.8	0.1	0.069	1.6	0.9	0	0	0
5	fine sand (FS)	0.021	1.8	1	0	0	0	0	0	0
6	silty medium sand (SMS)	0.021	1.8	0.3125	0.069	1.6	0.3125	0.0125	1.6	0.375
7	salty medium sand (SEM)	0.0125	1.6	0.2	0.052	1.5	0.8	0	0	0
8	salty silt fort (SEF)	0.0125	1.6	0.08	0.052	1.5	0.92	0	0	0
9	clay soil (Clay)	0	0	0	0	0	0	0	0	0
10	salt waste (SW)	0.0125	1.6	0.5	0.052	1.5	0.5	0	0	0
11	agricultural soil (AGS)	0.0125	1.6	1	0	0	0	0	0	0
12	salty fine sand (SES)	0.0125	1.6	0.1	0.052	1.5	0.4	0.021	1.8	0.5
13	silty coarse sand (SCS)	0.069	1.6	0.6	0.0125	1.6	0.4	0	0	0
21	mountain, rocks, town (M)	0	0	0	0	0	0	0	0	0
22	river, water (R)	0	0	0	0	0	0	0	0	0
23	farming (Cult)	0	0	0	0	0	0	0	0	0
24	irrigated farming (Ir)	0	0	0	0	0	0	0	0	0
99	ocean (O)	0	0	0	0	0	0	0	0	0

Table 2.2: Parameters of the log-normal mass distribution for the three modes of soil particles according to soil types (soil features). The median mass diameter (D_{med}) of each mode are given in cm. Geometric standard deviation are shown in the σ column. The relative contributions (between 0 and 1) of each mode to the total are indicated in the p columns.

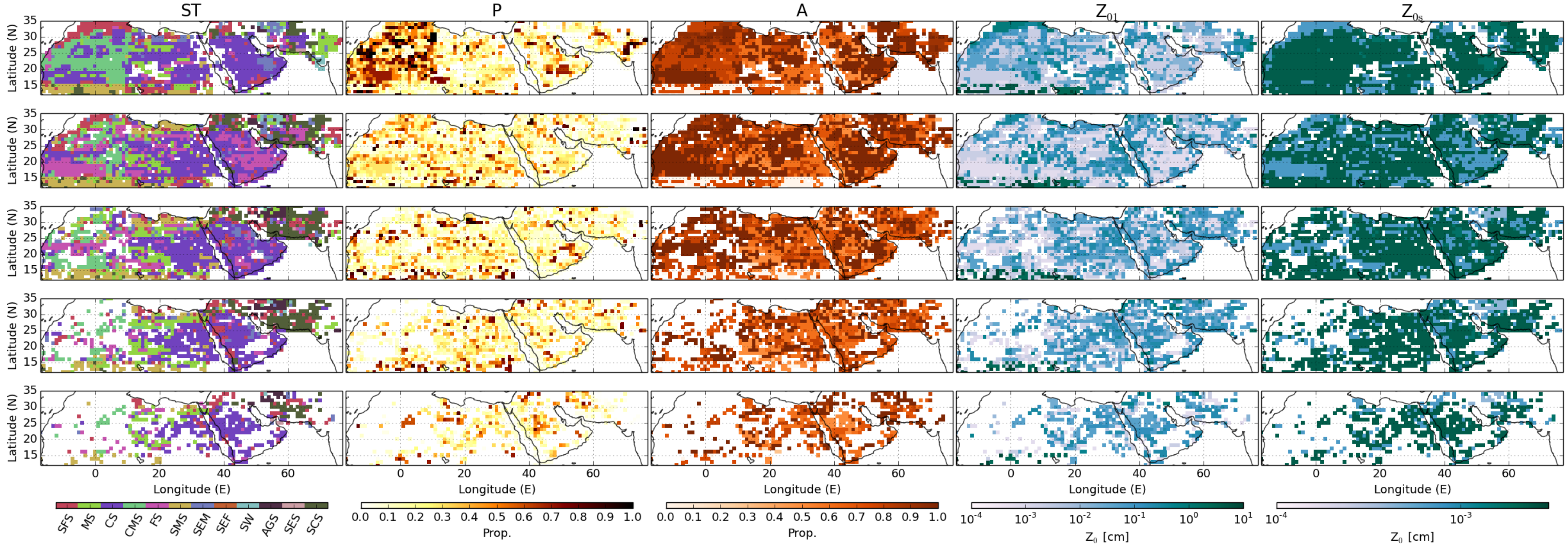

Figure 2.3: Relevant input data for the DPM. The data is shown for the 5 predominant soil types (for each pixel). *SOL* column indicates the soil type (*ST*) referenced in Table 2.2. P columns is the proportion of *ST* over the total of soil types (ranging between 0 and 1). *A* is the fraction of erodible material (ranging between 0 and 1). Z_{01} indicates the aerodynamic roughness length and Z_{0s} the smooth roughness length. Please note the different and logarithmic color scale in the last two columns.

where M_p is the total mass of the mode. Here we assume that it is possible to approximate the proportion of the surface covered by particles of type ST and diameter D_p by the proportion of the cross section of the particles of type ST and diameter D_p to the total cross section (Marticorena and Bergametti, 1995). The size distribution of the soil particle cross section is related to the mass size distribution through the equation

$$n_c^e(\ln D_p) \;=\; \frac{n_m^e(\ln D_p)}{\frac{2}{3}\,\rho_p\,D_p} \quad ,$$

where c denotes the cross section and we assume that the particles are spheres with density ρ_p. For each soil type ST, the normalized soil cross section distribution is calculated as

$$\frac{\mathrm{d}S(ST)}{\mathrm{d}\ln D_p} \;=\; \sum_{j=1}^{3} \frac{1}{\frac{2}{3}\,\rho_p\,D_p} \frac{p_j}{\sqrt{2\pi}\,(\ln\sigma_j(ST))} \exp\left(-\frac{1}{2}\frac{(\ln D_p - \ln D_{\mathrm{med},j}(ST))^2}{(\ln\sigma_j(ST))^2}\right) \quad ,$$

with j the index for each mode from Table 2.2. Recalling that

$$n_c(D_p) \;=\; n_c^e(\ln D_p)/D_p \quad ,$$

then

$$\frac{\mathrm{d}S(ST)}{dD_p} \;=\; \frac{1}{D_p}\frac{\mathrm{d}S^e(ST)}{\mathrm{d}\ln D_p} \quad .$$

We will define the relative surface contribution of each soil type and particle diameter by

$$\frac{\mathrm{d}S_{\mathrm{rel}}(ST)}{\mathrm{d}D_p} \;=\; \frac{1}{S_{\mathrm{tot}}(ST)}\frac{\mathrm{d}S(ST)}{\mathrm{d}D_p} \quad , \tag{2.1.2}$$

with

$$S_{\mathrm{tot}}(ST) \;=\; \int_{D_{\min}}^{D_{\max}} \frac{\mathrm{d}S(ST)}{\mathrm{d}D_p}\mathrm{d}D_p \quad ,$$

where $D_{\min}$ and $D_{\max}$ are the boundaries of the soil size distribution.

2.1.3.2 Wind velocity

The wind velocity from the model is the mean over the gridbox of the wind velocity. The dust emission flux being roughly proportional to the cube of the wind velocity, an accurate description of the subgrid wind velocity variability is important. The near-surface wind from the LMDZ model can be considered as being the mean over the gridbox. To have realistic dust emissions it is therefore necessary to parameterize the sub-grid scale variability of the wind velocity. We assume here that the sub-grid wind velocity can be described by a Weibull distribution which, in its continuous form, is given by the following probability density function:

$$p(u, k, A) \;=\; \frac{k}{A}\left(\frac{u}{A}\right)^{k-1} \exp\left[-\left(\frac{u}{A}\right)^{k}\right] \quad ,$$

where u is the subgrid-scale wind speed, and (k, A) are parameters of the Weibull distribution. The shape parameter k has been set equal to 3 as in Hourdin et al. (2015), and the A parameter is calculated for each grid cell and each timestep to fit the Weibull distribution expectancy with the mean wind velocity from the LMDZ model:

$$U \;=\; A\,\Gamma(1 + 1/k) \quad , \tag{2.1.3}$$

where U is the 10-meter mean wind for each gridcell and Γ the Gamma function. Previous versions of this DPM (e.g., Menut et al., 2013) assumed $A = U$. This approximation decreases the expectancy of the wind in the gridbox once the Weibull subgrid wind distribution is applied. As the DPM is highly sensitive to near surface wind velocity, the impact of this choice is important. Figure 2.4 shows both subgrid Weibull wind distributions, one calculated with Equation (2.1.3) and the other one calculated with $A = U$. It is clear from the upper panel that the $A = U$ has smaller values in the right tail of the distribution and thus the dust flux is expected to be lower. The lower panel shows the probability of both Weibull distributions of being larger than α times the mean wind, and the ratio between them. In the lower panel, the choice $A = U$ is always smaller than our choice (so the ratio between them is always larger than unity) and the ratio between them increases with α. This means that for larger winds (compared to the mean wind in the gridbox), this correction is significant. This impacts the dust emission fluxes by its polynomial dependence on the wind speed (as we will see later in Equation (2.1.4)). In practice, the sub-grid wind distribution is discretized in 12 bins, with the maximum value equal to twice the 10-meter mean wind velocity.

Over the surface, the wind friction velocity is the physical quantity that carries the wind energy information and exchanges momentum with the surface. In the DPM, the wind friction velocity is calculated assuming neutral conditions of stability, and with the LISA roughness length Z_{02}:

$$U^{*}(ST) \;= u\,\frac{k}{\ln(z_{10\mathrm{m}}/Z_{02}(ST))} \quad ,$$

with $k = 0.41$ the von Karman constant, $z_{10\mathrm{m}} = 10$ m and u the 10-meter wind velocity (for each bin of the Weibull discretization).

The DPM only emits dust if the wind friction velocity is over a threshold. In principle, the threshold friction velocity $U^{*}_{\mathrm{Shao}}(D_p)$ (in units of [m s^{-1}]) is calculated according to Shao and Lu (2000) as

$$U^{*}_{\mathrm{Shao}}(D_p) \;=\; \sqrt{a_n\left(\frac{\rho_p}{\rho_a}\,g\,D_p + \frac{\gamma}{\rho_a\,D_p}\right)} \quad ,$$

where D_p is the soil particle diameter (in units of [in m]), $a_n = 0.0123$, $\rho_p = 2.63 \times 10^3$ [kg m^{-3}]

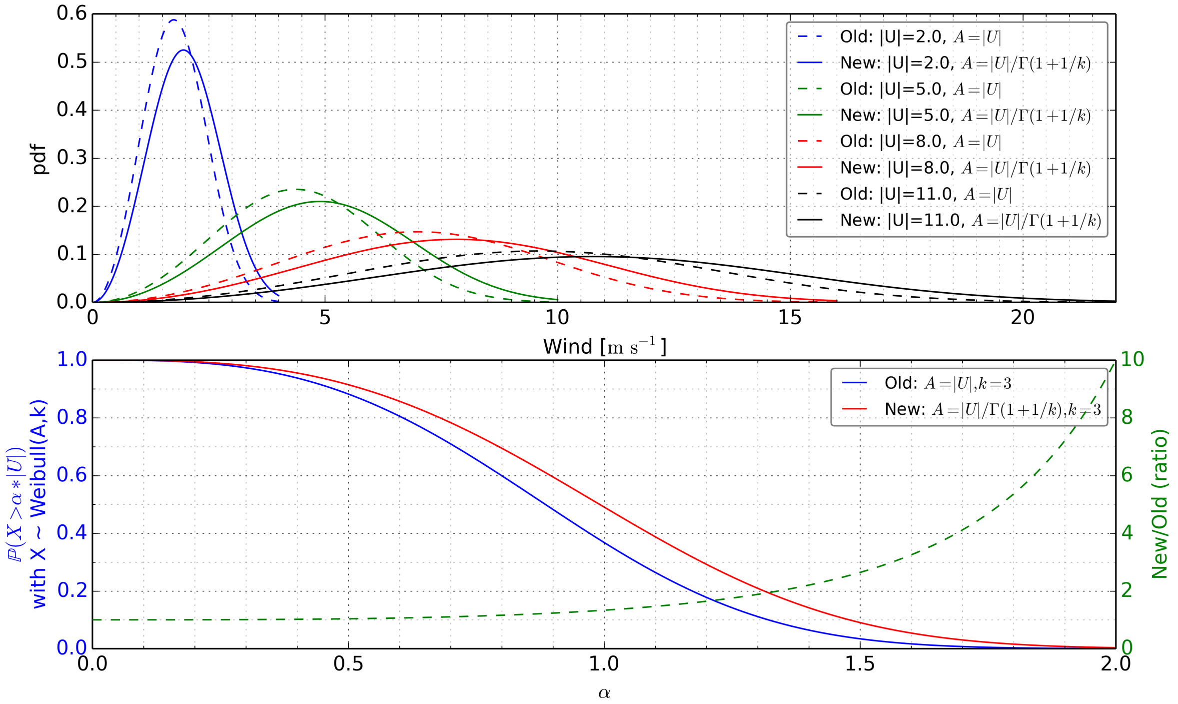

Figure 2.4: Probability density function of Weibull distribution for the original (*Old*) and the corrected (*New*) A parameter for several mean wind velocities and $k = 3$. Upper panel show the probability density function between 0 and $2 \times U$ for several values of U. Lower panel shows the probability of being larger than α times the mean wind U for both A parameters (blue and red lines) and the ratio between them (green line).

is the particle density, $\rho_a = 1.227$ [kg m^{-3}] the air density at the surface, $\gamma = 3 \times 10^{-4}$ [kg s^{-2}] and $g = 9.81$ [m s^{-2}].

The threshold friction velocity is increased depending on the surface properties in order to account for the kinetic energy partition between the soil and the roughness elements. The correction of the threshold wind velocity is calculated as in Marticorena et al. (1997) by a drag efficiency coefficient:

$$f_{\text{eff}}(ST) = 1 - \left(\frac{\ln(Z_{01}(ST)/Z_{0s}(ST))}{\ln(a_{\text{eff}}(x_{\text{eff}}/Z_{0s}(ST))^{0.8})} \right) \quad .$$

If $D_{ST} > 0$, the partition is calculated by a partition between the erodible surface and the roughness elements (as in the previous equation), multiplied by a partition between two kinds of roughness elements (Marticorena et al., 1997) as:

$$f_{\text{eff}}(ST) = \left[1 - \left(\frac{\ln(Z_{02}(ST)/Z_{01}(ST))}{\ln(a_{\text{eff}}(D_{ST}/Z_{01}(ST))^{0.8})} \right) \right] \left[1 - \left(\frac{\ln(Z_{01}(ST)/Z_{0s}(ST))}{\ln(a_{\text{eff}}(x_{\text{eff}}/Z_{0s}(ST))^{0.8})} \right) \right] \quad ,$$

with $a_{\text{eff}} = 0.35$, $x_{\text{eff}} = 10$ and the others parameters taken from the LISA database. Finally, the used threshold friction velocity is:

$$U_t^*(D_p, ST) = \frac{U^*_{\text{Shao}}(D_p)}{f_{\text{eff}}(ST)} \quad .$$

2.1.3.3 Horizontal flux

The horizontal flux dust is calculated according to the Marticorena and Bergametti (1995) saltation scheme, and multiplied by the contributions of the ST to the total soil surface (P from Figure 2.3) and by the fraction of erodible surface (A from Figure 2.3) as in Laurent et al. (2008):

$$\frac{\mathrm{d}F_h(ST)}{\mathrm{d}D_p} = P(ST)\,A(ST)\,\frac{K\,\rho_a\,U^*(ST)^3\,\frac{\mathrm{d}S_{\text{rel}}(ST)}{\mathrm{d}D_p}}{g}\left(1+\frac{U_t^*(D_p, ST)}{U^*(ST)}\right)\left(1-\frac{U_t^*(D_p, ST)^2}{U^*(ST)^2}\right) \ , \tag{2.1.4}$$

where ST is the soil type, D_p is the soil particle diameter, K is a constant value, ρ_a is the air density, g is the gravitational constant, U^* is the friction velocity (which depends on the soil type through the saltation roughness length parameter), U_t^* is the threshold friction velocity, and $\mathrm{d}S_{\text{rel}}(ST)/\mathrm{d}D_p$ is defined in Equation (2.1.2). In the case of $U_t^*(D_p, ST) > U^*(s)$, the friction velocity threshold is not reached by the model and there is no emission ($\mathrm{d}F_h(ST)/\mathrm{d}D_p = 0$). In this work, the value of K was set to its original value of 2.61 (Marticorena and Bergametti, 1995) instead of the value of 1.0 used in Hourdin et al. (2015) and in Menut et al. (2013). We will justify this choice later in this section.

As a side note, Equation (2.1.4) is derived from the formulation of White (1979). In this article the equation is written twice, in the *abstract* and in *Eq. 22*; but one of them is wrong. In fact, the *abstract* equation reads:

$$q = \frac{2.61\,\rho}{g}(V_* - V_{*t})(V_* + V_{*t})^2 \quad ,$$

with q the emitted flux (in units of [g cm^{-1} s^{-1}]), while the *Eq. 22* is written as

$$q = \frac{2.61\,\rho\,V_*}{g}\left(1-\frac{V_{*t}}{V_*}\right)\left(1+\frac{V_{*t}^2}{V_*^2}\right) \quad .$$

These two equations are actually not equivalent. The mistake in White (1979) is the derivation of Eq. 22 from Eq. 17. The correct equation is the one in the *abstract*, which is consistent with the one used by Marticorena and Bergametti (1995). However, a couple of publications copied the incorrect formulation, as in Chapter 5 of Knippertz and Stuut (2014) or in Menut et al. (2005) (but later corrected in Menut et al. (2013)).

	Mode 1	Mode 2	Mode 3
d	1.5	6.7	14.2
σ	1.7	1.6	1.5
e	3.61	3.52	3.46

Table 2.3: Dust mass size distribution and binding energies parameters for the sandblasting scheme (from Alfaro and Gomes (2001)). The parameters from the log-normal size distribution (similar to Equation (2.1.1)) are the median diameter (d) in µm and the geometric standard deviation σ. Binding energies e are expressed in [g cm^2 s^{-2}]. Binding energies used in this work differ from the energies shown in this table by a factor 1/6 (see text).

Case	p_1	p_2	p_3
$e_c < e_3 < e_2 < e_1$	0	0	0
$e_3 < e_c < e_2 < e_1$	0	0	1
$e_3 < e_2 < e_c < e_1$	0	$(e_c - e_2)/(e_c - e_3)$	$1 - p_2$
$e_3 < e_2 < e_1 < e_c$	$(e_c - e_1)/(e_c - e_3)$	$(1 - p_1)(e_c - e_2)/(e_c - e_3)$	$1 - p_2 - p_1$

Table 2.4: Fractions (p_i) of kinetic energy used to release particles from the three aerosol modes (from Alfaro and Gomes (2001)).

2.1.3.4 Vertical flux

The vertical flux is calculated according to Alfaro and Gomes (2001) sandblasting flux scheme. In this model, dust particles are emitted into the atmosphere (vertical flux) due to the impact between particles in the horizontal flux and the soil. Released particles can be either from the saltation flux or from the soil. The model assumes that the emitted particles are described using a combination of three fixed modes, independent from the soil type (Table 2.3).

Kinetic energy of each dust particle (in the horizontal flux) is calculated as:

$$e_c(D_p, ST) = \frac{100\,\pi}{3}\,\rho_p\,D_p^3\,U^*(ST)^2 \quad .$$

The model assumes that the quantity of dust emitted by each of the three modes from Table 2.3 depends on the kinetic energy of the saltation particles and the binding energy of each mode. The relative proportion of emitted dust of each mode is calculated from Table 2.4. For low kinetic energy of the particles (resulting, for example, from weak –but above the threshold– surface winds), only coarser mode particles (i.e., Mode 3 from Table 2.3) can be emitted due to its lower binding energy. In the case of larger kinetic energy the soil will release particles of the Mode 2 (from Table 2.3), and if the kinetic energy is large enough, it will emit the finer mode particles (i.e., Mode 1 from Table 2.3).

The vertical (sandblasting) flux is calculated for each of the three modes ($j = 1, 2, 3$) by

$$\frac{\mathrm{d}F_{v,j}(ST)}{\mathrm{d}D_p} = \frac{\pi}{6}\,\beta\,\rho_p\,\frac{p_j(D_p, ST)\,d_j^3}{e_j}\,\frac{\mathrm{d}F_h(ST)}{\mathrm{d}D_p} \quad ,$$

where $\beta = 16300$ cm s^{-2}, ρ_p is the particle density [in g cm^{-3}], d_j is the mass median diameter for the mode j of Table 2.3 [in cm], e_j is the binding energy for mode j, p_j is the fraction of kinetic energy for the mode j for a particle with kinetic energy $e_c(D_p, ST)$. For each of the three modes of the sandblasting scheme, the total dust flux for mode j is calculated by the sum of the contributions of all soil types and soil particle diameters:

$$F_{v,j} = \sum_{ST} \int_{D_p^{\min}}^{D_p^{\max}} \frac{\mathrm{d}F_{v,j}(ST)}{\mathrm{d}D_p} \mathrm{d}D_p \quad .$$

The previous equation is discretized as

$$F_{v,j} = \sum_{ST} \sum_{i=1}^{N} \int_{\underline{D_p^i}}^{\overline{D_p^i}} \frac{\mathrm{d}F_{v,j}(ST)}{\mathrm{d}D_p} \mathrm{d}D_p \quad ,$$

where the integral is calculated as

$$\int_{\underline{D_p^i}}^{\overline{D_p^i}} \frac{\mathrm{d}F_{v,j}(ST)}{\mathrm{d}D_p} \mathrm{d}D_p = \frac{\pi}{6} \beta \rho_p \frac{p_j(D_p^i, ST)\, d_j^3}{e_j} \int_{\underline{D_p^i}}^{\overline{D_p^i}} \frac{\mathrm{d}F_h(ST)}{\mathrm{d}D_p} \mathrm{d}D_p \quad ,$$

and the discretization of the horizontal flux is given by

$$\int_{\underline{D_p^i}}^{\overline{D_p^i}} \frac{\mathrm{d}F_h(ST)}{\mathrm{d}D_p} \mathrm{d}D_p = P(ST)\, A(ST)\, \frac{K \rho_a U^*(ST)^3}{g} \times \\ \left(1 + \frac{U_t^*(D_p^i, ST)}{U^*(ST)}\right) \left(1 - \frac{U_t^*(D_p^i, ST)^2}{U^*(ST)^2}\right) \int_{\underline{D_p^i}}^{\overline{D_p^i}} \frac{\mathrm{d}S_{\mathrm{rel}}(ST)}{\mathrm{d}D_p} \mathrm{d}D_p \quad .$$

The vertical flux is calculated for each dust mode and bin of the discretization of the wind velocity. The vertical flux by dust mode is calculated as the sum of the contributions of each wind bin discretization and then distributed in the three SPLA aerosol modes: fine mode aerosols, coarse mode dust and super-coarse mode dust.

Some of the key parameters of this scheme are the binding energy parameters (e_j from Table 2.3), that account for the necessary energy to release particles in the sandblasting processes for each soil mode used in the scheme. The work by Sow et al. (2011) shows that these binding energy parameters cannot be constant if emissions are to be fitted to in situ emission flux measurements. They may instead depend on the strength of the dust event. Sow et al. (2011) divide the binding energy parameters by a factor 2.5 in the case of a strong dust event, and by a factor of 5 in the case of a weaker event to fit in situ emission flux measurements. We also chose to tune the binding energy parameters and divide it by a factor 6. This is somewhat an arbitrary choice but is partly justified by the fact that we are interested in simulating the dust flux emission for a long period (and not only for dust events).

Data assimilation systems are sensitive to biases. In particular biases in the observations and in the observation operator (the LMDZ-SPLA model in our case) could deteriorate the analyses performance. To avoid this problem and to have a mean simulated AOD in the range of the (satellite and ground-based) observations, we apply an additional tuning multiplicative factor equal to 3.25 to the coarse and super-coarse dust emissions and 0.8 to the fine mode dust emissions. The tuning factor is not the same for the three emission bins due to the known overestimation of fine mode dust emissions in the DPM relative to the coarser modes (Nabat et al., 2012). This tuning has the only objective of making the prior AOD unbiased for the assimilation, and it was estimated by comparing the model mean AOD (and Ångström coefficient) and the observational one. The tuning factor (per emission bin) is unique for all periods and all regions. Later in this thesis we will show the assimilation results, where the elements in the control vector are indeed correction factors over the emissions, but with larger spatial and temporal variability. The analysis correction factors can be interpreted as multiplicative factors of these tuning parameters, after the information of the assimilated observations are incorporated into the system.

A second parameter was modified from the Hourdin et al. (2015) DPM, and it is the K parameter from Equation (2.1.4). This parameter is also a multiplicative factor of the emission flux. The model proposed by White (1979) (and then by Marticorena and Bergametti (1995)) uses $K = 2.61$. Later, Menut et al. (2005, 2013) and Hourdin et al. (2015) have used $K = 1$, based on the work by Gomes et al. (2003) who cites the work of Gillette and Chen (2001). In this latter work, the authors do not use exactly the same equation as White and they recommend to use smaller values (less than the unity) for supply-limited sources and larger values for supply-unlimited sources. Following the results of their field experiment, they recommend a mean value of $K = 1.1$ for a *typical* dust emission event. However, the experiment was performed in a site in the Chihuahuan desert (in New Mexico, United States) and they found a large dispersion of the calculated K value, ranging between 0.007 to 20 depending on the surface properties and the dust event. We think that an extrapolation of $K = 1$ (calculated in a sandy soil texture) to the whole Sahara desert is as arbitrary as choosing $K = 2.61$, the value proposed by White (1979). Additionally, this K parameter scales the emissions, so in practice, if we had chosen $K = 1$ we would have multiplied by 2.61 the tuning factors described in the previous paragraph in order to have an unbiased AOD suitable for the assimilation.

Figure 2.5 shows the calculated dust flux emission for the year 2006 over the Sahara and the Arabian Peninsula with the DPM described in this Section. Figure 2.6 shows the total emissions by month for the three dust modes of SPLA. The hour of emission is indicated in colors in the Figure. These emissions have been approximated using hourly instantaneous outputs from the model. More accurate emission fluxes are show in Figure 4.6. Figure 2.6 shows that a large part of the emission occurs before midday, in qualitative concordance with the daily cycle of dust emissions described in Tegen et al. (2013).

2.1.4 Other emissions

Along with the dust emissions presented in the previous section, we have included emissions for sea spray, biomass burning and industrial emissions. The configuration for these emissions is

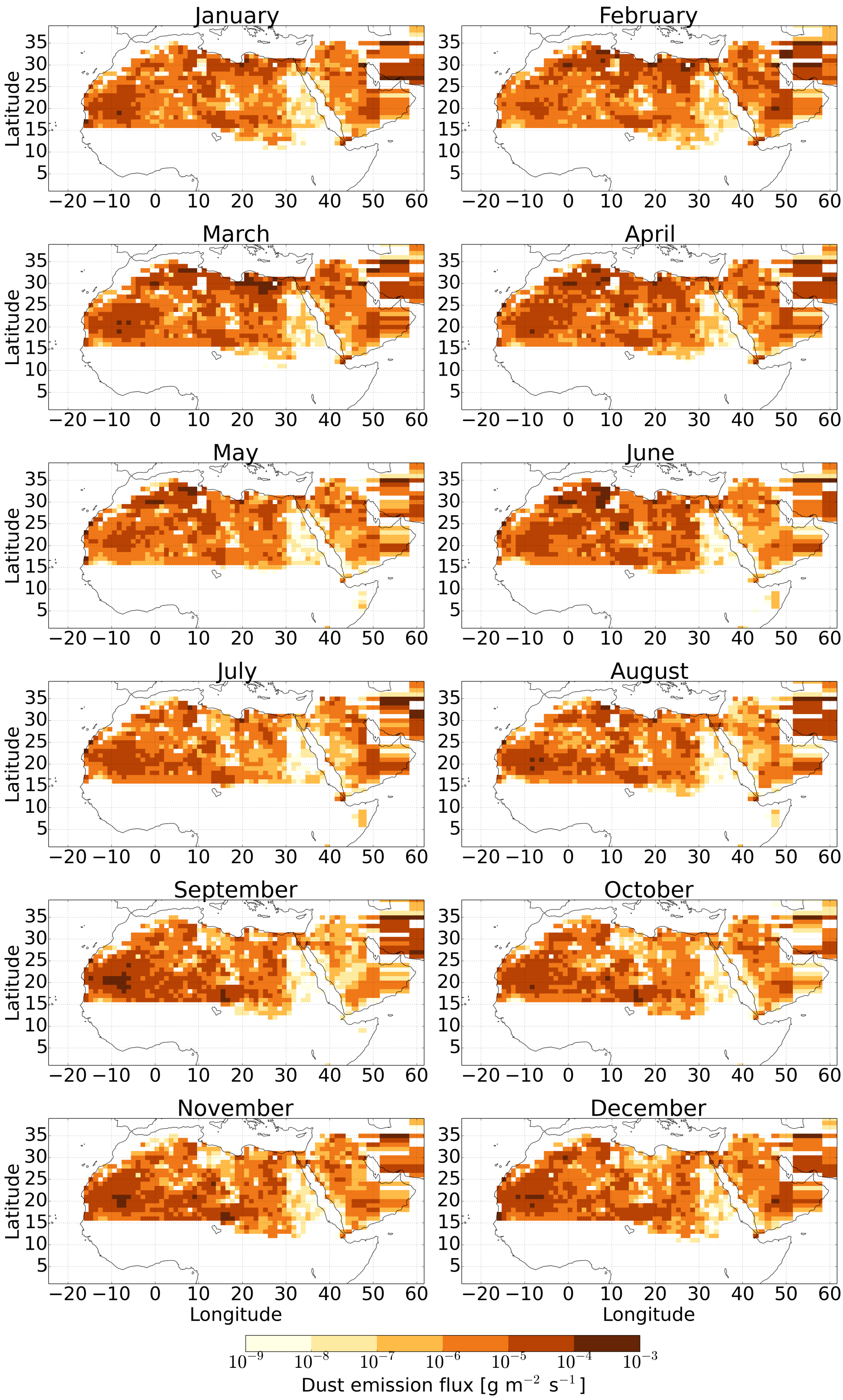

Figure 2.5: Monthly averages of dust emissions for the year 2006 (in units of g m^{-2} s^{-1}). Please note the logarithmic color scale.

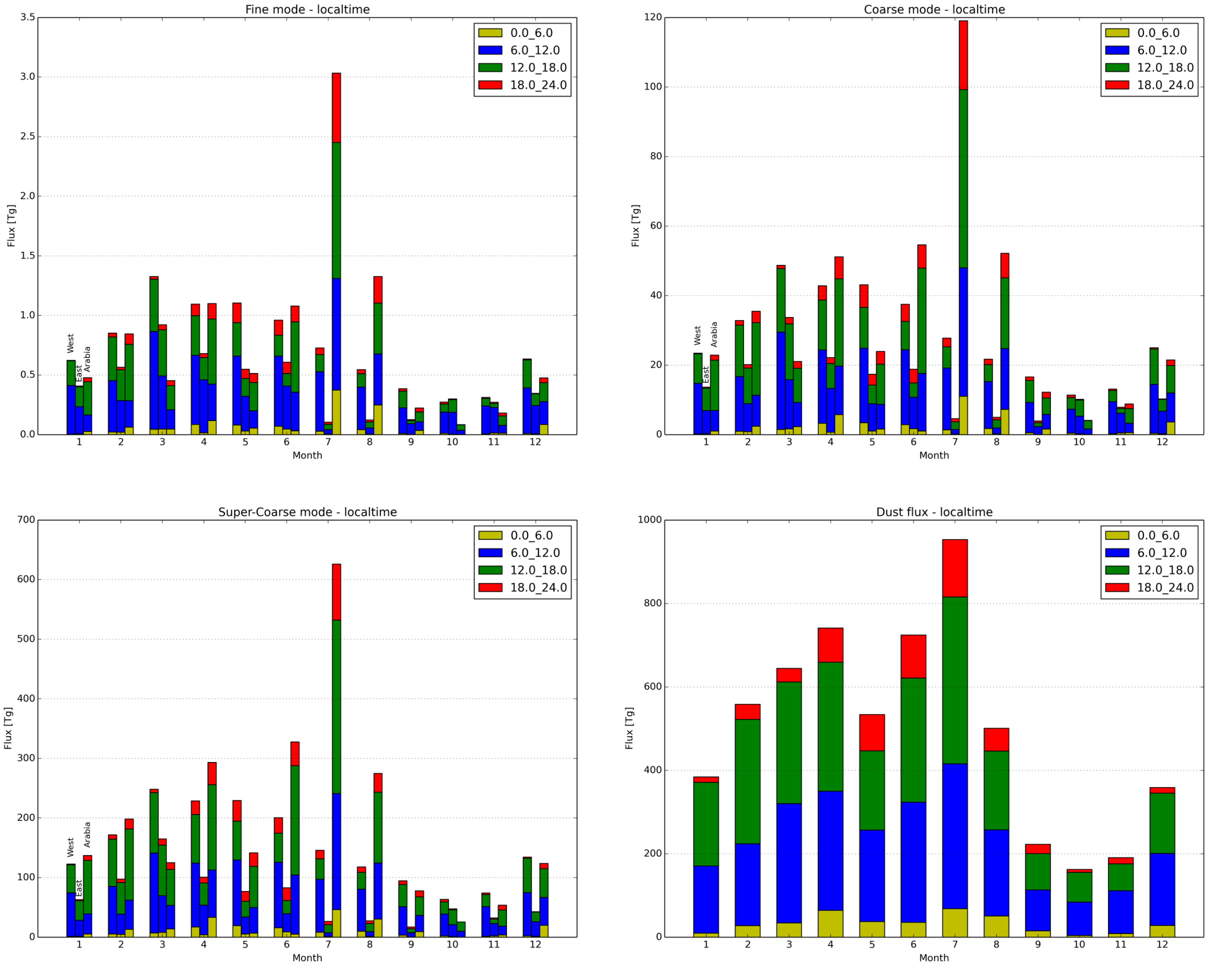

Figure 2.6: Total flux by month approximated from the hourly instantaneous outputs of the model. The Saharan desert is split into two regions, East (20°W to 14°W) and West (14°W to the Red sea). The Arabian region includes the Arabian Peninsula and the near the Middle East (eastern limit of 65°W and 40°N in the north). The colors represent the quantity of dust emitted for each time windows, in the local time (solar time).

described in Huneeus et al. (2013). As a brief summary, biomass burning (BB) emissions are taken from the GFED 3.1 inventory (van der Werf et al., 2010). The species used in this thesis from this inventory are black carbon (BC), particulate organic matter (POM) and SO_2.

Fossil fuel and industrial emissions were taken from the Lamarque et al. (2010) inventory, also for BC, POM and SO_2. Terpene emissions are taken from Lathière et al. (2006), Volcanic emission (SO_2) are prescribed, as in Huneeus et al. (2013), by the inventory prepared in Dentener et al. (2006). Sea salt emissions are calculated with the parameterization of Monahan et al. (1986) using ERA-Interim 10-meter wind speed. Dimethyl sulphide (DMS) emissions were updated with the near-surface climatology of DMS provided in Lana et al. (2011), and the fluxes were calculated with the parameterization of Nightingale et al. (2000) with ERA-Interim 10-meter wind speed.

2.2 Observations

In this section we will describe the observations used in this work. We assimilate the AOD derived from five satellite-borne instruments and we evaluate the analysis simulations using independent AOD measurements from the ground-based Aerosol Robotic Network (AERONET).

2.2.1 Satellite observations

Satellite observations are shown in Figure 2.7. This section describes the source of the information and the preprocessing procedures applied to the AOD products of Figure 2.7.

2.2.1.1 MODIS observations

The MODIS instrument is a 36 spectral band spectroradiometer on-board two low-orbiting sun-synchronous satellites, Terra and Aqua. The instrument has a swath of 2330 km at nadir and a spatial resolution of 1 km (or less, depending on the channel) for visible and near-visible bands. MODIS/Terra was launched in December 1999 in a near-polar descending orbit (i.e., that crosses the Equator from north to south at daytime). MODIS/Aqua was launched in the year 2002 with a near-polar ascending orbit. Aqua is part of the “A-Train” constellation. Terra overpasses the Equator at $\approx$ 10:30 Local Time (LT), while Aqua does it at $\approx$ 13:30 LT. Since the satellite launch, the AOD retrieval procedures have been continuously improving. We use Collection 6 of the MODIS AOD products, which use the same retrieval scheme for both platforms (Aqua and Terra). However the calibration of the two instruments differ, hence there could still be some (small) inconsistencies between the two MODIS aerosol products in addition to a different overpass time.

The MODIS retrieval algorithm uses reflected radiances at four wavelengths to calculate AOD at 550 nm. There are three algorithms to calculate AOD from MODIS radiances. Over ocean it is

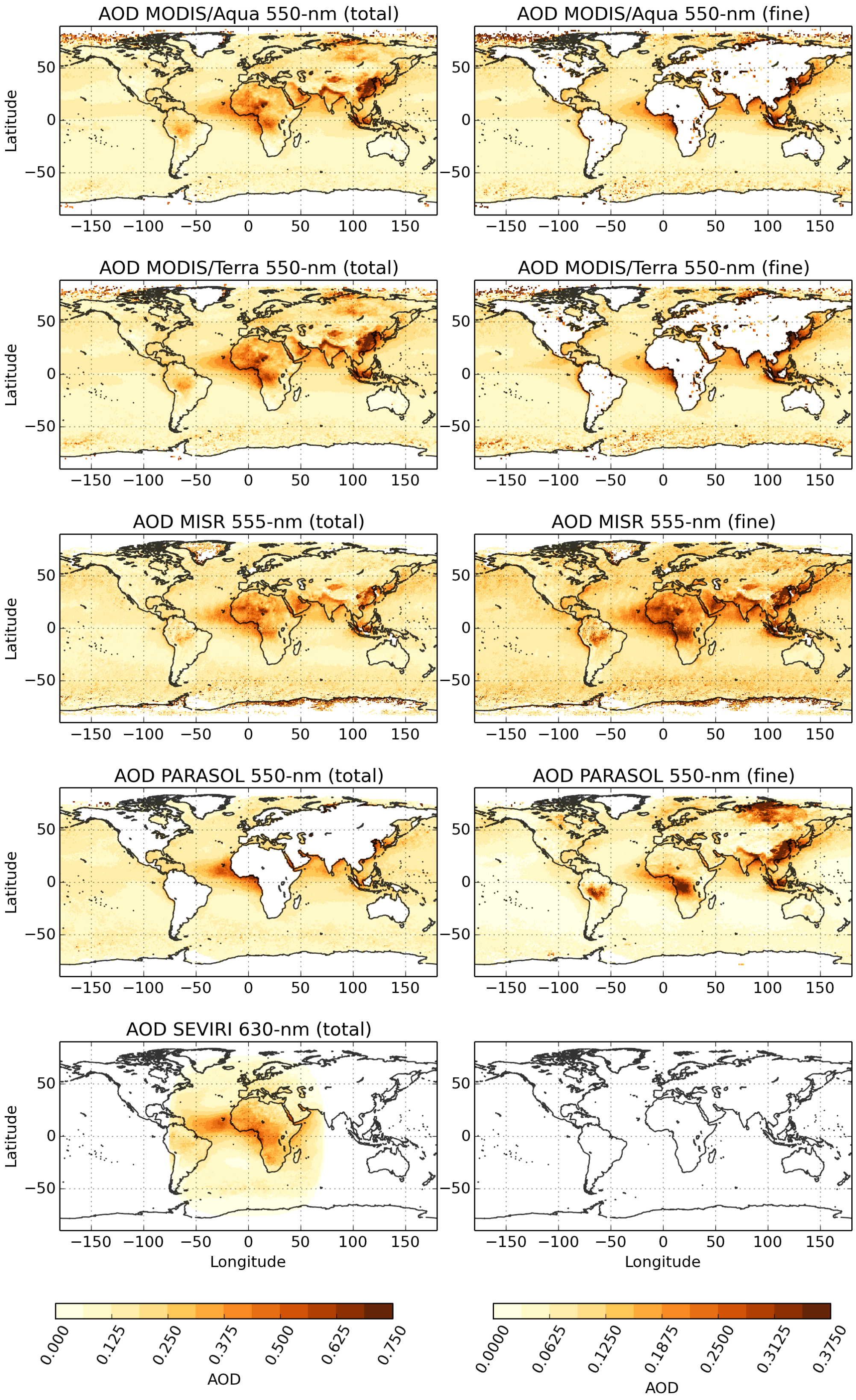

Figure 2.7: Averages for the year 2006 of the satellite-derived AOD used in this study, in a regular latitude-longitude grid of 0.5 degree resolution. Total AOD is shown on the left column and fine mode AOD on the right column (when available). Please note the different color scales between both columns and the different wavelengths of the reported AOD.

calculated with the “Dark Target” (DT) algorithm (Levy et al., 2013) which reports total 550 nm AOD and the proportion of this AOD due to fine aerosols (fine AOD) at 550 nm. Over land where the surface is “dark” enough (reflectance less 0.25 at the near infrared MODIS channel), only total AOD from the DT over land algorithm (Levy et al., 2013) is reported. Over brighter surfaces, the “Deep Blue” (DB) algorithm (Sayer et al., 2013) is preferred. Despite the fact that MODIS retrievals are reported in several wavelengths (e.g. 550, 670 and 865 nm for DT), in this work we only use AOD at 550 nm.

MODIS AOD retrievals are reported at horizontal resolutions of 3 and 10 km in their Level 2 product. MODIS 550 nm AOD uncertainties are quantified against a reference AOD (AERONET). Levy et al. (2013) define the expected error (EE) as the bounds that contains the 67% of the matchups between the reference AOD and the satellite AOD. For DT over land, this envelope is symmetrical around zero:

$$EE = \pm(0.05 + 0.15\,\tau_A) \quad ,$$

where τ_A is the reference AOD. Over ocean, the bounds for the EE are:

$$[-(0.02 + 0.1\,\tau_A)\,,\, +(0.04 + 0.1\,\tau_A)] \quad .$$

Despite the fact that the EE for the DB product in Sayer et al. (2013) is calculated using a reference AOD, Sayer et al. (2013) develop an expected error as a function of the DB AOD, and not against a reference AOD. Additionally and by the nature of the DB algorithm (that uses radiances at shorter wavelengths), the error of the DB AOD is highly dependent on the satellite viewing angle. This is quantified by the geometric atmospheric mass factor (AMF, the sum of the cosines of the solar and viewing angles). The EE envelope given by (Sayer et al., 2013) is:

$$EE = \pm\frac{0.086 + 0.56\,\tau_M}{\mathrm{AMF}} \quad ,$$

where τ_M is the DB AOD. Smaller AMFs (≈ 2) are reached when the satellite crosses the Equator, while larger ones can be found at mid and high latitudes. For an average AMF of the MODIS overpass (AMF= 2.8), they define an EE by:

$$EE = \pm(0.03 + 0.2\,\tau_M) \quad .$$

We use the Level 3 product, also provided by the MODIS team, which is calculated from the Level 2 product with additional filters over the quality of the AOD data. Horizontal resolutions of the Level 3 AOD is 1 degree in a latitude-longitude projection and additionally to the DT and DB products, a “Merged” product (Sayer et al., 2014) is produced and distributed. Over ocean the Merged AOD is the same as the DT AOD, but over land, if both DB and DT report valid AOD in the Level 2, the Merged product is a combination of both, and in general it is more accurate than either one of DT or DB (Sayer et al., 2014).

Due to the difference in type of surfaces and algorithms, the Merged product can exhibit discontinuities in the horizontal AOD field, especially along the coast and over transition regions (e.g. between an arid/semi-arid region and a vegetated region). Additionally, Sayer et al. (2013) indicates that the DB product is likely to underestimate AOD over deserts, and we will be concerned about this problem in the design of the adaptive bias correction in Chapter 6.

The Level 3 Merged 550 nm AOD is interpolated onto the model grid before the assimilation. The interpolation process will be presented in Section 2.2.1.5

2.2.1.2 MISR observations

The Multiangle Imaging SpectroRadiometer instrument (MISR, Diner et al., 1998) on-board the Terra satellite is a spectroradiometer with 36 channels, with four visible and near-infrared spectral bands. It can measure radiances from a given target with up to nine viewing angles (Kahn and Gaitley, 2015). At nadir, the swath of MISR is 380 km and the Level 2 AOD retrieval is reported at approximately 17.6 km resolution. The instrument observes the same atmospheric column from different viewing angles and for several air mass factors in a short period of time, which allows the retrieval algorithm to distinguish contributions from the surface and the atmosphere in the observed reflectance. Thus more information regarding the aerosol microphysics (Kahn et al., 2005) can be retrieved than for nadir-only instruments (e.g., MODIS).

Level 3 products are calculated from Level 2 AOD gridded in a regular latitude- longitude mesh of 0.5 degrees of resolution. Total AOD in Levels 2 and 3 are reported for the following wavelengths: 446, 557, 672 and 867 nm. The 557 nm wavelength is usually considered equivalent to 555 nm. The retrieval AOD is split into the AOD due to spherical and non-spherical aerosols, and into the AOD due to small (less than 0.35 μm of radii), medium (between 0.35 μm and 0.7 μm of radii) and large (more than 0.7 μm of radii) aerosols.

For the total AOD, Kahn et al. (2005) estimate the EE at 555 nm by

$$EE = \pm \max(0.05, 0.2\,\tau_A) \quad ,$$

with τ_A the AERONET AOD.

In this work use the Level 2 AOD, from the algorithm version 22 (Kahn and Gaitley, 2015). The process of estimating MISR AODs for total and fine mode (less than 0.5 μm of radii) as per our observation operator is described in Section 2.2.1.5.

2.2.1.3 PARASOL observations

Onboard the Polarization and Anisotropy of Reflectances for Atmospheric Sciences coupled with Observations from a Lidar (PARASOL) satellite, the POLarization and Directionality of the Earth's Reflectances (POLDER, Tanré et al., 2011) instrument measures reflected radiance in

9 spectral bands in the visible and near-infrared part of the electromagnetic spectrum. The POLDER instrument measures polarization in three of the 9 channels, and has several viewing directions along track and across track. Between the PARASOL launch in December 2004 and December 2009, the satellite was orbiting in the "A-train", along with the Aqua satellite.

The AOD retrieval algorithm takes advantage of the instrument polarization and multi-directional capabilities and report fine and coarse 670 and 865 nm AOD over ocean and the 865 nm fine AOD over land with their corresponding Ångström coefficient. The native resolution of Level 2 (daily) products is 18.5 km at nadir.

From Level 2 binary files (from Cloud-Aerosol-Water-Radiation Interactions, ICARE) the AOD is interpolated to 550 nm and then regridded onto a regular latitude-longitude with a resolution of 0.5 degrees using routines provided by François-Marie Bréon (LSCE). The data are then interpolated to the model grid with the procedure described in Section 2.2.1.5.

The "typical accuracy" of the ocean total AOD is shown in Tanré et al. (2011) by

$$\pm 0.05 \pm 0.05\,\tau \quad ,$$

where τ is the reference AOD. This estimate was calculated in Goloub et al. (1999) for the same algorithm, but for a previous POLDER instrument. Over land, the AOD is calculated only for the accumulation mode, because the algorithm only uses measured polarized radiance which are only sensitive to the smaller particles. To calculate AOD over land, the algorithm assumes that there are no coarser particles and uses a refractive index typical of biomass burning or polluted conditions (Tanré et al., 2011) of $1.47 + 0.01\,i$. Over bright (land) surfaces and over source regions the quality of the retrieved AOD could be lower than the ocean retrievals (Tanré et al., 2011), and also large amounts of coarse dust over land can contribute to the measured polarized light, a signal that can be misinterpreted by the retrieval algorithm as fine dust.

2.2.1.4 SEVIRI-AERUS observations

The above-mentioned instruments are carried by low orbiting satellites in sun-synchronous orbits. They overpass a point of the Earth over the Equator at most once during daylight and once during nighttime (keeping in mind that passive instruments cannot retrieve visible AOD in nighttime). On the contrary, the SEVIRI instrument on-board the geostationary satellite MSG (Meteosat Second Generation) captures a full-disk image of the Earth each 15 minutes; covering Europe, Africa and the eastern Atlantic Ocean.

All the above-mentioned satellite derived AOD products use the spectral signature of aerosols and surface reflectance to estimate the AOD. In contrast, Carrer et al. (2010) and Carrer et al. (2014) take advantage from the high temporal and spatial resolution of the SEVIRI images to produce an AOD product at 630 nm. The algorithm uses the multiple radiance measurements for different solar angles to derive, using only the 630 nm SEVIRI channel, surface reflectance and AOD simultaneously. Over land, the surface is modelled with a Bidirectional Reflectance Distribution Function (BRDF) and over ocean is assumed Lambertian. The parameters of the surface reflectance models are calculated for each day (along with the AOD), with assumptions on their timescales. For each day, the final AOD product is calculated with a filtering method using the 15-minute acquired images. The variance of the AOD error reported in the daily AOD is the variance of the analysis errors from this filter. We will use this error estimate in Chapter 5.

In this work, we filter the SEVIRI AOD products by only using the AOD calculated with information from the same day of the measurements; i.e., only using pixels when the flag "ZAge" is equal zero (D. Carrer, personal communication). This filter eliminates suspicious large and isolated AOD values over the tropical Atlantic Ocean.

2.2.1.5 Satellite interpolation procedure

To be compared with the model outputs, all observations are gridded into the model grid, which is a latitude–longitude grid with a zoom in it, which means that the grid size is not the same in all the pixels. Figure 4.2 shows the model grid used in this work. The source (observational) grid is usually finer than the model grid.

There are several standard interpolation procedures for meteorological data which can be used for our purposes. The "nearest neighbour" method finds the closest grid center of the source grid to the new grid and assigns this value to the new field. This could be highly inaccurate if the two grids have different resolutions, in addition with the potential large information loss. Linear and bilinear interpolation are a common choices for interpolating meteorological model data. For each grid point in the new grid, these methods need valid data from all the source grid points that provide information to the new grid point (close in latitude and longitude). Satellite observations usually show large amounts of pixels with missing data, which propagates the missing data to the new grid if it is coarser than the source grid, leading to an important information loss.

The general interpolation procedure for satellite observations used in this work is similar to the bilinear method, but it can handle the quantity of missing data in the new grid. We have written a *weighted-average* interpolation method that we will describe in the following paragraph.

For each model gridbox (blue lines in Figure 2.8), the area contribution of each source gridbox (green lines in Figure 2.8) to the model gridbox (most of them will be zero but not if both gridboxes overlap) is calculated. If the area covered by valid data in the source grid (green filled squares in Figure 2.8) is larger than a (configurable) threshold, then the value of the observation in the model grid is the average of the observations in the source grid, weighted by their relative contribution to the covered area of the model grid. If the threshold is not reached, the model observation is set to missing data.

In this work, the threshold parameter is set to 30%, which means that at least 30% of the area (per gridbox) have to be covered by valid observations to calculate the interpolated observations. If the threshold was set to 100%, only fully-covered gridbox would be set as valid data in the

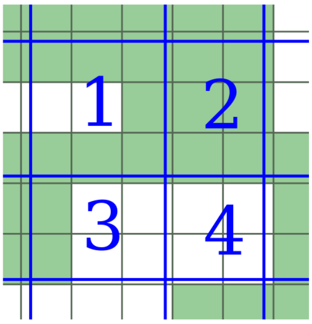

Figure 2.8: Schematic showing our interpolation method for observations. The blue lines represent the model grid, and the green lines the source grid. Square painted green represent valid data.

interpolated grid (number 2 in Figure 2.8). On the contrary, if the threshold is small, gridboxes like the numbers 3 or 4 of Figure 2.8 can be set as valid data, even though the overlap with valid source data is small. A value of 30% is a compromise between these two extremes, that gives a total data coverage similar to the source data. If the source data has all the gridbox with valid values, our method should give the same interpolated field as the one resulting from a bilinear interpolation. This method could be easily adapted to interpolate emission fluxes, changing the average operator by a weighted sum of the input data, and setting the threshold to zero.

MODIS and PARASOL data were interpolated with the method described above from a 0.5 degree resolution latitude-longitude grid to the model grid. SEVIRI AOD product has a higher resolution over North Africa (order of km), so the interpolation was done directly into the model grid. SEVIRI products reports the variance of the AOD error by pixels. To calculate the interpolated variance of AOD errors for this product, we assume that all the SEVIRI AOD errors within each model grid are fully correlated and gaussian distributed. This was done because the error covariances between nearby pixels are not reported in the standard SEVIRI product, and a fully correlation assumption seems to be more plausible than a zero-correlation assumption. However, it is expected that the true covariance lies between these two extremes. Additionally, with this assumption of fully-correlated errors it is possible to conserve the spatial structure of the errors variance in the model grid.

The interpolation procedure for MISR AOD was done in two steps. First, the fine and total AOD is calculated from Level 2 outputs and interpolated to a regular latitude-longitude grid of 0.5 degrees of resolution. Secondly, the above-mentioned interpolation method was use to regrid the AOD to the model grid. The next paragraph explains the first step of the MISR interpolation procedure.

2.2.1.6 MISR AOD redefinition of bins

As stated earlier, the standard MISR Level 3 product reports AOD for three aerosol size ranges: small, medium and coarse. Regrettably, the cut-off sizes of these bins do not match with the SPLA bins, with the cut-off between coarse and fine modes being close to the center of the MISR medium size classification.

The MISR algorithm finds the best fit between the simulated radiances given by 74 aerosol mixture models (Kahn and Gaitley, 2015) and the radiances observed by the satellite. The mixture models are themselves combinations of 8 basic aerosol types.

Fortunately, the key parameters of these models are well documented, and they are part of the standard Level 2 products. Additionally, optimum fit parameters for each model are also reported in the Level 2 products, along with the optical properties and parameters of the size distributions of the aerosol models. With this information, it is possible to calculate the contribution of each of the 8 basic aerosol types to the optimal fit given by the MISR algorithm.

With this disaggregated AOD by aerosol type and with the size distribution and optical aerosol parameters it is possible to approximately calculate the contribution arbitrary defined size bins to the total AOD. The approximation is because the size dependent extinction coefficients for each model are not reported in the Level 2 products and only the bulk extinction coefficients are given. In this step we assume homogeneity of the extinction coefficient over all the aerosol model size range. The error produced by the extinction coefficient assumption is in practice less than 5% of the total AOD value, for less than the 5% of the recalculated pixels.

The size bins were defined by the SPLA size bins limits, and then the MISR Level 2 AOD were calculated for these size bins. The last step is to filter the AOD by the quality flags reported in the MISR product, and regrid the data from the native Level 2 MISR grid (Space Oblique Mercator projection) to a regular latitude-longitude grid.

2.2.2 Ground-based observations

For validation purposes, we use AOD from the AERONET ground-based network of sunphotometers (Holben et al., 1998). It is common that the satellite AOD products are evaluated and, sometimes adjusted, by using AERONET data. Despite this, we will consider AERONET data and satellite-derived AOD to be independent observations, even if strictly speaking they are not independent.

AERONET is a network of sunphotometers with a large global and temporal coverage. The network is composed by hundreds of CIMEL sunphotometers over the globe, which are calibrated regularly (approximately once per year). Some standard wavelengths for the AOD measured by sunphotometers of this network are 440, 675, 870 and 1020 nm. AOD at 500 nm is measured in a large quantity of stations, and some of them also measure radiances at 340, 380 and 1640 nm.

In this work, we use Level 2 products from the algorithm version 2. Level 2 products are the final quality assured data provided by the AERONET team. This product is cloud-screened (Level 1.5) and post-calibrated (Level 2). The measurements are taken during daylight each 15 minutes approximately. We use the daily average of these measurements, also provided by the AERONET team.

Chapter 3

Emission fluxes inversion system

In the previous Chapter we have described two key components of the dust flux inversion system, namely the observations and the observation operator. In this chapter we describe the remaining ingredients of the flux inversion: the definition of the control vector, the error covariance matrices, the cost function and the procedure used to minimize the cost function.

We are interested in mineral dust emissions over North Africa and the Arabian Peninsula, so the observations are assimilated only over this region and the adjacent Atlantic Ocean. More precisely, the observations are assimilated in the area between 70°W and 65°E in longitude and between 0°N and 40°N in latitude.

Consequently, the control vector has been defined with the aim of better estimating the mineral dust emissions in this region, knowing that dominant aerosol types are of natural origin with mineral dust emitted over land and sea spray emitted over ocean.

3.1 Cost function and control vector

In this work, the control vector is composed of correction factors of the prior emissions. This is not the only possible choice for the control vector, however. In a source inversion problem, we can choose to directly control the aerosol emissions or a monotonic transformation of the aerosol emissions. For instance the control vector could consist of correction factors on the logarithm of the prior emissions. It would also be possible to control parameters of the emission model, but due to the non-linearities of these parameters with respect to the AOD, we have chosen to correct directly the fluxes. The advantage of using correction factors is that the prior emissions can be modified only in terms of their quantity without changing the spatio-temporal variability in emissions on scales smaller than the control vector resolution.

We adapt the approach used by Huneeus et al. (2012) to the dust source inversion problem with a focus on the Sahara desert and the Arabian Peninsula. This approach assumes that there exists a group of homogeneous geographical sub-regions in terms of prior emission errors. In practice this means that we assume that model gridboxes can be grouped into such geographical subregions with a similar emission correction in the analysis. This is a strong assumption but it allows to perform source inversions with current computing capabilities.

We determine the correction factor by partitioning the geographical and temporal space of the aerosol sources and we assume that the correction is a constant value on each element of the partition. This partition is done in geographical regions (*sub-regions*), aerosol source type (*categories*) and time periods (*sub-periods*). We will describe this partitioning in the next paragraphs, which effectively defines the control vector.

The emission categories are similar to those described in Huneeus et al. (2012), that is, they are associated to the aerosol types themselves defined from source types and modes of the size distribution. In this work, the following categories are defined:

- Fine dust
- Coarse dust
- Super coarse dust
- Biomass burning emissions
- Anthropogenic SO_2 and fossil fuel emissions
- Fine sea spray
- Coarse sea spray

For the inversion presented in Chapter 4, the coarse and super-coarse dust categories are lumped together, while in Chapter 5, the fine and coarse dust categories are lumped together. It would be possible define the three categories in the control vector, but preliminary tests have indicated that (i) the quality of the analysis does not improve and (ii) the computational burden increases considerably (which is an important constraint in Chapter 5).

Sub-periods are defined differently for each category of emission. Anthropogenic SO_2 and fossil fuel emissions have sub-periods of one month. In other words, the correction of the emissions is done only with a monthly resolution for each sub-region. This one-month resolution is consistent with the expected seasonal variability of the anthropogenic emissions. Moreover, this emission category can be seen almost as a boundary condition for the AOD field on the region of study, thus a finer temporal resolution of this control vector is not strictly needed. The same time resolution of the control vector applies for the biomass burning emissions. In this case, the biomass burning inventory has a daily resolution. With a monthly correction factor of this category is expected to control the emissions at the seasonal scale, without changing the (assumed correct) variability to the inventory within each month.

Dust correction factors have a time resolution of one month for the experiments of Chapter 4, and only three days for experiments of Chapter 5. To choose this time resolution of the dust control vector, we have performed several tests with the time resolution ranging from three days

Category	Number of sub-regions	Temporal resolution	
		Exp. 1	Exp. 2
Fine dust	19	1 month	3 days
Coarse dust	19	1 month	
Super-coarse dust	19		3 days
Biomass burning	2	1 month	1 month
Anthropogenic SO_2 and fossil fuel emissions	1	1 month	1 month
Fine sea spray	1	1 year	1 year
Coarse sea spray	1	1 year	1 year

Table 3.1: Summary of the control vector definition. Experiment 1 (Exp. 1) is shown in Chapter 4 and Experiment 2 (Exp. 2) in Chapter 5.

to one month. We realize that the three days control vector is a better compromise between the computational burden necessary to run the inversions and leaving the assimilation system enough freedom to be able to correct some dust events at the synoptic and sub-synoptic scale.

3.1.1 Control vector sub-regions

For sea spray and anthropogenic SO_2 and fossil fuel emissions only one (global) region is considered. For biomass burning (BB) emissions two sub-regions were considered and the classification was done based on the land cover class map of Kaiser et al. (2012). One BB sub-region, (*forest*) is composed by following land cover class of Kaiser et al. (2012):

- tropical forest
- extratropical forest
- extratropical forest with organic soil.

The rest of the land class cover types are grouped in the *grass* sub-region, that is,

- savannah
- savannah with organic soil
- agriculture
- agriculture with organic soil
- peat.

Figure 3.1 shows the BB sub-regions on the model grid.

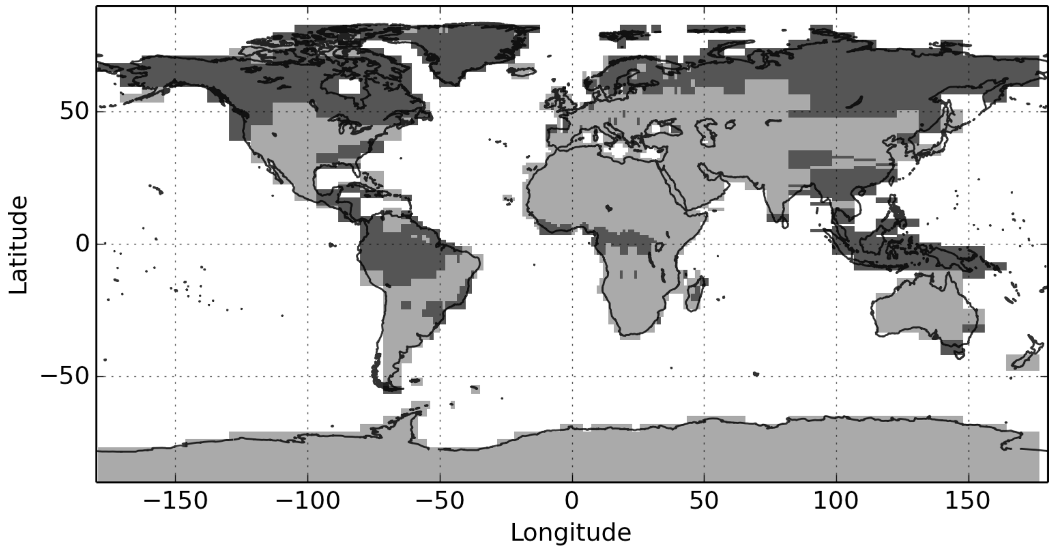

Figure 3.1: Description of biomass burning sub-regions. The forest sub-region is in dark grey and grass sub-region is in light grey. Latitude and longitude are expressed in degrees north and east respectively.

3.1.1.1 Dust sub-regions

The focus of this work is the Saharan desert and the Arabian Peninsula. We have constructed a set of 18 regions over this domain to which we add a 19^{th} region covering the rest of the globe. This 19^{th} region allows the assimilation system to control the dust emissions that can be transported to the region where the observations are assimilated.

The number of regions is a trade-off between the current computing capabilities and computational cost of the inversion system and the expected spatial resolution of the analysis. The 18 sub-regions were constructed by using clustering techniques over the prior simulation of dust fluxes. The control vector is constant over each sub-regions, so the aim of this procedure is to find sub-regions where the dust emissions could be homogeneously corrected. For this purpose, we will focus on the temporal behaviour of the aerosol emissions, in particular, on the relations between emissions of different model pixels in the temporal dimension.

In order to create the sub-regions, we only use information from the dust emissions of the prior simulation. We calculate, for each gridbox, the temporal correlation of this gridbox with the rest of the grid-boxes. Highly-correlated grid-boxes would have similar temporal emission patterns (if they have a linear relation). In that case, the heterogeneity of the emissions would be only in the spatial dimension within each sub-region.

To create the sub-regions partition, we use one year of hourly outputs of the total mineral dust flux and the correlation maps were calculated. Clustering analysis were applied to this correlation maps, creating close to 15 clusters. The clustering were performed with two standard methods: the K-means and the Gaussian Mixture Model (GMM). Both methods try to group similar correlation maps under different metrics and procedures. After the clusters are created,

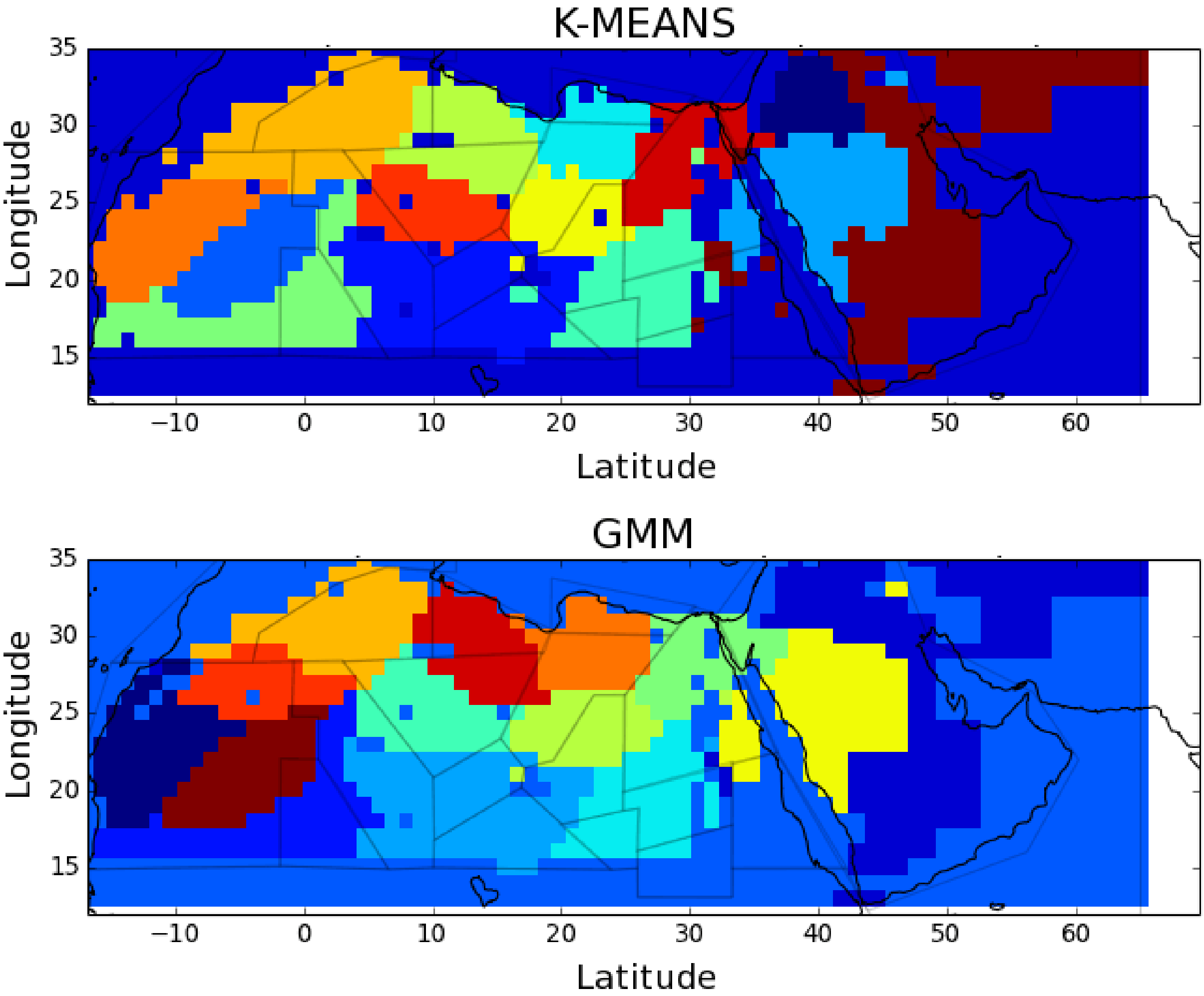

Figure 3.2: Clustering results from the K-Means (upper panel) and Gaussian Mixture Model (lower panel) methods. We combine both maps to create the dust sub-regions as is explained in the text. Lines in the figure show the first attempt to define the regions, using only information from the literature. The regions delimited by black lines are not used in this work.

the next step is to "predict" which correlation map belongs to which element in the cluster. The result of this step is shown in Figure 3.2 for the two methods used, setting the number of clusters to 15. It is not by chance that the regions predicted by the clustering methods are "agglomerated" and each region is mostly composed by only one (connected) component. For our purpose this is a desired behaviour because it allows geographically differentiating the sub-regions and it facilitates the analysis of the assimilation results. This behaviour is due to two main reasons. The first one is that the surface wind is the main driver of the temporal variability in dust emissions, so the synoptic patterns should be reflected in the correlation maps. Secondly, both methods (K-means and GMM) by construction, try to cluster the sample in groups with the least possible intra-group dispersion and with a group center laying inside the group, which results in "agglomerated" groups. We have manually combined the results from both methods in the constructing process of the dust sub-regions, along with the information described in the next paragraph.

Additional information is included into the sub-region creation process, extending the number of regions from 15 to 18 over North Africa and the Arabian Peninsula. With the aim of isolating known dust emission hot-spots of geographical features, we overlap these maps (Figure 3.2) with some literature information. In particular, works by Ginoux et al. (2012) and Schepanski et al. (2012) suggest source sub-regions based on an analysis of satellite retrievals. This additional information was manually included in our analysis, along with the GOCART preferential sources map by Ginoux et al. (2001) and Menut et al. (2013). Figure 3.3 shows the main information from the literature included in the sub-region creation process. The final 18 sub-regions are shown in Figure 4.1, which is reproduced here (Figure 3.4) for clarity.

3.1.2 Cost function

In this section we define the cost function used throughout this work. This form of the cost function is used in Chapters 4 and 5. Giving the control vector ($\mathbf{x}$) described in the previous section, the cost function reads

$$J(\mathbf{x}) \;=\; \frac{1}{2}\,(\mathbf{x}-\mathbf{x}^b)^T\,\mathbf{B}^{-1}\,(\mathbf{x}-\mathbf{x}^b) + \frac{1}{2}\,(\mathbf{y}-H(\mathbf{x}))^T\,\mathbf{R}^{-1}\,(\mathbf{y}-H(\mathbf{x})) \quad , \tag{3.1.1}$$

with $\mathbf{x}^b$ the prior control vector (equal to unity in our case), $\mathbf{B}$ the covariance matrix of the background errors, $\mathbf{R}$ the covariance matrix of the observation errors, $\mathbf{y}$ the observations (Section 2.2.1) and H the observation operator (Section 2.1). The observation operator H is approximated by its linear form, denoted by $\mathbf{H}$. In this work, the linear approximation is made around the prior by:

$$H(\mathbf{x}) \;\approx\; H(\mathbf{x}^b) + \mathbf{H}(\mathbf{x}-\mathbf{x}^b) \quad . \tag{3.1.2}$$

Physically-consistent emissions are non-negative and hence all elements of the control vector have to be non-negative. This restriction is written as a constraint in the minimization of the

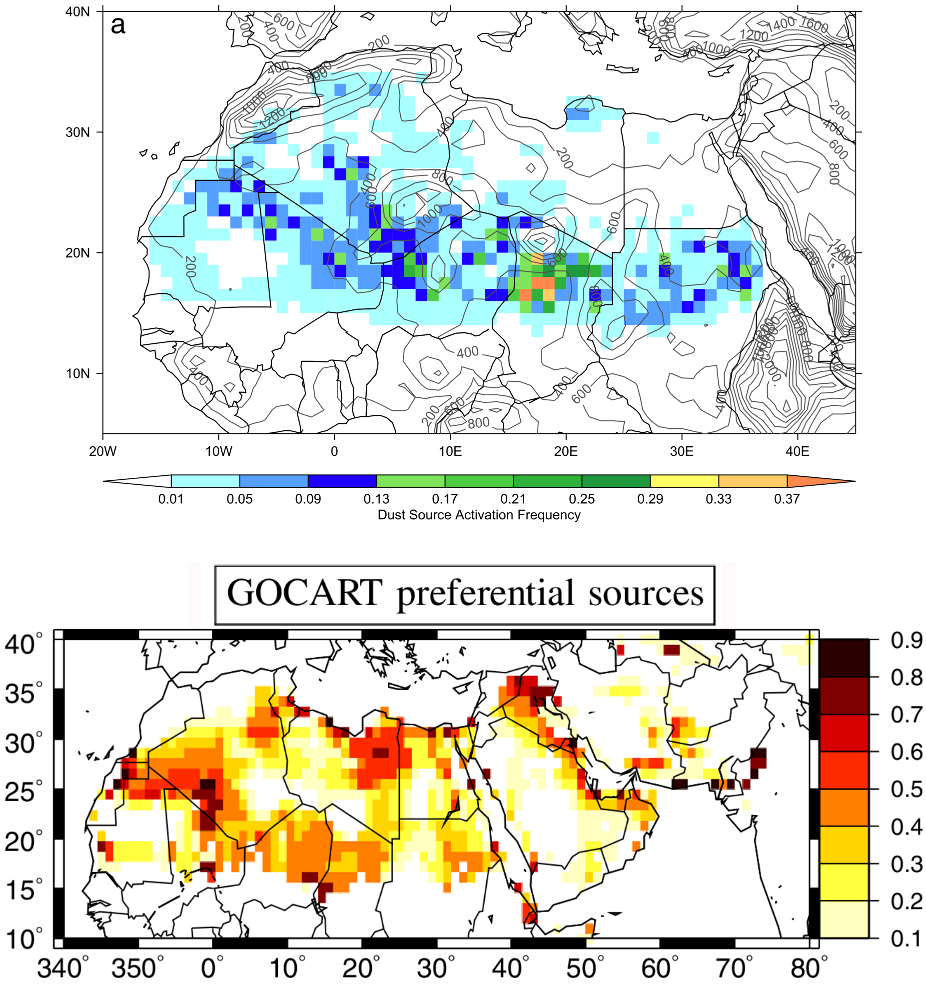

Figure 3.3: Additional information included in the sub-region creation process: dust source activation count from the work of Schepanski et al. (2012) on the upper panel, GOCART preferential sources map from the work of Ginoux et al. (2001) on the lower panel. The GOCART figure is extracted from Menut et al. (2013).

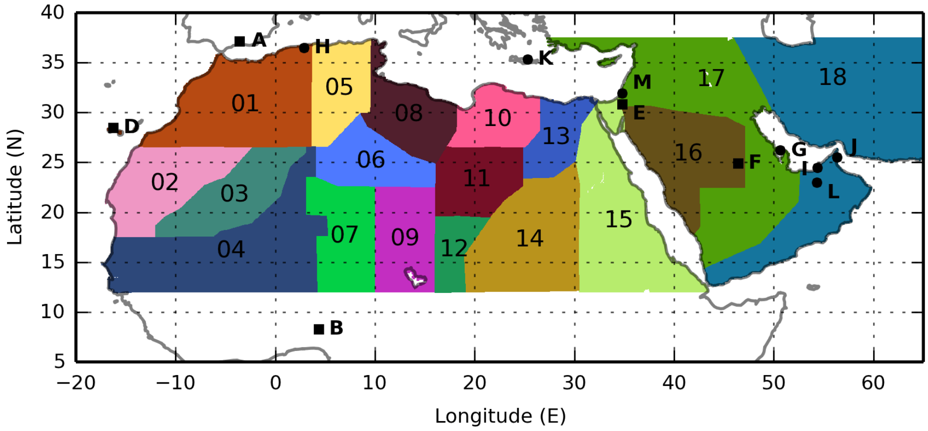

Figure 3.4: Numbered dust sub-regions used in this thesis. Figure from Escribano et al. (2016).

cost function. We will come back to this later in Section 3.3 and Chapter 6.

3.2 Error covariance matrices

Error covariance matrices $\mathbf{B}$ and $\mathbf{R}$ are two fundamental elements of the assimilation system. Equation (3.1.1) is a quadratic form on $\mathbf{x}$, and it can be seen as the sum of two terms, the cost of the observation (J_o) and the cost of the background (J_b) such that:

$$\begin{aligned} J(\mathbf{x}) &= J_b(\mathbf{x}) + J_o(\mathbf{x}) \quad , \qquad (3.2.1) \\ J_b(\mathbf{x}) &= \frac{1}{2}\,(\mathbf{x}-\mathbf{x}^b)^T\,\mathbf{B}^{-1}\,(\mathbf{x}-\mathbf{x}^b) \quad , \\ J_o(\mathbf{x}) &= \frac{1}{2}\,(\mathbf{y}-H(\mathbf{x}))^T\,\mathbf{R}^{-1}\,(\mathbf{y}-H(\mathbf{x})) \quad . \end{aligned}$$

The assimilation system minimizes Equation (3.2.1) in order to find the optimum value of $\mathbf{x}$, called the *analysis* ($\mathbf{x}^a$). Each term, J_o and J_b, can be interpreted as the square of the norm of a variable in the adequate space. We will clarify this statement in the next paragraphs.

Given a symmetric and positive definite matrix $\mathbf{M} \in \mathbb{R}^{n\times n}$, the following bilinear form can be defined

$$< \mathbf{x}, \mathbf{y} >_{\mathbf{M}} = \mathbf{x}^T\,\mathbf{M}\,\mathbf{y} \quad ,$$

for $\mathbf{x} \in \mathbb{R}^n$, $\mathbf{y} \in \mathbb{R}^n$. Consequently, the following expression is a norm in $\mathbb{R}^n$:

$$\|\mathbf{x}\|_{\mathbf{M}} = \sqrt{\mathbf{x}^T\,\mathbf{M}\,\mathbf{x}} \quad .$$

As $\mathbf{B}$ and $\mathbf{R}$ are covariance matrices, they are symmetric and semi-positive definite. However, to properly define Equation (3.2.1) it is necessary to require the positive definiteness of $\mathbf{B}$ and $\mathbf{R}$. In this case, it is possible to show that their inverses, $\mathbf{B}^{-1}$ and $\mathbf{R}^{-1}$, are also positive definite (and symmetric). With this in mind, it is possible to write the cost function as:

$$J(\mathbf{x}) = \frac{1}{2}\,\|\mathbf{x}-\mathbf{x}^b\|^2_{\mathbf{B}^{-1}} + \frac{1}{2}\,\|\mathbf{y}-H(\mathbf{x})\|^2_{\mathbf{R}^{-1}} \quad .$$

Therefore, $J_b(\mathbf{x})$ is the square of the norm of the difference between the control vector and the prior, with the norm induced by the background *precision* matrix $\mathbf{B}^{-1}$. Similarly, $J_o(\mathbf{x})$ is the square of the norm of the departures between the observations and the observation operator (evaluated in $\mathbf{x}$), with the norm induced by the *precision* matrix $\mathbf{R}^{-1}$. Thus, $\mathbf{B}$ and $\mathbf{R}$ define, at the end, the normed spaces where the cost function is minimized.

Any covariance matrix can be written as the product between a diagonal matrix, a correlation matrix and the same diagonal matrix. More precisely, if $\mathbf{M}$ is a covariance matrix, it can be written as:

$$\mathbf{M} = \mathbf{D}\,\mathbf{C}\,\mathbf{D} \quad , \qquad (3.2.2)$$

with $\mathbf{C}$ the associated correlation matrix and $\mathbf{D}$ a diagonal matrix composed by the square roots of the elements in the diagonal of $\mathbf{M}$, i.e., for the element of $\mathbf{M}$ in the row i and column j,

$$\mathbf{D}_{i,j} = \begin{cases} \sqrt{\mathbf{M}_{i,j}}, & \text{if } i = j \\ 0, & \text{otherwise.} \end{cases}$$

Hereinafter, we will implicitly use Equation (3.2.2) when we refer to the correlation matrix of the observational or backgrounds errors.

3.2.1 Covariance matrix of the background errors

We recall from Chapter 1 that the covariance matrix of the background errors $\mathbf{B}$ is defined as the covariance matrix of the random variable ε^b:

$$\mathbf{x}^b = \mathbf{x}^t + \varepsilon^b \quad ,$$

with $\mathbf{x}^t$ the true correction factors, projected in the control vector space. The mathematical expectancy of ε^b is assumed equal to zero, i.e., it is assumed that the prior $\mathbf{x}^b$ is unbiased. In this thesis, the elements of the control vector ($\mathbf{x}$) are correction factors for the sub-regions, periods and categories defined in Section 3.1. The prior, $\mathbf{x}^b$ is equal to the unity vector in all of this thesis, that is, the prior emissions are those from Section 2.1.3.

In principle, the standard deviation of the background errors are the same as in Huneeus et al. (2013). Biomass burning correction factors errors have a standard deviation of 1.3, anthropogenic and fossil fuel emissions a standard deviation of 0.18, sea salt correction factor errors a standard deviation of 2 and dust correction factors have a standard deviation of 3. The latter is for each dust emission mode namely fine, coarse and super-coarse.

We have included two correlation terms in the background error matrix, a temporal correlation and a correlation between the dust categories. The temporal correlation was imposed for each sub-region and dust emission category, that is, two elements in the control vector are temporally correlated if and only if they belong to the same sub-region and emission category. The temporal correlation was assumed Gaussian, and following Pannekoucke et al. (2008) is written as:

$$\rho_L = \exp\left(-\frac{(\Delta T)^2}{2\,L^2}\right) \quad , \tag{3.2.3}$$

with ΔT the time (in days) between the two sub-periods, and L the temporal correlation length (in days). This parameter L was set to 20 days in Chapter 4, where the temporal resolution of the dust control vector is one month. In Chapter 5 this parameter was fixed in 3 days, due to the shortened time resolution of the dust control vector. This was done to fully take advantage of the shortened timescale, with the aim to better capture some dust events in the analysis.

In addition to the temporal correlations, we add a correlation between different categories of dust correction factors. We set this correlation to $\rho_c = 0.6$. The justification for this value will be explained in Section 3.2.3.

The construction of the correlation matrix from the individual pairs of correlation described above is not direct. In fact, the correlation matrix has to be symmetric, semi-positive definite, with values between -1 and 1 and with ones in the diagonal. Just including the above mentioned correlations in a matrix does not necessary construct a correlation matrix. From these requirements, the semi-positiveness of the matrix is the most difficult property to fulfil. In practice, if the matrix is not semi-positive definite, the cost function could be not convex and the numerical minimizer could fail in the convergence to the optimum. To sort out of this problem, the following heuristic was applied.

First, we extrapolated the known (e.g., Olkin, 1981) constraints for a 3×3 correlation matrix to the whole correlation matrix. If two variables, let say, x and y are correlated by ρ_{xy} and, on the other side, a third variable z is correlated with x by ρ_{xz}, then the correlation between y and z is bounded by:

$$\rho_{xy}\,\rho_{xz} - (1-\rho_{xy}^2)(1-\rho_{xz}^2) \;\le\; \rho_{yz} \;\le\; \rho_{xy}\,\rho_{xz} + (1-\rho_{xy}^2)(1-\rho_{xz}^2) \quad .$$

In particular, the value $\rho_{yz} = \rho_{xy}\,\rho_{xz}$ is within the bounds. To construct the whole correlation matrix, we recursively calculate the third correlated variable with this estimate. For example, the correction factor of fine mode dust associated to the sub-region m in the sub-period p is correlated to the correction factor of the fine mode dust in the same sub-region m in the period $p+1$ by Equation (3.2.3) which itself is correlated with the super-coarse dust correction factor in the same sub-region m and sub-period $p+1$ by the fixed correlation $\rho_c = 0.6$ presented above. Then the correlation between the last correction factor and the first one (fine mode correction factor in the sub-region m and period p) is estimated by the product of the two correlations. This is repeated iteratively until all the pairs of correlations are processed. At this stage, we cannot guarantee that the constructed matrix is a correlation matrix.

The second step is to force the positiveness of the constructed matrix. This is done using the work of Qi and Sun (2006), which is an optimization algorithm which find the closest correlation matrix (in the Frobenius norm) of the input matrix. This was done by adapting the work of Qi and Sun (2006) to our needs. We translate the algorithm (originally written in MATLAB) into FORTRAN, with the technical advantages of a faster computing time and the possibility of handling large matrices. It is worth noting that, for most of the cases we have tested, this last step was not strictly necessary since the matrix was already a correlation matrix after the first step.

3.2.2 Covariance matrix of the observation errors

In Chapter 1 we defined the covariance matrix of the observation errors (**R** matrix) by the covariance matrix of the random variable ε^o, where

$$\mathbf{y} = H(\mathbf{x}^t) + \varepsilon^o \quad ,$$

with $\mathbf{y}$ the observations, H the observation operator and $\mathbf{x}^t$ the true correction factors (in the control vector space). For the moment, the observations are assumed unbiased. We will discuss this assumption later in Chapter 6.

Two different definitions were used for the diagonal elements of the **R** matrix. In Chapter 4 only MODIS/Aqua total 550 nm AOD is assimilated. Here we follow the AOD error estimates used in Huneeus et al. (2013) for this satellite product, that is, to define a constant value of 0.2 as the standard deviation of the MODIS/Aqua AOD errors over land and a value of 0.1 over ocean. For the experiments in Chapter 5 we follow the error estimated given in the literature and shown in Section 2.2.1. Table 5.1 summarizes the pixel-wise AOD errors used.

In both cases, the model error was defined with a standard deviation of 0.02, thus the total error in **R** is the sum of the model and the observational AOD error. Huneeus et al. (2012) show the low sensitivity of their analysis with respect to the model error, ranging between 0.02 to 0.5 in AOD.

For the results shown in Chapter 4 and Chapter 5 the **R** matrix is assumed diagonal. This assumption is not necessarily true because several sources of correlation in the AOD errors could exist. For example, collocated total and fine AOD from MODIS/Aqua should be correlated because both retrievals are calculated using the same radiance measurements, the same algorithm with similar assumptions. AOD errors from nearby pixels in a retrieval could also be correlated, as the AOD error could depend on the viewing geometry and/or surface properties.

Similarly, for the experiments in Chapter 5 would be necessary to include the correlations between simulated fine and total AOD errors. These errors should be included as part of the representativeness error (cf. Section 1.2), which is included in the model error in the **R** matrix. The above mentioned correlations were not included in this thesis due to the high complexity on their estimation.

3.2.3 Desroziers diagnostics

In this section we present the consistency diagnostics used in the assimilation system. These diagnostics were applied only for the inversion presented in Chapter 4. They are taken from the work of Desroziers et al. (2005) and further interpreted in this study. These consistency diagnostics are based on the solution for the minimization of the cost function (Equation (3.1.1)) under the linear approximation of the observation operator (Equation (3.1.2)), assuming (as usual) unbiased prior and observation errors and uncorrelated with each other. First, we recall that the solution of the minimization of the cost function is called *analysis* and it is denoted by $\mathbf{x}^a$. It can be proven that, under these assumptions, the covariance matrix of the analysis ($\mathbf{A}$) can be calculated by:

$$\mathbf{A} = (\mathbf{B}^{-1} + \mathbf{H}^T\,\mathbf{R}^{-1}\,\mathbf{H})^{-1} \quad .$$

The so-called Desroziers diagnostics are relations between the prescribed and the observed error covariance matrices in the observation space. They can be summarized through the following equations:

$$\begin{aligned} E[\mathbf{d}_b^a\,(\mathbf{d}_b^o)^T] &= \mathbf{H}\,\mathbf{B}\,\mathbf{H}^T \quad , && (3.2.4)\\ E[\mathbf{d}_b^o\,(\mathbf{d}_b^o)^T] &= \mathbf{H}\,\mathbf{B}\,\mathbf{H}^T + \mathbf{R} \quad , &&\\ E[\mathbf{d}_a^o\,(\mathbf{d}_b^o)^T] &= \mathbf{R} \quad , && (3.2.5)\\ E[\mathbf{d}_b^a\,(\mathbf{d}_a^o)^T] &= \mathbf{H}\,\mathbf{A}\,\mathbf{H}^T \quad , && (3.2.6) \end{aligned}$$

where E stands for the mathematical expectancy and the departures $\mathbf{d}$ are defined by:

$$\begin{aligned} \mathbf{d}_b^o &= \mathbf{y} - H(\mathbf{x}^b) \quad ,\\ \mathbf{d}_b^a &= H(\mathbf{x}^a) - H(\mathbf{x}^b) \quad ,\\ \mathbf{d}_a^o &= \mathbf{y} - H(\mathbf{x}^a) \quad . \end{aligned}$$

These matrices are in the observation space (of dimension p), so in practice the diagnostic is said to be fulfilled if the traces of the matrices on each side of Equations (3.2.4) to (3.2.6) are equal. To enforce the diagnostics, Desroziers et al. (2005) propose an iterative method to compute inflation factors $\alpha_{\mathbf{B}}$ and $\alpha_{\mathbf{R}}$ for the covariance matrices.

In order to calculate the temporal correlation length from Equation (3.2.3), the correlation between the errors of two different categories of correction factors, and the inflation factors for the $\mathbf{B}$ and $\mathbf{R}$ matrices, we have implemented some of these diagnostics in our assimilation system.

Before explaining how we calculated these values, we highlight that our methodology is not derived completely rigorously. It is based on the diagnostic presented before, including the assumptions made to derive these diagnostics. The objective of this methodology is to have a fair idea of the unknown parameters of the above-mentioned covariance matrices. In consequence, some decisions made in the process are arbitrary but they are nonetheless based on intuition and experience.

To complete the construction of $\mathbf{B}$ and $\mathbf{R}$ we have four free parameters: the inflation factor for the error covariance matrix ($\alpha_{\mathbf{R}}$), the inflation factor for the background covariance matrix ($\alpha_{\mathbf{B}}$), the temporal correlation length (L) of Equation (3.2.3) and the correlation between two related emission categories for the same sub-period and sub-region (ρ_c). The criteria to choose these parameters aim to:

- try to fulfil Desroziers's analysis diagnostic (Equation (3.2.6))
- try to fulfil Desroziers's observation diagnostic (Equation (3.2.5))
- have a realistic uncertainty in the dust prior emissions.

It is possible to design an algorithm to calculate the four free parameters simultaneously, but our preliminary tests indicate that this requires a considerable amount of computing resources (see also Berchet et al. (2015)). In addition, the nonlinearities in the analysis diagnostic increases the complexity of the problem to be solved. Instead, a second approach was implemented in order to get the **B** and **R** matrices. It consists in dividing the problem into two parts. First, we fix L and ρ_c and we get the best values of $\alpha_{\mathbf{R}}$ and $\alpha_{\mathbf{B}}$ that are consistent with the Desroziers diagnostics, and secondly we choose L and ρ_c such that the uncertainty of the background dust emissions is realistic. The next paragraphs detail how the process is done, and what "realistic" means in our case.

For fixed L and ρ_c, the **B** matrix depends only on the $\alpha_{\mathbf{B}}$ value, so we define the $\mathbf{B}_{\alpha_{\mathbf{B}}}$ matrix as:

$$\mathbf{B}_{\alpha_{\mathbf{B}}} = \alpha_{\mathbf{B}}\,\hat{\mathbf{B}} \quad ,$$

where

$$\hat{\mathbf{B}} = \tilde{\mathbf{B}}^{1/2}\,\mathbf{C}_{\mathbf{B}}\,\tilde{\mathbf{B}}^{1/2} \quad ,$$

with $\mathbf{C}_{\mathbf{B}}$ the correlation matrix constructed with L and ρ_c, $\tilde{\mathbf{B}}$ is the diagonal covariance matrix with the errors defined in Section 3.2.1 and the notation $\mathbf{M}^{\mathbf{1/2}}$ for the matrix such that $\mathbf{M}^{1/2}\,\mathbf{M}^{1/2} = \mathbf{M}$. We assume that the covariance matrix of the observation errors is diagonal, and then

$$\mathbf{R}_{\alpha_{\mathbf{R}}} = \alpha_{\mathbf{R}}\,\tilde{\mathbf{R}} \quad ,$$

with $\tilde{\mathbf{R}}$ the diagonal error covariance matrix defined in Section 3.2.1. Similarly, the matrix

$$\mathbf{A}_{\alpha_{\mathbf{B}},\alpha_{\mathbf{R}}} = (\mathbf{B}_{\alpha_{\mathbf{B}}}^{-1} + \mathbf{H}^T\,\mathbf{R}_{\alpha_{\mathbf{R}}}^{-1}\,\mathbf{H})^{-1} \quad ,$$

is the covariance matrix of the analysis errors. Following Equations (3.2.5) and (3.2.6), we define the departures as a function of the inflation factors (where applicable):

$$\begin{aligned}
\mathbf{d}_b^o &= \mathbf{y} - H(\mathbf{x}^b) \quad , \\
\mathbf{d}_b^a(\alpha_{\mathbf{B}}, \alpha_{\mathbf{R}}) &= H(\mathbf{x}^a_{\alpha_{\mathbf{B}},\alpha_{\mathbf{R}}}) - H(\mathbf{x}^b) \quad , \\
\mathbf{d}_a^o(\alpha_{\mathbf{B}}, \alpha_{\mathbf{R}}) &= \mathbf{y} - H(\mathbf{x}^a_{\alpha_{\mathbf{B}},\alpha_{\mathbf{R}}}) \quad ,
\end{aligned}$$

and the analysis $\mathbf{x}^a_{\alpha_{\mathbf{B}},\alpha_{\mathbf{R}}}$ depends on the inflation factors because it is the minimum of the cost function:

$$J_{\alpha_{\mathbf{B}},\alpha_{\mathbf{R}}}(\mathbf{x}) \;=\; \frac{1}{2}\,(\mathbf{x}-\mathbf{x}^b)^T\,\mathbf{B}^{-1}_{\alpha_{\mathbf{B}}}\,(\mathbf{x}-\mathbf{x}^b)+\frac{1}{2}\,(\mathbf{y}-H(\mathbf{x}))^T\,\mathbf{R}^{-1}_{\alpha_{\mathbf{R}}}\,(\mathbf{y}-H(\mathbf{x})) \quad .$$

The computation of the inflation factors is done by minimizing another cost function, F, which relates the trace of both matrices of the Desroziers diagnostics:

$$\begin{aligned} c_o(\alpha_{\mathbf{B}},\alpha_{\mathbf{R}}) &= \frac{\mathrm{Tr}(\mathbf{d}^o_a(\alpha_{\mathbf{B}},\alpha_{\mathbf{R}})\,(\mathbf{d}^o_b)^T)}{\mathrm{Tr}(\mathbf{R}_{\alpha_{\mathbf{R}}})} \quad , \\ c_a(\alpha_{\mathbf{B}},\alpha_{\mathbf{R}}) &= \frac{\mathrm{Tr}\,(\mathbf{d}^a_b(\alpha_{\mathbf{B}},\alpha_{\mathbf{R}})\,(\mathbf{d}^o_a(\alpha_{\mathbf{B}},\alpha_{\mathbf{R}}))^T)}{\mathrm{Tr}\,(\mathbf{H}\,\mathbf{A}_{\alpha_{\mathbf{B}},\alpha_{\mathbf{R}}}\,\mathbf{H}^T)} \quad , \\ F(\alpha_{\mathbf{B}},\alpha_{\mathbf{R}}) &= |c_a-1|+\left|\frac{1}{c_a}-1\right|+|c_o-1|+\left|\frac{1}{c_o}-1\right| \quad , \end{aligned} \tag{3.2.7}$$

where Tr denotes the trace of a matrix. The constraints $\alpha_{\mathbf{B}} \geq 0$ and $\alpha_{\mathbf{R}} \geq 0$ are imposed in the minimization of F. Each evaluation of F implies the minimization of the cost function $J_{\alpha_{\mathbf{B}},\alpha_{\mathbf{R}}}(\mathbf{x})$. Note that the cost function F is left bounded by zero, and if it is equal to zero, the observation and analysis diagnostics will be satisfied in the sense of the trace of the matrices. Also note that we have included the fractional terms in the cost function F only to weight similarly the denominator and numerator of the c_o and c_a terms in the minimization procedure. This problem (Equation (3.2.7)) is solved using a nonlinear minimizer for F. The subproblem of the minimization of J will be described in Section 3.3.

With the procedure described in the previous paragraphs we can obtain the best inflation parameters (according to our criteria) $\alpha_{\mathbf{R}}$ and $\alpha_{\mathbf{B}}$ for a given pair of ρ_c and L values.

Finally, we obtain the four free parameters by computing for different values of L and ρ_c, their corresponding inflation parameters $\alpha_{\mathbf{R}}$ and $\alpha_{\mathbf{B}}$. Now we can see these inflation parameters as functions of ρ_c and $L:\ \alpha_{\mathbf{R}}(L,\rho_c)$ and $\alpha_{\mathbf{B}}(L,\rho_c)$. The pairs of (L,ρ_c) were all the combinations of a sequence of ρ_c between $\rho_c = 0.0$ and $\rho_c = 0.9$ with a step of 0.1 (10 values in total), and L between $L = 5$ and $L = 85$ days with a step of 5 days (17 values in total). In total we calculated 170 pairs of $\alpha_{\mathbf{B}}$ and $\alpha_{\mathbf{R}}$.

The uncertainty in the model dust emissions can be estimated with the $\mathbf{B}$ matrix and the emission fluxes of the background simulation. If we denote by $\mathbf{f}$ the prior emission flux, it is composed in its i-th element by the total emission flux (integrated by time and space) associated to the i-th component of the control vector. The uncertainty of the emission flux (expressed as standard deviation) can be computed by:

$$\sqrt{\mathrm{Var}(\mathbf{f}^T\,(\mathbf{x}^t-\mathbf{x}^b))} \;=\; \sqrt{\mathbf{f}^T\,\mathbf{B}\,\mathbf{f}} \quad ,$$

where Var is the variance operator.

The last step is to choose the pair (L,ρ_c) such that the uncertainty of the background emissions is “realistic”. To do this, we consider that the standard deviation of a multimodel comparison is a realistic proxy for the background emission flux errors. From the AEROCOM project (Huneeus et al., 2011), the mean dust emission for dust over the Sahara and Middle East was approximately 1370 Tg yr^{-1}, and the standard deviation (std) between the models was 863 Tg yr^{-1}. These numbers give a std/mean ratio of 0.63, so the last criteria to choose L and ρ_c is to have a std/mean ratio of prior emission fluxes close to 0.63.

We have imposed $F < 0.5$ as a condition, to ensure that the Desroziers diagnostics are close to be satisfied. With this constraint, the group of parameters with std/mean ratio of emission fluxes close to 0.63 is $\rho_c = 0.6$, $L = 20$ days, $\alpha_{\mathbf{B}} = 4.08$ and $\alpha_{\mathbf{R}} = 1.095$.

3.3 Minimization

3.3.1 Technical aspects of the sensitivity matrix computation

An important aspect of the assimilation system is the computation of the derivative of the observation operator (also called *sensitivity matrix*). It is denoted by $\mathbf{H}$ and it is the linear approximation of the observation operator (Equation (3.1.2)) evaluated on the prior control vector. Most variational data assimilation systems avoid the explicit form of this matrix, and instead of computing $\mathbf{H}$, they compute the product of $\mathbf{H}$ with a vector by using an *tangent linear* model. In our assimilation system the $\mathbf{H}$ matrix is computed through finite difference, hence avoiding the development of a tangent linear (and adjoint) model. The accuracy of the linear approximation of Equation (3.1.2) is somehow evaluated in Section 5.2.

The sensitivity matrix $\mathbf{H}$ is calculated through forward finite differences, around the prior. The element in row i and column j of the $\mathbf{H}$ matrix is computed as:

$$\mathbf{H}_{i,j} = \frac{H(\mathbf{x}^b + \delta\mathbf{x}^j)_i - H(\mathbf{x}^b)_i}{\delta\mathbf{x}^j_j} \quad ,$$

where $\delta\mathbf{x}^j$ a vector in $\mathbb{R}^n$ with a nonzero value in the component j and zero in the rest of them; and the subscript notation indicates an element of the vector (or matrix). The perturbations $\delta\mathbf{x}^j$ can be defined for each category of emissions in the assimilation system. In our case they form the canonical base of $\mathbb{R}^n$, that is, the perturbed observation operator is computed with twice the prior emissions for all categories of emissions, sub-regions and sub-periods.

The j index ranges between 1 and n (the length of the control vector), while the i index ranges between 1 and p (the quantity of observations), thus the $\mathbf{H}$ matrix has p rows and n columns. In order to explicitly handle this large matrix, the computation of $\mathbf{H}$ is made only when it is necessary, avoiding zero-values entries. This also allows saving computing time. The next paragraphs explain how $\mathbf{H}$ is computed in the assimilation system.

Figure 3.5 is a schematic representation of the sensitivity matrix computation in the assimilation system. This Figure shows an example of the computation of one dust category and

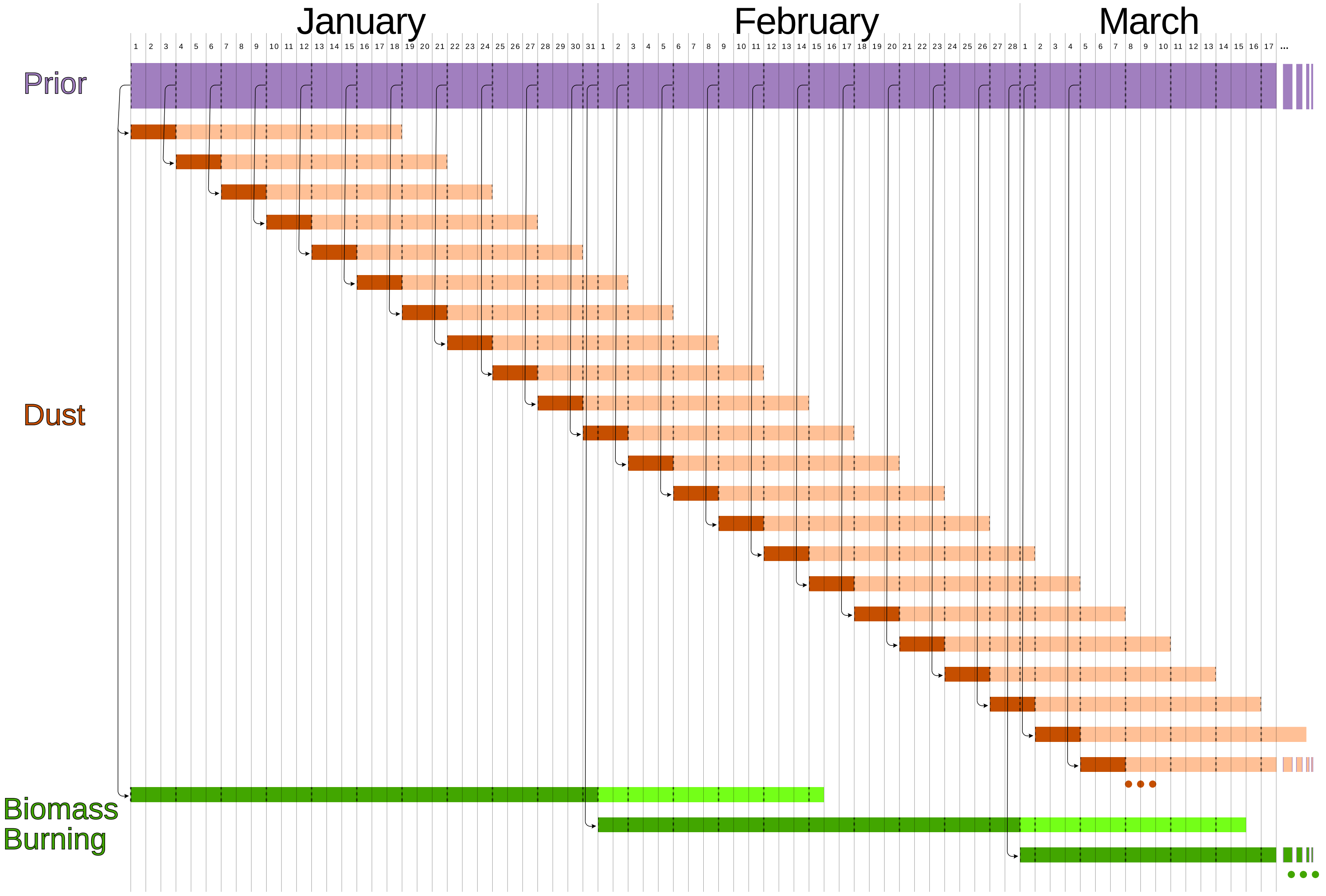

Figure 3.5: Schematic representation of the sensitivity matrix computing procedure.

sub-region (*dust* in the figure); and one biomass burning category and sub-region (*biomass burning* in the figure) for the firsts months of the experiments of Chapter 5. In Figure 3.5 we have omitted the spin-up of the model for clarity. To consider the spin-up, the first sub-period perturbation of each category and sub-region of emission should be extended back in time by one month, that is, starting on 1 December. In Figure 3.5, the temporal resolution of the dust control vector is three days and the temporal resolution of the biomass burning control vector is one month. Each row of Figure 3.5 is associated to one element in the control vector (i.e., a column in the **H** matrix) and each column is associated with one day in the simulation, representing all the observations of assimilated for each day, which is usually more than one row in the **H** matrix.

Obviously, the AOD can only be affected by an emission event *after* the event, so the computation of the perturbed AOD for each control vector element starts only when the perturbation starts; instead of simulating the whole year and only perturbing when it is necessary. Before the perturbation is made, all elements in the sensitivity matrix elements are set to zero. In the same way, as the aerosol has a residence time in the order of days, we decided to stop the perturbed simulations 15 days after the perturbation is made. In Figure 3.5, the dark color indicates a simulation with the perturbed emissions (i.e., the double of emissions in our case) while the light color indicates a simulation without perturbing emissions, but with the initial conditions of the end of the perturbed simulation. The latter is important to take into account the effect of the emissions in the AOD (especially when the time resolution of the control vector is high).

Giving the prescribed time resolutions of the control vector, the assimilation system calculates the dates when at least one perturbed simulation has to be started. This is indicated with black dashed lines in Figure 3.5. For each of them, the initial conditions are taken from the prior simulation (black arrows in Figure 3.5). Due to an unresolved problem in the nudged mode of LMDZ-SPLA model, the simulations have to be stopped and restarted at each day indicated with the dashed line, for all the perturbations.

We take advantage of the linearity of the output and the null interaction between the aerosol species to decrease the number of simulations. This is because the simulated AOD is computed as the addition of the AOD contributions of each aerosol specie in the model. For example, the total AOD is the sum of the fine mode AOD, the coarse sea salt AOD, coarse dust AOD and super-coarse dust AOD. As we have each of them as independent variables in the model output, it is possible to decrease the quantity of perturbations by grouping the perturbations of all the dust categories together, and do some post-processing to split them into the required categories. This efficiently reduces the needed computing time to create the **H** matrix. As **H** has a large quantity of zeros (before the perturbations and after 15 days of the perturbations) only the non-zero values are stored. This allows explicitly handling this matrix in the assimilation system and not having memory overflows during the computations. Also, the largest matrices needed for the assimilation (as the $\mathbf{R}^{-1}$ matrix or any p by n matrix) are stored in *sparse* format, along with useful routines to deal with these matrices, as for example, dot products by using block matrices.

From a more technical perspective, our assimilation system is written in PYTHON language, with some routines (as the nearest correlation matrix routine or the minimization solver of Chapter 6) in FORTRAN or C languages, and with interfaces to bash scripting. As it handles the dates where each perturbation is simulated, it also handles the preparation of input files for each simulation. Finally, it automatically launches the jobs to the queue system available on the supercomputer. The latter is driven by the progress of the prior simulation, and constrained by the number of active (or in queue) jobs that can be submitted to the supercomputer by the user.

3.3.2 Cost function minimization

As we have seen before, the cost function (Equation (3.1.1)) is the sum of two terms. Numerically, for each evaluation of the cost function two dot products have to be calculated for each of the two terms of Equation (3.1.1). We stated in Section 1.2 that for standard meteorological data assimilation the number of elements in the control vector is larger that the number of observations. In contrast, in this work, the quantity of assimilated observations (10^5 to 10^6) is orders of magnitude larger than the size of the control vector (500 to 5000). Therefore we could efficiently reduce the computational burden and increase the precision of the solution by reducing the quantity of operations needed to evaluate the cost function. In this section, we will show the exact form of the cost function minimized by the assimilation system. This cost function is conveniently written in the control vector space, avoiding as much as possible computations in the observation space.

We recall that the cost function is defined by:

$$J(\mathbf{x}) = \frac{1}{2}(\mathbf{x}-\mathbf{x}^b)^T\,\mathbf{B}^{-1}\,(\mathbf{x}-\mathbf{x}^b) + \frac{1}{2}(\mathbf{y}-H(\mathbf{x}))^T\,\mathbf{R}^{-1}\,(\mathbf{y}-H(\mathbf{x})) \quad . \tag{3.3.1}$$

In a more general form, the control vector could be bounded by two vectors. Later in this thesis we will use one of the bounds to avoid negative emissions of aerosols. For $\mathbf{c}_{\text{min}}$ and $\mathbf{c}_{\text{max}}$ in $\mathbb{R}^n$, the feasible domain is defined by:

$$\{\mathbf{x} \in \mathbb{R}^n \mid \mathbf{c}_{\text{min}} \leq \mathbf{x} \leq \mathbf{c}_{\text{max}}\} \tag{3.3.2}$$

where the inequalities are taken element-wise.

In order to efficiently minimize the cost function we include a preconditioning given by the Cholesky factorization of the symmetric and positive semi-definite covariance matrix $\mathbf{B}$. We define the vectors ξ and ξ^b by:

$$\begin{aligned} \xi &= \mathbf{L}^{-1}\,\mathbf{x} \quad , \\ \xi^b &= \mathbf{L}^{-1}\,\mathbf{x}^b \quad , \end{aligned}$$

with $\mathbf{B} = \mathbf{L}\,\mathbf{L}^T$. Equation (3.3.1) can be written as:

$$\begin{aligned}\tilde{J}(\xi) &= J(\mathbf{L}\,\xi) = J(\mathbf{x}) \\ &= \frac{1}{2}(\mathbf{L}\,\xi - \mathbf{L}\,\xi^b)^T\,\mathbf{B}^{-1}\,(\mathbf{L}\,\xi - \mathbf{L}\,\xi^b) \\ &+ \frac{1}{2}(\mathbf{y} - H(\mathbf{L}\,\xi))^T\,\mathbf{R}^{-1}\,(\mathbf{y} - H(\mathbf{L}\,\xi)) \quad .\end{aligned}$$

Hereinafter, we will assume a linearised observation operator around the prior by:

$$H(\mathbf{x}) = H(\mathbf{x}^b) + \mathbf{H}(\mathbf{x} - \mathbf{x}^b) \quad ,$$

with $\mathbf{H}$ the derivative of H evaluated in $\mathbf{x}^b$. Under this assumption, the cost function becomes:

$$\begin{aligned}\tilde{H}(\xi) &= H(\mathbf{L}\,\xi) = H(\mathbf{x}) \quad , \\ \tilde{H}(\xi) &= \tilde{H}(\xi^b) + \tilde{\mathbf{H}}(\xi - \xi^b) \quad .\end{aligned}$$

For numerical convenience, we can write all equations in terms of departures from ξ^b and from $\mathbf{x}^b$:

$$\begin{aligned}\delta\mathbf{x} &= \mathbf{x} - \mathbf{x}^b = \mathbf{L}\,\delta\xi \quad , \\ \delta\xi &= \xi - \xi^b \quad .\end{aligned}$$

Finally the cost function in term of the departures of the ξ variable can be expressed as:

$$\begin{aligned}\tilde{J}(\delta\xi) &= \frac{1}{2}\,(\delta\xi)^T\,\mathbf{L}^T\,\mathbf{B}^{-1}\,\mathbf{L}\,\delta\xi \\ &+ \frac{1}{2}\,(\mathbf{y} - H(\mathbf{x}^b))^T\,\mathbf{R}^{-1}\,(\mathbf{y} - H(\mathbf{x}^b)) \\ &- (\mathbf{y} - H(\mathbf{x}^b))^T\,\mathbf{R}^{-1}\,\mathbf{H}\,\mathbf{L}\,\delta\xi \\ &+ \frac{1}{2}\,(\delta\xi)^T\,\mathbf{L}^T\,\mathbf{H}^T\,\mathbf{R}^{-1}\,\mathbf{H}\,\mathbf{L}\,\delta\xi \quad ,\end{aligned} \tag{3.3.3}$$

which can be reduced to the standard quadratic form of:

$$\tilde{J}(\delta\xi) = (\delta\xi)^T\,\mathbf{Q}\,(\delta\xi) + \mathbf{q}^T\,\delta\,\xi + c \quad ,$$

where,

$$\begin{aligned}\mathbf{Q} &= \frac{1}{2}\,(\mathbf{I} + \mathbf{L}^T\,\mathbf{H}^T\,\mathbf{R}^{-1}\,\mathbf{H}\,\mathbf{L}) \quad , \\ \mathbf{q} &= -\mathbf{L}^T\,\mathbf{H}^T\,\mathbf{R}^{-1}\,(\mathbf{y} - H(\mathbf{x}^b)) \quad , \\ c &= \frac{1}{2}\,(\mathbf{y} - H(\mathbf{x}^b))^T\,\mathbf{R}^{-1}\,(\mathbf{y} - H(\mathbf{x}^b)) \quad .\end{aligned}$$

The minimization of the cost function from Equation (3.3.3) over the domain (3.3.2) is equivalent to solve

$$\begin{aligned} \text{minimize} \quad & (\delta\xi)^T\,\mathbf{Q}\,(\delta\xi) + \mathbf{q}^T\,\delta\xi \\ \text{subject to} \quad & -\mathbf{L}\,\delta\xi - \mathbf{x}^b \le \mathbf{c}_{\min} \\ & \mathbf{L}\,\delta\xi + \mathbf{x}^b \le \mathbf{c}_{\max} \quad . \end{aligned} \tag{3.3.4}$$

We recall here that the covariance matrix $\mathbf{R}$ is symmetric and positive definite, thus the matrix $\mathbf{Q}$ is also symmetric and positive definite so there exists a unique matrix $\mathbf{Q}^{1/2}$ such that $\mathbf{Q}^{1/2}\mathbf{Q}^{1/2} = \mathbf{Q}$. It can be shown that the problem defined in (3.3.4) is equivalent to:

$$\begin{aligned} \text{minimize} \quad & \|\mathbf{Q}^{1/2}\,(\delta\xi) + \frac{1}{2}\,\mathbf{Q}^{-1/2}\,\mathbf{q}\|^2 \\ \text{subject to} \quad & -\mathbf{L}\,\delta\xi - \mathbf{x}^b \le \mathbf{c}_{\min} \\ & \mathbf{L}\,\delta\xi + \mathbf{x}^b \le \mathbf{c}_{\max} \quad , \end{aligned}$$

which is equivalent to:

$$\begin{aligned} \text{minimize} \quad & t \\ \text{subject to} \quad & \|\mathbf{Q}^{1/2}\,(\delta\xi) + \frac{1}{2}\,\mathbf{Q}^{-1/2}\,\mathbf{q}\| \le t \\ & -\mathbf{L}\,\delta\xi - \mathbf{x}^b \le \mathbf{c}_{\min} \\ & \mathbf{L}\,\delta\xi + \mathbf{x}^b \le \mathbf{c}_{\max} \quad . \end{aligned}$$

We have taken advantage of the quadratic form of the cost function and the convexity of the constraints to rewrite the minimization problem as a convex minimization problem. Consequently we can solve the minimization problem with numerical solvers designed for convex problems, instead of more general non-linear numerical solvers.

In our assimilation system, we use the software interface developed by Diamond and Boyd (2016). Within this interface we have used two different algorithms, depending on the size of the control vector. For the smaller control vector in Chapter 4 we have use the ECOS software developed by Domahidi et al. (2013). For the larger control vector (Chapter 5), we found that the CVXOPT solver was considerably faster and more stable. The CVXOPT package is available at `http://cvxopt.org/`. In both cases we have set the lower bound ($\mathbf{c}_{\min}$) to zero and we did not set an upper bound ($\mathbf{c}_{\max} = \infty$).

Chapter 4

Article: Subregional inversions of North African dust sources

This Chapter presents our first subregional inversions of North African dust sources as an article published in the Journal of Geophysical Research Escribano et al. (2016). For copyright issues, we present here the last manuscript sent to the Journal which is almost identical to the published version. In this article we briefly describe the observation operator and the data assimilation system, and then we estimate dust emission sources for a one-year period with our inversion system. We evaluate the consistency of the inversion by comparing the analysis AOD against the assimilated observations, we analyse the behaviour of the analysis control vector, we compare our results against independent AOD observations and finally we estimate the dust emission flux.

We have also included in this chapter some interesting additional material about this work in Section 4.2. In this Section we show a comparison between the mean 10-meter wind velocity for three different datasets, the vertical structure of the simulated aerosol for the prior and the analysis, and we briefly show the AOD simulated for the dust outbreak of March 7–13 2006.

4.1 Published article

Subregional inversion of North African dust sources

Jerónimo Escribano[1], Olivier Boucher[1], Frédéric Chevallier[2] and Nicolás Huneeus[3,4]

[1]Laboratoire de Météorologie Dynamique, Université Pierre et Marie Curie / CNRS, Paris, France, [2]Laboratoire des Sciences du Climat et de l'Environnement, CEA, Saclay, France, [3]Geophysics Departement, University of Chile, Santiago, Chile, [4]Center for Climate and Resilience Research (CR)^2, Santiago, Chile.

Abstract

The emission of mineral dust aerosols in arid and semi-arid regions is a complex process whose representation in atmospheric models remains crude, due to insufficient knowledge about the aerosol lifting process itself, the lack of global data on soil characteristics, and the impossibility for the models to resolve the fine-scale variability in the wind field that drives some of the dust events. As a result, there are large uncertainties in the total emission flux of mineral dust, its natural variability at various timescales, and the possible contribution from anthropogenic land use changes. This work aims for estimating dust emissions and reduce their uncertainty over the Sahara Desert and the Arabian Peninsula –the largest dust source region of the globe. We use a data assimilation approach to constrain dust emission fluxes at a monthly resolution for 18 sub-regions. The MODIS satellite-derived aerosol optical depth is assimilated in a regional configuration of a general circulation model coupled to an aerosol model. We describe this data assimilation system and apply it for one year, resulting in a total mineral dust emissions flux estimate of 2900 Tg year^{-1} over the Sahara Desert and the Arabian Peninsula for the year 2006. The analysis field of aerosol optical depth shows an improved fit relative to independent AERONET measurements as compared to the model prior field.

4.1.1 Introduction

The role of desert dust in the climate system has been studied intensively in the past years (Knippertz and Stuut, 2014, and references therein). It has been shown that atmospheric mineral dust has a number of impacts on a wide range of components and scales in the Earth system. Saharan dust has a fertilization effect in the Atlantic Ocean and the Mediterranean Sea because of its iron content that can become biologically available to phytoplankton when dust is deposited at the ocean surface (Jickells et al., 2005; Mahowald et al., 2014). It also brings a large fraction of the aeolian input of phosphorus (a limiting nutrient) over the Amazon forest ecosystem (Koren et al., 2006; Mahowald et al., 2014). Mineral dust has impacts on air quality and human health (Goudie, 2014). Finally mineral dust also interacts with radiation and clouds in the atmosphere (e.g., Haywood et al., 2005; Atkinson et al., 2013), with gas-phase species through heterogeneous chemistry (Dentener et al., 1996) and it has been hypothesized that it may influence microphysical related processes in the cyclogenesis over the Atlantic Ocean (Bretl et al., 2015).

Despite the important and central roles of desert dust in the Earth system, the total mass of aerosol emissions is still highly uncertain (Huneeus et al., 2011). Observations, modeling and combined approaches have been used to narrow the uncertainty in emissions both at the global (Cakmur et al., 2006; Huneeus et al., 2012) and regional (Yumimoto et al., 2008; Huneeus et al., 2011) scales. Models continue to experience difficulties to simulate the correct seasonal cycle of dust emissions probably for a variety of reasons. First of all, the emission process is not well understood even though dust lifting models have been improved and complexified (Woodward, 2001; Zender et al., 2003; Kok, 2011). We also lack reliable data on soil characteristics (size distribution, mineral composition, crusting effect, etc) despite recent progress in mapping soil mineralogy (Journet et al., 2014). Furthermore atmospheric models do not resolve the fine-scale variability in the surface wind and parametrizations have to be introduced to represent these effects (Zhang et al., 2016).

The amount of dust in the atmosphere can be estimated from satellite-borne passive instruments, both in the ultraviolet-visible part of the electromagnetic spectrum with e.g. the MODerate resolution Imaging Spectroradiometer (MODIS, Levy et al., 2013), the Multi-angle Imaging SpectroRadiometer (MISR, Kahn et al., 2009), the Polarization and Anisotropy of Reflectances for Atmospheric Sciences coupled with Observations from a Lidar (PARASOL, Tanré et al., 2011) and in the infrared with e.g. the Infrared Atmospheric Sounder Interferometer (IASI, Peyridieu et al., 2013), as well as from ground-based passive instruments (e.g., sunphotometers). Active remote sensing methods can also be used in the visible part of the spectrum with either ground-based or satellite-based lidar systems. All these measurements are based on the interpretation of the interactions between dust aerosols and radiation, which introduces some uncertainty in the estimate because of uncertainties in dust morphology and particle shape, size distribution, and hence optical properties, as well as in the surface scattering properties. Several aerosol chemical and physical properties have been assessed in intensive measurement campaigns (Redelsperger et al., 2006; Washington et al., 2006; Ansmann et al., 2011; Washington et al., 2012), giving valuable information on dust aerosol emissions, transport, deposition processes and chemical and physical properties. However such surface or atmospheric measurements are very sparse in space and time, which limits their usefulness for constraining the regional or global cycle of mineral dust. Many studies rely on long-term series of observations (e.g. ground-based sunphotometers, ground-based lidar and satellite-borne instruments) to constrain the dust cycle. Regrettably, these long-term observations report the amount of atmospheric dust; they cannot be directly translated into estimates of dust fluxes and they are not enough on their own to constrain dust fluxes for large areas (such as the Sahara Desert or eastern Asia). In this context, data assimilation is an attractive tool that allows combining available observations with existing modeling tools in order to estimate emissions.

Data assimilation techniques are widely used in atmospheric chemistry to improve the modelled concentrations of various chemical species (Bocquet et al., 2015) and are necessary to produce realistic forecasts (Benedetti et al., 2009). These techniques also constitute a useful tool to constrain the atmospheric fluxes of a number of chemical species whether they are short-lived such as HCHO and CO (e.g., Fortems-Cheiney et al., 2012), or longer-lived such as CO_2 (e.g., Chevallier et al., 2010) or CH_4 (e.g., Bousquet et al., 2006). Such techniques have also been used for aerosol species, assimilating surface concentration observations (e.g., Hakami et al., 2005), aerosol extinction coefficients from lidar instruments (e.g., Yumimoto et al., 2008) or aerosol optical depth (e.g., Dubovik et al., 2008; Schutgens et al., 2012; Huneeus et al., 2012; Yumimoto and Takemura, 2013). One of the difficulty associated with aerosols is that aerosol optical depth (AOD) observations do not usually distinguish the chemical composition of the aerosol, which makes the inversion problem particularly underconstrained. For mineral dust, there is an additional difficulty in that the background emission flux need to be computed in the model rather than prescribed from an emission inventory.

The aim of this study is to quantify the dust flux emissions over the Sahara Desert and the Arabian Peninsula with sufficient temporal and spatial resolution to be able to capture the main emission features and variability over a one-year period. For this reason our emphasis is on a regional source inversion that can take full benefit of satellite data and increased model resolution.

Section 4.1.2 presents the data assimilation system used in this work, including the meteorological model, the dust emission model, the aerosol model and the assimilated observations. We show results of the AOD assimilation in Section 4.1.3, comparing model simulations with observations and estimating dust fluxes. Results and performance of the assimilation system are discussed in Section 4.1.4. We present our conclusions in Section 4.1.5.

4.1.2 Data and Methods

4.1.2.1 LMDz-SPLA Model

Meteorological and Aerosol Model

We use the simplified aerosol model (SPLA, Huneeus et al., 2009) coupled to the general circulation model of the Laboratoire de Météorologie Dynamique (LMDz, Hourdin et al., 2013). The LMDz is a hydrostatic model with hybrid vertical coordinate and a stretchable latitude-longitude horizontal grid. The model numerically solves the advection equations on a three dimensional grid (the so-called “dynamics”). Sub-grid scale processes, including radiative transfer, cloud, and boundary layer processes, are parameterized as part of the “physics” part of the model. The SPLA model is an aerosol model of intermediate complexity that is fully embedded in the LMDz model; it was originally designed for data assimilation purposes but has evolved in several aspects since then. Major changes of SPLA are listed in the next paragraphs of this Section, mainly associated to updates in emissions of natural aerosols and in physical processes parameterizations and also associated to changes in aerosol bin definitions (with a consistent update of sedimentation velocities and optical aerosol properties). The SPLA model has been used to estimate global aerosol emissions in Huneeus et al. (2012).

The following processes are included in the aerosol model for aerosols and their gaseous precursors: surface and elevated emissions, dry deposition, boundary layer mixing, transport from subgrid-scale thermals (Hourdin et al., 2015), sedimentation for coarse mode aerosols, gas-to-particle conversions, in-cloud and below-cloud scavenging, convective transport and large-scale transport.

As stated above, we have performed major updates to the SPLA model. The number of modelled species has been increased. The model presented in Huneeus et al. (2009) had four tracers: gaseous precursors of aerosols, coarse mode sea salt (with diameters between 1 and

40 µm), fine mode aerosols and coarse mode dust. In the present work, mineral dust aerosols are distributed in three bins that represent super-coarse dust (between 6 and 30 µm of diameter), coarse mode dust (between 1 and 6 µm of diameter), and fine mode dust (with diameter smaller than 1 µm). After emission, fine mode dust is included in the fine mode aerosols tracer (which also includes black carbon, particulate organic matter and sulfate aerosols), so in practice the SPLA model has only five tracers now. Additional work has been done to update the SPLA model according to the latest developments of the LMDz model, including the parameterization of thermals in the boundary layer (Hourdin et al., 2015) and the convective transport and scavenging scheme (Pilon et al., 2015).

Dust Emission Model

Over the Sahara Desert and the Arabian Peninsula, the mineral dust emissions are calculated online using a parametrization described below.

The dust production module (DPM) originally used in the CHIMERE-DUST air quality model (Menut et al., 2013) has been embedded in the SPLA model. Our implementation is based on the DPM adaptation from Hourdin et al. (2015), which calculates mineral dust emissions online and only over the Sahara Desert and the Arabian Peninsula. The DPM is composed essentially of a saltation flux scheme from Marticorena and Bergametti (1995) and a sandblasting model from Alfaro and Gomes (2001). Threshold friction velocities are estimated following Shao and Lu (2000) and corrected by a drag efficiency coefficient as in Marticorena et al. (1997). Input soil data over the Sahara Desert and the Arabian Peninsula are taken from the Laboratoire Interuniversitaire des Systèmes Atmosphériques (LISA) database (available at http://www.lisa.univ-paris12.fr/mod/data/index.php).

The DPM scheme includes a Weibull-like wind speed distribution to represent subgrid-scale variability as explained in Hourdin et al. (2015). The dust fluxes are calculated and summed over the bins of the discretized wind speed distribution, for each gridbox and each timestep of the physics of the model (set to 15 minutes). The subgrid wind speed distribution, in its continuous form, is given by the following probability density function:

$$p(u,k,A) = \frac{k}{A}\left(\frac{u}{A}\right)^{k-1} \exp\left[-\left(\frac{u}{A}\right)^{k}\right] \quad ,$$

where u is the subgrid-scale wind speed, and (k, A) are parameters of the Weibull distribution. The shape parameter k has been set equal to 3 as in Hourdin et al. (2015), and the A parameter is calculated for each grid cell and each timestep to fit the Weibull distribution expectancy with the mean wind velocity from the LMDz model: $U = A\,\Gamma(1+1/k)$ where U is the 10–meter mean wind for each gridcell and Γ the Gamma function.

For each soil type from the LISA database, the horizontal saltation flux F_h is calculated according to Marticorena and Bergametti (1995) as

$$F_h(D_p, s) \;=\; \frac{K\,\rho_a\,U^*(s)^3\,S_{rel}(D_p, s)}{g}\left(1 + \frac{U_t^*(D_p, s)}{U^*(s)}\right)\left(1 - \frac{U_t^*(D_p, s)^2}{U^*(s)^2}\right) \quad ,$$

where s is the soil type, D_p is the soil particle diameter, K is a constant value, ρ_a is the air density, g is the gravitational constant, U^* is the friction velocity (which depends on the soil type through the saltation roughness length parameter), U_t^* is the threshold friction velocity, and S_{rel} is the proportion of the surface covered by particles of type s with diameter D_p. In the case of $U_t^*(D_p, s) > U^*(s)$, the friction velocity threshold is not reached by the model and there are no emissions ($F_h(D_p, s) = 0$). In this work, the value of K is set to its original value of 2.61 (Marticorena and Bergametti, 1995) instead of the value of 1.0 used in Hourdin et al. (2015) and in Menut et al. (2013).

After the saltation scheme, the sandblasting model is used to calculate the vertical dust flux assuming that it is emitted by three soil modes (Alfaro and Gomes, 2001). For each soil type s, soil particle diameter D_p and soil mode i, the vertical flux F_v is

$$F_{v,i}(D_p, s) \;=\; \frac{\pi}{6}\,\beta\,\rho_p\,\frac{p_i(D_p, s)\,d_i^3}{e_i}\,F_h(D_p, s) \quad ,$$

where $\beta = 16300$ cm s^{-2}, ρ_p is the particle density, d_i is the mass median diameter for the mode i, e_i is the binding energy for the mode i, p_i is the fraction of kinetic energy for the binding energy e_i, calculated as in Alfaro and Gomes (2001). The total dust flux for the mode i is calculated by the sum of the contributions of all the soil types:

$$F_{v,i} \;=\; \sum_s \int_{D_p^{\min}}^{D_p^{\max}} F_{v,i}(D_p, s)\,\mathrm{d}D_p \quad ,$$

where $D_p^{\max}$ and $D_p^{\min}$ are the maximum and minimum particle diameters for the soil size distribution. Finally, the vertical flux of the three modes from Alfaro and Gomes (2001) scheme are redistributed into the SPLA tracers for fine, coarse and super-coarse mode dust.

Some of the key parameters of this scheme are the binding energy parameters, which account for the necessary energy to release particles in the sandblasting processes for each soil mode used in the scheme. The work by Sow et al. (2011) shows that these binding energy parameters should not be constant to fit in situ emission flux measurements, instead they may depend on the strength of the dust event. Sow et al. (2011) divide the binding energy parameters by a factor 2.5 in the case of a strong dust event, and by a factor of 5 in the case of a weaker event to fit in situ emission flux measurements. We also choose to tune the binding energy parameters and divide it by a six-fold factor. This is somewhat an arbitrary choice but is partly justified by the fact that we are interested in simulating the dust flux emission for a long period (and not only for dust events).

Data assimilation systems are sensitive to biases in the observations and in the observation operator (the LMDz-SPLA model in our case). Biases can be propagated to the analysis and deteriorate the analysis performance (e.g. Dee, 2005). The simulated AOD from the LMDz-SPLA model is systematically low over the region of focus, and the study of the source of this bias is out of the scope of this work. To avoid a bias in the observation operator and in order to have a mean simulated AOD in the range of the (satellite and ground-based) observations, we apply a tuning multiplicative factor equal to 3.25 to the coarse and super-coarse dust emissions and 0.8 to the fine mode dust emissions. The tuning factor is not the same for the three emission bins due to the known overestimation of fine mode dust emissions in the DPM relative to the coarser modes (Nabat et al., 2012).

Although our focus is over the Sahara and the Arabian Peninsula, it is likely that dust emitted outside this region can be advected to our region of interest. To address this, dust emissions outside the Sahara and the Arabian Peninsula are calculated offline from ERA-Interim 10-meter wind speed as in Huneeus et al. (2013).

Other Emissions

Emissions of remaining aerosol species and gaseous precursors, except DMS, are similar to those used in Huneeus et al. (2013). The climatology of ocean near-surface dimethlysulfide (DMS) concentration has been updated with the work of Lana et al. (2011), and the DMS emission flux is calculated (like in Huneeus et al. (2013)) with the parameterization by Nightingale et al. (2000). Anthropogenic emissions for the year 2000 from Lamarque et al. (2010) have been used. Daily biomass burning (BB) emissions fluxes are taken from the GFED 3.1 inventory (van der Werf et al., 2010). In the region of interest, almost all BB emissions fluxes are located south to the Saharan desert, and they have a strong annual cycle with BB emissions being maximum between November and February.

4.1.2.2 Observations

Total AOD at 550 nm is assimilated from satellite retrievals, while ground-based measurements are used only for validation purposes. We use total 550 nm AOD retrievals from the daily Level 3 Merged Dark Target/Deep Blue (Levy et al., 2013) product from the Moderate resolution Imaging Spectroradiometer (MODIS) instrument, on-board the polar sun-synchronous orbit satellite Aqua.

For validation purpose, we use daily 500 nm AOD Level 2 retrievals from the Aerosol Robotic Network (AERONET) sunphotometers (Holben et al., 1998), without any post- or pre-processing. For satellite data only, we regrid the AOD retrievals into the model grid.

4.1.2.3 Data Assimilation System

Our objective is to find the best emission estimate, combining information from models and observations. The optimality of the assimilated emissions is formulated in terms of the minimization, over the control vector $\mathbf{x}$, of the following cost function:

$$J(\mathbf{x}) = \frac{1}{2}(\mathbf{x}-\mathbf{x}^b)^T\,\mathbf{B}^{-1}\,(\mathbf{x}-\mathbf{x}^b) + \frac{1}{2}(\mathbf{y}^o - H(\mathbf{x}))^T\,\mathbf{R}^{-1}\,(\mathbf{y}^o - H(\mathbf{x})) \quad , \tag{4.1.1}$$

where $\mathbf{x}^b$ is the background (or prior) control vector, $\mathbf{y}^o$ is the observation vector, H is the observation operator, $\mathbf{B}$ is the covariance matrix of the background errors and $\mathbf{R}$ is the covariance matrix of the observations errors. The minimum of the cost function is achieved for the "analysis", it is denoted $\mathbf{x}^a$ and calculated in this work through the use of a constrained minimization algorithm, given the constraints over the control vector, as explained in the next sections.

Control Vector

The control vector $\mathbf{x}$ is composed of multiplicative correction factors of the model emissions. We split the spatial domain of interest in a number of "sub-regions", and the temporal domain in a number of "sub-periods". We also define a number of emission "categories", which are related to the type of aerosol (or aerosol precursor) included in the emission scheme of the model.

We assume constant correction factors over each sub-region, sub-period and emission category. The number of sub-regions and sub-periods depend on the category of emission. Following the approach applied in Huneeus et al. (2013), we define 6 emission categories: fine desert dust, coarse and super-coarse desert dust, biomass burning emissions, fine mode sea salt, coarse mode sea salt, and anthropogenic SO_2 and fossil fuel emissions. Only one region is considered for fine sea salt, coarse sea salt, anthropogenic SO_2 and fossil fuel emissions, which covers the entire globe. The seasonality of sea salt emissions is assumed to be correct in the model and only one time period (of one year) is used for sea salt. For biomass burning emissions, two sub-regions are constructed based on the land cover class map of Kaiser et al. (2012), one for grassland-like (including savannah) land cover and a second one for forest-like land cover. The correction factors have a monthly resolution for biomass burning.

We define 18 dust sub-regions over the area of interest (Figure 4.1) as we expect that most of the AOD observed in the assimilation region (Figure 4.2) is due to aerosol emitted over the Sahara Desert, the Arabian Peninsula and over the Atlantic Ocean. However, a 19th dust sub-region is also defined for the rest of the globe, because its emissions can also occasionally influence the AOD in the region of interest. The sub-regions are the same for the three categories of dust. Their number is a trade off between the expected spatial resolution of the analysis and the computational cost of our inversion system. The maximum possible number of sub-regions would correspond to the number of model grid-boxes. The main idea is to construct sub-regions that are as large as possible but also homogeneous, so as to get an affordable quantity of sub-regions consistent with the information content of the observations.

We define the dust sub-regions in the following way: first, the distribution of the dust emitted flux is calculated for a long period (one year in our case) at an hourly output resolution. We then compute the temporal correlation of the emission flux in each grid-box with the other grid-boxes.

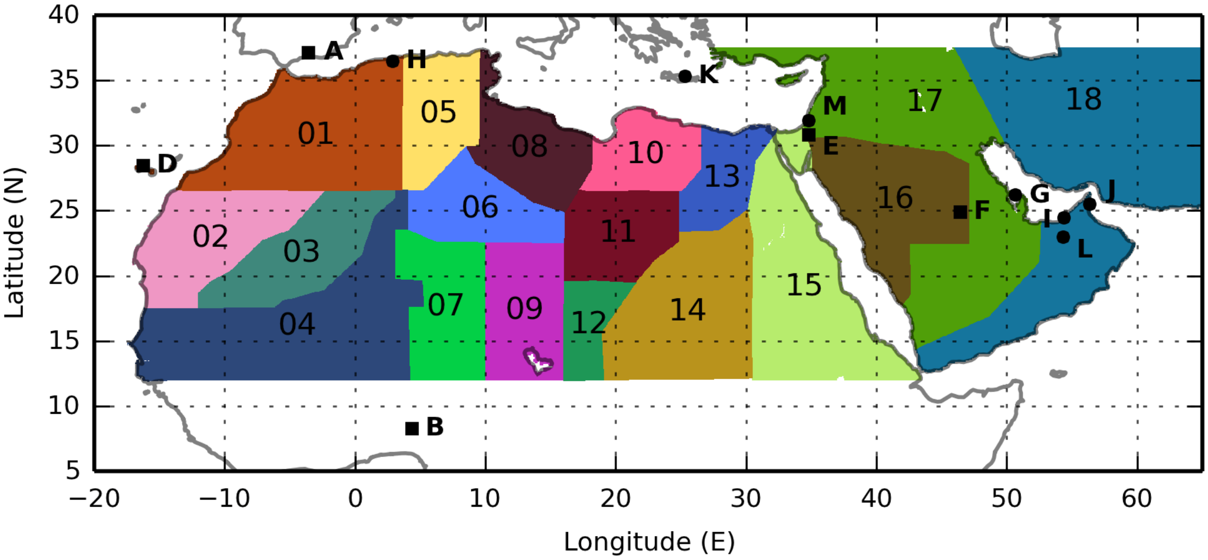

Figure 4.1: Numbered sub-regions for fine dust and coarse and super-coarse dust correction factors (composing the control vector elements). AERONET sites used in this study (Figure 4.5 and Table 4.1) are shown with letters A–F (squares). Remainig AERONET sites (circles) of Table 4.1 are shown with letters G–M. The AERONET sites are: Granada (A), Ilorin (B), La Parguera (C, not shown in this Figure), Santa Cruz Tenerife (D), Sede Boker (E), Solar Village (F), Bahrain (G), Blida (H), Dhabi (I), Dhadnah (J), Forth Crete (K), Hamim (L) and Nes Ziona (M).

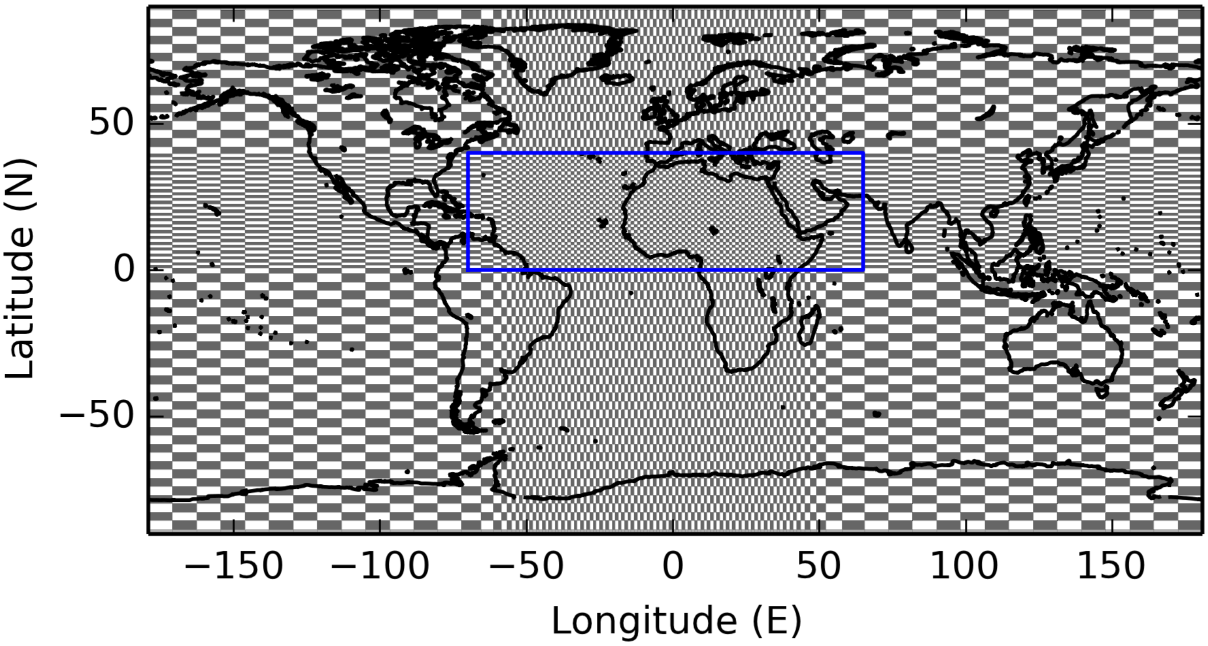

Figure 4.2: Representation of the LMDz grid. The blue rectangle depicts the assimilation region as described in the text.

With this calculation, we obtain a correlation map for each grid-box in the region of interest (not shown). The idea is then to group the most similar grid-boxes into sub-regions, so that the temporal emission patterns of grid-boxes within a given subregion are similar. For this purpose, two clustering methods have been used: K-means and Gaussian Mixture Model (implemented by Pedregosa et al., 2011). These two methods allow creating a spatial partition of the region of interest, but they only use information from the model dust fluxes. The final step is to manually modify the sub-regions created by the clustering analysis by including information on the dust source that is available in the literature (Schepanski et al., 2007; Ginoux et al., 2012), and to join or split the sub-regions in order to i) keep a known dust source location into a single sub-region, and ii) keep well-known dust sources as separate sub-regions. This last step in the sub-region construction has an arbitrary or subjective component, but is a way to include key information in the construction process.

Alternatively, it would be possible to define the sub-regions based on the AOD retrievals within the inversion process itself (Bocquet et al., 2011). However, given the associated substantial increase of the computational burden, we prefer to define the sub-regions using model information only.

In terms of temporal resolution, our inversion system allows for a different number of sub-periods for each category of correction factors in the control vector. In this work, coarse sea salt and fine sea salt are defined with one element per year, which means that the correction factors for fine and coarse sea salt emissions have a yearly resolution. For the rest of the elements in the control vector, we set a monthly resolution, which means that we have one element in the control vector per category of emissions, sub-region and month. In summary, for a one-year assimilation, the number of elements in the control vector is 19×12 for fine dust, 19×12 for coarse and super-coarse mode dust (lumped together), 2×12 for biomass burning, 1×12 for anthropogenic and fossil fuel emissions, 1 for fine sea salt and 1 for coarse sea salt, which gives a total of 494 elements for the control vector.

Observation Operator and Minimization Procedure

The 550 nm AOD estimation by the LMDz-SPLA model from the emissions is used as the observation operator. To compare the model output with the MODIS/Aqua retrievals, the model AOD is sampled at 13:30 equatorial local time to match the satellite overpass time. We discard all the pixels with an AOD difference larger than 1 with regard to the prior simulation because large differences between the prior simulation and the observations can deteriorate the quality of the analysis (Lorenc and Hammon, 1988). The number of observations discarded by this filter is less than the 2 percent of the total number of observations. Comparison with AERONET is done using the model daily mean AOD at the model grid-box level. We extrapolate the simulated 550 nm AOD into a 500 nm AOD using the 550-670 Ångström coefficient that is also computed in the model. As neither the linear tangent nor the adjoint model have been coded for the new version of LMDz-SPLA model, the minimization of Equation (4.1.1) is done only using the forward model. In order to minimize Equation (4.1.1), the observation operator is approximated by:

$$H(\mathbf{x}) \;=\; H(\mathbf{x}^b) + \mathbf{H}(\mathbf{x} - \mathbf{x}^b) \quad ,$$

where $\mathbf{H}$ is the Jacobian of the nonlinear observation operator H, evaluated at the $\mathbf{x}^b$ point, and calculated trough finite differences. Perturbations are chosen equal to one, and they are within the expected order of magnitude of correction factor differences between the analysis and the prior.

In principle it is necessary to perform a number of forward simulations (at least) equal to the number of elements in the control vector plus one (for the background or prior simulation), to fully construct the $\mathbf{H}$ matrix. With the aim of saving computing time, only the background simulation is made for the whole one-year period. To compute the AOD due to perturbations in the elements of the control vector (and to reduce the computing time), we take advantage of the relative short residence time of atmospheric aerosols and we assume that the effect of the perturbation in emission is negligible beyond 15 days after the end of the perturbation for each sub-period, and by definition is equal to zero for all the days before the emission perturbation is perturbed. Under this assumption, each simulation associated with a one-month sub-period is calculated by simulating only one and a half month instead of a whole year, thus saving a considerable amount of computing time.

With the linear approximation of H, the cost function is a quadratic function, and the solution space is bounded by the constraint of the non-negativeness of the control vector that we choose to impose. As the solution space of the optimization problem is bounded, we cannot use the standard linear algebra solution from the unconstrained problem. Instead we directly minimize the cost function using an appropriate numerical solver, which takes advantage of the convexity of the optimization problem. The minimization is performed for all the elements of the control vector simultaneously.

We use the inverse of the Hessian of the cost function (evaluated at the analysis point) to estimate the analysis error covariance matrix $\mathbf{A}$. In an unconstrained framework, the $\mathbf{A}$ matrix is estimated as :

$$\mathbf{A} \;=\; (\mathbf{H}^T\,\mathbf{R}^{-1}\,\mathbf{H} + \mathbf{B}^{-1})^{-1} \quad . \tag{4.1.2}$$

In the constrained case, the computation of $\mathbf{A}$ is the same as in Equation (4.1.2), because the bounds do not change the Hessian of the cost function in the solution space. Standard deviations of analysis errors are estimated as the square root of the diagonal terms of $\mathbf{A}$.

B and R Matrices

In principle we use variances of background ($\mathbf{B}$) and observations ($\mathbf{R}$) errors from Huneeus et al. (2013). Standard deviations of the observational errors are set to 0.2 for MODIS AOD over land and 0.1 for MODIS AOD over ocean in $\mathbf{R}$. Standard deviation of the model error is set to 0.02

in **R**. Errors associated with dust bin discretization and other model equation discretizations are implicitly embedded in the model error in the **R** matrix. Huneeus et al. (2012) show that 0.02 is an appropriate value for the model error of the LMDz-SPLA AOD observation operator. Standard deviations of the background errors are set as 3.0 for dust emissions (coarse and super-coarse modes lumped together and fine mode), 1.3 for biomass burning emissions, 2.0 for sea salt emissions (fine and coarse) and 0.18 for anthropogenic and fossil fuel emissions in **B**. Unlike Huneeus et al. (2013), we have included two types of non-diagonal terms in the **B** matrix. The first accounts for the correlation between the errors in the dust emission of the two dust categories in a same sub-period. We have fixed this through a correlation coefficient of 0.6. A second correlation has been introduced between different sub-periods for the same sub-region and category of emission. We assume a Gaussian correlation (Pannekoucke et al., 2008) and we use a time scale L of 20 days so that:

$$\rho_L = \exp\left(-\frac{(\Delta T)^2}{2\,L^2}\right) \quad ,$$

where ΔT is the time between the two sub-periods associated to the pair of elements in the control vector, in the same units as the time scale L.

The matrices **B** and **R** have been inflated to satisfy two of the a posteriori diagnostics presented in Desroziers et al. (2005) for the trace of the matrices, and specifically the diagnostic related to the observational errors and the one related to the analysis errors. In other words, we have calculated two scalars $\alpha_\mathbf{B}$ and $\alpha_\mathbf{R}$ such that:

$$\begin{aligned}
\mathrm{Tr}(\mathbf{d}_a^o(\mathbf{d}_b^o)^T) &= \mathrm{Tr}(\mathbf{R}_{\alpha_\mathbf{R}}) \quad ,\\
\mathrm{Tr}(\mathbf{d}_b^a(\mathbf{d}_a^o)^T) &= \mathrm{Tr}(\mathbf{H}\,\mathbf{A}_{\alpha_\mathbf{B},\alpha_\mathbf{R}}\,\mathbf{H}^T) \quad ,
\end{aligned}$$

where Tr is the trace of the matrix and

$$\begin{aligned}
\mathbf{d}_b^o &= \mathbf{y}^o - H(\mathbf{x}^b) \quad ,\\
\mathbf{d}_b^a &= H(\mathbf{x}^a) - H(\mathbf{x}^b) \quad ,\\
\mathbf{d}_a^o &= \mathbf{y}^o - H(\mathbf{x}^a) \quad ,\\
\mathbf{R}_{\alpha_\mathbf{R}} &= \alpha_\mathbf{R}\mathbf{R} \quad ,\\
\mathbf{A}_{\alpha_\mathbf{B},\alpha_\mathbf{R}} &= \left(\mathbf{H}^T\,(\alpha_\mathbf{R}\mathbf{R})^{-1}\,\mathbf{H} + (\alpha_\mathbf{B}\mathbf{B})^{-1}\right)^{-1} \quad ,\\
H(\mathbf{x}) &= H(\mathbf{x}^b) + \mathbf{H}(\mathbf{x} - \mathbf{x}^b) \quad ,
\end{aligned}$$

and

$$\mathbf{x}^a = \mathrm{argmin}_{\mathbf{x}\geq 0}\left\{\frac{1}{2}(\mathbf{x}-\mathbf{x}^b)^T\,\mathbf{B}_{\alpha_\mathbf{B}}^{-\mathbf{1}}\,(\mathbf{x}-\mathbf{x}^b) + \frac{1}{2}\,(\mathbf{y}^o - H(\mathbf{x}))^T\,\mathbf{R}_{\alpha_\mathbf{R}}^{-\mathbf{1}}\,(\mathbf{y}^o - H(\mathbf{x}))\right\} \quad .$$

After calculations, the inflation factor for the **R** matrix ($\alpha_\mathbf{R}$) is equal to 1.09 and the inflation factor for the **B** matrix ($\alpha_\mathbf{B}$) is 4.08. Consequently, we define $\mathbf{B}' = 4.08 \times \mathbf{B}$ and $\mathbf{R}' = 1.09 \times \mathbf{R}$.

The factor $\alpha_{\mathbf{B}} = 4.08$ may account for missing covariances of the background errors. The factor is calculated in the observational space using diagnostics of the analysis, thus the interpretation of the factor $\alpha_{\mathbf{B}}$ in the parameter space is not direct. However, this factor leads to a prior uncertainty of the dust fluxes in the expected range (see Section 4.1.3.5).

4.1.2.4 Experimental Configuration

We focus this study on the Sahara Desert and Arabian Peninsula region, and we take advantage of the zoom capability of the atmospheric model to choose a model grid with a horizontal resolution close to 1° by 1° over the Sahara Desert (Figure 4.2). The model grid has an average resolution of 1° in latitude and 1.4° in longitude in the latitude-longitude box defined by the corners [0°N,70°W] and [40°N,70°E]. This grid is a compromise between the computing cost of the system and our computing capabilities; it is also selected to reduce the impact of the regridding process of the dust emission model input data, which is provided at the 1° by 1° resolution, into the atmospheric model grid. The global atmospheric model has an horizontal grid of 128 by 88 points, and 39 levels in the vertical coordinate. The model zonal and meridional winds are nudged to the ECMWF ERA-Interim reanalysis (Dee et al., 2011), as described in Hourdin et al. (2015). The nudging of the model is performed with a relaxation time of 48 hours inside the zoom and 3 hours outside the zoom. The nudging (or relaxation) of the model winds consists in adding a non-physical term into the model equations to push the model to follow the reanalysis winds. Outside the zoom, the short relaxation time forces the model to follow closely the reanalysis winds. However, inside the zoom, the model is able to develop its own diurnal cycle and the features of the model physics and dynamics can fully develop (for example, the near surface wind in Hourdin et al. (2015)). Sea surface temperature and surface ice and snow cover are also prescribed from ERA-Interim. The simulation period is the year 2006 for all our simulations and analysis, and the spin up was performed over one year with nudged winds from ERA-Interim reanalysis.

Despite the global coverage of the model and the observations, we only assimilate observations in a reduced region of the globe. The selected assimilation region, defined as a rectangle with coordinates ranging from 70°W to 65°E in longitude and 0°N to 40°N in latitude, allows the system to assimilate both the aerosol AOD over Africa and the adjacent Atlantic Ocean (Figure 4.2).

4.1.3 Results

4.1.3.1 Cost Function Decrease

The data assimilation system successfully reduces the cost function $J(\mathbf{x})$ (Equation (4.1.1)) to a value close to 2/3 of the prior cost function value. In a consistent data assimilation system, the final value of $J(\mathbf{x})$ should be close to half the number of the observations (Talagrand, 1998). In our case, with $\approx 709,000$ observations and with an initial value of the cost function equal

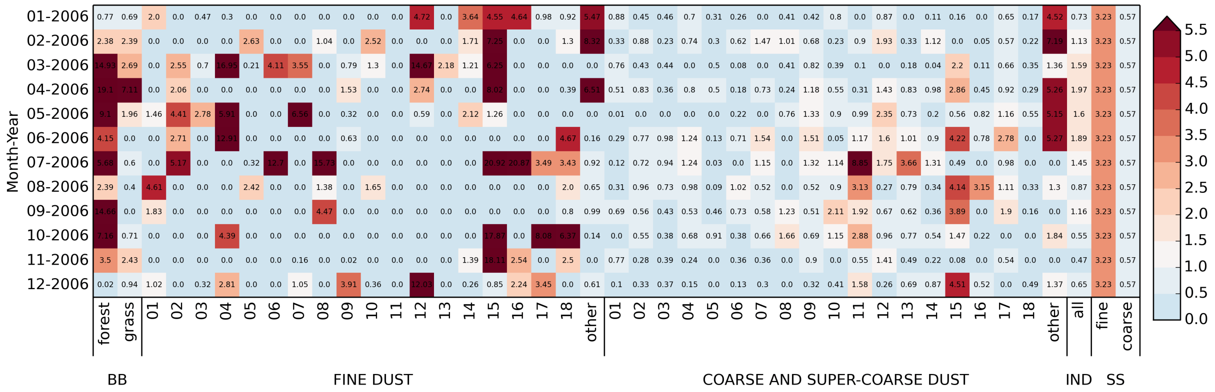

Month-Year	BB		FINE DUST																		
	forest	grass	01	02	03	04	05	06	07	08	09	10	11	12	13	14	15	16	17	18	other
01-2006	0.77	0.69	2.0	0.0	0.47	0.3	0.0	0.0	0.0	0.0	0.0	0.0	0.0	4.72	0.0	3.64	4.55	4.64	0.98	0.92	5.47
02-2006	2.38	2.39	0.0	0.0	0.0	0.0	2.63	0.0	0.0	1.04	0.0	2.52	0.0	0.0	0.0	1.71	7.25	0.0	0.0	1.3	8.32
03-2006	14.93	2.69	0.0	2.55	0.7	16.95	0.21	4.11	3.55	0.0	0.79	1.3	0.0	14.67	2.18	1.21	6.25	0.0	0.0	0.0	0.0
04-2006	19.1	7.11	0.0	2.06	0.0	0.0	0.0	0.0	0.0	0.0	1.53	0.0	0.0	2.74	0.0	0.0	8.02	0.0	0.0	0.39	6.51
05-2006	9.1	1.96	1.46	4.41	2.78	5.91	0.0	0.0	6.56	0.0	0.32	0.0	0.0	0.59	0.0	2.12	1.26	0.0	0.0	0.0	0.0
06-2006	4.15	0.0	0.0	2.71	0.0	12.91	0.0	0.0	0.0	0.0	0.63	0.0	0.0	0.0	0.0	0.0	0.0	0.0	0.0	4.67	0.16
07-2006	5.68	0.6	0.0	5.17	0.0	0.0	0.32	12.7	0.0	15.73	0.0	0.0	0.0	0.0	0.0	0.0	20.92	20.87	3.49	3.43	0.92
08-2006	2.39	0.4	4.61	0.0	0.0	0.0	2.42	0.0	0.0	1.38	0.0	1.65	0.0	0.0	0.0	0.0	0.0	0.0	0.0	2.0	0.65
09-2006	14.66	0.0	1.83	0.0	0.0	0.0	0.0	0.0	0.0	4.47	0.0	0.0	0.0	0.0	0.0	0.0	0.0	0.0	0.0	0.8	0.99
10-2006	7.16	0.71	0.0	0.0	0.0	4.39	0.0	0.0	0.0	0.0	0.0	0.0	0.0	0.0	0.0	0.0	17.87	0.0	8.08	6.37	0.14
11-2006	3.5	2.43	0.0	0.0	0.0	0.0	0.0	0.0	0.16	0.0	0.02	0.0	0.0	0.0	0.0	1.39	18.11	2.54	0.0	2.5	0.0
12-2006	0.02	0.94	1.02	0.0	0.32	2.81	0.0	0.0	1.05	0.0	3.91	0.36	0.0	12.03	0.0	0.26	0.85	2.24	3.45	0.0	0.61

Month-Year	COARSE AND SUPER-COARSE DUST																			IND	SS	
	01	02	03	04	05	06	07	08	09	10	11	12	13	14	15	16	17	18	other	all	fine	coarse
01-2006	0.88	0.45	0.46	0.7	0.31	0.26	0.0	0.41	0.42	0.8	0.0	0.87	0.0	0.11	0.16	0.0	0.65	0.17	4.52	0.73	3.23	0.57
02-2006	0.33	0.88	0.23	0.74	0.3	0.62	1.47	1.01	0.68	0.23	0.9	1.93	0.33	1.12	0.0	0.05	0.57	0.22	7.19	1.13	3.23	0.57
03-2006	0.76	0.43	0.44	0.0	0.5	0.08	0.0	0.41	0.82	0.39	0.1	0.0	0.18	0.04	2.2	0.11	0.66	0.35	1.36	1.59	3.23	0.57
04-2006	0.51	0.83	0.36	0.8	0.5	0.18	0.73	0.24	1.18	0.55	0.31	1.43	0.83	0.98	2.86	0.45	0.92	0.29	5.26	1.97	3.23	0.57
05-2006	0.01	0.0	0.0	0.0	0.0	0.22	0.0	0.76	1.33	0.9	0.99	2.35	0.73	0.2	0.56	0.82	1.16	0.55	5.15	1.6	3.23	0.57
06-2006	0.29	0.77	0.98	1.24	0.13	0.71	1.54	0.0	1.51	0.05	1.17	1.6	1.01	0.9	4.22	0.78	2.78	0.0	5.27	1.89	3.23	0.57
07-2006	0.12	0.72	0.94	1.24	0.03	0.0	1.15	0.0	1.32	1.14	8.85	1.75	3.66	1.31	0.49	0.0	0.98	0.0	0.0	1.45	3.23	0.57
08-2006	0.31	0.96	0.73	0.98	0.09	1.02	0.52	0.0	0.52	0.9	3.13	0.27	0.79	0.34	4.14	3.15	1.11	0.33	1.3	0.87	3.23	0.57
09-2006	0.69	0.56	0.43	0.53	0.46	0.73	0.58	1.23	0.51	2.11	1.92	0.67	0.62	0.36	3.89	0.0	1.9	0.16	0.0	1.16	3.23	0.57
10-2006	0.0	0.55	0.38	0.68	0.91	0.38	0.66	1.66	0.69	1.15	2.88	0.96	0.77	0.54	1.47	0.22	0.0	0.0	1.84	0.55	3.23	0.57
11-2006	0.77	0.28	0.39	0.24	0.0	0.36	0.36	0.0	0.9	0.0	0.55	1.41	0.49	0.22	0.08	0.0	0.54	0.0	0.0	0.47	3.23	0.57
12-2006	0.1	0.33	0.37	0.15	0.0	0.13	0.3	0.0	0.32	0.41	1.58	0.26	0.69	0.87	4.51	0.52	0.0	0.49	1.37	0.65	3.23	0.57

Figure 4.3: Analysis correction factors by sub-period (months) on the ordinate axis and sub-region and category of emission on the abscissa axis. BB stands for biomass burning, IND for anthropogenic and fossil fuel emissions and SS for sea salt emissions.

to $\approx 650,000$, the system reaches the cost function value of $\approx 431,000$ in the analysis, which is somewhat larger than the ideal expected value of the cost function minimum.

This result could be explained by an imbalance between the prescribed $\mathbf{R}$ matrix and the covariance matrix of the innovation vector $(\mathbf{y} - H(\mathbf{x}^b))$ and/or a systematic bias in the observation or in the observation operator (model simulated AOD). In our case, the use of the Desroziers diagnostics to inflate $\mathbf{R}$ prevents the unbalance between the diagonal terms of the $\mathbf{R}$ matrix and the innovation vector, so we think that the difficulty to reach the theoretical minimum is more likely to be due to a combination of a bias in the observations, a bias in the observation operator and the lack of off-diagonal terms in the $\mathbf{R}$ matrix.

It is interesting to note that the value of the cost function in the analysis is equal to $\approx 431,000$ when the full nonlinear model is used as observation operator, and $\approx 434,000$ when the linear approximation of the model is used instead. The small difference between the two values gives a qualitative confidence to the linear assumption of the observation operator, which is applied in the cost function minimization.

4.1.3.2 Correction Factors

Figure 4.3 shows the analysis control vector values $(\mathbf{x}^a)$, i.e., the optimal correction factors for the emission fluxes calculated with the data assimilation system. Given the information provided, the analysis is the most likely assignment for different aerosol types, sub-regions and sub-periods. In Figure 4.3 the control vector elements are grouped by sub-region and by category of emission in the abscissa and by sub-period (months) in the ordinate.

For fine mode dust, 84% of the analysis correction factors are less than unity, which means that most corrections reduce fine dust model emissions. For the fine mode emissions, 60% of the elements of the analysis $\mathbf{x}^a$ equal zero but some elements have relatively large values.

For the coarse and super-coarse mode dust, 77% of the analysis correction factors are less than unity, but unlike for the fine mode dust, the correction factors have a rather homogeneous distribution, with only 15% of the values close to zero and 8% of values greater than 2. It seems to be contradictory to have, for the same sub-region and sub-period, positive coarse and super-coarse dust emission and zero fine mode dust emissions. We will address this in Section 4.1.4.

We can identify three groups of dust sub-regions in Figure 4.3. The eastern group includes sub-regions ranging from 1 to 8, where coarse and super-coarse dust correction factors are mostly smaller than 1 and fine mode dust correction factors are predominantly either close to zero or larger than 2 (except in November). In particular, the transatlantic dust plume between March and September is generated by strongly emitting fine mode dust and decreasing coarse and super-coarse mode dust emissions. We distinguish a second group of sub-regions numbered between 9 to 14 where coarse and super-coarse dust correction factors are larger than the correction factors of the first group, and between May and November fine mode correction factors are small. A third group (composed by sub-regions numbered between 15 and 18) has a more heterogeneous behavior of dust correction factors than the two previous groups. This last group of correction factors is sensitive to the assimilated observations over the Arabian Peninsula and the Arabian Sea, while the other two previous groups are sensitive to assimilated AOD over the Sahara, the Sahel and the Atlantic Ocean.

Forest biomass burning correction factors are greater than 2 between February and November, but these large correction factors do not strongly impact the analysis because the months with more forest biomass burning emission fluxes are December and January. On the other side, grass biomass burning correction factors in November, December and between January and April do impact the analysis emissions. For sea salt emissions, Figure 4.3 shows an optimal correction factor of 3.2 for coarse mode sea salt emissions and 0.6 for fine mode emissions. This is associated with a strong posterior error anticorrelation (correlation factor of -0.9) between both elements in the control vector. As both fine and coarse mode sea salt correction factors share the same geographical emission region, the data assimilation system is unable to separate their relative contributions to the total 550 nm AOD and thus, what is really optimized is the sum of both contributions to the total AOD.

4.1.3.3 Comparison with MODIS

The internal consistency of the inversion system can be qualitatively assessed by comparing the assimilated observations with the simulated AOD. A quantitative validation is given later in Section 4.1.3.4.

Qualitatively, the prior model can reproduce the main features in AOD observed in the monthly averages (Figure 4.4). To some extent, the transported dust plume is well represented in the months when the dust emission is maximum, from June to August, and the model can produce dust levels in the Bodélé depression (17°N, 18°E) throughout the year. The local maximum of AOD in the Arabian Sea is also simulated. The westward transport of biomass burning

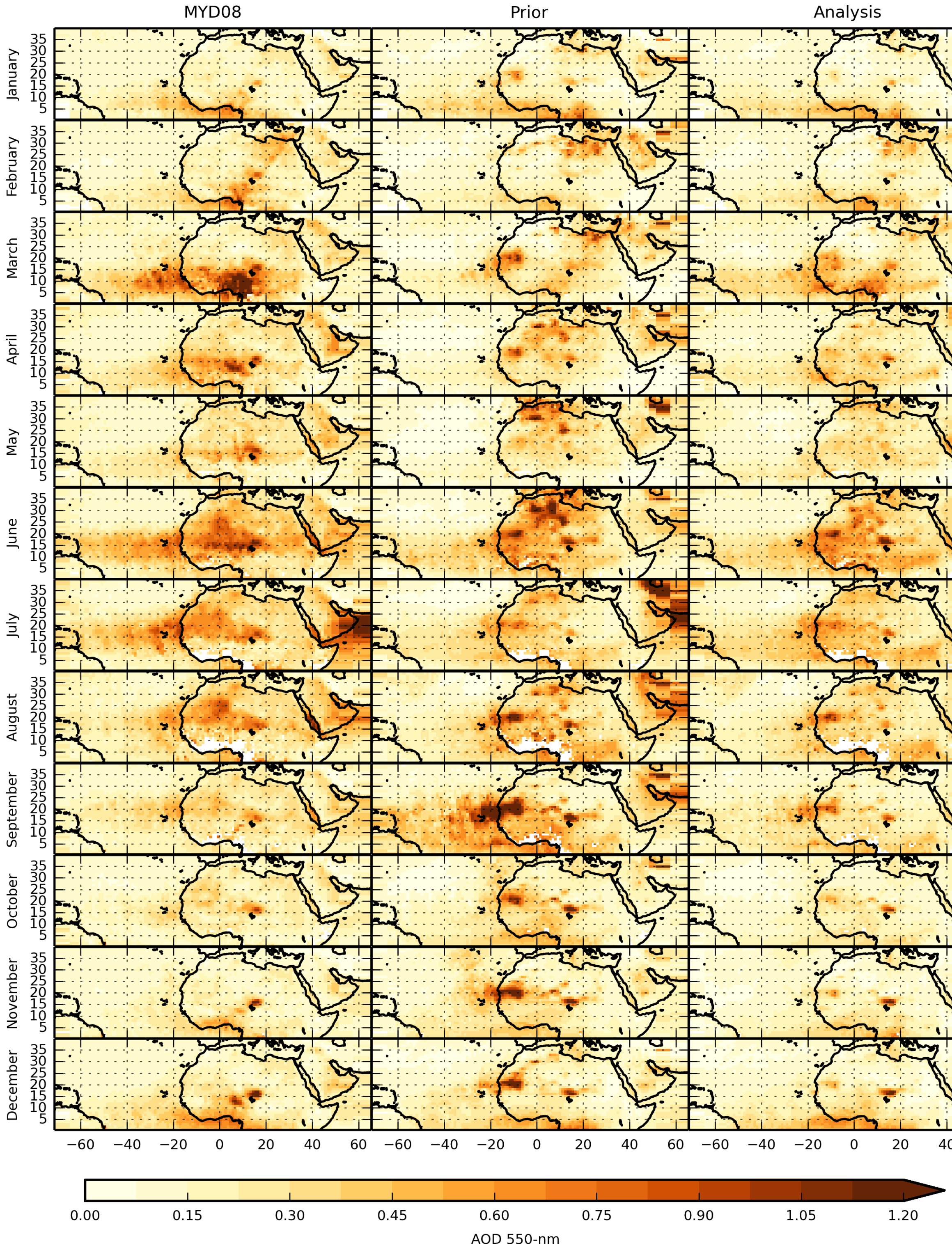

Figure 4.4: Monthly averages of 550 nm AOD from the MODIS/Aqua product (left), the prior simulation (center) and the analysis simulation (right). The latitude is in the ordinate (in degrees north) and the longitude in the abscissa (degrees east). All the monthly averages were calculated by sampling only times when the MODIS product reports valid data. Complete lack of data for the month is depicted in white.

aerosols to Central and South America in the boreal winter, as visible in the southern part of the panels, is noticeable.

The analysis efficiently reduces emissions in the northern part of the Sahara Desert, and achieves a better agreement with the assimilated AOD than the prior, as can be seen between March and August. A similar feature is found in the reduction of model emissions in the prior emission hotspot close to 10°W in longitude and 20°N in latitude; and in the prior emission hotspot in the Iranian desert.

It appears that generally speaking the data assimilation system is more efficient in decreasing emissions than in increasing them. However there are cases where the assimilation system can effectively increase emissions. For example, in the dust outbreak of March 7–13 (showed in Figure 4.4 as an AOD maximum close to [10°E,7°N] given the MODIS/Aqua sampling), it is clear that the assimilation system improves the fit with the observations by increasing emissions of fine mode dust in sub-regions 12 and 14. Even though this increase is not large enough to allow reproducing the AOD maximum, it represents an improvement with respect to the prior. Another example of the increase of AOD is for the month of July, when the analysis AOD over the Sahara is, in general, larger than the prior AOD.

The inversion system is designed to optimize not only dust emissions but rather all the emissions detailed in Figure 4.3. In particular, an increase of AOD of the analysis with respect to the prior can be seen over the Atlantic Ocean close to 35°N, which is the least dust–influenced area of Figure 4.4. These increase of AOD can be likely attributed to an increase in the local sea spray emissions or/and to an increase in emissions outside the assimilation region that are transported into the ocean.

4.1.3.4 Comparison with AERONET

To evaluate the performance of the analysis in comparison to the prior simulation, we select AERONET stations in the region of interest with a number of daily observations greater than half of the maximum number of observations in the year, i.e. stations with at least 182 daily AOD retrievals. This resulted in 13 stations for which the statistics against the two model simulations are presented in Table 4.1. We group the 13 stations into 6 groups according to their geographic locations, and for each group we select the one station with the longest record for which we show the time series of the simulated and observed AOD in Figure 4.5. The geographic location of AERONET sites is shown in Figure 4.1.

The overall statistics of the model performance against AERONET are summarized in Table 4.1. It should be noted that the AOD of the analysis is smaller than the AOD of the prior at all AERONET stations except Ilorin and La Parguera. The increase in AOD over the Caribbean station La Parguera is consistent with the larger fine mode dust fluxes of the analysis, as we will show in Section 4.1.3.5. There is a clear improvement of the analysis simulation with respect to the prior one in two of our skill scores: the root mean square error (RMSE) is smaller for all the

Station	Lat. (°N)	Lon. (°E)	Elev. (m.a.s.l.)	N obs.	Mean			Bias		RMSE		ρ	
					Obs	FG	AN	FG	AN	FG	AN	FG	AN
Bahrain	26.21	50.61	25	201	0.433	0.476	0.385	0.044	-0.047	0.365	0.237	0.275	0.516
Blida	36.51	2.88	230	195	0.258	0.321	0.244	0.063	-0.013	0.356	0.188	0.59	0.647
Dhabi	24.48	54.38	15	243	0.434	0.412	0.32	-0.022	-0.114	0.397	0.254	0.231	0.509
Dhadnah	25.51	56.32	81	324	0.404	0.456	0.318	0.052	-0.086	0.465	0.251	0.147	0.428
Forth Crete	35.33	25.28	20	283	0.196	0.267	0.247	0.071	0.05	0.254	0.182	0.37	0.38
Granada	37.16	-3.6	680	276	0.177	0.216	0.186	0.039	0.009	0.246	0.138	0.653	0.719
Hamim	22.97	54.3	209	263	0.314	0.349	0.273	0.035	-0.041	0.264	0.168	0.449	0.675
Ilorin	8.32	4.34	350	270	0.705	0.431	0.46	-0.274	-0.245	0.6	0.537	0.073	0.371
La Parguera	17.97	-67.05	12	251	0.148	0.147	0.155	-0.001	0.008	0.148	0.103	0.28	0.38
Nes Ziona	31.92	34.79	40	185	0.226	0.242	0.21	0.016	-0.016	0.141	0.115	0.463	0.529
Santa Cruz Tenerife	28.47	-16.25	52	233	0.171	0.182	0.146	0.011	-0.025	0.183	0.117	0.385	0.556
Sede Boker	30.86	34.78	480	335	0.2	0.263	0.24	0.063	0.04	0.235	0.161	0.537	0.55
Solar Village	24.91	46.40	764	335	0.372	0.373	0.367	0.001	-0.005	0.273	0.252	0.393	0.497

Table 4.1: AERONET sites used in this study and statistics of the simulated 550 nm AOD against daily AERONET measurements. FG stands for the prior simulation and AN for the analysis simulation. The statistics shown are the mean 550 nm AOD (Mean), the mean bias (Bias), the root mean square error (RMSE) and the Pearson correlation coefficient (ρ).

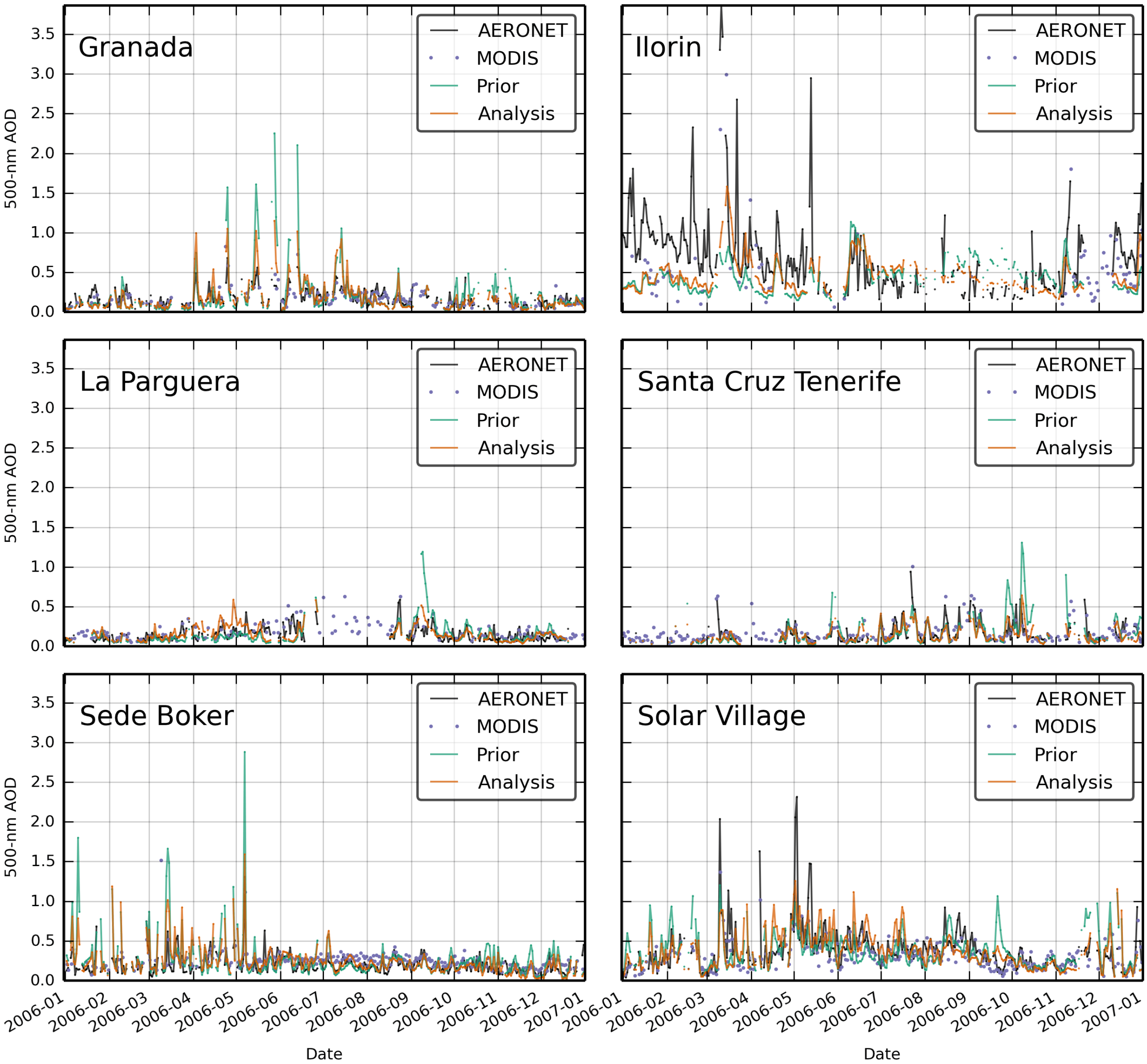

Figure 4.5: Model/AERONET comparison over 6 selected AERONET sites. Time series of AERONET 500 nm AOD (in black) and the two simulations with the prior simulation in green and the analysis simulation in orange. The name of each AERONET station is indicated on each panel. MODIS/Aqua retrievals are shown in purple. Simulated AOD is shown only for days when AERONET reports valid data.

stations in the analysis run, and the Pearson correlation coefficient is also closer to unity in all the analysis simulations. The absolute value of the bias is reduced in 5 stations and it is increased in other 7 stations, and in general terms, the prior simulation is positively biased, while the analysis simulation is negatively biased.

Time series of simulated and observed AOD are shown in Figure 4.5. In general terms, the analysis simulation is capable of reducing a large number of AOD peaks of the prior simulations that are not observed by AERONET (e.g., at the Granada site in April, Santa Cruz Tenerife site in October or Solar Village site in September). In some cases the assimilation system increases the AOD towards the observations, as for example in March at the Ilorin site. Even though the bias in La Parguera site is increased in the analysis, the variability of the observed minus simulated AOD is improved by the analysis. Part of the errors in the analysis simulation can be attributed to the mismatch between AERONET and MODIS AOD, the assimilated product. For example, most of the model inaccuracy at Ilorin site (see Table 4.1) comes from the first three months of simulation, where the AERONET observations are considerably larger than both the model simulations and the MODIS/Aqua retrievals.

On monthly to seasonal temporal scales (not shown), the analysis performance is rather homogeneous, with calculated statistics similar to those of the whole year (Table 4.1) except for the bias and root mean square error (RMSE) for Granada and Blida stations (northern stations of Figure 4.1) where the improvement of the analysis is better in April, May and June; in La Parguera, where there is a significant improvement of the bias and RMSE in September; and in Santa Cruz Tenerife where the bias and RMSE of the analysis are smaller than the prior simulation in September and October.

4.1.3.5 Emission Fluxes

Dust and biomass burning emission fluxes are summarized in Figure 4.6. The total amount of emitted dust in the prior simulation is 6690 Tg, of which 4095 Tg are emitted in Northern Africa and 2595 Tg in the rest of the domain (sub-regions 16, 17 and 18 of Figure 4.1). The total dust flux is reduced to 2897 Tg in the analysis simulation (2179 Tg emitted in Northern Africa and 718 Tg in the rest of the domain). The AEROCOM project (Huneeus et al., 2011) reports a plausible range of emissions between 400 and 2200 Tg yr^{-1} for North Africa and between 26 and 526 Tg yr^{-1} for Middle East. Although the analysis simulation is in the higher limit of this range, more recent studies suggest larger values of Saharan (Evan et al., 2014) (4500 ± 1500 Tg yr^{-1}) and global (Zhao et al., 2013) (≈ 6000 Tg yr^{-1}) dust emission fluxes.

Dust emission of coarse and super-coarse mode bins are orders of magnitude larger than that for the fine mode, so the total amount of dust fluxes (in terms of mass) is controlled by the emission of the coarser particles. In the prior simulation, the flux of the coarse and super-coarse modes is 6662 Tg while in the analysis this flux is 2866 Tg, with the reduction occurring for all months. The seasonal cycle of the coarser emissions is slightly different between the analysis and the prior simulations. Both of them show larger values in boreal summer than in winter, but the

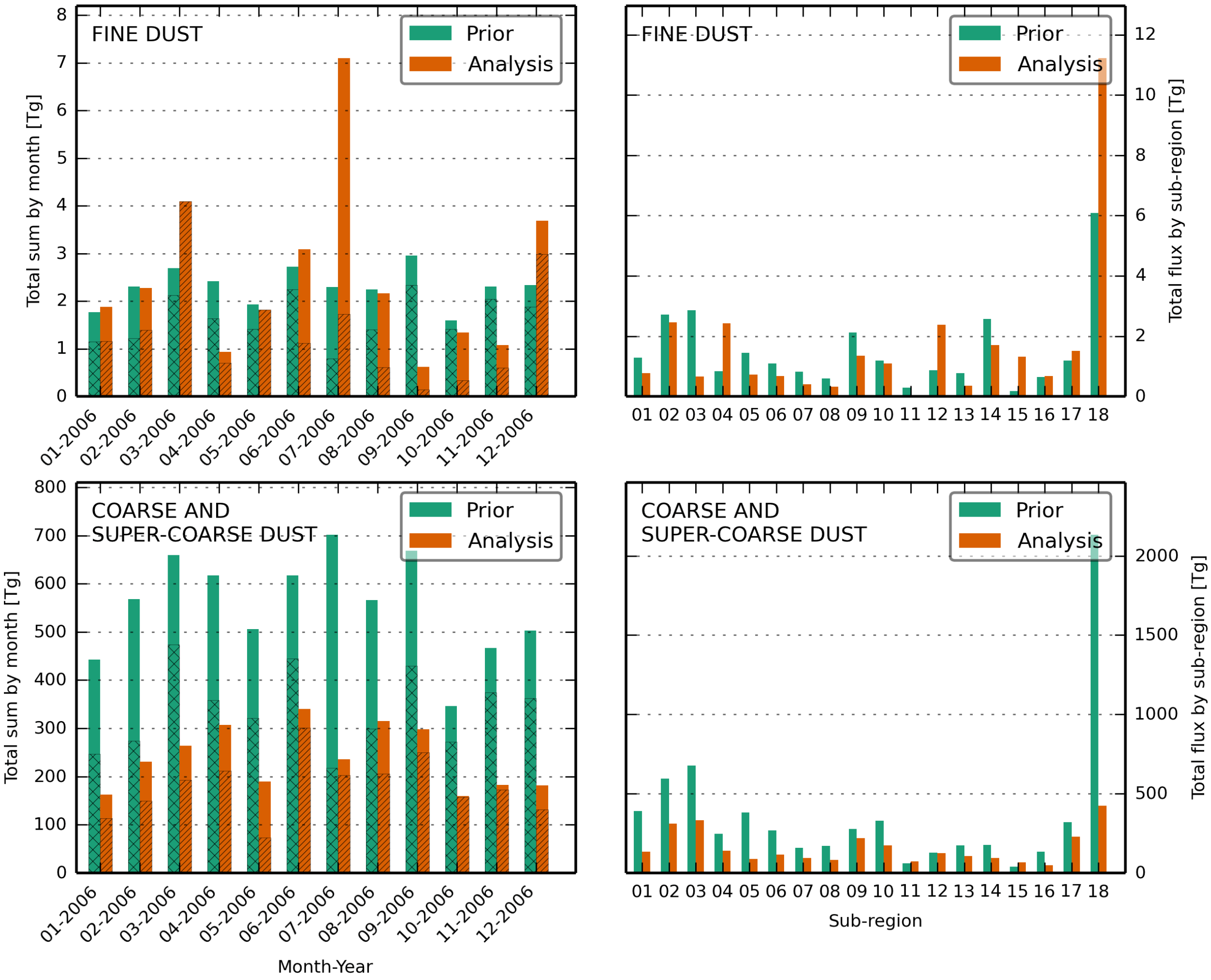

Figure 4.6: Dust emission fluxes in Tg for the two model (prior and analysis) simulations. Upper panels show the emission fluxes for the fine mode and lower panels show the coarse and super-coarse modes. Monthly sums of emissions are shown on the left panels, and yearly 2006 emissions disaggregated by sub-region are presented on the right panels. Total flux for northern Africa (sub-regions 1 to 15) is indicated with a hatch pattern in the left panels.

months of maximum emission are not the same: July, September and March for the prior and June, August and April for the analysis. In the spatial distribution, only two sub-regions (11 and 15) have more coarse and super-coarse dust emissions in the analysis simulation than in the prior one. The data assimilation system identifies large observational departures of AOD over sub-region 18 (see Figure 4.4) and consequently produces a strong decrease of the analysis dust coarse mode emissions in this sub-region (compared to prior emission).

On the contrary, fine mode dust emissions are larger in the analysis (30 Tg) than in the prior simulation (27.6 Tg), despite the suppression of the fine mode dust emissions in several sub-regions of the analysis due to the null correction factor shown in Figure 4.3. Fine mode dust emissions are less important in terms of mass flux, but they are crucial for the 550 nm AOD field due to their larger mass extinction coefficient and longer residence time than the coarser dust. There is an important decrease of emissions between the prior and the analysis in sub-regions 3 and 11, but in both cases, an adjacent sub-region (4 and 12, respectively) strongly increases emissions. The fine mode emission increase in July is due to values of the analysis correction factor larger than 3 in the eastern part of the region (sub-regions between 15 and 18), and it is also reflected in the large value of the overall emission flux for sub-region 18.

In terms of flux uncertainty, we deliberately inflate the background error covariance matrix to obtain a prior dust emission flux uncertainty in the range of the dust flux spread reported in Huneeus et al. (2011). The standard deviation of the prior dust flux error for the whole region is therefore close to 4140 Tg. For the analysis, this uncertainty measure is reduced to 31 Tg, which seems to be unrealistically low and will be discussed in Section 4.1.4.

4.1.4 Discussion

The data assimilation system successfully modifies the dust fluxes in order to improve the agreement with the AOD observations, but there are pending challenges to be solved.

Over the Sahara, the shorter residence time of the coarse mode dust (relative to the fine mode) incites the assimilation system to preferably adjust the coarse mode dust emissions to get closer to the MODIS observations over land, while MODIS observations over the ocean are more relevant to the fine mode dust because of its longer residence time (Figure 4.4, left column). However dust AOD over the ocean results from dust emitted over a large source area (e.g. Schepanski et al., 2007; Ginoux et al., 2012) in the Sahara and is subject to long-range transport and mixing along the air mass trajectory. The convergence of the fine mode dust emitted over the desert into a single dust plume over the Atlantic Ocean, results in a difficult inversion problem for fine mode dust. In order to reduce the model AOD departures with respect to MODIS over the dust plume, the data assimilation system has various ways to adjust the fine mode dust emissions (Huneeus et al. (2016) showed how different emissions lead to a similar AOD behaviour after long-range transport). In this context, the assimilation system prefers strongly decreasing the emissions for a large number of sub-regions and increasing the emissions for some sub-regions. It should be noticed that zero emissions for the fine mode dust cannot realistically coexist with non-zero emissions for the coarse and super-coarse mode dust.

In order to address the above, a higher quality total AOD and fine mode AOD product over land would be needed. The impact of including this product into assimilated observations has not been addressed yet, but we think that it could help the assimilation system to differentiate between fine and coarse mode dust emissions, and hopefully avoid the problem of having zero dust fluxes in the fine mode. Preliminary tests indicate that assimilating MODIS fine mode AOD over ocean in addition to total AOD does not significantly improve neither the simulated comparison against AERONET nor the issue of having large number of sub-regions with zero fine mode emissions. For this reason, we think that fine mode AOD over land would be a more beneficial piece of information that is not currently available from MODIS.

A valuable product of the data assimilation is the quantification the analysis uncertainty. Our system underestimates the uncertainty of the analysis fluxes (see Section 4.1.3.5). We have performed several sensitivity experiments (not shown) over the inflation parameters of **R** and **B** matrices (see Section 4.1.2.3), concluding that neither the analysis control vector nor the **A** matrix are highly sensitive to these parameters. Off-diagonal terms in **R** are usually omitted and the inflation of the **R** matrix should be enough to compensate the lack of these terms in most of the variational sub–optimal assimilations systems (Rabier, 2005). We would like to investigate if this holds for our inversion system, but more work is needed in order to properly define the off-diagonal terms of **R** and to quantify the impact of these terms in our analysis uncertainty.

Another question is whether there is a possible bias in the assimilated observations that should be corrected. MODIS AOD is retrieved from the Dark Target algorithm over ocean, and we use the retrievals either from the Deep Blue algorithm (for bright surfaces, as the desert) or from the Dark Target algorithm over land (Levy et al., 2013). Therefore, a discontinuity in the AOD field is possible close to the coast. In Figure 4.4, this discontinuity can be noted mostly between the months of June and September, where the AOD close to the coast over land is smaller than that over the ocean at the same latitude. In this region, the AOD maximum is due to mineral dust emissions, which are only emitted over land and then transported westward. Over the desert, the Deep Blue algorithm systematically underestimates the AOD (Sayer et al., 2013) and the (assimilated) combined product could have discontinuities in regions where both Deep Blue and Dark Target algorithms report successful retrievals (Sayer et al., 2014). This systematic bias between both MODIS AOD retrievals close to the coast may affect the analysis, providing contradictory information to the assimilation system. However, our tests indicates that assimilating data over the desert leads to better results than assimilating only the Dark Target product.

Besides the land/ocean bias described above, recent progress has been done to properly define and narrow the expected error (EE) estimates for the MODIS AOD products (Levy et al., 2013; Sayer et al., 2013). In order to take advantage of these developments in a data assimilation framework, it would be necessary to include these EE in the **R** matrix. Preliminary tests show that the analysis performance decreases when the observational error is defined by a linear function of the MODIS AOD, and thus we set a constant value for the observational error. However, these could change if the full EE derived in Sayer et al. (2013) is used (including the dependence of the error to the satellite viewing geometry). This EE has not been addressed yet in the source inversion system and would be interesting to implement it in the near future.

An additional source of error could come from the design of the data assimilation system. We assimilate daily AOD observations but the control vector has only a monthly resolution. The variability of dust emissions at the scale of the sub-regions and sub-periods is completely determined by the atmospheric and the dust production model, and errors at these scales negatively impact the inversion system, as they cannot be corrected by the assimilation system. Manual inspection of the model performance suggests that the issues discussed in the previous paragraphs are not necessarily associated with errors of sub-monthly scales of dust emission or transport, but further work should be done to quantify these errors.

4.1.5 Conclusions

We have estimated one year of dust fluxes over the Sahara and the Arabian Peninsula, by assimilating total AOD from MODIS in the aerosol transport model coupled to a dust production model and to the zoomed version of a general circulation model. Our adjoint-free assimilation system allows calculating correction factors for 18 sub-regions at a monthly resolution, and at an affordable computational cost over a one year period.

We present and apply an assimilation system that can perform natural aerosol source inversions over larger time-windows and spatial coverage (e.g., by including the Arabian Peninsula) than previous regional studies with reasonable results.

In general terms, the analysis simulation is closer to the AOD observations than the prior simulation over the available AERONET stations. The data assimilation system is capable of improving spatial features observed in MODIS AOD with respect to the free-assimilation simulation.

The total amount of dust emitted in the region is estimated to be ca. 2900 Tg for the 2006 year, with most of the mass flux emitted by the coarse and super-coarse mode bins of the DPM (with diameters over 1 μm).

A large temporal window for the source inversion (of at least one decade) is needed in order to create a useful dataset to be used by the aerosol and climate community, and would help to have a more robust estimate of the annual dust emission over the region. The well known interannual variability of dust sources is an interesting question to address, but before applying our framework to this problem it is necessary to solve some critical issues detailed in the previous Section.

The quality of the analysis partially depends on the quality of the atmospheric model. In particular, dust flux calculations improve when the model resolution increases. The source estimation approach presented in this work is applicable to other modeling systems (without needing an adjoint model) with increased horizontal resolution. We expect that the application of this inversion system in higher resolution models will lead to a better and more accurate estimate of mineral dust fluxes.

This inversion system could be applied to tune parameters in the dust emission model instead of correction factors of the emissions, but this could be done in this framework only if perturbations of the parameters lead to linear (or approximatively linear) perturbations in the simulated observations. In this case, the assimilation system would need minimal modifications to attempt this task. More work is needed in order to identify and estimate plausible dust emissions parameters in the DPM that can be efficiently adjusted through this method.

In the near future, we will try to assimilate more information than the total 550 nm AOD in order to improve our results in terms of fine mode emissions. To this end, a satellite retrieval with similar spatial and temporal coverage of MODIS total AOD, but only for fine mode aerosols 550 nm AOD over the desert would be useful. Alternatively, it is also possible to modify the SPLA model to have more dust bins, but with cut-off diameters that are compatible with the small, medium and large AOD retrievals from the MISR satellite, or with the small and coarse cut-off radii of the POLDER/PARASOL instrument.

Acknowledgments

The authors would like to thank the MODIS and AERONET teams for making the data available. MODIS AOD products are available at `http://modis-atmos.gsfc.nasa.gov` and AERONET AOD is available at `http://aeronet.gsfc.nasa.gov`. Input soil data used in this study is available at `http://www.lisa.univ-paris12.fr/mod/data/index.php`. The work was partially funded by the project OSIRIS from MEDDE/INSU and by the France-Chile ECOS project number C14U01, and co-funded by the Copernicus Atmosphere Monitoring Service, implemented by the European Centre for Medium-Range Weather Forecasts (ECMWF) on behalf of the European Commission. Part of the work was done using computing time from the TGCC under the GENCI projects t2014012201 and t2015012201. Nicolás Huneeus acknowledges support from FONDAP 15110009 and FONDECYT 1150873.

4.2 Further information

4.2.1 Near surface winds

Wind velocity near the surface is an important factor in the dust production module. In this thesis, the LMDZ simulated 10-meter surface wind is used to compute dust emissions over North Africa and the Arabian Peninsula. The strong relation between dust emissions and wind velocity (roughly power of 3) makes it necessary to asses the performance of the simulated surface winds in a dust emission problem.

In practice, it is difficult to directly validate the model winds against measurements of wind velocity over the Sahara, due to the lack of measurements on this region. Instead, a common practice is to evaluate model variables against reanalysis datasets. However, this approach is not exempt of problems. Largeron et al. (2015) evaluated the surface wind velocity from three different reanalysis products (ERA-Interim, NCEP-CFSR and MERRA) over the Sahelian region, founding seasonal biases and deficiencies in the representation of the wind velocity diurnal cycle in all three analysed datasets.

We show in Figures 4.7 and 4.8 the average of the (instantaneous) 10-meter wind velocity for three different datasets: LMDZ simulated 10-meter wind (this work), ERA-Interim and CRU-NCEP analysed 10-meter winds. We recall here that the LMDZ simulations are nudged by the ERA-Interim winds (above the boundary layer). The three datasets are regridded and shown on the LMDZ grid. The latter dataset is a mixture between the NCEP reanalysis diurnal cycle of the near-surface winds and the gridded CRU observational climatology (`http://www.cru.uea.ac.uk/data`), prepared originally as a forcing dataset for land surface models such as ORCHIDEE at the LSCE.

The mean value of the wind velocity is in general larger for the ERA-Interim reanalysis than for the other two datasets (Figure 4.7). It also can be seen that the LMDZ mean winds are closer to the CRU-NCEP winds than to the ERA-Interim ones. As the CRU-NCEP wind is adjusted to fit the monthly wind observations measured and gridded in the CRU dataset, we expect that the CRU-NCEP mean wind velocity is fairly close to the true mean wind velocity at 10 m.

The diurnal cycle of the 10-meter wind can be seen in Figure 4.8. In this case, we cannot assert which of the three datasets has the best representation of the diurnal cycle of the winds. In particular, the CRU-NCEP diurnal cycle is driven by the NCEP reanalysis wind diurnal cycle. Nevertheless, the wind velocity maxima over the desert are clearly reached at 6 and 12 UTC for the ERA-Interim dataset and at 12 UTC for the LMDZ simulations, while the CRU-NCEP diurnal cycle is less strong.

In this Section we cannot state that the LMDZ near surface winds overperform those from the ERA-Interim or CRU-NCEP datasets, because we do not have enough observations to carry out a

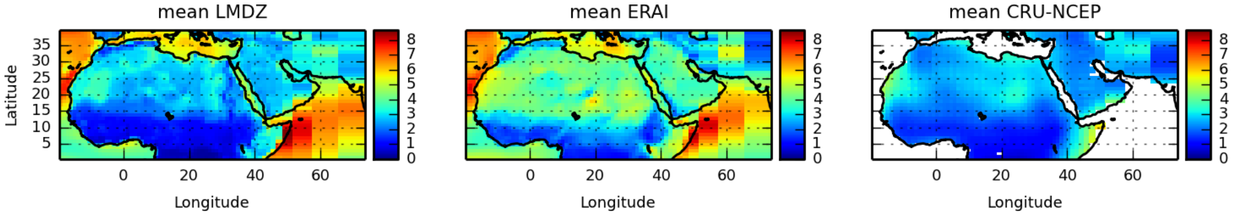

Figure 4.7: Average of the 10-meter wind velocity for three datasets over the year 2006 [units of m s^{-1}]. From left to right: LMDZ simulations (this work), ERA-Interim reanalysis and CRU-NCEP.

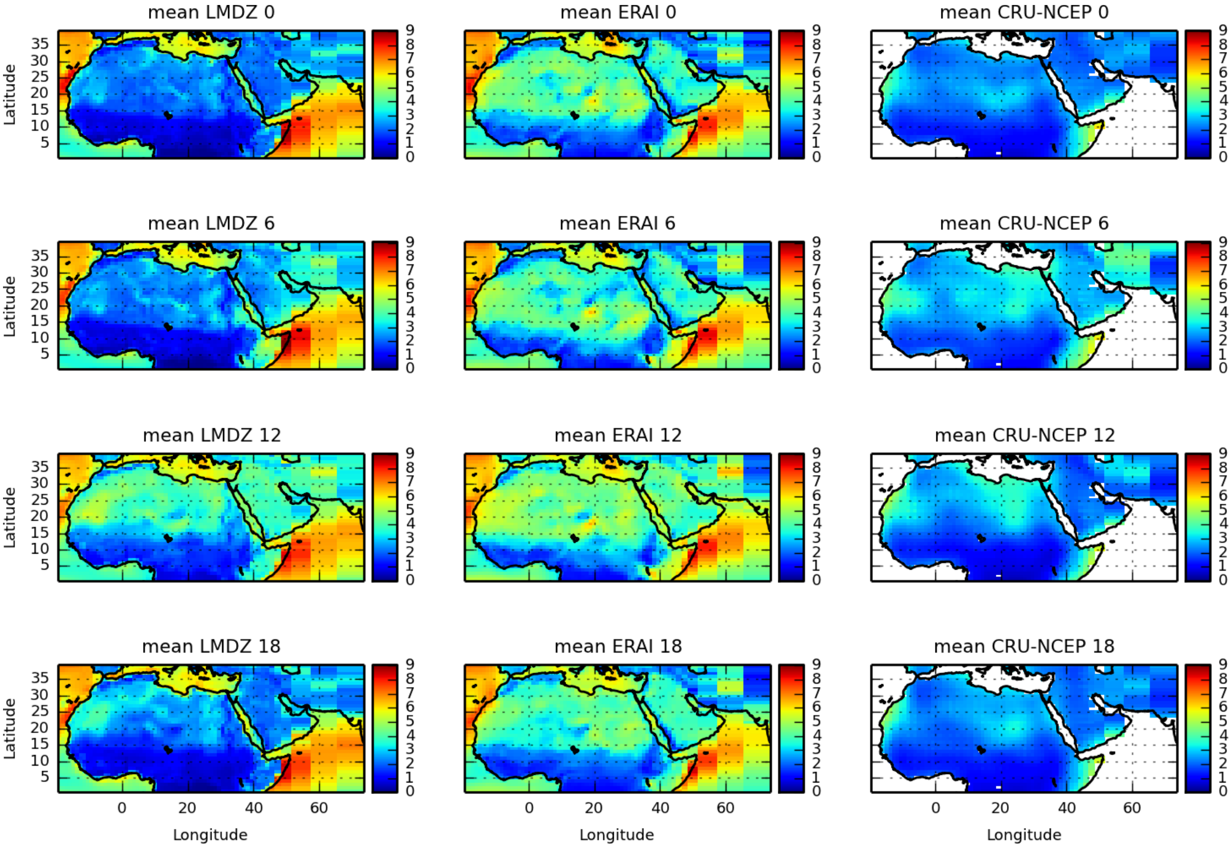

Figure 4.8: Surface wind velocity average for three datasets over the year 2006 [units of m s^{-1}]. The three columns represent the average 10-meter wind for the LMDZ simulation, the ERA-Interim reanalysis, and the CRU-NCEP dataset. The rows indicates the time (UTC), with the first row at 0 UTC, the second at 6 UTC, the third at 12 UTC and the fourth at 18 UTC.

proper evaluation. We can nevertheless comment on this as our model version and configuration is similar to the one used in Hourdin et al. (2015). This work (to which I contributed) performed a comparison against wind velocity measurements over the Sahelian region. Figures 4 and 7 (for the "NP48" simulation) of the Hourdin et al. (2015) article show a relatively good agreement between the model and the observations.

4.2.2 Dust outbreak

Figure 4.4 of the above presented article (Section 4.1) shows monthly averages of AOD for the assimilated observation, the prior and the analysis simulations. Even though these monthly averages can qualitatively describe the seasonal behaviour of the AOD, they can easily mask the AOD variability at shorter scales, and they can conceal possible sampling issues on the observations.

It is well known that large amounts of dust can be released into the atmosphere in relatively short periods of time. As we said, these events are hardly noticed in the monthly averages of AOD but they can be significant for the net flux of dust, even at the monthly scale. One example of a dust event occurred in March 2006, and it is responsible for the relative maximum of AOD shown in Figure 4.4 of Section 4.1 for the March panel (as is discussed in the text of the article). We found it interesting to qualitatively evaluate the performance of the prior simulation on this event, and how the analysis tries to be closer to the assimilated observations.

Daily values of MODIS AOD, prior and analysis AOD are shown in Figure 4.9 for the dust outbreak that occurred between March 6 and 13. The prior cannot fully reproduce the strength of the event, but it is possible to see the right timing of emissions in northern Sahara and the propagation of the dust load of the prior with respect to the MODIS AOD. The analysis decreases the AOD in the western part of the dust plume and increases it in the southern part (between days 11 to 13).

4.2.3 Vertical profile

We have focused our analysis assessment on the (column integrated) AOD. In this section we will justify this choice, showing the vertical profile of the extinction coefficient for both simulations, the prior and the analysis.

Figure 4.10 shows the mean vertical profile of aerosol mid-visible extinction coefficient across the Atlantic Ocean and Saharan region for a latitude band between 10 and 30 °N (the same latitude band shown in Peyridieu et al. (2013)). The first panel is the average of all the available CALIOP extinction profiles for year 2006 (from CALIPSO launch in June to December), calculated from quality-assured (QA) filtered Level 2 data included both day and night profiles, and regridded to the model horizontal grid. The filtering process of the Level 2 data was done following the recommendations from the CALIOP/CALIPSO team (`https:`

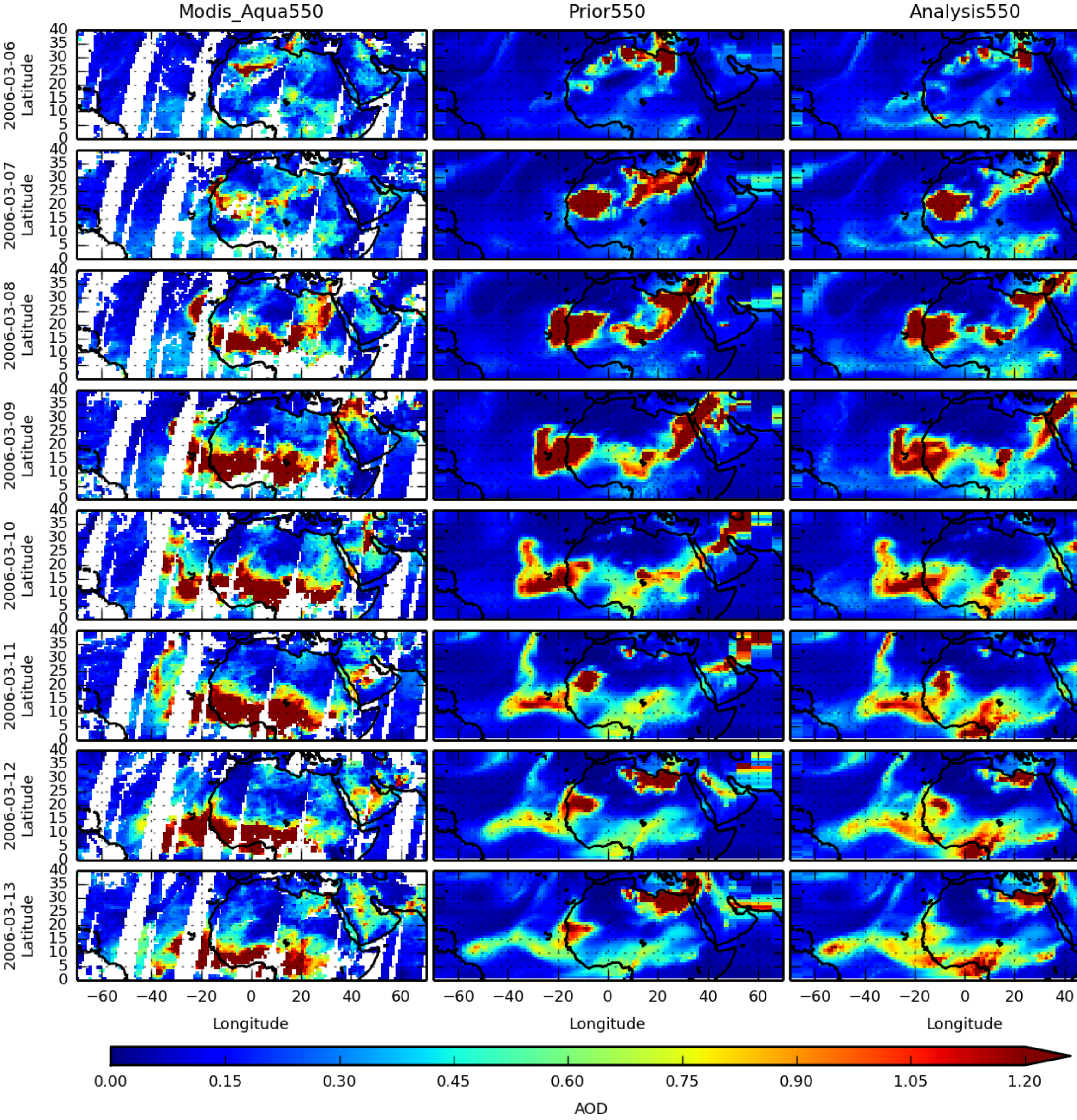

Figure 4.9: March 6-13 dust outbreak. AOD at 550-nm derived from MODIS/Aqua product (left), prior simulation (center) and analysis (right). Each row corresponds to one day (see left labels)

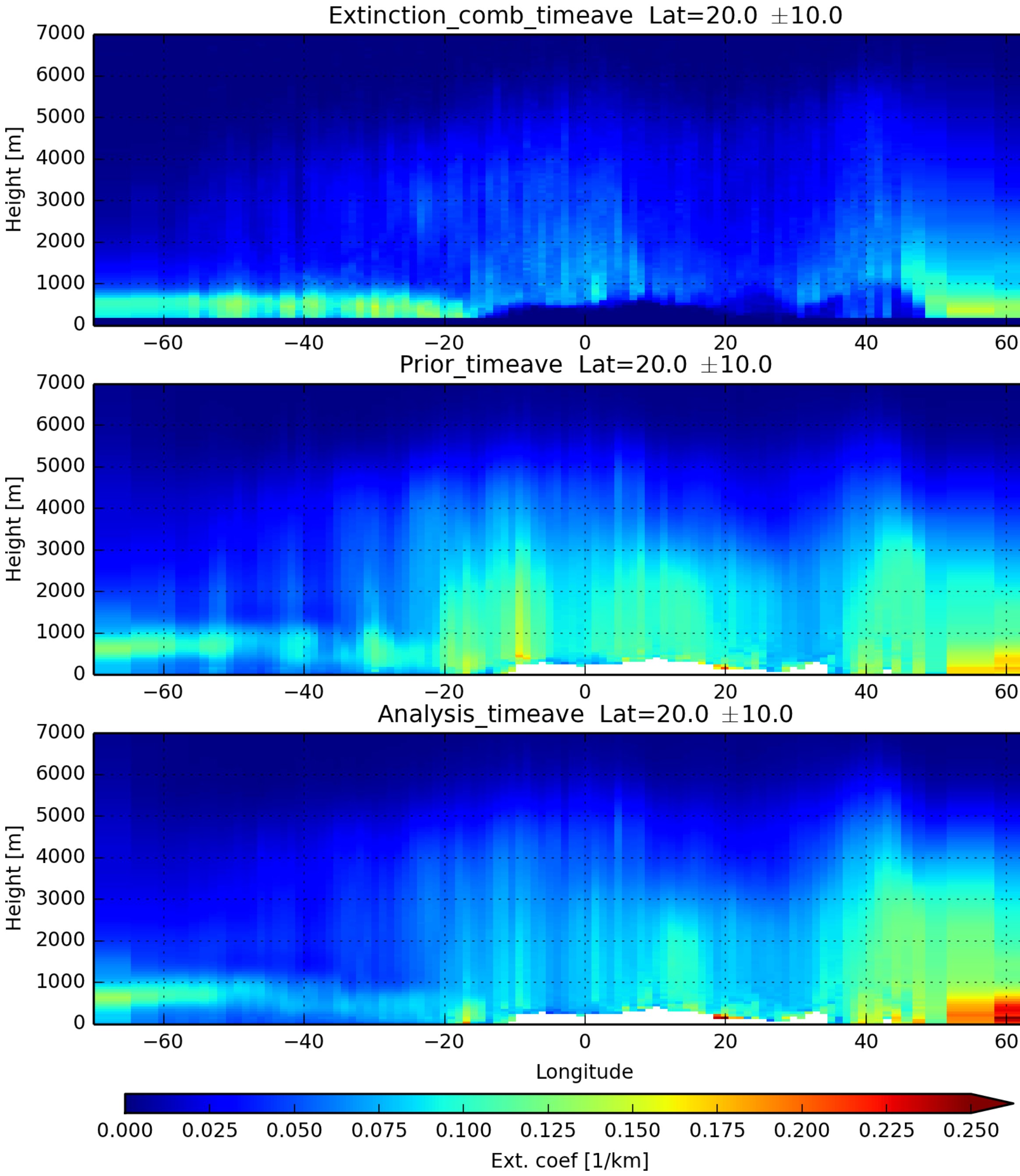

Figure 4.10: Vertical profile of the mean extinction coefficient (km^{-1}) at 532 nm from CALIOP (upper panel), prior (middle panel) and analysis (lower panel). The figure shows the average of the retrievals (and their coincident simulated extinction coefficient at 550 nm) for all the available period (June to December) for the year 2006. The data here shown is also averaged in a latitude band between 10° N and 30° N.

`//www-calipso.larc.nasa.gov`). The two following panels show the prior and the analysis extinction coefficients, interpolated to the vertical resolution of the CALIOP data (60 meters), and sampled from the model output daily average for grid-boxes where CALIOP reports QA data (in this case we use daily averages because for this experiment we do not have the simulation outputs of the aerosol extinction coefficient for Aqua overpass time). Despite the small remaining differences in temporal and spatial sampling, the model is able to reproduce the low altitude layer over the Atlantic Ocean (likely sea spray in the boundary layer), the height of the aerosol layer top, and in some cases, the vertical profile of extinction coefficient observed by CALIOP.

Over the continent and over the Atlantic ocean (excluding the planetary boundary layer) the aerosol layer is expected to be mainly dust and some differences between the prior and the analysis can be highlighted. Consistently with Section 3 of the article presented above discussing the AOD results, the analysis extinction coefficients are systematically smaller than the prior, due to the overall reduction in dust emissions in the analysis. The vertical pattern of the extinction profile remains similar between the two runs, and this is due to the same meteorological conditions between the two simulations, the linear correction of the emission in the analysis and the relatively long assimilation period (1 month) for each element in the control vector.

In this Chapter we have performed the first inversion of mineral dust emission fluxes of this thesis, and we have evaluated the performance of the analysis. We have assimilated total AOD retrievals from the MODIS/Aqua instrument, but as we said in the last paragraph of the conclusions (in Section 4.1), this work can be extended to the assimilation of several satellite retrievals. Doing this, we expect to better identify model biases and to narrow estimates on the uncertainties of mineral dust fluxes. Furthermore, by exploring the assimilation of different satellite retrievals we are able to draw an inference on the strengths and limitations of each dataset in this context. We show this sensitivity study in the next Chapter.

Chapter 5

Article: Impact of the choice of the satellite AOD product in a sub-regional dust emission inversion

This chapter presents the second submitted article issued from this thesis (Escribano et al., 2017). We have noticed that most of the source inversion studies in the literature rely on a single assimilated observational dataset (usually AOD from MODIS), even though there are several satellite retrievals suitable for the assimilation. In this work we explore the impact on the assimilation and the dust flux estimates of assimilating five different AOD retrievals. It should be noted that we as simulate the AOD retrievals one by one and do not attempt to assimilate more than one product at a time. For this task, we take advantage of the design of the assimilation system, which does not requires extra computing time to assimilate more than one AOD dataset once the sensitivity matrix is computed. We have been careful in keeping the assimilation system configuration as fixed as possible, except for the observational errors, that are now computed with the error estimates from the literature (cf. Section 2.2).

We present the transcription of the submitted article, and continue with some sub-products of this inversion. Through this thesis we have claimed that the linear form of the observation operator is a good approximation of the fully non-linear observation operator, and we have trusted the optimality of the analysis to this claim. This strong assumption will be justified in Section 5.2, where we will use the AOD simulated by the non-linear observation operator computed from the five analyses (from the article below, Section 5.1) to evaluate the accuracy of the AOD computed by the linear observation operator at these points. We will see that the linear approximation is good enough in that case. Finally, we show an alternative to this sensitivity study in Section 5.3.

5.1 Submitted article

Impact of the choice of the satellite AOD product in a sub-regional dust emission inversion

Jerónimo Escribano[1], Olivier Boucher[1], Frédéric Chevallier[2] and Nicolás Huneeus[3,4]

[1]Laboratoire de Météorologie Dynamique, Université Pierre et Marie Curie / CNRS, Paris, France, [2]Laboratoire des Sciences du Climat et de l'Environnement, CEA, Saclay, France, [3]Geophysics Departement, University of Chile, Santiago, Chile, [4]Center for Climate and Resilience Research (CR)^2, Santiago, Chile.

Abstract

Mineral dust is the major continental contributor to the global atmospheric aerosol burden with important effects on the climate system. Regionally, a large fraction of the emitted dust is produced in North Africa, however the total emission flux from this region is still highly uncertain. In order to reduce these uncertainties, emission estimates through top-down approaches (i.e., usually models constrained by observations) had been successfully developed and implemented. Such studies usually rely on a single observational dataset and propagate the possible observational errors of this dataset onto the emission estimates. In this study, aerosol optical depth (AOD) products from five different satellites are assimilated one by one in a source inversion system to estimate dust emission fluxes over northern Africa and the Arabian Peninsula. We estimate mineral dust emissions for the year 2006 and discuss the impact of the assimilated dataset on the analysis. We find a relatively large dispersion in flux estimates among the five experiments, which can likely be attributed to differences in the assimilated observation datasets and their associated error statistics. We also show how the assimilation of a variety of AOD products can help to identify systematic errors in models.

5.1.1 Introduction

Aerosol optical depth (AOD) retrieved from satellites is probably the most used indirect measurement of aerosol in atmospheric and climate modelling studies. The large temporal and spatial coverage of satellite AOD makes these retrievals a unique and useful product, however they cannot provide a complete four-dimensional description of the atmospheric aerosol. Data assimilation techniques have been developed to combine in the best possible way model and observational information and their application results in new aerosol analysis and reanalysis products (e.g., Benedetti et al., 2009; Lynch et al., 2016). In the recent years, satellite-derived AOD has been also used to estimate aerosol surface emissions in the so-called *top-down* approach (e.g., Dubovik et al., 2008; Schutgens et al., 2012; Huneeus et al., 2012). This approach is often embedded in a data assimilation framework, where observations and model are systematically combined in order to estimate emissions. With these methodologies, estimates of aerosol emissions depends on the model performance, on the detail of the data assimilation system and on the quality and coverage of the observations.

Mineral dust is the major continental contributor to the global atmospheric aerosol burden. Airborne dust interacts with clouds, solar and terrestrial radiation and atmospheric chemistry. Deposition over the cryosphere has effects on surface albedo (Bond et al., 2013), which modulates the impact of black carbon deposition on snow and ice surfaces. Dust is a source of Fe and P nutrients. The deposition of dust on some continental ecosystems has some impact on the vegetation and the carbon cycle. Deposition at the surface of the oceans can also fertilize the phytoplankton in so-called high-nutrient low-chlorophyll regions, with impacts on marine biogeochemical cycles (Wang et al., 2015). Atmospheric dust is also known to affect human health and air quality. Among others uncertainties, emission fluxes of mineral dust are still highly uncertain. For instance dust emissions from the Saharan desert, a key dust region worldwide, have been estimated to range between 400 $\mathrm{Tg\,yr^{-1}}$ (e.g., Huneeus et al., 2011) to 4500 $\mathrm{Tg\,yr^{-1}}$ (e.g., Evan et al., 2014). While some of the uncertainty may be related to the choice of the cut-off size for dust emissions, with larger cut-off size resulting in larger dust emission fluxes and shorter atmospheric residence time, it is nevertheless desirable to decrease the uncertainty in the dust emission flux.

Satellite observations can help reducing these emission uncertainties. The combined use of satellite observations and models may potentially lead to superior estimates of aerosol emissions (e.g. Dubovik et al., 2008; Huneeus et al., 2012). In this study we focus on the role of observations and we quantify the plausible range of emissions uncertainties as a function of the chosen observational dataset. To this aim, we assimilate AOD from five different datasets in the data assimilation system presented in Escribano et al. (2016, hereafter EBCH16) with a fixed configuration for both the model and the assimilation system.

Moderate Resolution Imaging Spectroradiometer (MODIS) aerosol products have been largely used for aerosol data assimilation (e.g., Dubovik et al., 2008; Benedetti et al., 2009; Lynch et al., 2016, EBCH16). This is not surprising because the MODIS aerosol retrieval algorithms have received a lot of attention for over a decade (e.g., Remer et al., 2005, 2008; Levy et al., 2010) and, as a result, the MODIS aerosol products are of a relatively high quality (Levy et al., 2013). Over ocean and dark land surfaces, the MODIS Dark Target (MODIS-DT) algorithm is capable of retrieving AOD at visible wavelengths, while over bright surfaces AOD is retrieved through the MODIS Deep Blue (MODIS-DB) algorithm. Furthermore the MODIS instrument is onboard both the Aqua and Terra satellites, with morning and afternoon overpasses respectively, allowing for a large temporal and spatial coverage. However MODIS products are not totally free of problems. Sayer et al. (2013) evaluated the latest collection of MODIS Deep Blue aerosol product and found a low bias in AOD over the Sahara Desert. On the contrary, it is possible that MODIS-DT is biased high over the ocean, at least in dust outflow regions (Levy et al., 2003).

Aerosol products from other satellite sensors are also suitable for use in aerosol data assimilation. In the visible spectrum, this includes aerosol products from several instruments onboard low-Earth orbiting satellites like the Multiangle Imaging Spectroradiometer (MISR), Polarization and Anisotropy of Reflectances for Atmospheric Sciences Coupled with Observations from a Lidar (PARASOL), Advanced Along-Track Scanning Radiometer (AATSR) and Visible/Infrared Imaging Radiometer Suite (VIIRS). From geostationary satellites, AOD is available from the Spinning Enhanced Visible and Infrared Imager (SEVIRI) instrument onboard Meteosat Second Generation (MSG) and the Advanced Himawari Imager (AHI) onboard the Japanese geostationary meteorological satellite Himawari-8. In the infrared, aerosol products are available from the Advanced Infrared Radiation Sounder (AIRS) and the Infrared Atmospheric Sounder Interferometer (IASI) instruments, particularly for dust aerosols that have a strong signature in the longer wavelengths. Finally it is also possible to assimilate the vertical profile of the extinction coefficient from the Cloud-Aerosol Lidar with Orthogonal Polarization (CALIOP) sensor onboard the Cloud-Aerosol Lidar and Infrared Pathfinder Satellite Observation (CALIPSO) mission but this is also fraught with difficulties as such inversion is fairly sensitive to assumptions made on the aerosol model.

An evaluation of some of these products is done in de Leeuw et al. (2015). The authors found that most of the compared satellite products have a good performance of AOD retrievals with respect to ground-based AOD measurements. In theory it should be possible to take advantage of their complementarity either in terms of aerosol information content or in terms of temporal and spatial coverage. In practice, assimilating several aerosol products simultaneously is fraught with difficulties because the satellite products may be inconsistent with each other, or inconsistent with the aerosol model. To our knowledge there are few (e.g., Saide et al., 2014; Zhang et al., 2014) data assimilation studies that seek to combine different aerosol products.

In EBCH16 we described an inversion system and presented a dust source inversion for North Africa assimilating 550 nm AOD from the MODIS/Aqua instrument. We now broaden the analysis and consider several retrieval products. Rather than combining different aerosol products, we seek to understand how different aerosol products perform on their own in the data assimilation system, in order to assess the strengths and weaknesses of each aerosol dataset in the context of Saharan dust and possible inconsistencies between the products. We thus compare the assimilation of five satellite AOD retrievals with the aim to narrow uncertainties in dust emission estimates for North Africa and the Arabian Peninsula.

The next Section presents the assimilated observations and the observations used in the validation. The assimilation system is briefly described in Sect. 5.1.2, the main results and mineral dust flux estimates are shown in Sect. 5.1.3. We finish this work with our conclusions in Sect. 5.1.4.

5.1.2 Inversion system

5.1.2.1 Observation operator

The observation operator is described in EBCH16 and references therein. As a brief summary, the observation operator consists of the AOD estimation given by the coupling of the LMDz meteorological model (Hourdin et al., 2013) with a simplified aerosol model (Huneeus et al., 2009, hereafter referred as SPLA). The dust emissions are calculated as in EBCH16, which itself follows the Alfaro and Gomes (2001) and Marticorena and Bergametti (1995) emission scheme. The SPLA model is an Eulerian aerosol model of intermediate complexity (Huneeus et al., 2009) with four aerosol species (fine mode aerosols, coarse sea salt, coarse mineral dust and super-coarse mineral dust) and one tracer for gaseous aerosol precursors. In this model we parameterized the processes of boundary layer mixing, dry and wet deposition and sedimentation (for coarser particles). In the model, mineral dust aerosol are emitted in three bins. Fine mode dust has diameter less than 1 µm, coarse dust has diameter between 1 µm and 6 µm and super-coarse dust is between 6 µm and 30 µm in diameter. Once in the atmosphere, coarse and super-coarse dust are both independent model species, while fine dust is treated in the fine mode aerosols tracer. A detailed description of the aerosol model is provided in Huneeus et al. (2009) and updated in EBCH16.

In this work, the model has been configured with 39 vertical levels, and with an horizontal zoom centered over North Africa. The horizontal resolution over North Africa is approximately 1° by 1°, and the average horizontal resolution in between 70°W and 70°E; and 0°N and 40°N is approximately 1° in latitude and 1.4° in longitude. The one-year spin-up and the model simulations for the year 2006 where performed with a wind nudging from ERA-Intermim reanalysis (Dee et al., 2011) as is explained in EBCH16.

5.1.2.2 Control vector

The control vector is composed of multiplicative correction factors of the model emissions as in EBCH16. These correction factors are assumed homogeneous for each element of a partition of the emission flux in space (sub-regions), time (sub-periods) and type of aerosol (categories). Five categories of emissions are defined (as in EBCH16) namely i) sea salt, ii) biomass burning emissions, iii) fine dust and coarse dust, iv) super-coarse dust, and v) fossil fuel and anthropogenic SO_2 emissions. In this work, correction factors of fine dust and coarse dust are lumped together, while super-coarse dust has separate correction factors. Preliminary test have shown low sensitivity of the analysis to the to the grouping of the three dust correction factors in only two, either fine and coarse dust together and supercoarse independent (as in this work) or coarse and super-coarse dust lumped together and fine dust independent (as in EBCH16). Additionally, our test show that if the three dust correction factors are independent elements in the control vector, the assimilation results do not improve and the computational burden increases.

Sub-regions are defined depending on the emission category and they are the same as in EBCH16. For fossil fuel and anthropogenic SO_2 emissions and for sea salt emissions only one global sub-region is considered. For biomass burning emissions, two sub-regions have been defined, according to a grass-like and forest-like land cover maps. For both categories of mineral dust, 19 sub-regions are been defined: 15 of the over northern Africa, 3 of them over the Arabian Peninsula and Middle East and one sub-region for the rest of the globe. We refer to Fig. 1 of EBCH16 for a map of the dust sub-regions.

The correction factors are assumed constant within each sub-period. Like EBCH16, sea salt has a sub-period of one year, biomass burning and fossil fuel and anthropogenic SO_2 emissions have a sub-period of one month. A substantial difference with EBCH16 is the length of the sub-period for dust emissions. It was set to one month in EBCH16 but is reduced in this work to only three days. With this shorter sub-period (corresponding to the sub-synoptic to synoptic scale), we expect to better capture the dust emission variability in the analysis. This results in a control vector of 4674 components (that is about 10 times larger than in EBCH16), which required some modifications in how to deal with the inversion matrices. The later is mainly relates to technical concerns, as carefully avoid numerical errors in matrices multiplication and inversions, the use of efficient algorithms to ensure semi positiveness of some matrices involved in the inversion, and a satisfactory computational memory management of these large matrices.

5.1.2.3 Observations

In addition to the MODIS/Aqua total 550-nm AOD retrievals that we used in EBCH16, we now also assimilate fine mode 550-nm AOD over ocean in this study. Furthermore we consider a range of other aerosol products from passive instruments measuring solar reflectances. We do not consider aerosol products from passive instruments operating in the infrared or from active instruments as they would require different observational operators, which would introduce further complications in the interpretation of the results.

MODIS/Terra is a MODIS instrument on-board the low Earth orbiting satellite Terra (with equatorial overpass around 10:30 Local Time). The AOD retrievals from MODIS/Terra are calculated with the same algorithms than for MODIS/Aqua (Levy et al. (2013); Sayer et al. (2013, 2014)) providing total 550-nm AOD over land (Deep Blue and Dark Target algorithms) and fine mode and total 550-nm AOD over ocean (Dark Target algorithm only). We use the Level 3 AOD merged product from the Collection 6 for MODIS/Terra and MODIS/Aqua.

The POLarization and Directionality of the Earth's Reflectances instrument (POLDER, Tanré et al., 2011) onboard the PARASOL satellite measures radiances in 9 narrow channels in the visible to near-infrared spectrum with up to 16 viewing geometries and information on polarization in 3 of the channels. Through an advanced algorithm it reports total 670 and 865-nm AOD over ocean and the 865 nm fine AOD over land with their corresponding Ångström coefficient. Using this coefficient we derive the 550-nm AOD from these retrievals, for total and fine mode over ocean and fine mode over land. During year 2006, this instrument was orbiting in the "A-Train" along with the Aqua satellite. As the swath of the POLDER instrument onboard PARASOL (1600 km) is relatively close to that of MODIS (2330 km), PARASOL and MODIS/Aqua have fairly similar spatial and temporal coverage although the two algorithms differ in the clear-sky mask they use, and hence on the spatial coverage of the AOD products.

The MISR instrument onboard the Terra satellite reports 555 nm AOD over land and ocean (Kahn et al., 2009). The MISR algorithm uses multi-angular and multi-spectral information to retrieve the AOD. The swath of this instrument is smaller than the swath of MODIS which results in less coverage. Specifically, the standard Level 2 (individual soundings) and Level 3 (daily mean maps) MISR products report 555 nm AOD for fine (less than 0.7 µm of diameter), medium (between 0.7 and 1.4 µm of diameter) and large (more than 1.4 µm of diameter) aerosols. Regrettably, the size cut-off between the MISR products and the SPLA model are not compatible so we need to post-process the MISR products before assimilation. We do it in the following way. The MISR retrieval algorithm calculates the best linear combination of 74 aerosol *mixture* models in order to fit the measured radiances for each observed pixel. These fitting parameters and the main parameters of the aerosol models are reported in Level 2 of the MISR products. With this information and with the reported Level 2 AOD, we have calculated an estimate of the MISR 555 nm AODs with the same diameter cut-off than the SPLA model, i.e., for fine (less than 1 µm of diameter), coarse (between 1 and 6 µm of diameter) and super-coarse (larger than 6 µm of diameter) aerosols. Briefly, the post-processing of the MISR AOD was the following: (i) we calculated the contribution of each aerosol model to the total AOD, using the reported fitting parameters and considering the 8 *basic* aerosol models of MISR algorithm; (ii) assuming that the reported extinction coefficient for each model is independent from the size distribution, we estimated the contribution of each bin (as the SPLA definitions) to the total AOD. In practice, our approximation of the AOD reprojected on the three modes of the SPLA model is accurate with a relative error of (maximum) 5% of the total AOD for the 5% less accurate recomputed retrievals. In this work we only used the recomputed fine mode and total 555-nm MISR AOD.

The AERUS-GEO product (Aerosol and surface albEdo Retrieval Using a directional Splitting method-application to GEOstationary data, Carrer et al., 2010, 2014) is a full-disk daily 630 nm AOD retrieval calculated from the measured radiances of the SEVIRI instrument. These retrievals cover Europe and Africa. Unlike the above mentioned products, AERUS-GEO uses only one spectral band to calculate the daily AOD product, based on measurements done in a relatively high spatial and temporal resolution in different (i.e. time-varying) conditions of solar angles. The native spatial resolution of this product is 3 km by 3 km close to the Equator. We use the total 630 nm AOD from this product. We have screened all the pixels where the “ZAge” flag of the product is greater than zero [D. Carrer, personal communication]. This filter removes suspicious large and persistent AOD values in the equatorial Atlantic ocean which are related to a time persistence assumption in the algorithm. After this screening, the 80 % of the full-disk valid data is kept over land and the 56 % over ocean.

Most common regridding techniques have problems handling missing data (e.g. bilinear interpolation) or can be inaccurate when the spatial resolutions of the input and output grids are too different (e.g. nearest neighbour). In the present work the regridding of all AOD satellite products into the model grid was performed with a weighted-area procedure. Furthermore only the model grid-boxes covered with 30% or more of satellite valid data are considered; they are otherwise set to a missing value. This arbitrary value of 30% approximately propagates the same coverage area of the satellite products into the model grid. This regridding method successfully handles the missing values and large differences in grid resolutions. Moreover, if the input field has no missing values and both are latitude-longitude grids, this method is equivalent to a bilinear interpolation.

Figure 5.1 shows the average AOD for the year 2006 for each instrument described above. It is important to note the difference in the sampling time of each product. The SEVIRI product is retrieved using a combination of all the available observations per day, thus achieving a mean coverage of 75% per day in our assimilation region for the year 2006. The low Earth orbiting satellites typically sample only once per day our region of interest coverage. However MISR has a more narrow swath than MODIS and POLDER (on PARASOL) so its coverage is less. We say more about the number of observations in the next Section.

5.1.2.4 Error covariance matrices and assimilation configuration

The covariance matrix of the background errors **B** is defined with similar values to the ones from EBCH16. The standard deviation of the control vector errors (i.e. the square root of the diagonal terms of **B**) are 1.3 for for biomass burning emissions, 3.0 for mineral dust emissions, 2.0 for sea salt emissions and 0.18 for anthropogenic and fossil fuel emissions. We have included correlations between control vector errors. For the same sub-region and category of dust emission (fine and coarse dust, super-coarse dust) we have defined a Gaussian correlation between sub-periods with a time-length scale of three days. In comparison with EBCH16, this shortened timescale giving more freedom to the assimilation system. It allows the assimilation system to take advantage of the shortened sub-period, with the aim of improving the representation of dust events at these scales. Furthermore, the shorter sub-period of the dust control vector of this work compared to EBCH16 (3 days versus 1 month) raises the size of the control vector from 494 to 4,674 elements. For the same sub-region and sub-period, the correlation of errors between the fine and coarse dust emission correction factors and the super-coarse correction factor is set to 0.7.

A substantial difference with EBCH16 is the construction of the covariance matrix of the observational errors (**R**). In EBCH16 the standard deviation of the observational errors were set to a fixed value of 0.2 and 0.1 for MODIS AOD products over land and ocean, respectively. In this work we keep a diagonal **R** matrix but the errors are defined according to the observational errors reported in the literature. A summary of these definitions is shown in Table 5.1. For the sake of simplicity, the errors were calculated using the satellite AOD as the reference AOD, despite the fact that most of the derivations of these error formulae were done using an independent AOD dataset as a reference. The standard deviation of the observational errors have to be prescribed to the data assimilation system. For MODIS and MISR, the errors are characterized

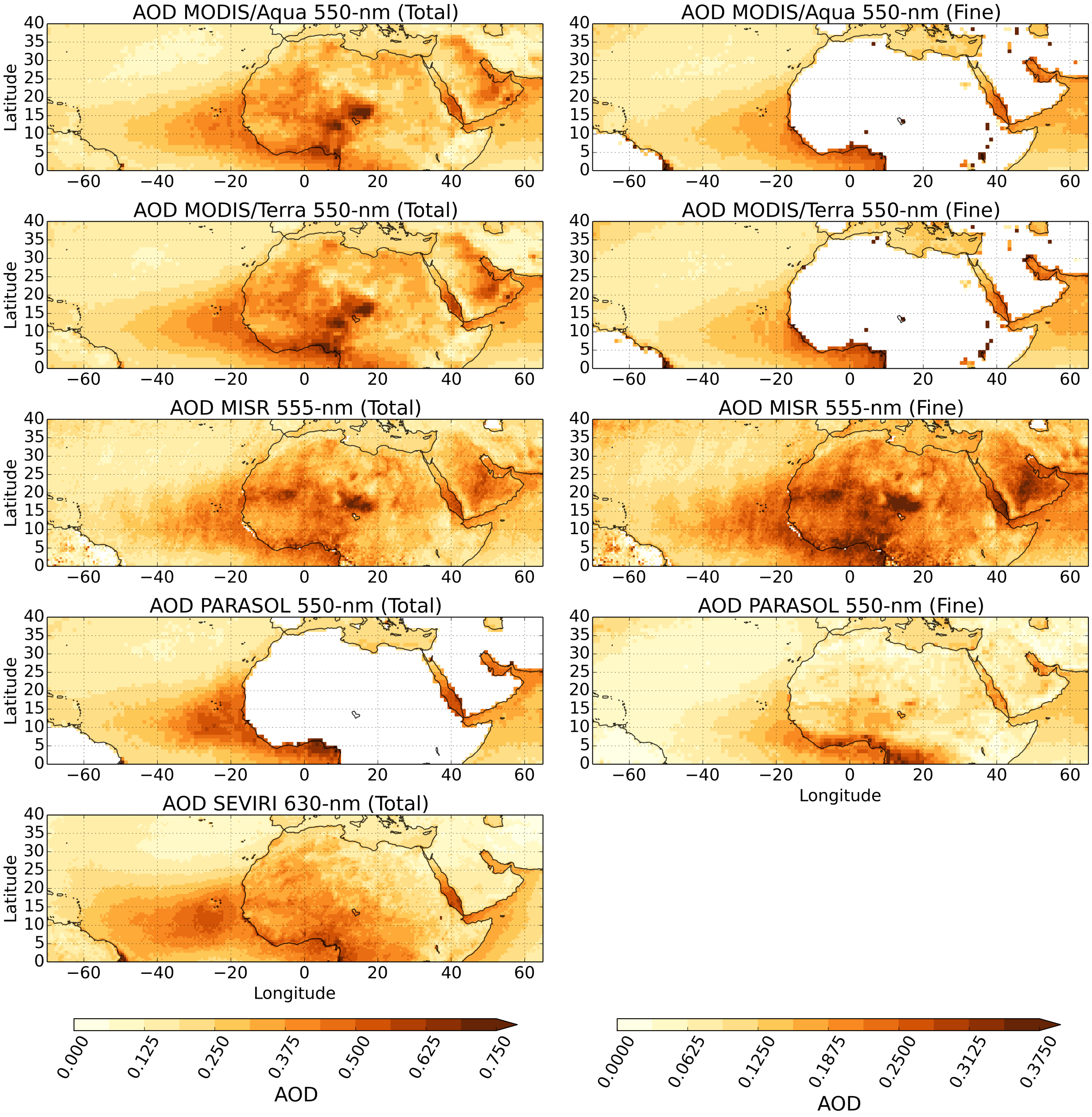

Figure 5.1: Averages for the year 2006 of the satellite-derived AOD products used in this study. The AOD products are all regridded to a regular latitude-longitude grid of 0.5° resolution for MISR and SEVIRI and 1° for MODIS and PARASOL. The total AOD is shown on the left column and the fine mode AOD (when available) on the right column. Please note that the different color scales between the two columns and the (somewhat) different wavelengths of the reported AOD.

Dataset	Error estimate (from reference)	Error adapted to this work	Reference
MODIS-DB	$\pm(0.03 + 0.2\tau)$	$0.03 + 0.2\tau$	Sayer et al. (2013)
MODIS-DT ocean	$[-(0.02 + 0.1\tau), +(0.04 + 0.1\tau)]$	$0.03 + 0.1\tau$	Levy et al. (2013)
MODIS-DT land	$\pm(0.05 + 0.15\tau)$	$0.05 + 0.15\tau$	Levy et al. (2013)
MISR	$\pm \max(0.05, 0.2\tau)$	$\max(0.05, 0.2\tau)$	Kahn et al. (2005)
PARASOL	$\pm 0.05 \pm 0.05\tau$	$\sqrt{0.05^2 + (0.05\tau)^2}$	Tanré et al. (2011)
SEVIRI	$\sqrt{C_k}$	$\sqrt{C_k}$	Carrer et al. (2010, 2014)

Table 5.1: Definitions of diagonal terms in the observational error covariance matrix. The main references for the errors are shown in the table. The original error formulae were adapted for the assimilation purposes. The error shown for MODIS-DT over land is not used in this work. Errors for the SEVIRI dataset (C_k) are described in Carrer et al. (2010, 2014).

by an *expected error* (EE) which defines the boundaries of a region that contains the 67% of the matchups between the satellite AOD and the reference AOD. For the MODIS merged product over land there is no equivalent error quantification. In this work, the majority of the assimilated observations over land are over North Africa and the Arabian Peninsula, where most of the AOD is retrieved by the MODIS-DB algorithm. Hence, we adopt MODIS-DB error quantification as the standard deviation for MODIS land AOD. Over ocean, the MODIS merged AOD is the same as the Dark Target product, but the DT EE is not centered on zero. We adopt the approximation shown in Table 5.1 for MODIS over ocean, shifting the EE to be symmetrical around zero at their minima. For PARASOL AOD, we assume that both terms shown in Table 5.1 are independent and Gaussian distributed in order to calculate the error estimate for the data assimilation system. Due to the lack of separate error estimates of fine AOD, we assume the error estimates of Table 5.1 for fine AOD of MODIS, MISR and PARASOL. SEVIRI reports pixel-wise variance of the errors which are themselves the diagonal elements of the covariance matrix of the analysis errors in the AERUS-GEO retrieval algorithm. As we do not have information about the correlation of the errors of nearby pixels, we compute the regridded SEVIRI AOD error assuming that all the SEVIRI pixels in the native grid are fully correlated within each model gridbox. In our case this assumption conserves the spatial structure of the AOD errors. This is done only for SEVIRI AOD, as they report pixel-wise AOD error variance in their daily product.

Unlike EBCH16, we do not inflate the covariance matrices in order to fulfil the Desroziers et al. (2005) diagnostics. Desroziers et al. (2005) diagnostics help to detect and correct possible imbalances between the error covariance matrices in a variational assimilation framework in the observational space. These diagnostics assume that both the observations and the prior control vector do not have any bias. This assumption does not necessarily hold for all the experiments in this work, so we decided not to inflate the covariance matrices. Additionally, a common configuration for all the inversions is fairer to draw consistent conclusions across the five observational datasets.

The number of assimilated observations (once reprojected onto the model grid) is considerably larger than the ones used in EBCH16 due to the inclusion of fine AOD. The number of assimilated observations is 1,469,252 for MODIS/Aqua, 1,486,774 for MODIS/Terra, 906,949 for PARASOL, 385,638 for MISR, and 1,299,764 for SEVIRI. As discussed previously the differences for the instruments onboard sun-synchronous orbit satellites arise from the swath of the instruments, the amount of land retrievals, and details of the cloud masking algorithm that may reject more or less satellite pixels during the retrieval.

We compute the analysis with the assimilation system described below for five satellite retrievals dataset (MODIS/Aqua, MODIS/Terra, MISR, PARASOL and SEVIRI) for the year 2006. The assimilated observations are total AOD and fine AOD where it is available, that is, total AOD over ocean for all the retrievals; total AOD over land for MODIS, MISR and SEVIRI retrieval; fine AOD over ocean for MODIS, MISR and PARASOL; and fine AOD over land for MISR and PARASOL datasets. For satellites in the "A-Train" (MODIS/Aqua and PARASOL) the sampling is done at 13:30 local time. For instruments on-board the Terra satellite (MISR, MODIS/Terra) the sampling is done at 10:30 local time. For SEVIRI, the whole day average is considered. Only observations between 70°W and 65°E in longitude and between 0°N and 40°N in latitude are assimilated.

It is necessary to note that the fine AOD derived from the satellite observations is comparable to the model fine mode AOD but there are small differences across instruments. For MODIS and PARASOL products, the fine AOD is the contribution of preselected fine mode aerosol models to the total AOD in their respective retrieval algorithms, and they are comparable (but not necessarily equivalent) to the LMDZ-SPLA fine mode AOD. For fine AOD from MISR, our post-processing of the MISR products ensures the equivalence and comparability between the model and the assimilated fine mode AOD.

As a consequence of the structure of the control vector, where fine and coarse dust correction factors are lumped together, the assimilated fine AOD partially constrains the coarse dust correction factor. In contrast the super coarse dust correction factors are solely directly constrained by the Total dust AOD. Finally, the nonzero covariances between errors of both dust correction factors propagate the assimilation of the fine mode AOD to the super-coarse dust correction factor.

5.1.3 Results

5.1.3.1 Some words about the observations

Figure 5.1 shows the annual average for year 2006 of the observations described in Sect. 5.1.2.3. Several characteristics can be identified in these yearly averages of AOD and they will impact the assimilation analysis. All panels clearly show the transatlantic dust plume and the local maximum of AOD in the south of the Red Sea. However, maximum values of AOD over and downwind Bodélé depression are hardly shown in the SEVIRI and PARASOL observations. For total AOD, the SEVIRI plume over the Atlantic seems to be more extended than the rest of the products. Maximum values of total AOD over the Atlantic ocean are found close the African coast except for SEVIRI. MODIS retrievals share similar yearly AOD means for fine AOD and total AOD. In comparison, MISR AOD shows a local maximum of AOD close to (18°N, 5°W) that is not observed in the rest of the products, while an AOD local maximum at (12°N, 9°E) is only observed in the MODIS products.

For the fine AOD there are notorious differences between PARASOL and MISR products, especially over the Sahara. PARASOL AODs are significantly smaller than MISR fine mode AOD over land and ocean.

To (roughly) be able to discriminate the effect of the satellite coverage against the effect of the sampling time of the assimilated products, we have computed an equivalent of Fig. 5.1 but only for pairs of simultaneous AOD retrievals that correspond to (approximately) the same overpass time. These yearly averages are shown in Fig. 5.2. In Fig. 5.2 the observations of two instruments onboard the Terra satellite (MISR and MODIS/Terra) were screened in order to compute the yearly average with pixels where both MISR and MODIS/Terra report valid data. A similar procedure was applied to the instruments onboard satellites of the A-train constellation, MODIS/Aqua and PARASOL. This screening allows a fair comparison between two pairs of retrievals.

For the collocated averages over the ocean, MODIS/Aqua and PARASOL show a similar spatial pattern for the total AOD, with collocated maxima of AOD over the Atlantic Ocean in the 5 to 15°N latitude band; both share a relative large AOD over the Gulf of Guinea and the AOD gradient in the Red Sea (with larger values in the south of the Sea). However total AOD from MODIS/Aqua panel in Fig. 5.2 is slightly smaller than its PARASOL counterpart on the eastern transatlantic dust plume, while for the fine mode AOD, PARASOL shows smaller values.

For MODIS/Terra and MISR the differences mentioned in the description of Fig. 5.1 still holds when the observations are collocated (Fig. 5.2). Over the Arabian Peninsula, a spatial mismatch between MODIS products and MISR AOD can be identified in both Fig. 5.1 and Fig. 5.2.

5.1.3.2 Assimilation results: Departures

The assimilation performance will be explained only in terms of observation departures. Comparisons with the assimilated AOD are qualitatively similar to those presented in EBCH16.

Figure 5.3 shows histograms (in 200 bins) of the departures of the prior AOD (i.e., the difference between assimilated observations and the simulated prior AOD) and the departures of the analysis (i.e., the difference between the assimilated observations and the analysis AOD). This is shown for all 5 experiments. A common and expected feature of Fig. 5.3 is the smaller dispersion of the analysis departures with respect to the prior ones. The mode value of the histogram of the departures for the analysis is also closer to zero than for the prior in all the panels for the total AOD.

All prior histograms except PARASOL, are slightly shifted to the right instead of being centered on zero, which means that the observations are generally larger than the prior, or said

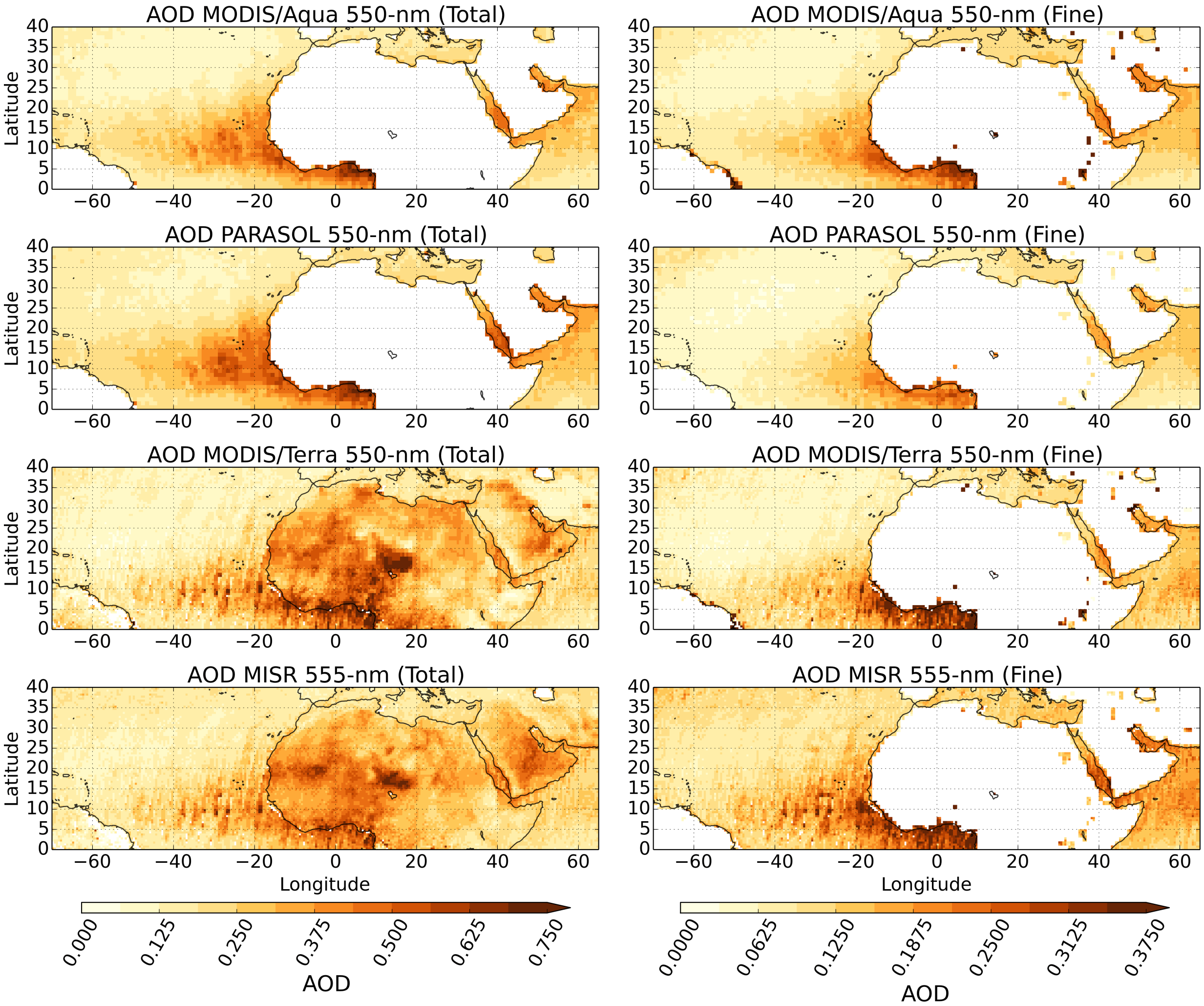

Figure 5.2: Averages for the year 2006 of the satellite-derived AOD products, similar to Fig. 5.1 but for colocated MISR and MODIS/Terra observations, and colocated PARASOL and MODIS/Aqua observations.

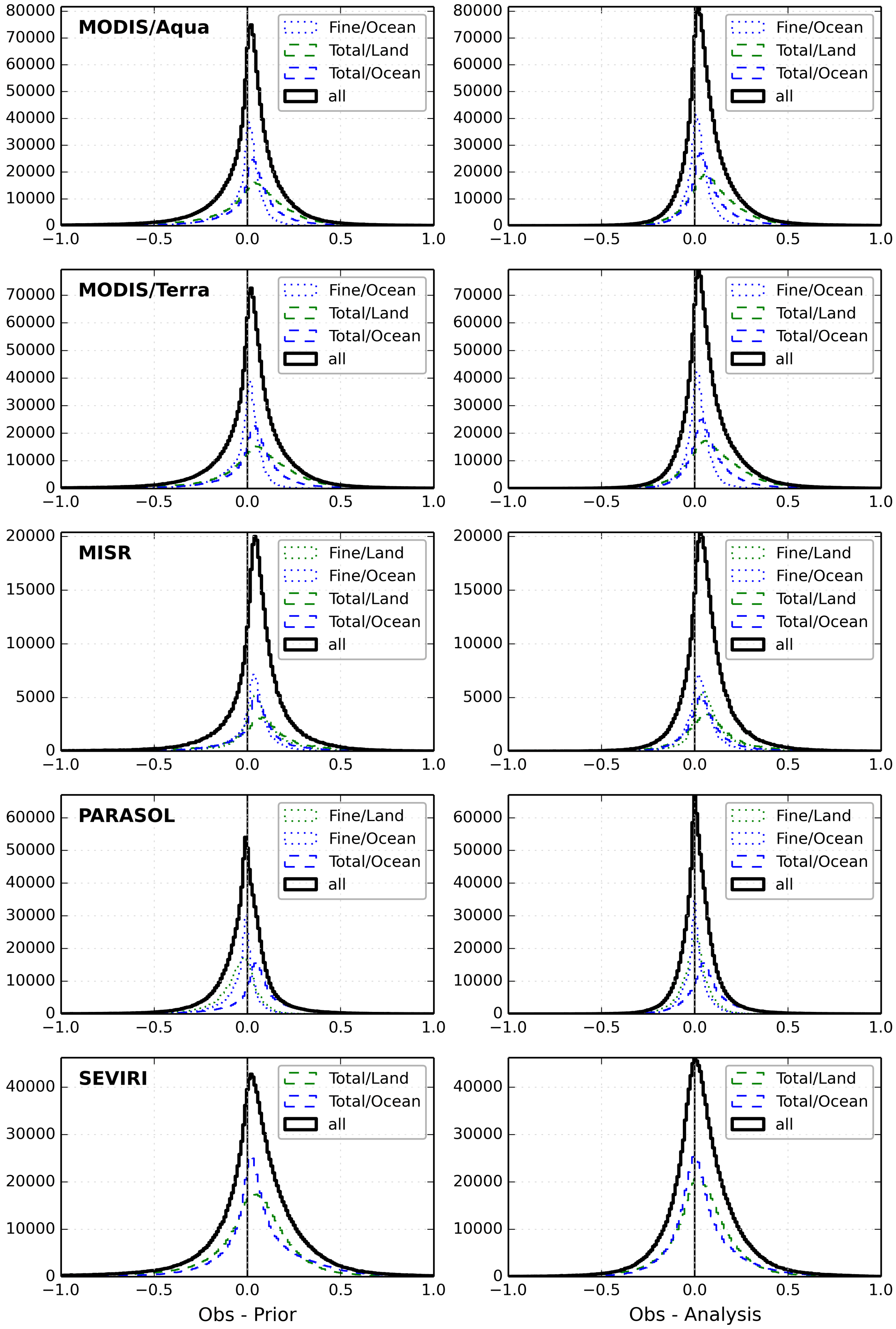

Figure 5.3: Frequency plot of departures. Observational departures with respect to the prior simulation are shown on the left column and departures with respect to the analysis are shown on the right column. Histograms are plotted between -1 and 1 in 200 bins each. Pixels over land are in green, over ocean in blue and both of them in black. Fine mode AOD in dotted lines and Total AOD in dashed lines.

differently that the model has a low bias. This is repeated to a lesser extent in the analysis histograms for MODIS/Terra, MODIS/Aqua and MISR. For these three instruments, the land and ocean departures of the total AOD share similar characteristics, that is, ocean departures have less spread than land departures, and the right tails of land departures are heavier than their ocean counterpart.

We recall that the prior simulation is the same for all panels, and the difference in prior lies in the local time and gridboxes for which the model values are sampled. Despite the sampling difference and given the differences between the collocated AODs (above explained) we nevertheless think that most differences between the histograms of Fig. 5.3 are due to observational differences.

The only instrument that does not have available total AOD over land is the PARASOL instrument. Departures of total AOD over ocean are larger in the PARASOL panel than for the rest of the satellites, with a notable shift to the right, meaning that the observations are, in most of the cases, larger than the prior and analysis simulations. These large departures in the prior are mostly related to the large AOD values of the dust transatlantic plume over the Eastern Atlantic Ocean.

Validation against Aerosol Robotic Network (AERONET Holben et al., 1998) is qualitatively similar to the one shown in EBCH16 for all the experiments. A table summarizing the main statistics for each experiment is included in Appendix 5.1.5.

5.1.3.3 Analysis AOD

Figure 5.4 shows the simulated 550 nm AOD for the prior and the 5 analyses. Larger AOD values are simulated in boreal summer (June-July-August or JJA) for all the analysis and the prior. Compared to the prior, the analysis decreases AOD in the northern Sahara for all the analysis except PARASOL in JJA and boreal spring (March-April-May or MAM). There is not a large difference in AOD when the two MODIS analyses are compared between them, which is consistent with the discussion of the observations in Sect. 5.1.3.1. AOD from the MISR assimilation is larger in MAM than in the MODIS analysis.

In the PARASOL analysis the assimilation system increases the coarser dust emissions in order to improve the fit over the ocean. As PARASOL does not report total AOD over land, dust emissions of the coarser dust bins (and thus also with the shorter atmospheric residence time) are not fully constrained by near-source observations. This results in a large and possible unrealistic increase in coarser mode dust emissions. For this reason we exclude this dataset from our emission flux analysis.

The SEVIRI analysis shows a larger transatlantic dust plume in MAM and JJA along with larger values of AOD over land. Observational uncertainties for SEVIRI are generally larger over land than over ocean. This allows the assimilation system to favour a better fit of the AOD over the ocean than over land, which results in large AOD values over land.

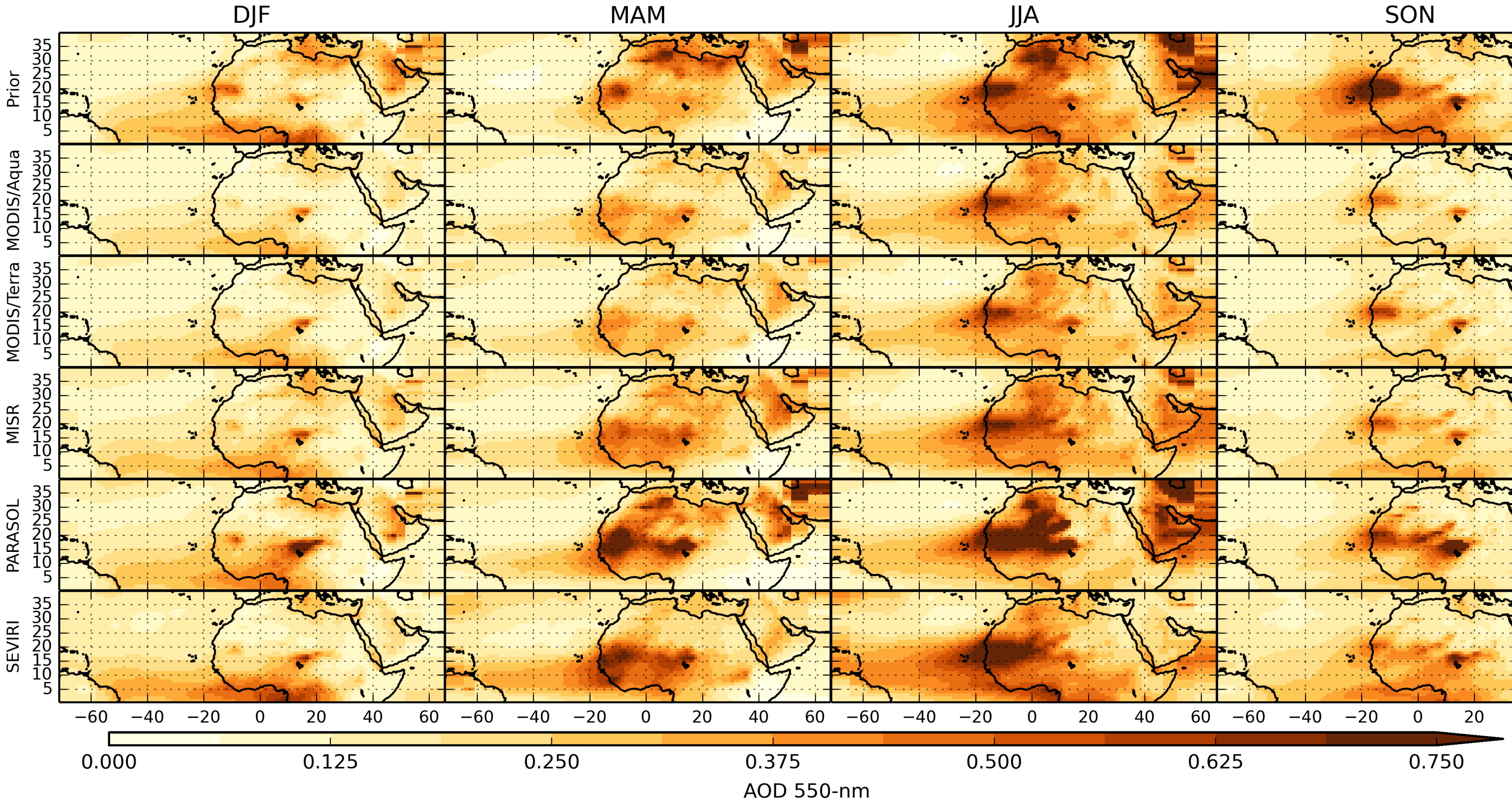

Figure 5.4: Simulated prior and analysis AOD at 550 nm for the 5 assimilation configurations. The panels show the averaged AOD for each experiment (rows) over the months indicated in the head of the columns. MAM stands for March, April and May; JJA for June, July and August, SON for September, October and November and DJF for December, January and February. In the later we include the first two months and the last month of the year 2006.

	Prior	MODIS/Terra	MODIS/Aqua	MISR	PARASOL	SEVIRI
Total AP+Africa	6657	3267	2697	3680	15748	2547
Total Africa	4085	2788	2361	2638	9447	2404
Total AP	2571	478	337	1043	6301	143
Total Africa West	3161	1808	1484	1699	6672	1544
Total Africa East	924	980	877	938	2775	860
Fine and Coarse AP+Africa	1087	644	630	853	874	670
Fine and Coarse Africa	709	452	431	585	527	567
Fine and Coarse AP	378	192	199	268	347	103
Fine and Coarse Africa West	526	294	290	376	357	379
Fine and Coarse Africa East	183	158	141	209	170	188
Super-coarse AP+Africa	5570	2623	2067	2827	14873	1877
Super-coarse Africa	3376	2336	1930	2052	8920	1837
Super-coarse AP	2193	287	138	775	5954	39
Super-coarse Africa West	2635	1514	1194	1324	6314	1165
Super-coarse Africa East	741	822	736	729	2605	672

Table 5.2: Total emission flux by region and by observational dataset for the year 2006 in Tg year^{-1}. AP stands for Arabian Peninsula. Western Africa refers to the longitude band between the Atlantic coast and approximately 16°E corresponding to regions 01 to 09 in EBCH16. East Africa refers to regions 10 to 16 in EBCH16, that is, to a longitude band between approximately 16°E and the Red Sea.

The relatively large AOD over land of the last two analyses (PARASOL and SEVIRI) could indicate a deficiency in the model in the transport of the dust plume. We will come back to this point later in this work.

5.1.3.4 Mineral dust flux

Mineral dust emissions were estimated with the data assimilation system using the five satellite products one by one. Total estimated flux over the Sahara and the Arabian Peninsula are shown in Table 5.2. Excluding the PARASOL analysis, the total mineral dust fluxes for the year 2006 ranges between 2547 and 3680 Tg. We recall that these estimates are for emitted dust particles in a diameter range between 0.06 and 30 µm. The emission estimate is highly dependent on the size cut-off of the emitted particles. For airborne dust smaller than 6 µm of diameter, the total flux is estimated between 630 and 853 Tg for the year 2006. The range is therefore much smaller when we exclude the largest dust mode. Table 5.2 shows detailed estimates for these categories and for three geographical regions: Western North Africa, Eastern North Africa and the Arabian Peninsula.

Similarly to the emissions presented in Laurent et al. (2008), Western Sahara has larger emissions than Eastern Sahara. This is indeed the case in all the analysis. For both fine and coarse dust emissions, the contribution of the Arabian Peninsula (AP) is significant, indicating that is an important dust source even though it does not receive much attention in the literature. However, super-coarse dust emissions of AP are, in general, one order of magnitude smaller than

North African emissions.

Figure 5.5 shows emission fluxes split by month for the three bins of SPLA. It can be seen that most of the dust emission flux is achieved in the super-coarse size range. For the reasons explained above, super-coarse dust emissions of the PARASOL analysis are much larger than expected. However, this is not the case for the coarse dust flux of the PARASOL analysis due to the structure of the control vector, where the fine and coarse dust correction factors are lumped together. As it was the case in EBCH16, the dust emission fluxes from the analysis are systematically smaller than for the prior simulation, for almost all dust bins, regions and months. This is largely noticeable for the super-coarse dust emission panel.

In general, coarse and fine dust emissions have maximum values in July, June, March and December while the super-coarse dust emission peaks on September. Throughout the year, coarse and fine dust fluxes share the same emission cycle, indicating consistent seasonality across the various assimilated observational datasets. However, we cannot completely discard that a model bias (at the seasonal scale) generates this feature.

Sensitivity to the observation sampling time and coverage is not explored in this work explicitly, but the impact of the sampling time can be somehow inferred from a comparison between the two MODIS analyses. Both MODIS retrievals are expected to have similar performance when compared against reference datasets (Levy et al., 2015; Sayer et al., 2015). Our results indicate that, despite the relatively large spread (hundreds of Tg per year) on the overall analysed dust flux from the two instruments, the seasonal cycle of these two analyses is similar.

If both instruments are unbiased (or at least if they have the same bias), the sampling time of the products would be the most important difference in the data assimilation system. In this case, the mismatch on the overall emission flux, which is controlled by emissions from the super-coarse dust, can be likely attributed to the representation of the diurnal cycle of model emissions and boundary layer processes.

5.1.4 Conclusions

We have assimilated AOD from five satellite retrievals into a common data assimilation system. The control vector elements consist of correction factors for the prior aerosol emission flux over sub-regions of the Sahara and the Arabian Peninsula. Observational error statistics were adapted from the literature. For four of the five AOD datasets fine mode AOD was assimilated when it was available. As expected, the analysis departures are, in general, smaller than the prior departures. The a posteriori estimated mineral dust flux shares a common seasonal variation between the various data assimilation configurations, but there is a relative large spread in the yearly total amount. This work estimates a total amount of emitted mineral dust over North Africa and the Arabian Peninsula ranging between 2550 and 3680 $\mathrm{Tg\,yr^{-1}}$, for mineral dust particles smaller than 30 µm of diameter in the year 2006. For mineral dust smaller than 6 µm of diameter, the estimated flux is between 630 and 850 $\mathrm{Tg\,yr^{-1}}$.

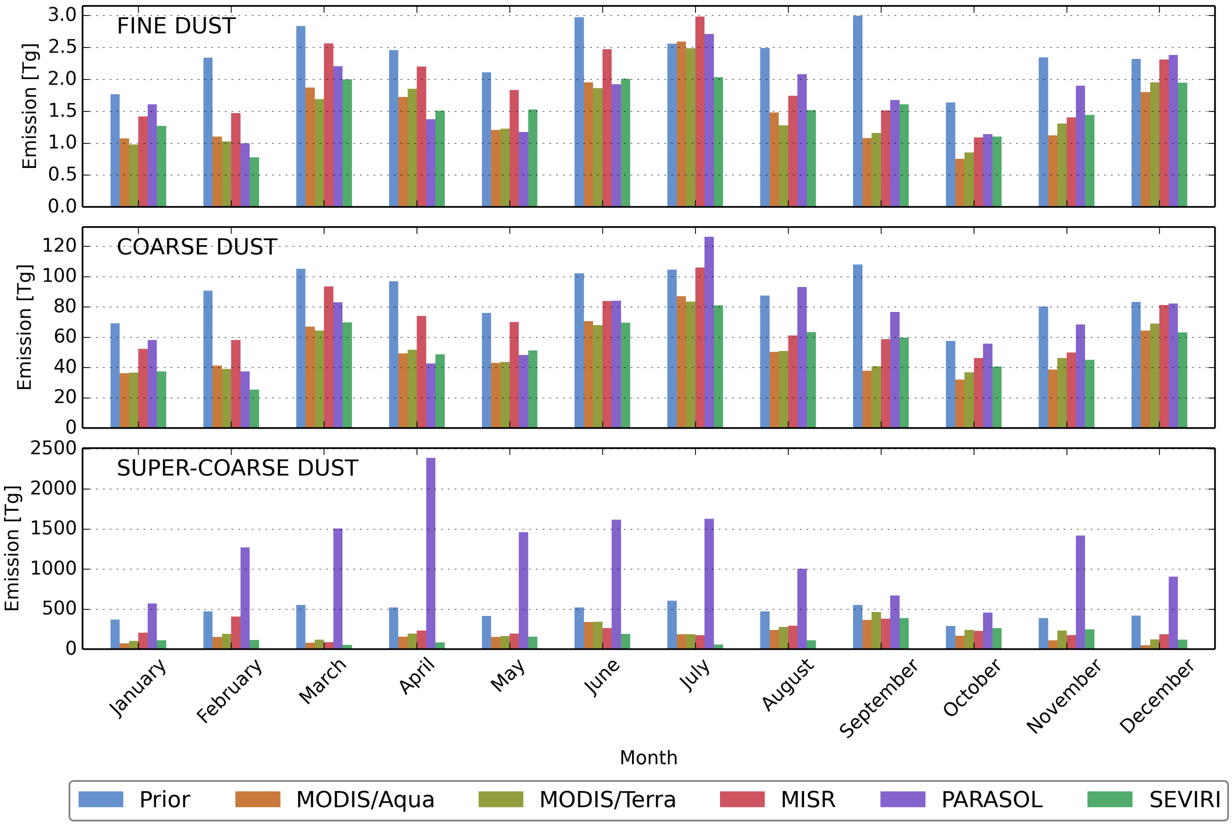

Figure 5.5: Total dust flux per month over the Sahara and the Arabian Peninsula. Fine mode dust is shown in the first panel, coarse mode dust in the middle panel and super-coarse mode dust in the lower panel. The different bars show the total mineral dust flux over the Sahara and the Arabian Peninsula by experiment and month. The three plots use different scales.

We isolated the role of the assimilated observation dataset (by freezing the rest of the inversion configuration) and showed that the large spread of these fluxes is likely associated to differences between these datasets (including their associated error statistics) rather than to model biases or deficiencies in the data assimilation system. This is despite the satellite AOD observations being similarly good quality (or at least perceived as such). The dust emission fluxes are nevertheless sensitive to model biases or missing or under-represented processes in the model. In fact, the large emission of super-coarse dust in the PARASOL experiment could indicate that the model is not able to well reproduce airborne dust transport and removal processes. For this product, a coarse AOD retrieval over land would be beneficial in the assimilation.

Despite the fact that MISR has a smaller swath compared to the other assimilated products, the capability of report total and fine AOD over land is beneficial to the assimilation. This can be seen when the analysis was compared against AERONET AOD (Appendix 5.1.5), the MISR analysis skills are similar to the rest of the analyses although the number of assimilated observations is smaller.

It is important to maintain the variety of current AOD retrieval approaches, explored by different groups with different algorithms, while improving the quality and achieving some convergence (through error reduction of the individual products). There are however two limitations in our treatment of observational errors due to the lack of information about the assimilated products. First, the assimilated fine AOD error variance was assumed to be similar to the total AOD error variance. Indeed, the characteristics of fine AOD errors are unknown, but this information would be useful and could, in principle, improve the analysis. Secondly, we assumed uncorrelated errors between fine and total assimilated AOD. As both AODs are computed simultaneously in the retrievals using similar hypotheses and radiance measurements, this assumption does not necessarily hold. Ideally, these statistics should be provided by the retrieval algorithm and reported along with the observations. Likewise it would be useful to consider error covariances in space (and possibly in time). A new generation of aerosol retrieval algorithms based on statistically optimized fitting of observations, such as that of GRASP (Dubovik et al., 2014), can in principle provide such information. It would be interesting to test the impact of including such improved error statistics in the source inversion.

The year-to-year variability of dust emission fluxes was not considered in this study. It could increase or decrease the spread in dust emission fluxes estimates. Although different satellite aerosol instruments are available for different periods, there are sufficient overlaps between instruments to gain understanding from multi-year retrievals.

Finally reducing modelled and observational biases is another key to improve top-down emission flux estimates. Pope et al. (2016) evaluated the analysis increments in a data assimilation framework and found that large increments were associated with meteorological conditions for which the model lacks performance. Another approach which we leave for future work would be to optimize some of key model parameters in the dust source function.

5.1.5 Appendix: Comparison with AERONET

For validation, we select AERONET stations in the same way as in EBCH16. We only consider stations with at least 182 valid daily 500 nm AOD retrievals of Level 2 product (Version 2). The following stations meet this criteria for the year 2006 in the region of interest: Bahrain, Blida, Dhabi, Dhadnah, Forth Crete, Granada, Hamim, Ilorin, La Parguera, Nes Ziona, Santa Cruz Tenerife, Sede Boker and Solar Village. The model AOD is recomputed at 500 nm for comparison with the AERONET AOD. The summary of statistics is shown in Table 5.3.

Acknowledgements

The authors would like to thank the MODIS, MISR, PARASOL, AERUS-GEO and AERONET teams for making their retrieval available, F.-M. Bréon and D. Carrer for their advice with the POLDER/PARASOL and the AERUS-GEO retrievals, respectively. The POLDER/PARASOL and AERUS-GEO data were downloaded from the ICARE analysis and data centre (`http://www.icare.univ-lille1.fr/`). MODIS AOD products are available at `http://modis-atmos.gsfc.nasa.gov`, MISR AOD were downloaded from the Atmospheric Science Data Center at NASA (`https://eosweb.larc.nasa.gov/`) and AERONET AOD is available at `http://aeronet.gsfc.nasa.gov`. Input soil data used in this study is available at `http://www.lisa.univ-paris12.fr/mod/data/index.php`. The work was co-funded by the project OSIRIS from MEDDE/INSU, the Copernicus Atmosphere Monitoring Service, implemented by the European Centre for Medium-Range Weather Forecasts (ECMWF) on behalf of the European Commission, and by the France-Chile ECOS project number C14U01. Part of the work was done using computing time from the TGCC under the GENCI projects t2014012201, t2015012201 and t2016012201. Nicolás Huneeus acknowledges support from FONDAP 15110009 and FONDECYT 1150873.

Station		Bahrain	Blida	Dhabi	Dhadnah	Forth Crete	Granada	Hamim	Ilorin	La Parguera	Nes Ziona	Santa Cruz Tenerife	Sede Boker	Solar Village
Latitude (°N)		26.21	36.51	24.48	25.51	35.33	37.16	22.97	8.32	17.97	31.92	28.47	30.86	24.91
Longitude (°E)		50.61	2.88	54.38	56.32	25.28	-3.6	54.3	4.34	-67.05	34.79	-16.25	34.78	46.4
Elevation (m.a.s.l.)		25	230	15	81	20	680	209	350	12	40	52	480	764
N obs.		201	195	243	324	283	276	263	270	251	185	233	335	335
Mean	Obs.	0.433	0.258	0.434	0.404	0.196	0.177	0.314	0.705	0.148	0.226	0.171	0.2	0.372
	Prior	0.472	0.313	0.411	0.454	0.273	0.209	0.346	0.434	0.145	0.245	0.178	0.263	0.37
	MODIS/Aqua	0.304	0.179	0.236	0.242	0.176	0.127	0.196	0.319	0.113	0.14	0.119	0.168	0.276
	MODIS/Terra	0.309	0.187	0.238	0.241	0.184	0.133	0.196	0.329	0.116	0.151	0.126	0.187	0.289
	MISR	0.429	0.216	0.321	0.326	0.221	0.161	0.262	0.392	0.135	0.198	0.146	0.274	0.383
	PARASOL	0.452	0.197	0.349	0.372	0.166	0.129	0.286	0.379	0.109	0.141	0.138	0.204	0.449
	SEVIRI	0.267	0.22	0.208	0.203	0.222	0.173	0.188	0.487	0.194	0.192	0.166	0.219	0.267
Bias	Prior	0.04	0.056	-0.023	0.05	0.076	0.032	0.032	-0.271	-0.003	0.019	0.007	0.063	-0.002
	MODIS/Aqua	-0.128	-0.079	-0.198	-0.162	-0.02	-0.05	-0.118	-0.386	-0.035	-0.085	-0.052	-0.031	-0.097
	MODIS/Terra	-0.123	-0.071	-0.196	-0.163	-0.012	-0.044	-0.118	-0.376	-0.032	-0.075	-0.045	-0.013	-0.083
	MISR	-0.003	-0.041	-0.113	-0.078	0.024	-0.016	-0.053	-0.313	-0.013	-0.028	-0.025	0.074	0.011
	PARASOL	0.019	-0.061	-0.085	-0.032	-0.031	-0.048	-0.028	-0.326	-0.039	-0.085	-0.033	0.004	0.077
	SEVIRI	-0.165	-0.038	-0.226	-0.201	0.026	-0.004	-0.126	-0.218	0.046	-0.034	-0.005	0.019	-0.105
RMSE	Prior	0.365	0.349	0.397	0.465	0.266	0.229	0.257	0.598	0.146	0.144	0.176	0.235	0.272
	MODIS/Aqua	0.264	0.172	0.306	0.28	0.143	0.109	0.191	0.607	0.087	0.142	0.112	0.129	0.264
	MODIS/Terra	0.258	0.167	0.307	0.28	0.145	0.108	0.193	0.604	0.086	0.14	0.109	0.155	0.258
	MISR	0.366	0.186	0.283	0.276	0.176	0.127	0.178	0.564	0.086	0.138	0.106	0.576	0.269
	PARASOL	0.381	0.21	0.295	0.286	0.158	0.144	0.226	0.566	0.094	0.152	0.112	0.294	0.478
	SEVIRI	0.273	0.156	0.329	0.288	0.155	0.113	0.205	0.518	0.11	0.132	0.1	0.188	0.261
ρ	Prior	0.256	0.572	0.232	0.147	0.367	0.658	0.454	0.086	0.284	0.464	0.396	0.546	0.393
	MODIS/Aqua	0.465	0.67	0.384	0.307	0.379	0.716	0.589	0.439	0.465	0.463	0.665	0.532	0.452
	MODIS/Terra	0.468	0.685	0.357	0.28	0.393	0.718	0.569	0.432	0.458	0.447	0.669	0.496	0.472
	MISR	0.352	0.632	0.355	0.29	0.423	0.702	0.539	0.436	0.406	0.434	0.649	0.556	0.43
	PARASOL	0.274	0.635	0.374	0.308	0.403	0.676	0.537	0.434	0.406	0.431	0.647	0.382	0.205
	SEVIRI	0.486	0.676	0.286	0.348	0.415	0.681	0.495	0.406	0.461	0.43	0.683	0.274	0.484

Table 5.3: Statistics of the analyses against AERONET 500-nm AOD for selected sites. The acronym m.a.s.l. stands for meters above sea level, RMSE for root mean square error and ρ is the Pearson correlation coefficient.

5.2 About the linear approximation

In our assimilation system, the optimality of the analysis relies on the assumption of the linear approximation of Equation (3.1.2), that we recall here:

$$H(\mathbf{x}) \approx H(\mathbf{x}^b) + \mathbf{H}(\mathbf{x} - \mathbf{x}^b) \quad . \tag{5.2.1}$$

In this section, we will compare the AOD simulated by the fully non-linear observation operator (H) and by the linear approximation of the observation operator. For this purpose, we take advantage of the already computed non-linear simulations of Section 5.1, that is, the non-linear observation operator evaluated in the analysis for the five experiments (which correspond to the five assimilated satellite retrievals). These AODs are compared with the linear approximations of the observation operator (Equation (5.2.1)) as can be seen in Figure 5.6.

Figure 5.6 shows the comparison of both observation operators, when they are evaluated for (five) different values of the control vector. We have used only the AODs over the Arabian Peninsula, North Africa and the neighbouring Atlantic Ocean (blue rectangle of Figure 4.2). As expected, the correlation coefficient in the figures is almost unity, and the slope and intercept of the linear regression are close to one and zero, respectively. Most of the matchups are close in the 1:1 line, indicating that the linear approximation is excellent in our inversions.

A second view of this comparison is shown in Figure 5.7. On this figure we intend to show how large the errors made by the linear approximation are, as a function of the distribution of the errors percentiles. In general, for the five analyses, the absolute error of the linear approximation is less than 0.01 for 80% of the AOD. While both MODIS experiments and the SEVIRI experiment share a similar curve in the absolute error of Figure 5.7, the PARASOL experiment has larger errors. This could be due to the larger analysis values of this experiment as compared to the rest of the assimilations, thus the linear approximation (which is local by nature), will have larger errors. The upper right panel of Figure 5.7 is a zoom over the larger values on the x-axis. It shows, for example, that 3% of the AOD approximations have errors larger than 0.02 for MODIS/Aqua, MODIS/Terra and SEVIRI, while this value is reached for 1% of the AOD in the MISR experiment and for more than 5% of the AOD in the PARASOL experiment.

The lower panels of Figure 5.7 show the same error as the upper panels, but relative to the AOD (i.e., relative error). Similarly, larger errors are found in the PARASOL experiment, both MODIS assimilations have similar errors and the MISR experiment has lower errors.

It is not worth showing monthly (or even daily) maps of AOD for the two AOD computations since their differences are hardly perceptible in a color scale. However, we show in Figure 5.8 a comparison of both approximations against AERONET observations for the MODIS/Aqua experiments. We have chosen the same stations selected in Chapter 4. It can be seen that the AOD simulated by the linear approximation is similar to the AOD simulated by the non-linear observation operator, for almost all the time series. Small differences can be appreciated in the

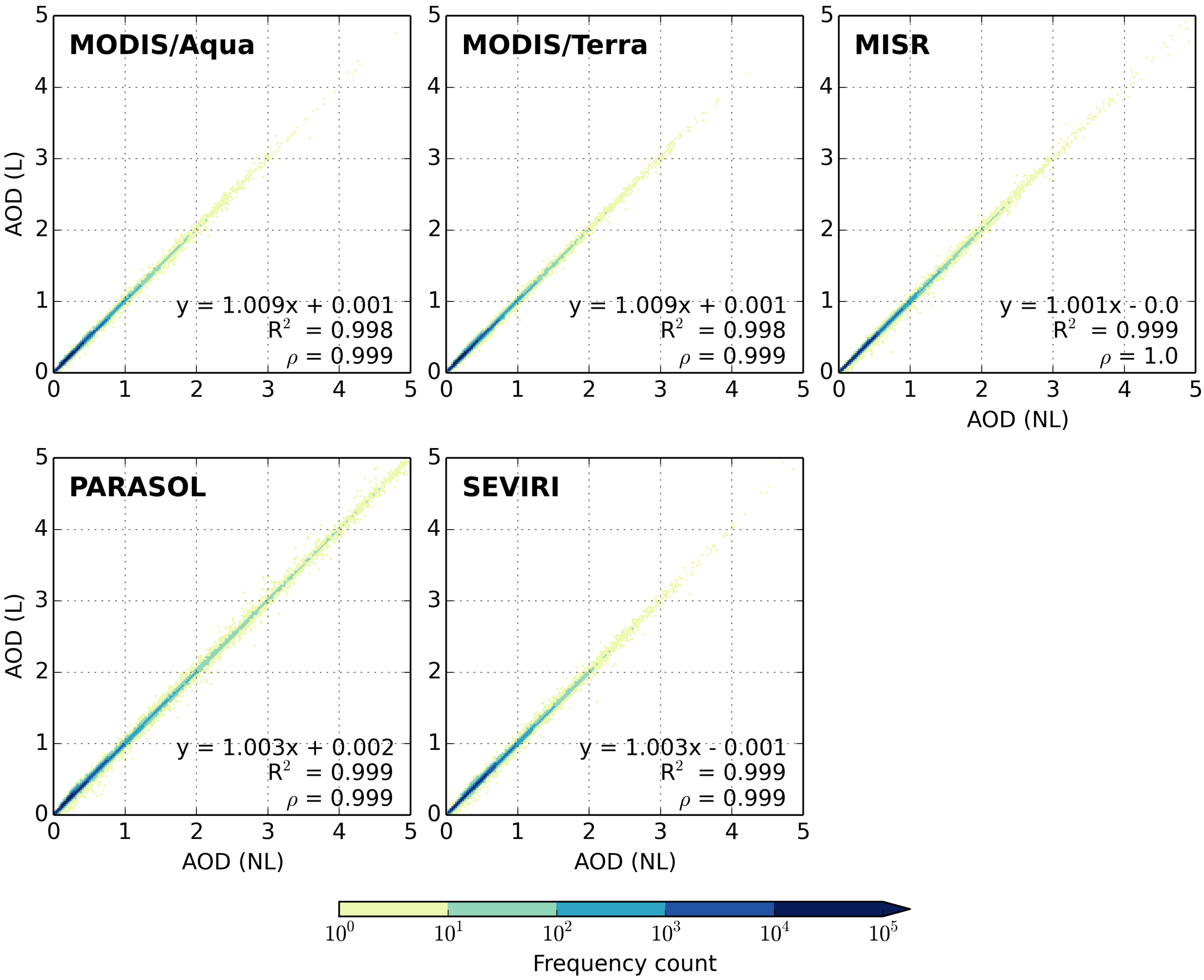

Figure 5.6: Frequency plots comparison between non-linear (NL) and linear (L) simulated AODs. The panels correspond to the analyses of the assimilated satellite experiments described in Section 5.1. The two-dimensional histograms are made of 200 bins, so the color scale indicates the quantity of matchups between the NL and L AOD in a range of $\Delta AOD = 0.025$. In each panel we also indicate the linear regression fit, the R^2 determination coefficient of the regression and the Pearson correlation coefficient (ρ) between the two simulated AODs. Please note the logarithmic color scale.

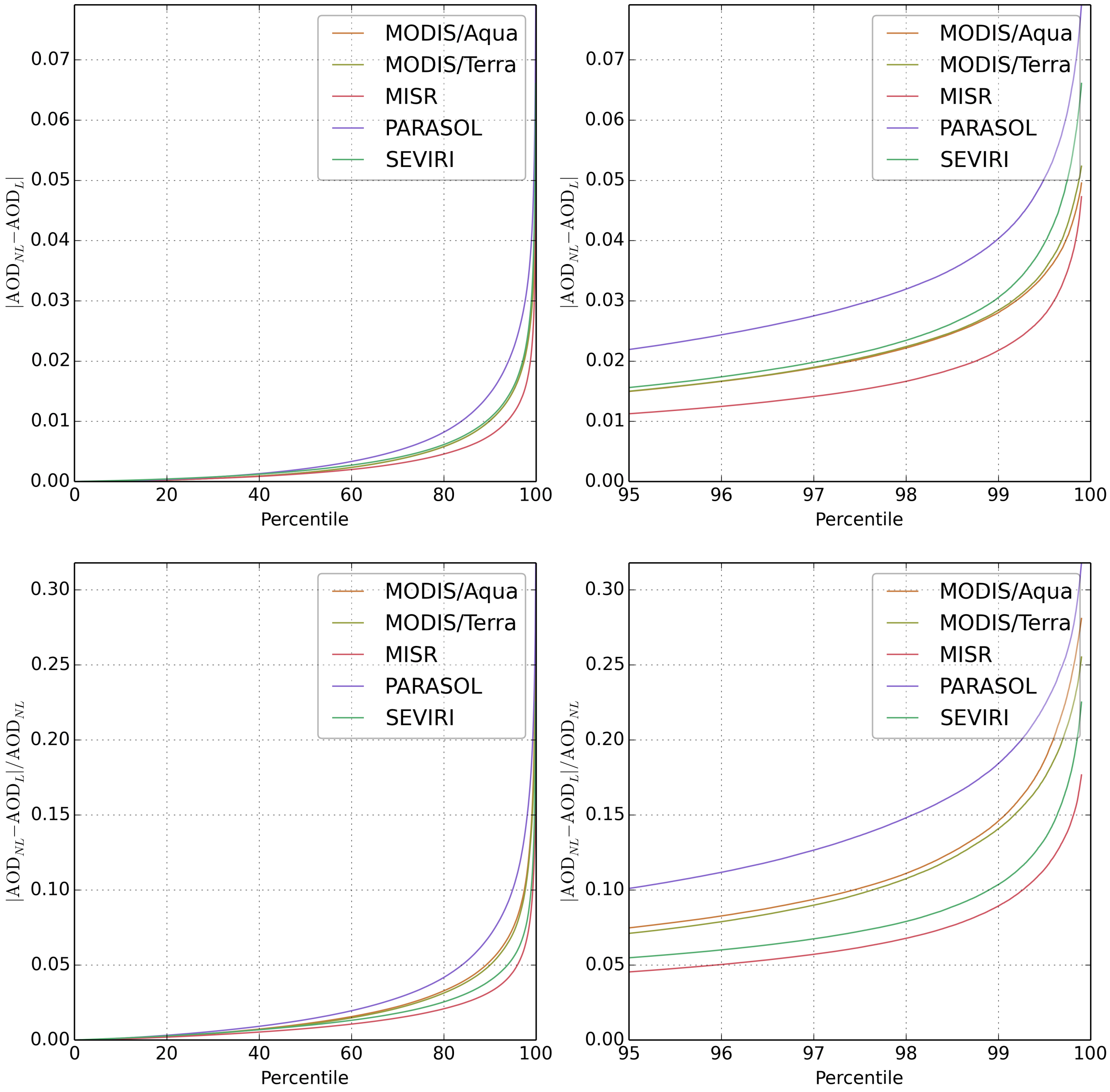

Figure 5.7: Absolute and relative errors of the linear approximation. On the x-axis is shown the percentile of the distribution for the absolute error (upper panels) and for the relative error (lower panels). AOD_{NL} and AOD_L stand for AODs computed with the non-linear and linear observation operators, respectively. Panels on the right column show a zoom of the left column panels for the tail of the distribution of the approximation errors.

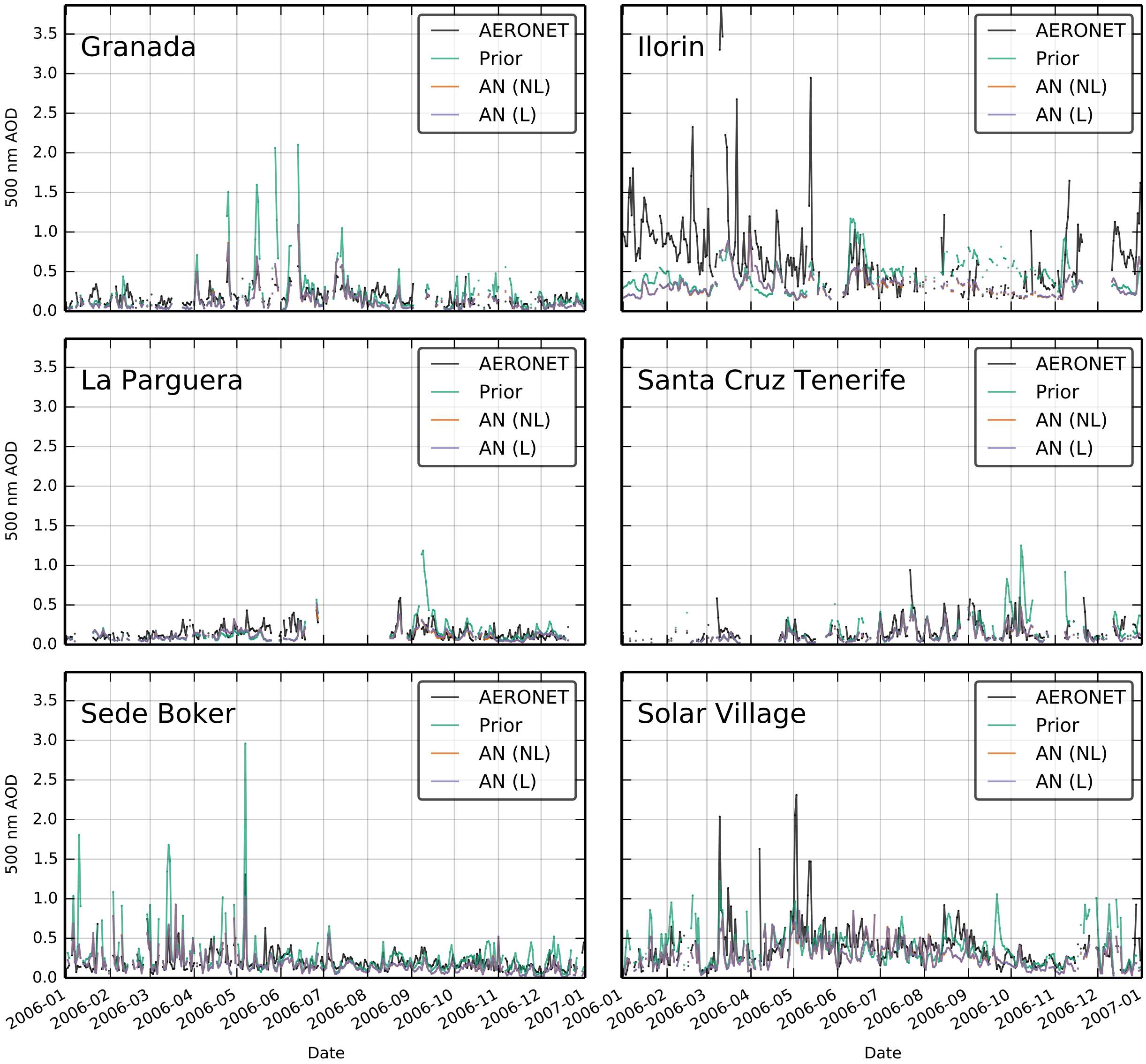

Figure 5.8: Model/AERONET comparison over 6 selected AERONET sites. Time series of AERONET 500 nm AOD (in black) and the three simulations with the prior simulation in green, the non-linear analysis simulation in orange (AN (NL)) and the linear simulated AOD in purple (AN (L)). The simulations correspond to the MODIS/Aqua experiment of Section 5.1. The name of each AERONET station is indicated on each panel. Simulated AOD is shown only for days when AERONET reports valid data.

La Parguera and Ilorin panels.

Even though this cannot be considered a strict evaluation of the quality of the linear hypothesis, we think that this hypothesis is good enough for our needs.

5.3 Coarse and fine AOD assimilation

In this section we will present an alternative way to assimilate the size distribution information content of the observations. In Chapter 4, we have only assimilated total AOD, while in Section 5.1 of this chapter we have included the fine AOD reported by the satellite retrieval, when it is available.

In principle, the assimilation of total AOD and fine AOD should be, more or less, equivalent to assimilating the coarse AOD and fine AOD. For the satellite products used in this thesis, the reported fine AOD is associated to the contribution of AOD from the fine mode aerosol models to the total AOD in the satellite retrieval algorithms. For MODIS, PARASOL and MISR, fine and total AOD are retrieved simultaneously from the same radiance measurements, and the total AOD is computed as the sum of the AOD due to the fine and coarser aerosol models fitted by the algorithms. We think that total AOD and fine AOD errors could be correlated, even though we have assumed that they are not correlated in Section 5.1. This assumption was made because we do not have any information about these correlations. For the same reason, we can alternatively choose to assimilate coarse AOD and fine AOD instead of total AOD and fine AOD. Correlations between coarse and fine AOD errors could still exist, but no information about them is provided by the retrieval teams. From this perspective, it would be possible (and equivalent) to consider the total AOD as the sum of coarse and fine AOD. However, the most important advantage of assimilate total and fine AOD instead of coarse and fine AOD is the availability of the error statistics (only for total AOD) and the documented validation of the (total) AOD products by the scientific community.

As the coarse AOD is not a standard product of the retrieval algorithms (excepted MISR), we could roughly understand as coarse AOD the difference between the total and fine AOD. In terms of the model AOD, the observational coarse AOD is compared to the (simulated) total AOD minus the (simulated) AOD attributed to fine mode aerosols; or equivalently, the sum of the coarse dust, super-coarse dust and coarse sea spray contributions to the AOD of the SPLA model.

The main goal of this section is to evaluate the arbitrary decision of assimilating total–fine AOD versus the, also arbitrary, decision of assimilating coarse–fine AOD. The differences will be presented in the same way as in Section 5.1, that is, by the analysis AOD spatial field, comparisons with AERONET measurements and dust flux estimates. At this point, we will anticipate that this comparison will be not consistent, but the results presented in this section are still valid independently from Section 5.1, or in other words, as an *alternative* to the work presented in

	Land			Ocean		
	Fine	Coarse	Total	Fine	Coarse	Total
MODIS/Aqua			X	X		X
MODIS/Aqua-fc			X	X	X	
MODIS/Terra			X	X		X
MODIS/Terra-fc			X	X	X	
MISR	X		X	X		X
MISR-fc	X	X		X	X	
PARASOL	X			X		X
PARASOL-fc	X			X	X	
SEVIRI			X			X

Table 5.4: Summary of the assimilated observations used in this Section (tagged with “fc”); and the assimilated observation of Section 5.1.

Section 5.1.

The configurations of the observation operator and of the assimilation system are the same as in Section 5.1. The only changes with respect to Section 5.1 are the assimilated observations and their error statistics. The assimilated observations are as described below, that is, instead of assimilating total AOD, we try to assimilate coarse AOD. This can be done only if it is possible to compute the coarse AOD, that is, when total and fine AOD are available. If fine AOD is not available, we assimilate total AOD. We summarize the assimilated AOD, for each dataset, in Table 5.4. Hereafter we tag these experiments with the “fc” label.

As is shown in Table 5.4, the SEVIRI dataset does not report fine AOD, so we will exclude this dataset in this section. For MISR, it is possible to compute coarse AOD over land and ocean, while for the MODIS product it is only possible to compute the coarse AOD over ocean because the fine AOD over land is not reported in their standard products. PARASOL only retrieves fine AOD over land, but over ocean it is possible to compute the coarse AOD along with the reported fine AOD.

One of the issues on using coarse AOD instead of total AOD is that the coarse (as well as the fine) AOD usually are not validated by the retrieval teams. Consequently, they lack a description of the statistics of their observational errors. In Section 5.1 we have handled this issue by defining the fine AOD errors using the same total AOD error definitions (described in Table 5.1). In this section, we keep the same assumptions for the fine AOD; and we define the coarse AOD errors statistics following the same assumptions, that is, by using the error characterization of total AOD of Table 5.1. We note here that this is our best guess of the observational error descriptions for fine and coarse AOD, but it is likely that this assumption do not hold.

Before presenting the assimilation results, we would like to justify why the assimilations performed in Section 5.1 cannot be directly compared with those performed here. The main reason is due to the definition of the observational errors. Both definitions would be inconsistent if we put them together, as we will briefly show with the following example. For a given instrument (e.g., MODIS/Aqua), the total retrieved AOD will be notated by τ_t. This is, in our framework, an estimate of the *true* total AOD in the observation space (τ_t^t) with an unbiased error ε_t, as:

$$\tau_t = \tau_t^t + \varepsilon_t \quad .$$

By our definitions of coarse and fine AOD, the following relations have to be fulfilled:

$$\begin{aligned} \tau_c &= \tau_c^t + \varepsilon_c \quad , \\ \tau_f &= \tau_f^t + \varepsilon_f \quad , \\ \tau_t &= \tau_f + \tau_c \quad , \\ \tau_t^t &= \tau_f^t + \tau_c^t \quad , \end{aligned}$$

where the subscript c stands for coarse AOD, f for fine AOD, the superscript t for the *true* AOD and ε for their errors.

Now we will include the errors defined in Table 5.1. We can write the MODIS errors as $\mathrm{Var}(\varepsilon^o) = (a\,\tau + b)^2$, for two constants a and b. The consistency between the error definitions from Section 5.1 and those from this section is quantified by the conservation of the error budget, which at the end is the conservation of the quantity of information contained in the observational errors. We will now show that if we simultaneously assume that fine, coarse and total observational AOD errors are estimated with the same values of Table 5.1, and additionally that the errors between total and fine AOD are uncorrelated, the variance of the errors is not, in general, conserved. More precisely, we will give a necessary (but not sufficient) condition for which the variance of the errors is conserved, which is not physically achievable for all cases.

First, we will note that:

$$\tau_t^t = \tau_f^t + \tau_c^t \quad ,$$

then,

$$\varepsilon_t = \varepsilon_f + \varepsilon_c \quad ,$$

so,

$$\mathrm{Var}(\varepsilon_t) = \mathrm{Var}(\varepsilon_f + \varepsilon_c) \quad .$$

We include now the assumption of uncorrelated errors between fine and total AOD used in

Section 5.1:

$$\begin{aligned} 0 = \operatorname{Cov}(\varepsilon_t, \varepsilon_f) &= \operatorname{Cov}(\varepsilon_c + \varepsilon_f, \varepsilon_f) \\ &= \operatorname{Var}(\varepsilon_f) + \operatorname{Cov}(\varepsilon_c, \varepsilon_f) \\ \implies -\operatorname{Var}(\varepsilon_f) &= \operatorname{Cov}(\varepsilon_c, \varepsilon_f) \\ \implies \operatorname{Var}(\varepsilon_f)^2 &= \operatorname{Cov}(\varepsilon_c, \varepsilon_f)^2 \\ &\leq \operatorname{Var}(\varepsilon_c)\operatorname{Var}(\varepsilon_f) \end{aligned}$$

where the last step is due to the Cauchy-Schwarz inequality. We will assume that $\operatorname{Var}(\varepsilon_f)$ is strictly positive, then:

$$\operatorname{Var}(\varepsilon_f) \leq \operatorname{Var}(\varepsilon_c) \quad .$$

Now we assume that the error standard deviation is in the form of $a\tau + b$, with a and b positive (or zero) values. Then:

$$a\tau_f + b \leq a\tau_c + b \quad .$$

If $a > 0$ then the following condition is needed:

$$\tau_f \leq \tau_c \quad ,$$

which does not necessarily hold in realistic situations.

In the previous lines we have shown one necessary (but not sufficient) condition that have to be met in order to conserve the variance of the errors within our hypotheses, but there could exist other (maybe more restrictive) conditions that make a straightforward comparison between the results from this section and those from Section 5.1 incompatible.

5.3.1 Results

We have performed the four “fc” experiments (Table 5.4) with the same configuration of the observation operator and the assimilation system described in Section 5.1, except for the observations. Figure 5.9 shows the average analysis AOD for the four experiments. For practical reasons, in this section we use the linear version of the model (cf. Section 5.2). Similarly to Section 5.1, the analyses decrease the AOD in the northern part of the African continent in th MAM and JJA panels. Both MODIS analyses are qualitatively similar, while the PARASOL analysis shows larger AOD values over land, with maximum values in MAM and JJA. A small difference with respect to the AOD maps presented in Section 5.1 is the MISR AOD in comparison with MODIS AOD. In Figure 5.9, MISR analysis AOD is, in general, smaller than both MODIS analyses AOD, while in Section 5.1 MISR AOD is larger than those from MODIS analyses.

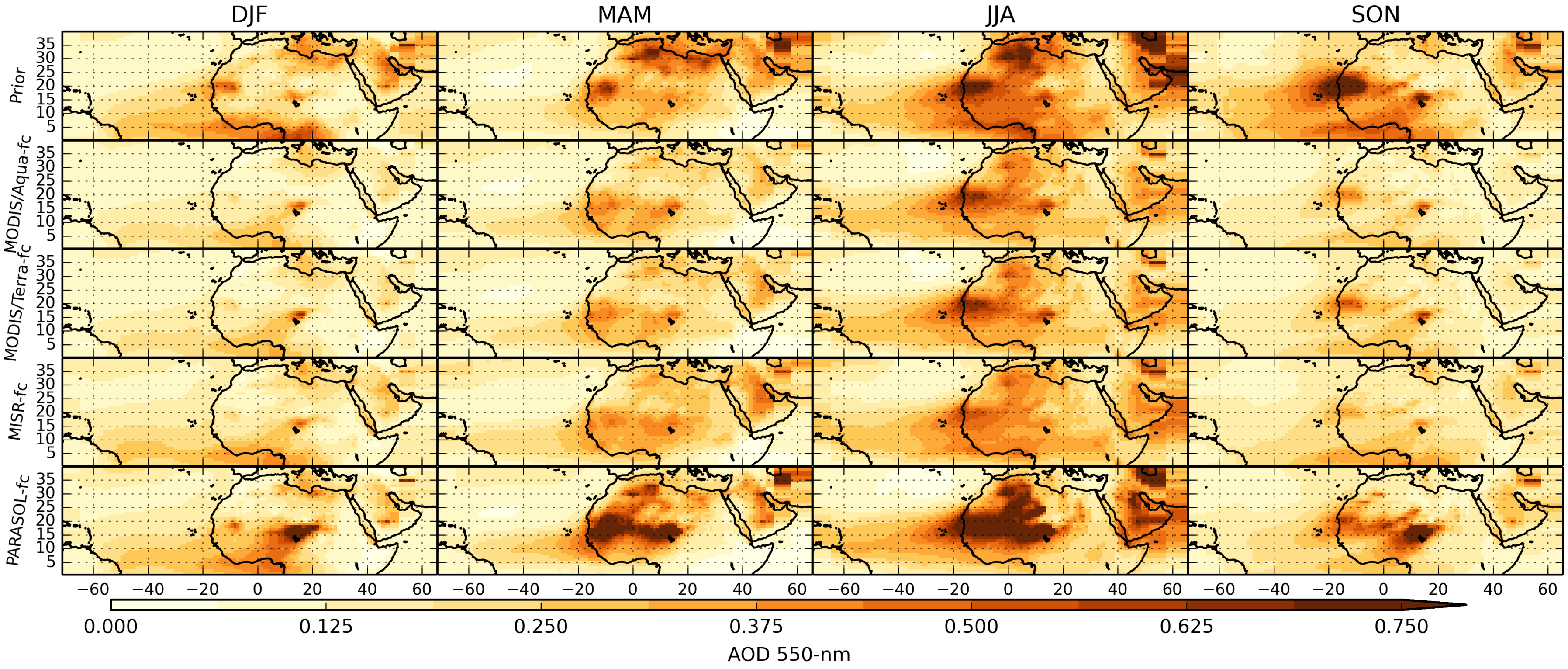

Figure 5.9: Simulated 550 nm AOD for the “fc” experiments (rows), averaged over groups of months of the year 2006 (columns). In the head of the columns, MAM stands for March, April and May; JJA for June, July and August; SON for September, October and November; and DJF for December, January and February.

We summarize the estimated analyses flux for mineral dust in the region of study in Table 5.5. Following the same arguments presented in Section 5.1, we will exclude the PARASOL experiment from our dust fluxes estimates. For the rest, the total dust flux ranges between 1800 and 2850 Tg year^{-1} for the year 2006. Unlike Section 5.1, the lower bound is due to the MISR analysis and MODIS/Terra is the upper bound of our estimates. In consistency with Chapter 4 and Section 5.1, the analysis fluxes are smaller than the prior dust flux.

The last figure shown is this section is Figure 5.10. Like in Figure 5.5, all the analyses share a similar dust emission seasonal cycle. For fine and coarse emissions, the analyses are, in general, smaller than the prior for all months except July. Only for information, the main statistics on the comparison with AERONET AOD at 500 nm are shown in Table 5.6. Qualitatively, the analysis AOD for these experiments is roughly similar to the one presented in Section 5.1 when it is compared against AERONET measurements. Even though the MISR experiment reports almost the half of the emission fluxes, the AOD coincident with AERONET is slightly smaller, leading to a larger (in absolute value) bias; but the root mean square error is decreased.

	Prior	MODIS/Aqua-fc	MODIS/Terra-fc	MISR-fc	PARASOL-fc
Total AP+Africa	6657	2375	2851	1799	14183
Total Africa	4085	2018	2333	1230	10186
Total AP	2571	357	519	569	3997
Total Africa West	3161	1234	1471	710	6744
Total Africa East	924	784	861	521	3442
Fine and Coarse AP+Africa	1087	693	740	773	922
Fine and Coarse Africa	709	477	523	531	579
Fine and Coarse AP	378	216	217	243	344
Fine and Coarse Africa West	526	311	329	334	380
Fine and Coarse Africa East	183	165	194	197	199
Super-coarse AP+Africa	5570	1682	2112	1025	13260
Super-coarse Africa	3376	1541	1810	700	9607
Super-coarse AP	2193	141	302	326	3653
Super-coarse Africa West	2635	923	1142	375	6364
Super-coarse Africa East	741	619	668	324	3243

Table 5.5: Total emission flux by region and by observational dataset for the year 2006 in Tg year^{-1}. AP stands for Arabian Peninsula. Western Africa refers to the longitudinal band between the Atlantic coast and approximately 16°E corresponding to regions 01 to 09 in Figure 4.1. East Africa refers to regions 10 to 16 in Figure 4.1, that is, to a longitudinal band between approximately 16°E and the Red Sea.

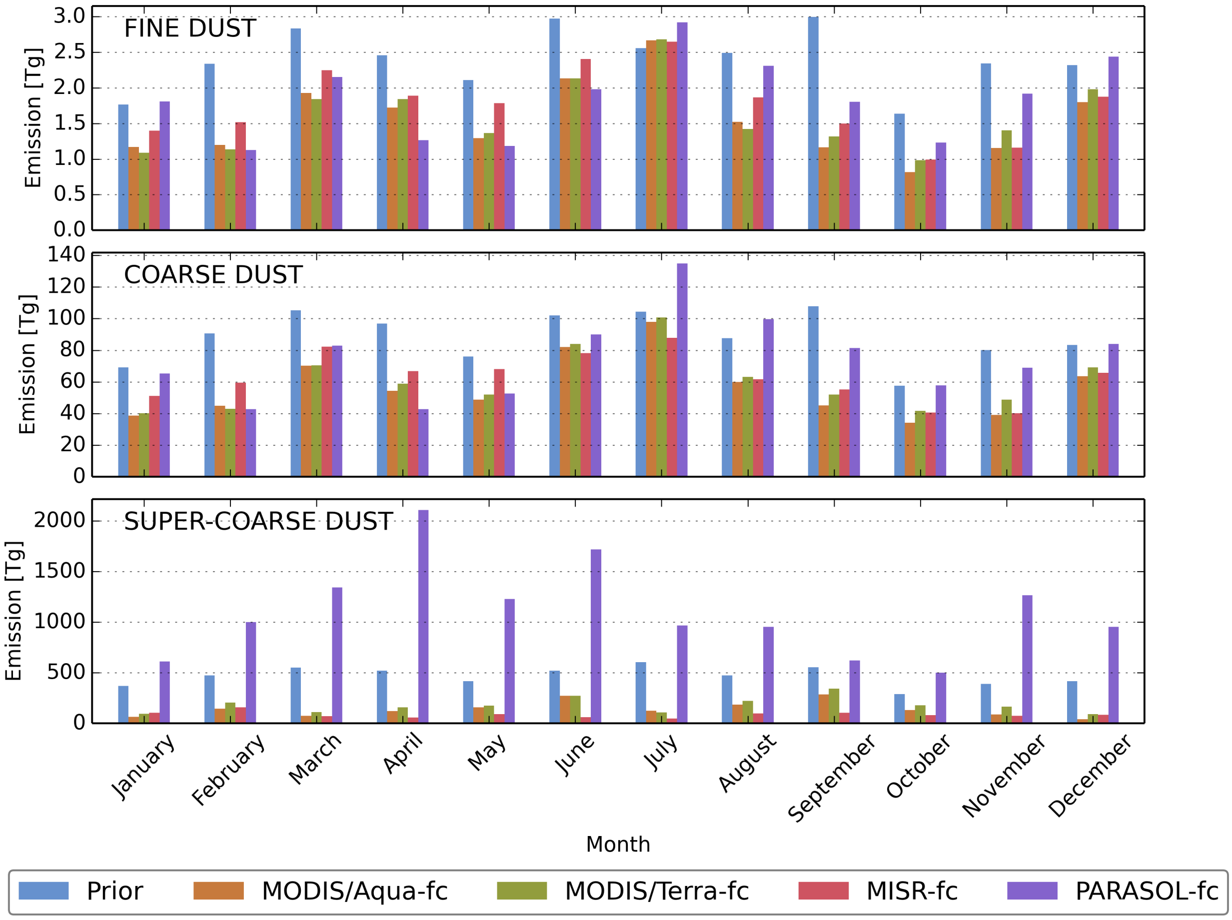

Figure 5.10: Total dust flux per month over the Sahara and the Arabian Peninsula for the experiments of this Section. Fine mode dust is shown in the first panel, coarse mode dust in the middle panel and super-coarse mode dust in the lower panel. The different bars show the total mineral dust flux over the Sahara and the Arabian Peninsula by experiment and month. The three plots use different scales.

Station		Bahrain	Blida	Dhabi	Dhadnah	Forth Crete	Granada	Hamim	Ilorin	La Parguera	Nes Ziona	Santa Cruz Tenerife	Sede Boker	Solar Village
Latitude (°N)		26.21	36.51	24.48	25.51	35.33	37.16	22.97	8.32	17.97	31.92	28.47	30.86	24.91
Longitude (°E)		50.61	2.88	54.38	56.32	25.28	-3.6	54.3	4.34	-67.05	34.79	-16.25	34.78	46.4
Elevation (m.a.s.l.)		25	230	15	81	20	680	209	350	12	40	52	480	764
N obs.		201	195	243	324	283	276	263	270	251	185	233	335	335
Mean	Obs.	0.433	0.258	0.434	0.404	0.196	0.177	0.314	0.705	0.148	0.226	0.171	0.200	0.372
	Prior	0.472	0.313	0.411	0.454	0.273	0.209	0.346	0.434	0.145	0.245	0.178	0.263	0.370
	MODIS/Aqua-fc	0.294	0.181	0.225	0.232	0.170	0.124	0.185	0.320	0.108	0.132	0.117	0.161	0.265
	MODIS/Terra-fc	0.300	0.190	0.226	0.231	0.175	0.128	0.185	0.327	0.108	0.138	0.124	0.179	0.280
	MISR-fc	0.384	0.212	0.283	0.292	0.218	0.153	0.241	0.373	0.137	0.195	0.142	0.257	0.353
	PARASOL-fc	0.383	0.192	0.303	0.320	0.152	0.118	0.244	0.407	0.102	0.116	0.136	0.182	0.394
Bias	Prior	0.040	0.056	-0.023	0.050	0.076	0.032	0.032	-0.271	-0.003	0.019	0.007	0.063	-0.002
	MODIS/Aqua-fc	-0.138	-0.076	-0.209	-0.172	-0.026	-0.053	-0.129	-0.385	-0.040	-0.094	-0.054	-0.039	-0.107
	MODIS/Terra-fc	-0.132	-0.068	-0.208	-0.173	-0.022	-0.049	-0.130	-0.378	-0.040	-0.087	-0.047	-0.021	-0.092
	MISR-fc	-0.048	-0.046	-0.152	-0.112	0.021	-0.024	-0.073	-0.332	-0.011	-0.031	-0.029	0.057	-0.019
	PARASOL-fc	-0.050	-0.066	-0.131	-0.084	-0.045	-0.059	-0.071	-0.299	-0.046	-0.110	-0.035	-0.018	0.022
RMSE	Prior	0.365	0.349	0.397	0.465	0.266	0.229	0.257	0.598	0.146	0.144	0.176	0.235	0.272
	MODIS/Aqua-fc	0.271	0.176	0.315	0.288	0.146	0.113	0.198	0.608	0.090	0.149	0.113	0.135	0.271
	MODIS/Terra-fc	0.271	0.177	0.317	0.291	0.150	0.116	0.200	0.608	0.090	0.150	0.109	0.173	0.267
	MISR-fc	0.293	0.178	0.274	0.252	0.169	0.114	0.169	0.586	0.089	0.134	0.108	0.474	0.252
	PARASOL-fc	0.304	0.213	0.301	0.283	0.164	0.143	0.205	0.564	0.103	0.165	0.113	0.278	0.446
ρ	Prior	0.256	0.572	0.232	0.147	0.367	0.658	0.454	0.086	0.284	0.464	0.396	0.546	0.393
	MODIS/Aqua-fc	0.459	0.670	0.379	0.290	0.382	0.702	0.590	0.423	0.452	0.451	0.672	0.498	0.432
	MODIS/Terra-fc	0.433	0.674	0.346	0.259	0.399	0.700	0.574	0.394	0.455	0.429	0.679	0.463	0.441
	MISR-fc	0.384	0.630	0.438	0.342	0.415	0.686	0.606	0.354	0.356	0.435	0.637	0.561	0.480
	PARASOL-fc	0.302	0.617	0.355	0.297	0.407	0.646	0.559	0.367	0.383	0.419	0.650	0.376	0.185

Table 5.6: Statistics of the analyses against AERONET 500 nm AOD for selected sites. The acronym m.a.s.l. stands for meters above sea level, RMSE for root mean square error and ρ is the Pearson correlation coefficient.

Chapter 6

Inversion with bias correction

6.1 Motivation

We mentioned in Chapter 4 the possibility of a discontinuity of the AOD field close to the Western North African coast. We recall here that it can be appreciated in Figure 4.4 for the MODIS AOD column between June and September. In these months, the AOD over the continent (close to the ocean) is larger than the AOD over ocean (close to the continent). This discontinuity can be also noticed in the yearly averages of Figure 5.1 for both MODIS products. We stated in that chapter that this discontinuity is not surprising, since MODIS retrievals are computed with different algorithms over land and ocean. We also mentioned that Levy et al. (2003) suspect an overestimation of dust AOD over ocean due to the assumption of spherical aerosols in the retrieval algorithm, that could lead to errors for the typical viewing geometry of the MODIS instrument [A. Sayer, personal communication]. On the contrary, MODIS Deep-Blue could underestimate AOD over the Saharan desert (Sayer et al., 2013).

All algorithms that retrieve AOD from passive radiance measurements of instruments on-board satellites basically share the same principles. The algorithms have to differentiate the contributions to the reflected radiance of the surface and the atmosphere, in order to calculate the AOD. The strong differences between land and ocean reflectance properties, and the use of different algorithms over land and ocean, lead us to think that all assimilated observations would present this kind of problem at some degree.

For MODIS products, the dataset described in Zhang and Reid (2006) and Hyer et al. (2011) is available for operational purposes. This product is specially designed for data assimilation, and it consists in MODIS level 2 visible AOD, after a strict cloud screening process and an *offline* bias correction. The bias correction algorithm was based on the comparison between MODIS AOD and AERONET AOD. The last version of the MODIS-NRT product is based on an older version of the MODIS product (Collection 5). Instead, in this work, we prefer the latest MODIS Collection 6 retrievals: thus we do not use this product in this chapter. We are not aware of the availability of this kind of products for other satellite retrievals.

Biases are the *black beast* of all assimilations systems. Throughout this thesis we have assumed that both the prior and the observations are unbiased. This is an usual assumption in data assimilation, that does not necessarily hold that well. In this chapter we explore the possibility to perform an *online* bias correction of the AOD observations.

6.2 Cost function with bias correction

Once more time, we recall the cost function minimized in Chapters 4 and 5:

$$J(\mathbf{x}) = \frac{1}{2}(\mathbf{x}-\mathbf{x}^b)^T\mathbf{B}^{-1}(\mathbf{x}-\mathbf{x}^b) + \frac{1}{2}(\mathbf{y}-H(\mathbf{x}))^T\mathbf{R}^{-1}(\mathbf{y}-H(\mathbf{x})) \quad . \tag{6.2.1}$$

We aim to include a bias correction term in the cost function. Unless it is stated otherwise, we assume that the bias is only due to the observations. The new cost function is defined as:

$$\begin{aligned} J(\mathbf{x},\beta) =& \frac{1}{2}(\mathbf{x}-\mathbf{x}^b)^T\mathbf{B}^{-1}(\mathbf{x}-\mathbf{x}^b) \\ &+\frac{1}{2}(\mathbf{y}-\mathbf{b}(\beta,\mathbf{y})-H(\mathbf{x}))^T\mathbf{R}^{-1}(\mathbf{y}-\mathbf{b}(\beta,\mathbf{y})-H(\mathbf{x})) \\ &+\frac{1}{2}(\beta-\beta^b)^T\mathbf{B}_\beta^{-1}(\beta-\beta^b) \quad , \end{aligned} \tag{6.2.2}$$

where $\mathbf{b}$ is a bias function depending on parameters β and $\mathbf{B}_\beta$ is the error covariance matrix of the β parameters of the bias function. The observation operator is linearized around the background control vector as:

$$H(\mathbf{x}) = H(\mathbf{x}^b) + \mathbf{H}(\mathbf{x}-\mathbf{x}^b) \quad ,$$

with $\mathbf{H}$ the Jacobian of the observation operator evaluated in $\mathbf{x}^b$. The bias correction is noticed in Equation (6.2.2) by the inclusion of the correction term in the observational departures ($\mathbf{b}(\beta,\mathbf{y})$) and by the inclusion of a prior for the β variable (with the corresponding covariance matrix of its errors, $\mathbf{B}_\beta$). The *online* character of this correction is clear from the left side of the equation: the cost function depends on both the control vector and the β variable at the same time.

The bias correction is designed here as a multiplicative factor of the observations with only two values, one value for observations over land and the other for observations over ocean, i.e., $\beta = (\beta_{\text{land}}, \beta_{\text{ocean}})$. This is justified by the use of different retrieval algorithms and different surface types over land and ocean, as discussed above. The bias function $\mathbf{b}$ is therefore defined as:

$$\mathbf{b}(\beta, \mathbf{y}) \;=\; (\beta_i\, \mathbf{y}_i)_{i=1\ldots p} \quad ,$$

where p is the number of observations, i is the i-th element of the vector $\mathbf{y}$, β_i is equal to β_{land} if the observation $\mathbf{y}_i$ is over land and β_i is equal to β_{ocean} otherwise. In other words, β are homogeneous multiplicative factors of the assimilated observations, with one value for the retrievals over land and another one over ocean.

To avoid unrealistic negative emission fluxes, we have imposed a non-negativity constraint over $\mathbf{x}$ (i.e., $\mathbf{x} \geq 0$). Given the definition of the control vector as correction factors for the emissions, the minimum of the second term of the cost function (the observational term) of Equation (6.2.2) is reached when $\mathbf{x} = 0$ and $\beta = 1$ component-wise. This would mean that $\mathbf{y} - \mathbf{b}(\beta, \mathbf{y}) = 0$ and $H(\mathbf{x}) = 0$. To avoid this unphysical solution of the minimization, we assume that the overall average of the bias function is zero, i.e., we assume that the bias is compensated between land and ocean. We include the additional constraint over β:

$$\sum_{i=1}^{p} \beta_i\, \mathbf{y}_i\, \delta_i = 0 \quad ,$$

where the constraint is active only in a subset of the observations defined by the delta function δ_i. The subset depends on the observation dataset used. As a general rule, when the observational dataset reports values of the same type over land and ocean then $\delta_i = 1$ and $\delta_i = 0$ otherwise. For example the MODIS merged product (Collection 6) reports data of total AOD over land and ocean, so for total AOD $\delta_i = 1$, while $\delta_i = 0$ for fine mode AOD due to the lack of this product over land. For the sake of simplicity, we have omitted the grid-box size in this constraint formulation. However, each term should be weighted by the grid area in a more accurate formulation.

Similarly to the previous experiments, the prior value of $\mathbf{x}$ is set to unity. For the bias correction variable, the prior of β is zero.

6.3 Implementation

The minimization of the cost function in Equation (6.2.2) is to some extent similar to the minimization of the cost function in Equation (6.2.1). The most important difference is that this new cost function is not convex. Following the same arguments presented in Section 3.3.2, we have written the cost function (and its derivatives) in a similar way to the Equation (3.3.4) but including the bias term. We do not to explicitly show this formulation in this chapter.

In Section 3.3.2 we solved the minimization problem by using a numerical solver designed for convex problems. In this case, as the function is not convex, we use the more general nonlinear minimization solver L-BFGS-B (Zhu et al., 1997). This algorithm allows including bounds in the control vector (and the bias variable β), however, in our case the use of bounds in this solver will not allow the use of the preconditioning $\mathbf{L}$ of Section 3.3.2. Without preconditioning, the minimizer usually cannot find the optimum value, so we decided to keep $\mathbf{L}$ and, instead of using the *bounds* capability of the numerical solver, we include the constraints in the cost function with a quadratic penalty function. The cost function with penalty term writes:

$$\tilde{J}_M(\mathbf{x},\beta) \;=\; J(\mathbf{x},\beta) + M\,P(\mathbf{x},\beta) \quad , \tag{6.3.1}$$

with M a positive real value, and P the penalty function, which is zero when the constraint are fulfilled and positive if not. We can decompose this penalty function into two functions, which correspond to the constraints over the control vector and over the bias variables:

$$P(\mathbf{x},\beta) \;=\; P_x(\mathbf{x}) + P_\beta(\beta) \quad ,$$

with

$$\begin{aligned} P_x(\mathbf{x}) \;&=\; \sum_{i\in D} \mathbf{x}_i^2 \quad \text{with } D = \{i \,\in\, \{1,2,\dots,p\} \;:\; \mathbf{x}_i < 0\} \quad , \\ P_\beta(\beta) \;&=\; \frac{1}{p}\left(\sum_{i=1}^{p} \beta_i\,\mathbf{y}_i\,\delta_i\right)^2 \quad , \end{aligned}$$

where $1/p$ is only used as a normalizing factor for the penalty term associated to the bias variables. The parameter M controls the accepted tolerance in violating the constraints. Theoretically, if $M = \infty$ the optimal value of the (unconstrained) minimization of Equation (6.3.1) will be inside the feasible domain (of the constrained optimization problem). However, if M is large, the cost function will have a large slope close to the borders of the feasible domain, which pose problems to the numerical solver. In practice, we did not find any adequate M parameter that could be useful for a straightforward minimization of Equation (6.3.1). Instead, we solve the problem iteratively.

First, we define the starting point of the numerical solver as the prior. We consider a monotonically increasing sequence of M, let us say, $\{M_i\}_i$. For each M_i, we minimize the cost function:

$$\tilde{J}_{M_i}(\mathbf{x},\beta) \;=\; J(\mathbf{x},\beta) + M_i\,P(\mathbf{x},\beta) \quad ,$$

from which we compute the optimum value of $(\mathbf{x}_i^a, \beta_i)$. Then, we use this value as the starting point for the minimization of $J_{M_{i+1}}$, and so on.

In our minimization, we select a $\{M_i\}_i$ set of 15 values, ranging between 10^{-6} to 10, logarithmic-equally spaced. We have tested (not shown here) the performance of this minimization against the one described in Section 3.3.2, with the convex cost function defined in Section 3.3.2. Our tests indicates that this method (L-BFGS-B plus the sequence of M) reaches the same optimum value that the numerical solver used in Chapters 4 and 5, but it needs considerably more computing time. Other minimization approaches could be also tested (as for example interior-point methods) or we could replace the penalty function by a barrier function. However, we think that the method presented here is sufficient for our work.

6.4 Results

For this chapter we combined the inversion configuration from both Chapters 4 and 5. In the model space, we use the same control vector definitions of Chapter 4, that is, dust correction factors with a monthly resolution. In comparison with those of Chapter 5 (3 day resolution), the number of variables to minimize is affordable (ca. 500) with the method described in the previous section. In terms of observations, we consider the same observations than those of Chapter 5, that is, the retrievals of five instruments onboard the following satellites: MODIS/Aqua, MODIS/Terra, MISR, PARASOL and SEVIRI.

The covariance matrix of the observation errors is the same as in Chapter 5, that is, computed with the error estimates from the literature. In this chapter we do not use the diagnostics of the departures to compute inflation factors, as we expect to compare these results with those of Chapter 5. The covariance matrix of the background errors is also similar to the one described in Chapter 5. For the bias variable β, the covariance matrix of the β errors is assumed diagonal, with a standard deviation of 0.1. The temporal correlation length for the correlation of the background errors (Equation (3.2.3)) is fixed to 20 days; while the correlation ρ_c that accounts for correlations between correction factors errors between the same sub-region and sub-period, but different between categories of emissions (cf. Section 3.2.1) is fixed to $\rho_c = 0.7$.

In this section we will show some equivalent figures to those of Chapter 5, but with our adaptive bias correction. In first place, we show in Figure 6.1 the simulated AOD for the five experiments (equivalent to Figure 5.4). We can appreciate that, in general terms the simulated AOD is smaller than the one in Chapter 5. PARASOL and SEVIRI analyses do not show as large AOD as in Chapter 5, as the observations over land are strongly corrected by the bias term, so their large AOD over land is not as strong as in Chapter 5. We still can identify maximum values of AOD in the boreal summer, the local maximum of AOD near the Bodélé depression and the mineral dust plume over the Atlantic.

The above mentioned differences with respect to the previous chapter are mostly due to the inclusion of the bias correction term in the cost function. Table 6.1 shows the analysis β values, that is, the bias parameters for these experiments.

If we assume that all the bias comes from the observations, negative β values mean that the corresponding observations have to be increased and positive values mean that they have to

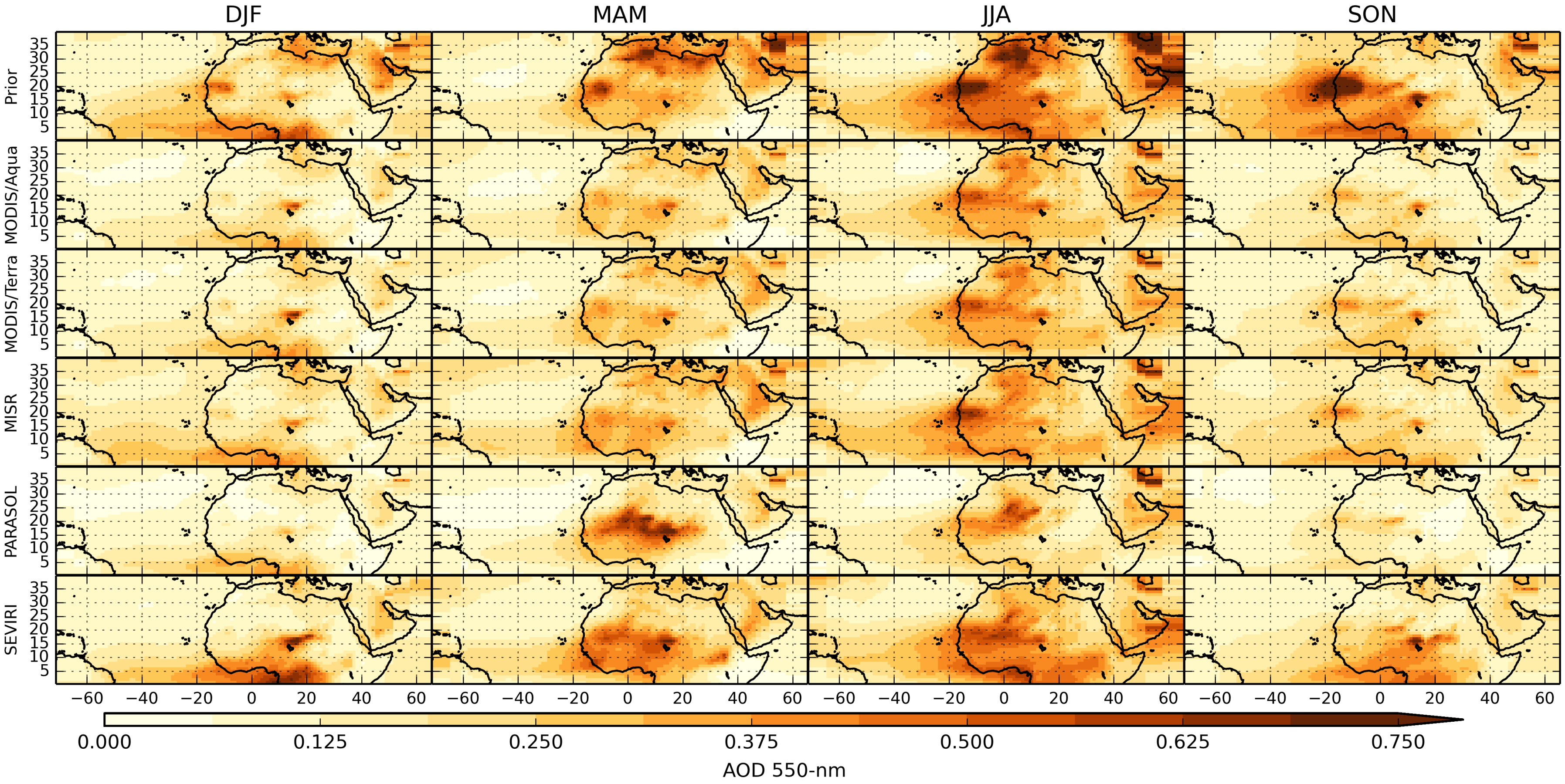

Figure 6.1: Simulated prior and analysis AOD at 550 nm for the 5 assimilation configurations with adaptive bias correction. The panels show the averaged AOD for each experiment (rows) over the months indicated in the head of the columns. MAM stands for March, April and May; JJA for June, July and August, SON for September, October and November and DJF for December, January and February. In the later we include the first two months and the last month of the year 2006.

	β_{land}	β_{ocean}
MODIS/Aqua	–0.16	0.24
MODIS/Terra	–0.13	0.21
MISR	0.06	–0.09
PARASOL	–0.39	0.49
SEVIRI	–0.33	0.37

Table 6.1: Adaptive bias results. Analysis of the β variables, which control the bias correction in the observational space.

	β_{land}	β_{ocean}
MODIS/Aqua-nS	–0.13	0.2
MODIS/Terra-nS	–0.11	0.18
MISR-nS	0.04	–0.06
PARASOL-nS	–0.36	0.45
SEVIRI-nS	–0.32	0.35

Table 6.2: Adaptive bias results, but with a fixed sea spray correction factor of 1.25.

be decreased. All experiments, except MISR, show negative β over land, and positive β over ocean. This means either an underestimate of AOD over land (or equivalently an overestimate over ocean), or an underestimate of the simulated AOD over ocean with respect to the AOD over land, or a combination of both factors. It is important to note that, for MODIS products, the β values of Table 6.1 are consistent with the above mentioned overestimation of AOD over ocean and underestimation of AOD over land.

At this point we have realized that the prior underestimates the AOD over ocean with respect to all the assimilated observations. This underestimation negatively impacts the bias correction analysis, as it assumes that the departures are due to observational biases. As the adaptive bias correction cannot differentiate between biases in the observation operator and errors in the observations, we have set the sea-salt bias correction to a 1.25 multiplicative factor, in order to have an unbiased estimate of the sea salt AOD in the model in dust-free regions and improve the performance of the bias correction for dust aerosols.

The computed β_{land} and β_{ocean} for these new experiments are shown in Table 6.2. Hereafter we have tagged these experiment with the “nS” label.

Even though the bias correction analysis in Table 6.1 are, in magnitude, smaller than those of Table 6.2, they are still very large. Values close to 0.1 would mean that, under our assumptions, the AOD retrieved is biased by 10%. For the cases of SEVIRI and PARASOL experiments, the biases computed by our system are estimated between 32% and 45%. We have already noticed, in Chapter 5, that the PARASOL assimilation experiment is not convincing because of the lack of total AOD over land. Based on the results shown in this chapter, the conclusions regarding this dataset still holds.

In term of fluxes, Figure 6.2 shows the estimated dust emission flux for the experiments

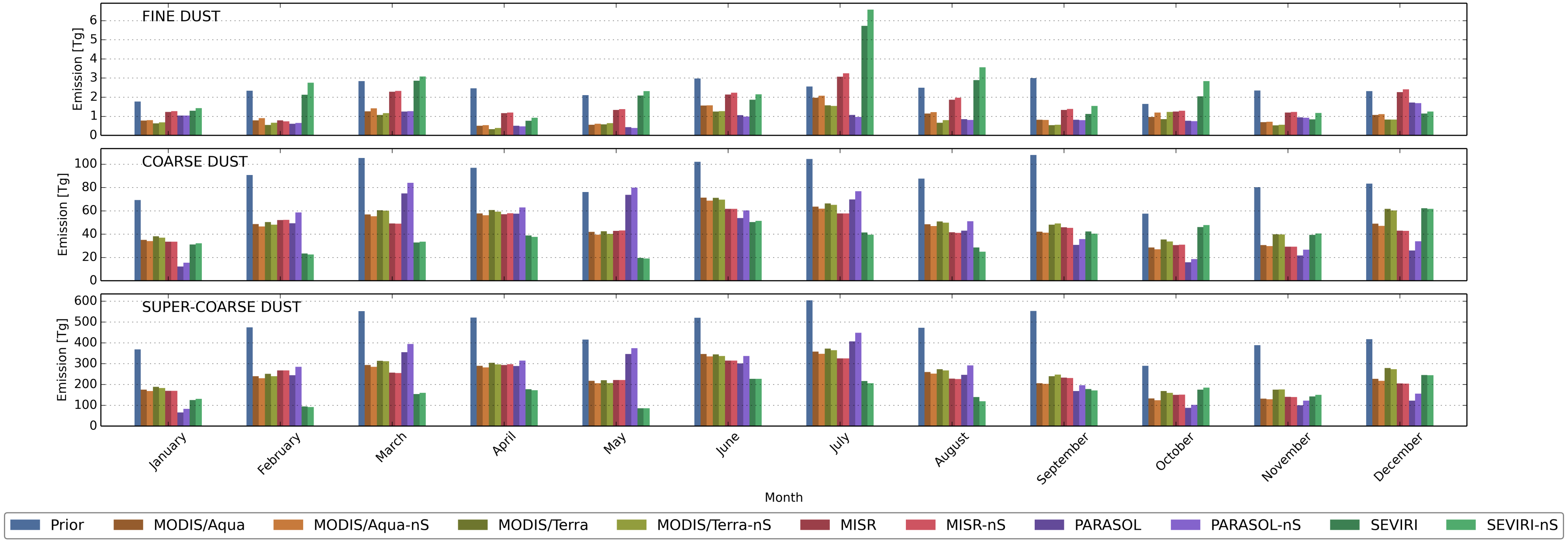

Figure 6.2: Total dust flux per month over the Sahara and the Arabian Peninsula. Fine mode dust is shown in the first panel, coarse mode dust in the middle panel and super-coarse mode dust in the lower panel. The different bars show the total mineral dust flux over the Sahara and the Arabian Peninsula by experiment and month. The three plots use different scales.

performed in this chapter. For each assimilated satellite, there is no strong difference in the dust emission flux between both analyses (one with sea spray correction factor in the control vector, and the other without sea spray correction, and with a prior of 1.25 on this control vector element). In comparison with the experiments without bias correction (previous chapters), the emissions computed in this chapter are, in general, of the same magnitude. The large emissions of the super-coarse dust for the PARASOL experiment of Chapter 5 are drastically decreased in this experiments. This is mainly for two reasons. In first place, in Chapter 5 we had two categories of dust correction factors: one for fine and coarse dust emissions (lumped together) and other for super-coarse dust emissions. In this chapter, the two categories for dust correction factors are the coarse and the super-coarse dust emissions (lumped together), and fine mode dust; similar to the simulations of Chapter 4. Secondly, the large value of the analysis of the β_{ocean} variable, means that the effective AOD assimilated over ocean is almost the half of the AOD assimilated in Chapter 5 over ocean. As PARASOL lacks a total AOD product over land, the main piece of information about total AOD (that the inferred coarse and super-coarse emissions are aware of) to the assimilation system is due to the ocean AOD. To some extent, the assimilation of fine AOD over land could also impact the coarse dust emissions through the non-diagonal terms in the background error covariance matrix. Both reasons contribute to the fact that, at the end, the analysis control vector in the PARASOL experiment does not produce large emissions of super-coarse dust.

In the same way as Chapter 5, both datasets MODIS/Terra and MODIS/Aqua have similar performance. This is true in terms of bias corrections, dust flux seasonality and simulated AOD in the analyses.

In a more quantitative approach, the overall fluxes for the ten experiments are shown in Table 6.3. This time we have included the total dust emissions only, for the same geographical regions than in Chapter 5. It can be noticed that for each experiment, there are no large differences in the total fluxes between the two configurations of the assimilation system (with or without sea spray correction factor). MISR analysis emissions are 10 % larger than those of Chapter 5, but for the SEVIRI experiments, the total emissions are smaller. Most important differences can be found in the PARASOL experiment which estimates the total emission within the range of the estimated emission from the other experiments. Both MODIS experiments increase their emissions with respect to the Chapter 5 results (and Chapter 4 for MODIS/Aqua). We attribute this increase to the bias correction scheme which has, in the analysis, negative values of β_{land} thus the effective AOD assimilated by the system is larger over land, and lower over ocean than those assimilated in previous Chapters.

We finish this section by showing the statistics of the analysis AOD against AERONET measurements in Table 6.4. Most of the results stated in Chapters 4 and 5 regarding the AERONET validation still hold. We are referring to the reduction of the root square mean error, the increase of the bias of the analysis AOD with respect to the prior simulation, and the better performance of the Pearson correlation coefficient of the analyses with respect to the prior simulation. With respect to the bias, we show that the simulations performed in this chapter have, in general, a

	AP+Africa	Africa	AP	Africa West	Africa East
Prior	6657	4085	2571	3161	924
MODIS/Aqua	3422	2560	862	1656	904
MODIS/Aqua-nS	3313	2464	849	1597	867
MODIS/Terra	3730	2869	860	1842	1028
MODIS/Terra-nS	3657	2799	859	1806	993
MISR	3344	2241	1103	1454	787
MISR-nS	3348	2243	1105	1446	797
PARASOL	3193	1835	1357	1386	449
PARASOL-nS	3640	2122	1518	1509	613
SEVIRI	2408	2307	101	1392	916
SEVIRI-nS	2382	2264	118	1369	895

Table 6.3: Total emission flux by region and by observational dataset for the year 2006 in Tg year^{-1}. AP stands for Arabian Peninsula. Western Africa refers to the longitudinal band between the Atlantic coast and approximately 16°E corresponding to regions 01 to 09 in Figure 3.4. East Africa refers to regions 10 to 16 in Figure 3.4, that is, to a longitudinal band between approximately 16°E and the Red Sea.

larger bias than those from the previous chapters. This results indicate that the bias correction scheme implemented in this section would not be satisfactory, in the sense that the analyses presented here are more biased than those without the adaptive bias correction. In summary, our results indicate that for these experiments the model biases are more important than the observational ones. We will further explore with this idea in the next section.

Station		Bahrain	Blida	Dhabi	Dhadnah	Forth Crete	Granada	Hamim	Ilorin	La Parguera	Nes Ziona	Santa Cruz Tenerife	Sede Boker	Solar Village
Latitude (°N)		26.21	36.51	24.48	25.51	35.33	37.16	22.97	8.32	17.97	31.92	28.47	30.86	24.91
Longitude (°E)		50.61	2.88	54.38	56.32	25.28	-3.6	54.3	4.34	-67.05	34.79	-16.25	34.78	46.4
Elevation (m.a.s.l.)		25	230	15	81	20	680	209	350	12	40	52	480	764
N obs.		201	195	243	324	283	276	263	270	251	185	233	335	335
Mean	Obs	0.433	0.258	0.434	0.404	0.196	0.177	0.314	0.705	0.148	0.226	0.171	0.200	0.372
	Prior	0.472	0.313	0.411	0.454	0.273	0.209	0.346	0.434	0.145	0.245	0.178	0.263	0.370
	MODIS/Aqua	0.281	0.173	0.217	0.221	0.174	0.122	0.187	0.299	0.099	0.127	0.098	0.167	0.264
	MODIS/Aqua-nS	0.277	0.176	0.217	0.220	0.177	0.125	0.185	0.300	0.111	0.125	0.106	0.165	0.261
	MODIS/Terra	0.292	0.186	0.222	0.223	0.188	0.132	0.188	0.315	0.105	0.144	0.105	0.189	0.281
	MODIS/Terra-nS	0.290	0.188	0.224	0.223	0.190	0.134	0.188	0.316	0.116	0.141	0.112	0.186	0.278
	MISR	0.337	0.219	0.259	0.265	0.224	0.165	0.226	0.361	0.154	0.194	0.139	0.231	0.318
	MISR-nS	0.345	0.220	0.265	0.270	0.225	0.165	0.232	0.367	0.139	0.200	0.131	0.237	0.327
	PARASOL	0.249	0.123	0.194	0.198	0.132	0.087	0.160	0.252	0.072	0.104	0.076	0.124	0.240
	PARASOL-nS	0.263	0.130	0.204	0.208	0.136	0.092	0.167	0.266	0.086	0.105	0.088	0.128	0.253
	SEVIRI	0.303	0.193	0.266	0.254	0.207	0.149	0.244	0.476	0.141	0.185	0.109	0.212	0.329
	SEVIRI-nS	0.315	0.197	0.288	0.271	0.210	0.150	0.261	0.483	0.143	0.181	0.113	0.214	0.342
Bias	Prior	0.040	0.056	-0.023	0.050	0.076	0.032	0.032	-0.271	-0.003	0.019	0.007	0.063	-0.00
	MODIS/Aqua	-0.152	-0.085	-0.217	-0.183	-0.022	-0.055	-0.128	-0.406	-0.048	-0.099	-0.073	-0.033	-0.10
	MODIS/Aqua-nS	-0.156	-0.082	-0.217	-0.184	-0.019	-0.052	-0.130	-0.406	-0.037	-0.101	-0.065	-0.034	-0.11
	MODIS/Terra	-0.140	-0.072	-0.212	-0.181	-0.009	-0.045	-0.126	-0.390	-0.042	-0.082	-0.066	-0.011	-0.09
	MODIS/Terra-nS	-0.143	-0.070	-0.211	-0.181	-0.007	-0.043	-0.126	-0.390	-0.032	-0.085	-0.059	-0.013	-0.09
	MISR	-0.096	-0.039	-0.175	-0.139	0.027	-0.011	-0.088	-0.344	0.006	-0.032	-0.032	0.032	-0.05
	MISR-nS	-0.088	-0.038	-0.170	-0.134	0.029	-0.012	-0.082	-0.338	-0.009	-0.026	-0.040	0.038	-0.04
	PARASOL	-0.184	-0.135	-0.240	-0.206	-0.065	-0.089	-0.154	-0.453	-0.076	-0.122	-0.094	-0.076	-0.13
	PARASOL-nS	-0.169	-0.128	-0.230	-0.196	-0.060	-0.085	-0.148	-0.439	-0.061	-0.121	-0.083	-0.072	-0.11
	SEVIRI	-0.129	-0.065	-0.168	-0.150	0.011	-0.028	-0.070	-0.229	-0.006	-0.041	-0.062	0.012	-0.04
	SEVIRI-nS	-0.117	-0.061	-0.146	-0.133	0.013	-0.027	-0.053	-0.223	-0.005	-0.045	-0.058	0.014	-0.03
RMSE	Prior	0.365	0.349	0.397	0.465	0.266	0.229	0.257	0.598	0.146	0.144	0.176	0.235	0.272
	MODIS/Aqua	0.274	0.176	0.314	0.291	0.154	0.109	0.199	0.641	0.097	0.146	0.132	0.145	0.279
	MODIS/Aqua-nS	0.276	0.176	0.314	0.291	0.154	0.110	0.201	0.640	0.094	0.147	0.129	0.144	0.280
	MODIS/Terra	0.271	0.176	0.311	0.287	0.155	0.108	0.195	0.635	0.096	0.137	0.127	0.165	0.267
	MODIS/Terra-nS	0.273	0.176	0.312	0.288	0.155	0.110	0.197	0.634	0.094	0.138	0.125	0.163	0.267
	MISR	0.260	0.179	0.295	0.274	0.169	0.116	0.180	0.588	0.099	0.129	0.122	0.228	0.262
	MISR-nS	0.257	0.181	0.292	0.271	0.169	0.116	0.178	0.584	0.096	0.130	0.121	0.233	0.261
	PARASOL	0.317	0.205	0.342	0.314	0.148	0.122	0.224	0.634	0.110	0.162	0.144	0.145	0.378
	PARASOL-nS	0.322	0.202	0.340	0.313	0.148	0.121	0.223	0.621	0.104	0.163	0.139	0.146	0.385
	SEVIRI	0.260	0.178	0.277	0.252	0.142	0.108	0.173	0.524	0.106	0.124	0.126	0.147	0.270
	SEVIRI-nS	0.262	0.181	0.274	0.249	0.147	0.115	0.178	0.524	0.105	0.123	0.124	0.155	0.277
ρ	Prior	0.256	0.572	0.232	0.147	0.367	0.658	0.454	0.086	0.284	0.464	0.396	0.546	0.393
	MODIS/Aqua	0.483	0.658	0.425	0.300	0.329	0.721	0.583	0.250	0.381	0.457	0.571	0.589	0.410
	MODIS/Aqua-nS	0.482	0.656	0.419	0.301	0.331	0.712	0.580	0.265	0.355	0.461	0.552	0.592	0.409
	MODIS/Terra	0.483	0.653	0.419	0.304	0.325	0.719	0.599	0.220	0.355	0.443	0.580	0.590	0.448
	MODIS/Terra-nS	0.477	0.651	0.397	0.295	0.329	0.712	0.586	0.224	0.339	0.448	0.561	0.593	0.448
	MISR	0.467	0.623	0.371	0.274	0.360	0.703	0.570	0.389	0.329	0.421	0.501	0.592	0.439
	MISR-nS	0.471	0.626	0.373	0.277	0.367	0.714	0.568	0.388	0.369	0.420	0.532	0.592	0.442
	PARASOL	0.465	0.583	0.368	0.309	0.334	0.676	0.532	0.585	0.368	0.442	0.605	0.483	0.174
	PARASOL-nS	0.458	0.575	0.359	0.303	0.339	0.663	0.520	0.582	0.294	0.438	0.571	0.483	0.170
	SEVIRI	0.456	0.621	0.470	0.458	0.422	0.701	0.614	0.397	0.335	0.478	0.573	0.519	0.401
	SEVIRI-nS	0.423	0.625	0.427	0.440	0.435	0.699	0.595	0.382	0.354	0.488	0.570	0.522	0.374

Table 6.4: Statistics of the analyses against AERONET 500 nm AOD for selected sites. The acronym m.a.s.l. stands for meters above sea level, RMSE for root mean square error and ρ is the Pearson correlation coefficient.

6.5 Conclusions

We have shown the results of the assimilation system with the proposed bias correction in the observational space. We think that, even though the adaptive bias correction is reasonable, in the sense of the sign of the correction, the magnitude of the correction is in general too large. We therefore have to revisit our first assumption that all the bias is observational. In Chapter 5 we suggest that a bias in the model is likely, as the extent of the dust plume over the Atlantic ocean is not fully represented in the model. Now, we confirm our hypothesis by noting that the bias correction tries to fit the observations to the model, increasing the assimilated AOD over land and decreasing it over ocean. This behaviour deteriorates the analyses statistics against AERONET AOD. We conclude that, in our case, it is not possible to successfully implement this particular scheme of bias correction with the current state of the observation operator. However, it is still an open question if this scheme is applicable with a (likely) unbiased observation operator.

Chapter 7

Conclusions and perspectives

7.1 Summary

Mineral dust is an important component of the Earth system. It is the major continental contributor to the global aerosol burden. Mineral dust interacts with meteorology, climate, and biogeochemical cycles. It also affects human health.

Large uncertainties about mineral dust propagate to uncertainties in the global radiative balance. Part of them are due to the lack of understanding of processes such as dust dry and wet deposition and sedimentation, or the interaction with clouds and to uncertainties in radiative parameters, or to the quantity, timing and location of dust emission. We have focused this work on the reduction of the uncertainties in the latter processes, that is, the mineral dust emission fluxes.

Over the globe, the major source of dust is North Africa. The amount of emissions from this region is still highly uncertain. To improve our knowledge in this research field, we have used both observation and models. Indirect observations of aerosols are currently available from several satellite-borned instruments, mostly in the form of aerosol optical depth which is a column-integrated measure of light extinction by the aerosols. Models provide a global and comprehensive picture of aerosol processes. Even though they may be incomplete and simplified, these modelling systems are a useful tool for the study the physical (and chemical) drivers of mineral dust in the Earth system.

We have combined both types of information in a variational data assimilation system in order to estimate mineral dust emissions for North Africa and the Arabian Peninsula for a one year period. The observation operator includes a dust production module, which is coupled to an atmospheric chemistry-transport model. We have tested, coupled and adjusted the dust production model for our purposes. In this thesis we have fully described this module, which is a partially described in previous publications. The aerosol model has been updated and we have updated the dust size distribution and incremented their quantity of bins in the SPLA aerosol model. Observations were taken from either one or several satellite retrievals. We have processed these observations and, in some cases, we have recomputed them with the aim to make them appropriate to our needs. We have compared and evaluated the performance of the prior simulation, the analysis simulations and the assimilation system in a systematic manner; we have tried to identify the main limitations and strengths of our approach and we have drawn our conclusions accordingly.

We have explored the sensitivity of the inferred mineral dust fluxes with respect to the assimilated observational dataset. To our knowledge, this is the first work that has studied and compared the assimilation of different observational datasets in the context of aerosol inversions. In this part of the work, we have isolated the effect of the choice of the assimilated dataset in the assimilation system, and thus we have been able to quantify their effect on the dust emission estimation. We have identified biases and deficiency in both the model and the observations that could be helpful for further developments in this research field.

Our estimates of mineral dust fluxes are roughly in the mid-top range of previous mineral dust emission estimates. Our assimilation system can modify the spatial distribution of the prior dust emissions (e.g., incrementing the emissions on Eastern North Africa, Figure 4.3 (sub-region 15)), and adjust the temporal behaviour of such emissions (e.g. Figure 5.5), in consistency with the assimilated observations. We think that, in comparison to a purely modelling or observational approach, the estimation of dust fluxes using both observations and models can effectively increase the robustness of dust emission estimates. Nonetheless, we are aware that these inferred fluxes are highly dependent on the aerosol size cut-off. Further, we have focused our study on the year 2006 and could therefore not study the inter-annual variability of the emissions.

Throughout this work, we have taken advantage of the design of the assimilation system, which allows us to include an implementation of statistical diagnostics in the observational space in our inversions (with the aim to balance the observation and background errors statistics in the assimilation system). The design also allowed us to perform several AOD assimilation from a variety of satellite retrievals almost without extra computational cost, and to estimate the non-diagonal element of the background error covariance matrix.

We have given special attention to the data assimilation system and to the observation treatment. Observational and background error statistics have been defined accordingly. However, we have stressed the need for more detailed information concerning these statistics that, we think, could further improve our results. In particular, a step forward would be validation of a wider range of AOD products, as the fine mode AOD or the multi-wavelength AOD retrievals. It would also be useful to have available of a more detailed description of error statistics for fine, coarse and total AOD, for AOD at several wavelengths, correlation of errors among nearby AOD pixels, correlations of errors between fine, coarse and total AOD or between AOD errors at several wavelengths. These statistics would certainly help the aerosol data assimilation community, and they would have to be provided by the retrieval teams, ideally computed in the retrieval algorithm along with the AOD products.

7.2 Perspectives

In this section we present some possible further work that could be done after this thesis.

As a first point, we should revisit the limitations of the assimilation system. Two important decisions were made in the source inversion system. In particular, the spatial and time resolution of the control vector was a choice (somewhat based on our computational capabilities) that could be modified. We have already evaluated a change in the time resolution of the control vector (1 month in Chapter 4 against 3 days in Chapter 5), but we think that there are still some room for improvements. If the information content of the observation is enough, we could increase the resolution of the control vector up to the gridbox level, and the daily variability of the dust emissions could be directly inferred from the model inversion (e.g. Dubovik et al., 2008). In contrast, we think that we would still require a dust production module in the observation operator. This constraint leads to physically consistent emissions (taking into account the soil texture and dust availability, for example), besides with the advantageous decrease of the degrees of freedom of the inversion system.

A second and non-negligible choice was the form of the control vector. In this work we have defined correction factors for the prior emissions. In a more physical approach, the optimization of parameters in the dust production module would be more appropriate. We have not followed this path due to the above-mentioned practical advantages of our current formulation of the inversion. Moreover, the linear relation between the simulated AOD and the correction factors is fundamental for the accuracy of the results here presented. In the case of parameters in the dust production module, this linear relation would be more difficult to fulfil, which implies that, either the assimilation system would have to be updated and modified to be able to handle such non-linearities, or further work would have to be done in order to find possible linear relations between the dust production model parameters (or transformations of such parameters) and the simulated AOD. Besides, additional efforts would have to be done in order to properly define the background error covariance matrix (which is a fundamental element of the data assimilation system); and the observational errors should be increased in order to account for the errors of the dust production module parameterizations (as part of the observation operator).

Biases in the model hampered our attempts of computing non-diagonal terms of the observational error covariance matrix. In this direction, an efficient bias correction system would be largely beneficial.

It is not outside our perspectives to use this work to improve the performance of the prior model itself. By finding the correct linear relations (or modifying the assimilation system to be able to handle non-linear relations), it would be possible to estimate sensitive parameters in the aerosol model. Parameters related to dry deposition, sedimentation velocity or to the large scale and convective scavenging parameters are suitable for this procedure. In this work, we have (mostly) used the original parameters from the SPLA model, but a fine tuning of them would improve the analysis, and they will also be useful for future simulations with our model. We note that, along with the identification of the parameters, it is also necessary to quantify the main statistics of their errors.

Other aerosol measurements could be assimilated in the inversion system. By including infrared optics in the aerosol model, it would be possible to assimilate retrievals of aerosol (dust) optical depth from IASI or AIRS instruments. Doing this, vertical profile information of aerosols could be assimilated. From the visible part of the electromagnetic spectrum measured by CALIOP, vertical profiles of extinction coefficients are retrieved. In the current state of the assimilation system, the straightforward assimilation of these retrievals would be possible after minor modifications. However, we think that an important amount of work would have to be done in order to define the associated observational error statistics.

Estimating emissions of mineral dust is a complex problem. They are difficult to measure and hard to model. From the modelling point of view there are several conditions that have to be met in order to accurately estimate the total amount of emissions. Along with a fairly good estimate of the near surface winds, the process of dust emission has to be well represented in the dust production models, and the soil properties have to be well characterized. If these conditions are met, models with higher resolution could compute better estimates of emissions. Then, our assimilation system would be a useful tool to improve these (prior) emissions by including in the estimating processes the observed information about aerosols in the atmosphere.

We think that we have moved towards a more accurate estimation of mineral dust emissions, despite all the limitations of assimilation system, observations and observation operator. We also think that it is important to include both, the observations about aerosols and the modelling of the emissions and transport (representing the physical drivers) in these estimates. Both parts help to constrain, as much as possible, the uncertainties associated with dust fluxes.

We have focused our work on mineral dust emissions. Our assimilation system is easily applicable to other types of aerosols. In the near future, we will use this assimilation system to estimate biomass burning emissions. To do this, some modifications have to be done in the aerosol model: splitting the fine aerosol model into several aerosol types, and including the optics for the absorbing part of the AOD, in order to assimilate (and validate against) absorbing aerosol optical depth form the AERONET network.

Appendix A

List of acronyms

AATSR	Advanced Along-Track Scanning Radiometer
AEROCOM	Aerosol Comparison between Observations and Models
AERONET	Aerosol Robotic Network
AERUS-GEO	Aerosol and surface albEdo Retrieval Using a directional Splitting method-application to GEOstationary data
AHI	Advanced Himawari Imager
AIRS	Advanced Infrared Radiation Sounder
AI	Aerosol index
AMF	Geometric atmospheric mass factor
AMMA	Analyses Multidisciplinaires de la Mousson Africaine
AOD	Aerosol optical depth
AOT	Aerosol optical thickness
AP	Arabian Peninsula
BB	Biomass burning
BC	Black carbon
BRDF	Bidirectional reflectance distribution function
CALIOP	Cloud-Aerosol Lidar with Orthogonal Polarization
CALIPSO	Cloud-Aerosol Lidar and Infrared Pathfinder Satellite Observation
CCN	Cloud condensation nuclei
CFSR	Climate Forecast System Reanalysis
DA	Data assimilation
DB	Deep Blue
DJF	December-January-February
DMS	Dimethyl sulfide
DPM	Dust production module
DT	Dark Target
ECMWF	European Centre for Medium-Range Weather Forecasts
EDX	Energy-dispersive X-ray
EE	Expected error
ERA-Interim	European Centre for Medium-Range Weather Forecasts interim reanalysis
FG	First guess
GFED	Global Fire Emissions Database

GMM	Gaussian mixture model
GOCART	Goddard Chemistry Aerosol Radiation and Transport model
GRASP	General Retrieval of Aerosol and Surface Properties
IASI	Infrared Atmospheric Sounder Interferometer
IN	Ice nuclei
JJA	June-July-August
L-BFGS-B	Limited-memory Broyden–Fletcher–Goldfarb–Shanno algorithm for bound constrained optimization
LEO	Low earth orbit
LISA	Laboratoire Interuniversitaire des Systèmes Atmosphériques
LMDZ	Laboratoire de Météorologie Dynamique zoom model
LSCE	Laboratoire des Sciences du Climat et de l'Environnement
LT	Local time
MAM	March-April-May
MERRA	Modern-Era Retrospective Analysis for Research and Applications
MISR	Multiangle Imaging Spectroradiometer
MMD	Mass median diameter
MODIS	Moderate Resolution Imaging Spectroradiometer
MSG	Meteosat Second Generation
NASA	National Aeronautics and Space Administration
NCEP	National Centers for Environmental Prediction
NRT	Near real time
OMI	Ozone Monitoring Instrument
ORCHIDEE	Organizing Carbon and Hydrology in Dynamic Ecosystems
PARASOL	Polarization and Anisotropy of Reflectances for Atmospheric Sciences coupled with Observations from a Lidar
POLDER	Polarization and Directionality of the Earth's Reflectances
POM	Particulate organic matter
QA	Quality-assured
RF	Radiative forcing
RMSE	Root mean square error
SAMUM	Saharan Mineral Dust Experiment
SEVIRI	Spinning Enhanced Visible and Infrared Imager
SON	September-October-November
SPLA	SimPlified Aerosol model
SS	Sea spray
ST	Soil type
TOA	Top of the atmosphere
TOMS	Total Ozone Mapping Spectrometer
UTC	Coordinated universal time
VIIRS	Visible/Infrared Imaging Radiometer Suite

References

Alfaro, S. C. and Gomes, L. (2001). Modeling mineral aerosol production by wind erosion: Emission intensities and aerosol size distributions in source areas. *Journal of Geophysical Research: Atmospheres*, 106(D16):18075–18084.

Ansmann, A., Petzold, A., Kandler, K., Tegen, I., Wendisch, M., Mueller, D., Weinzierl, B., Mueller, T., and Heintzenberg, J. (2011). Saharan mineral dust experiments SAMUM–1 and SAMUM–2: what have we learned? *Tellus B*, 63(4):403–429.

Atkinson, J. D., Murray, B. J., Woodhouse, M. T., Whale, T. F., Baustian, K. J., Carslaw, K. S., Dobbie, S., O'Sullivan, D., and Malkin, T. L. (2013). The importance of feldspar for ice nucleation by mineral dust in mixed-phase clouds. *Nature*, 498(7454):355–358.

Benedetti, A., Morcrette, J.-J., Boucher, O., Dethof, A., Engelen, R. J., Fisher, M., Flentje, H., Huneeus, N., Jones, L., Kaiser, J. W., Kinne, S., Mangold, A., Razinger, M., Simmons, A. J., and Suttie, M. (2009). Aerosol analysis and forecast in the European Centre for Medium–Range Weather Forecasts Integrated Forecast System: 2. Data assimilation. *Journal of Geophysical Research: Atmospheres*, 114(D13). D13205.

Berchet, A., Pison, I., Chevallier, F., Bousquet, P., Bonne, J.-L., and Paris, J.-D. (2015). Objectified quantification of uncertainties in bayesian atmospheric inversions. *Geoscientific Model Development*, 8(5):1525–1546.

Bocquet, M. (2014). Introduction to the principles and methods of data assimilation in the geosciences. Lecture notes, Available at http://cerea.enpc.fr/HomePages/bocquet/teaching/.

Bocquet, M., Elbern, H., Eskes, H., Hirtl, M., Žabkar, R., Carmichael, G. R., Flemming, J., Inness, A., Pagowski, M., Pérez Camaño, J. L., Saide, P. E., San Jose, R., Sofiev, M., Vira, J., Baklanov, A., Carnevale, C., Grell, G., and Seigneur, C. (2015). Data assimilation in atmospheric chemistry models: current status and future prospects for coupled chemistry meteorology models. *Atmospheric Chemistry and Physics*, 15(10):5325–5358.

Bocquet, M., Wu, L., and Chevallier, F. (2011). Bayesian design of control space for optimal assimilation of observations. Part i: Consistent multiscale formalism. *Quarterly Journal of the Royal Meteorological Society*, 137(658):1340–1356.

Bohren, C. F. and Clothiaux, E. E. (2006). *Fundamentals of Atmospheric Radiation*. Wiley-VCH Verlag GmbH.

Bond, T. C., Doherty, S. J., Fahey, D. W., Forster, P. M., Berntsen, T., DeAngelo, B. J., Flanner, M. G., Ghan, S., Kärcher, B., Koch, D., Kinne, S., Kondo, Y., Quinn, P. K., Sarofim, M. C., Schultz, M. G., Schulz, M., Venkataraman, C., Zhang, H., Zhang, S., Bellouin, N., Guttikunda, S. K., Hopke, P. K., Jacobson, M. Z., Kaiser, J. W., Klimont, Z., Lohmann, U., Schwarz, J. P., Shindell, D., Storelvmo, T., Warren, S. G., and Zender, C. S. (2013). Bounding the role of black carbon in the climate system: A scientific assessment. *Journal of Geophysical Research: Atmospheres*, 118(11):5380–5552.

Boucher, O., Randall, D., Artaxo, P., Bretherton, C., Feingold, G., Forster, P., Kerminen, V.-M., Kondo, Y., Liao, H., Lohmann, U., Rasch, P., Satheesh, S., Sherwood, S., Stevens, B., and Zhang, X. (2013). Clouds and aerosols. In Stocker, T., Qin, D., Plattner, G.-K., Tignor, M., Allen, S., Boschung, J., Nauels, A., Xia, Y., Bex, V., and Midgley, P., editors, *Climate Change 2013: The Physical Science Basis. Contribution of Working Group I to the Fifth Assessment Report of the Intergovernmental Panel on Climate Change*, pages 571–657. Cambridge University Press, Cambridge, United Kingdom and New York, NY, USA.

Bousquet, P., Ciais, P., Miller, J. B., Dlugokencky, E. J., Hauglustaine, D. A., Prigent, C., Van der Werf, G. R., Peylin, P., Brunke, E.-G., Carouge, C., Langenfelds, R. L., Lathiere, J., Papa, F., Ramonet, M., Schmidt, M., Steele, L. P., Tyler, S. C., and White, J. (2006). Contribution of anthropogenic and natural sources to atmospheric methane variability. *Nature*, 443(7110):439–443.

Bretl, S., Reutter, P., Raible, C. C., Ferrachat, S., Poberaj, C. S., Revell, L. E., and Lohmann, U. (2015). The influence of absorbed solar radiation by Saharan dust on hurricane genesis. *Journal of Geophysical Research: Atmospheres*, 120(5):1902–1917. 2014JD022441.

Buizza, R., Houtekamer, P. L., Pellerin, G., Toth, Z., Zhu, Y., and Wei, M. (2005). A comparison of the ECMWF, MSC, and NCEP Global Ensemble Prediction Systems. *Monthly Weather Review*, 133(5):1076–1097.

Cakmur, R. V., Miller, R. L., Perlwitz, J., Geogdzhayev, I. V., Ginoux, P., Koch, D., Kohfeld, K. E., Tegen, I., and Zender, C. S. (2006). Constraining the magnitude of the global dust cycle by minimizing the difference between a model and observations. *Journal of Geophysical Research: Atmospheres*, 111(D6). D06207.

Carrer, D., Ceamanos, X., Six, B., and Roujean, J.-L. (2014). AERUS-GEO: A newly available satellite-derived aerosol optical depth product over Europe and Africa. *Geophysical Research Letters*, 41(21):7731–7738.

Carrer, D., Roujean, J.-L., Hautecoeur, O., and Elias, T. (2010). Daily estimates of aerosol optical thickness over land surface based on a directional and temporal analysis of SEVIRI MSG visible observations. *Journal of Geophysical Research: Atmospheres*, 115(D10). D10208.

Chevallier, F., Ciais, P., Conway, T. J., Aalto, T., Anderson, B. E., Bousquet, P., Brunke, E. G., Ciattaglia, L., Esaki, Y., Fröhlich, M., Gomez, A., Gomez-Pelaez, A. J., Haszpra, L., Krummel, P. B., Langenfelds, R. L., Leuenberger, M., Machida, T., Maignan, F., Matsueda, H., Morguí, J. A., Mukai, H., Nakazawa, T., Peylin, P., Ramonet, M., Rivier, L., Sawa, Y., Schmidt, M., Steele, L. P., Vay, S. A., Vermeulen, A. T., Wofsy, S., and Worthy, D. (2010). CO2 surface fluxes at grid point scale estimated from a global 21 year reanalysis of atmospheric measurements. *Journal of Geophysical Research: Atmospheres*, 115(D21). D21307.

Cressman, G. P. (1959). An operational objective analysis system. *Monthly Weather Review*, 87(10):367–374.

de Leeuw, G., Holzer-Popp, T., Bevan, S., Davies, W. H., Descloitres, J., Grainger, R. G., Griesfeller, J., Heckel, A., Kinne, S., Klüser, L., Kolmonen, P., Litvinov, P., Martynenko, D., North, P., Ovigneur, B., Pascal, N., Poulsen, C., Ramon, D., Schulz, M., Siddans, R., Sogacheva, L., Tanré, D., Thomas, G. E., Virtanen, T. H., von Hoyningen Huene, W., Vountas, M., and Pinnock, S. (2015). Evaluation of seven European aerosol optical depth retrieval algorithms for climate analysis. *Remote Sensing of Environment*, 162:295 – 315.

Dee, D. P. (2005). Bias and data assimilation. *Quarterly Journal of the Royal Meteorological Society*, 131(613):3323–3343.

Dee, D. P., Uppala, S. M., Simmons, A. J., Berrisford, P., Poli, P., Kobayashi, S., Andrae, U., Balmaseda, M. A., Balsamo, G., Bauer, P., Bechtold, P., Beljaars, A. C. M., van de Berg, L., Bidlot, J., Bormann, N., Delsol, C., Dragani, R., Fuentes, M., Geer, A. J., Haimberger, L., Healy, S. B., Hersbach, H., Hólm, E. V., Isaksen, L. aa nd Kållberg, P., Köhler, M., Matricardi, M., McNally, A. P., Monge-Saa nz, B. M., Morcrette, J.-J., Park, B.-K., Peubey, C., de Rosnay, P., Tavolato, C., Thépaut, J.-N., and Vitart, F. (2011). The ERA–Interim reanalysis: configuration and performance of the data assimilation system. *Quarterly Journal of the Royal Meteorological Society*, 137(656):553–597.

Dentener, F., Kinne, S., Bond, T., Boucher, O., Cofala, J., Generoso, S., Ginoux, P., Gong, S., Hoelzemann, J. J., Ito, A., Marelli, L., Penner, J. E., Putaud, J.-P., Textor, C., Schulz, M., van der Werf, G. R., and Wilson, J. (2006). Emissions of primary aerosol and precursor gases in the years 2000 and 1750 prescribed data-sets for AeroCom. *Atmospheric Chemistry and Physics*, 6(12):4321–4344.

Dentener, F. J., Carmichael, G. R., Zhang, Y., Lelieveld, J., and Crutzen, P. J. (1996). Role of mineral aerosol as a reactive surface in the global troposphere. *Journal of Geophysical Research: Atmospheres*, 101(D17):22869–22889.

Desroziers, G., Berre, L., Chapnik, B., and Poli, P. (2005). Diagnosis of observation, background and analysis–error statistics in observation space. *Quarterly Journal of the Royal Meteorological Society*, 131(613):3385–3396.

Diamond, S. and Boyd, S. (2016). CVXPY: A Python-Embedded Modeling Language for Convex Optimization. *Journal of Machine Learning Research*, 17(83):1–5.

Diner, D. J., Beckert, J. C., Reilly, T. H., Bruegge, C. J., Conel, J. E., Kahn, R. A., Martonchik, J. V., Ackerman, T. P., Davies, R., Gerstl, S. A. W., Gordon, H. R., Muller, J. P., Myneni, R. B., Sellers, P. J., Pinty, B., and Verstraete, M. M. (1998). Multi-angle Imaging SpectroRadiometer (MISR) instrument description and experiment overview. *IEEE Transactions on Geoscience and Remote Sensing*, 36(4):1072–1087.

Domahidi, A., Chu, E., and Boyd, S. (2013). ECOS: An SOCP solver for embedded systems. In *European Control Conference (ECC)*, pages 3071–3076.

Dubovik, O., Lapyonok, T., Kaufman, Y. J., Chin, M., Ginoux, P., Kahn, R. A., and Sinyuk, A. (2008). Retrieving global aerosol sources from satellites using inverse modeling. *Atmospheric Chemistry and Physics*, 8(2):209–250.

Dubovik, O., Lapyonok, T., Litvinov, P., Herman, M., Fuertes, D., Ducos, F., Lopatin, A., Chaikovsky, A., Torres, B., Derimian, Y., et al. (2014). GRASP: a versatile algorithm for characterizing the atmosphere. *SPIE: Newsroom*.

Escribano, J., Boucher, O., Chevallier, F., and Huneeus, N. (2016). Subregional inversion of North African dust sources. *Journal of Geophysical Research: Atmospheres*, 121(14):8549–8566. 2016JD025020.

Escribano, J., Boucher, O., Chevallier, F., and Huneeus, N. (2017). Impact of the choice of the satellite aerosol optical depth product in a sub-regional dust emission inversion. *Atmospheric Chemistry and Physics Discussions*, 2017:1–22.

Evan, A. T., Flamant, C., Fiedler, S., and Doherty, O. (2014). An analysis of aeolian dust in climate models. *Geophysical Research Letters*, 41(16):5996–6001. 2014GL060545.

Fortems-Cheiney, A., Chevallier, F., Pison, I., Bousquet, P., Saunois, M., Szopa, S., Cressot, C., Kurosu, T. P., Chance, K., and Fried, A. (2012). The formaldehyde budget as seen by a global-scale multi-constraint and multi-species inversion system. *Atmospheric Chemistry and Physics*, 12(15):6699–6721.

Gillette, D. A. and Chen, W. (2001). Particle production and aeolian transport from a “supply-limited” source area in the Chihuahuan desert, New Mexico, United States. *Journal of Geophysical Research: Atmospheres*, 106(D6):5267–5278.

Ginoux, P., Chin, M., Tegen, I., Prospero, J. M., Holben, B., Dubovik, O., and Lin, S.-J. (2001). Sources and distributions of dust aerosols simulated with the GOCART model. *Journal of Geophysical Research: Atmospheres*, 106(D17):20255–20273.

Ginoux, P., Prospero, J. M., Gill, T. E., Hsu, N. C., and Zhao, M. (2012). Global-scale attribution of anthropogenic and natural dust sources and their emission rates based on MODIS Deep Blue aerosol products. *Reviews of Geophysics*, 50(3). RG3005.

Goloub, P., Tanre, D., Deuze, J. L., Herman, M., Marchand, A., and Breon, F. M. (1999). Validation of the first algorithm applied for deriving the aerosol properties over the ocean using the POLDER/ADEOS measurements. *IEEE Transactions on Geoscience and Remote Sensing*, 37(3):1586–1596.

Gomes, L., Rajot, J., Alfaro, S., and Gaudichet, A. (2003). Validation of a dust production model from measurements performed in semi-arid agricultural areas of Spain and Niger. *CATENA*, 52(3–4):257 – 271. Wind Erosion in Europe.

Goudie, A. and Middleton, N. J. (2006). *Desert Dust in the Global System.* Springer-Verlag Berlin Heidelberg.

Goudie, A. S. (2014). Desert dust and human health disorders. *Environment International*, 63:101–113.

Guelle, W., Balkanski, Y. J., Schulz, M., Marticorena, B., Bergametti, G., Moulin, C., Arimoto, R., and Perry, K. D. (2000). Modeling the atmospheric distribution of mineral aerosol: Comparison with ground measurements and satellite observations for yearly and synoptic timescales over the North Atlantic. *Journal of Geophysical Research: Atmospheres*, 105(D2):1997–2012.

Hakami, A., Henze, D. K., Seinfeld, J. H., Chai, T., Tang, Y., Carmichael, G. R., and Sandu, A. (2005). Adjoint inverse modeling of black carbon during the Asian Pacific Regional Aerosol Characterization Experiment. *Journal of Geophysical Research: Atmospheres*, 110(D14). D14301.

Haywood, J. M., Allan, R. P., Culverwell, I., Slingo, T., Milton, S., Edwards, J., and Clerbaux, N. (2005). Can desert dust explain the outgoing longwave radiation anomaly over the Sahara during July 2003? *Journal of Geophysical Research: Atmospheres*, 110(D5). D05105.

Holben, B., Eck, T., Slutsker, I., Tanré, D., Buis, J., Setzer, A., Vermote, E., Reagan, J., Kaufman, Y., Nakajima, T., Lavenu, F., Jankowiak, I., and Smirnov, A. (1998). AERONET–A Federated Instrument Network and Data Archive for Aerosol Characterization. *Remote Sensing of Environment*, 66(1):1 – 16.

Hourdin, F., Grandpeix, J.-Y., Rio, Catherine a Bony, S., Jam, A., Cheruy, F., Rochetin, N., Fairhead, L., Idelkadi, A., Musat, I., Dufresne, J.-L., Lahellec, A., Lefebvre, M.-P., and Roehrig, R. (2013). LMDZ5B: the atmospheric component of the IPSL climate model with revisited parameterizations for clouds and convection. *Climate Dynamics*, 40(9-10):2193–2222.

Hourdin, F., Gueye, M., Diallo, B., Dufresne, J.-L., Escribano, J., Menut, L., Marticoréna, B., Siour, G., and Guichard, F. (2015). Parameterization of convective transport in the boundary layer and its impact on the representation of the diurnal cycle of wind and dust emissions. *Atmospheric Chemistry and Physics*, 15(12):6775–6788.

Huneeus, N., Basart, S., Fiedler, S., Morcrette, J.-J., Benedetti, A., Mulcahy, J., Terradellas, E., Pérez García-Pando, C., Pejanovic, G., Nickovic, S., Arsenovic, P., Schulz, M., Cuevas, E., Baldasano, J. M., Pey, J., Remy, S., and Cvetkovic, B. (2016). Forecasting the northern African dust outbreak towards Europe in April 2011: a model intercomparison. *Atmospheric Chemistry and Physics*, 16(8):4967–4986.

Huneeus, N., Boucher, O., and Chevallier, F. (2009). Simplified aerosol modeling for variational data assimilation. *Geoscientific Model Development*, 2(2):213–229.

Huneeus, N., Boucher, O., and Chevallier, F. (2013). Atmospheric inversion of SO_2 and primary aerosol emissions for the year 2010. *Atmospheric Chemistry and Physics*, 13(13):6555–6573.

Huneeus, N., Chevallier, F., and Boucher, O. (2012). Estimating aerosol emissions by assimilating observed aerosol optical depth in a global aerosol model. *Atmospheric Chemistry and Physics*, 12(10):4585–4606.

Huneeus, N., Schulz, M., Balkanski, Y., Griesfeller, J., Prospero, J., Kinne, S., Bauer, S., Boucher, O., Chin, M., Dentener, F., Diehl, T., Easter, R., Fillmore, D., Ghan, S., Ginoux, P., Grini, A., Horowitz, L., Koch, D., Krol, M. C., Landing, W., Liu, X., Mahowald, N., Miller, R., Morcrette, J.-J., Myhre, G., Penner, J., Perlwitz, J., Stier, P., Takemura, T., and Zender, C. S. (2011). Global dust model intercomparison in AeroCom phase I. *Atmospheric Chemistry and Physics*, 11(15):7781–7816.

Hyer, E. J., Reid, J. S., and Zhang, J. (2011). An over-land aerosol optical depth data set for data assimilation by filtering, correction, and aggregation of MODIS Collection 5 optical depth retrievals. *Atmospheric Measurement Techniques*, 4(3):379–408.

Jickells, T. D., An, Z. S., Andersen, K. K., Baker, A. R., Bergametti, G., Brooks, N., Cao, J. J., Boyd, P. W., Duce, R. A., Hunter, K. A., Kawahata, H., Kubilay, N., laRoche, J., Liss, P. S., Mahowald, N., Prospero, J. M., Ridgwell, A. J., Tegen, I., and Torres, R. (2005). Global iron connections between desert dust, ocean biogeochemistry, and climate. *Science*, 308(5718):67–71.

Journet, E., Balkanski, Y., and Harrison, S. P. (2014). A new data set of soil mineralogy for dust-cycle modeling. *Atmospheric Chemistry and Physics*, 14(8):3801–3816.

Kahn, R., Nelson, D., Garay, M., Levy, R., Bull, M., Diner, D., Martonchik, J., Paradise, S., Hansen, E., and Remer, L. (2009). MISR aerosol product attributes and statistical comparisons with MODIS. *Geoscience and Remote Sensing, IEEE Transactions on*, 47(12):4095–4114.

Kahn, R. A. and Gaitley, B. J. (2015). An analysis of global aerosol type as retrieved by MISR. *Journal of Geophysical Research: Atmospheres*, 120(9):4248–4281. 2015JD023322.

Kahn, R. A., Gaitley, B. J., Martonchik, J. V., Diner, D. J., Crean, K. A., and Holben, B. (2005). Multiangle Imaging Spectroradiometer (MISR) global aerosol optical depth validation based on 2 years of coincident Aerosol Robotic Network (AERONET) observations. *Journal of Geophysical Research: Atmospheres*, 110(D10). D10S04.

Kaiser, J. W., Heil, A., Andreae, M. O., Benedetti, A., Chubarova, N., Jones, L., Morcrette, J.-J., Razinger, M., Schultz, M. G., Suttie, M., and van der Werf, G. R. (2012). Biomass burning emissions estimated with a global fire assimilation system based on observed fire radiative power. *Biogeosciences*, 9(1):527–554.

Kirkland, T. N. and Fierer, J. (1996). Coccidioidomycosis: a reemerging infectious disease. *Emerging Infectious Diseases*, 2(3):192–199.

Knippertz, P. and Stuut, J.-B. W. (2014). *Mineral Dust – A Key Player in the Earth System*. Springer Netherlands.

Kok, J. F. (2011). A scaling theory for the size distribution of emitted dust aerosols suggests climate models underestimate the size of the global dust cycle. *Proceedings of the National Academy of Sciences*, 108(3):1016–1021.

Koren, I., Kaufman, Y. J., Washington, R., Todd, M. C., Rudich, Y., Martins, J. V., and Rosenfeld, D. (2006). The Bodélé depression: a single spot in the Sahara that provides most of the mineral dust to the Amazon forest. *Environmental Research Letters*, 1(1):014005.

Lamarque, J.-F., Bond, T. C., Eyring, V., Granier, C., Heil, A., Klimont, Z., Lee, D., Liousse, C., Mieville, A., Owen, B., Schultz, M. G., Shindell, D., Smith, S. J., Stehfest, E., Van Aardenne, J., Cooper, O. R., Kainuma, M., Mahowald, N., McConnell, J. R., Naik, V., Riahi, K., and van Vuuren, D. P. (2010). Historical (1850–2000) gridded anthropogenic and biomass burning emissions of reactive gases and aerosols: methodology and application. *Atmospheric Chemistry and Physics*, 10(15):7017–7039.

Lana, A., Bell, T. G., Simó, R., Vallina, S. M., Ballabrera-Poy, J., Kettle, A. J., Dachs, J., Bopp, L., Saltzman, E. S., Stefels, J., Johnson, J. E., and Liss, P. S. (2011). An updated climatology of surface dimethlysulfide concentrations and emission fluxes in the global ocean. *Global Biogeochemical Cycles*, 25(1). GB1004.

Largeron, Y., Guichard, F., Bouniol, D., Couvreux, F., Kergoat, L., and Marticorena, B. (2015). Can we use surface wind fields from meteorological reanalyses for Sahelian dust emission simulations? *Geophysical Research Letters*, 42(7):2490–2499. 2014GL062938.

Lathière, J., Hauglustaine, D. A., Friend, A. D., De Noblet-Ducoudré, N., Viovy, N., and Folberth, G. A. (2006). Impact of climate variability and land use changes on global biogenic volatile organic compound emissions. *Atmospheric Chemistry and Physics*, 6(8):2129–2146.

Laurent, B., Marticorena, B., Bergametti, G., Léon, J. F., and Mahowald, N. M. (2008). Modeling mineral dust emissions from the Sahara desert using new surface properties and soil database. *Journal of Geophysical Research: Atmospheres*, 113(D14). D14218.

Levy, R. C., Mattoo, S., Munchak, L. A., Remer, L. A., Sayer, A. M., Patadia, F., and Hsu, N. C. (2013). The Collection 6 MODIS aerosol products over land and ocean. *Atmospheric Measurement Techniques*, 6(11):2989–3034.

Levy, R. C., Munchak, L. A., Mattoo, S., Patadia, F., Remer, L. A., and Holz, R. E. (2015). Towards a long-term global aerosol optical depth record: applying a consistent aerosol retrieval algorithm to MODIS and VIIRS-observed reflectance. *Atmospheric Measurement Techniques*, 8(10):4083–4110.

Levy, R. C., Remer, L. A., Kleidman, R. G., Mattoo, S., Ichoku, C., Kahn, R., and Eck, T. F. (2010). Global evaluation of the Collection 5 MODIS dark-target aerosol products over land. *Atmospheric Chemistry and Physics*, 10(21):10399–10420.

Levy, R. C., Remer, L. A., Tanré, D., Kaufman, Y. J., Ichoku, C., Holben, B. N., Livingston, J. M., Russell, P. B., and Maring, H. (2003). Evaluation of the Moderate-Resolution Imaging Spectroradiometer (MODIS) retrievals of dust aerosol over the ocean during PRIDE. *Journal of Geophysical Research: Atmospheres*, 108(D19). 8594.

Liou, K.-N. (2002). *An introduction to atmospheric radiation*, volume 84. Academic press.

Lorenc, A. C. and Hammon, O. (1988). Objective quality control of observations using Bayesian methods. theory, and a practical implementation. *Quarterly Journal of the Royal Meteorological Society*, 114(480):515–543.

Lynch, P., Reid, J. S., Westphal, D. L., Zhang, J., Hogan, T. F., Hyer, E. J., Curtis, C. A., Hegg, D. A., Shi, Y., Campbell, J. R., Rubin, J. I., Sessions, W. R., Turk, F. J., and Walker, A. L. (2016). An 11-year global gridded aerosol optical thickness reanalysis (v1.0) for atmospheric and climate sciences. *Geoscientific Model Development*, 9(4):1489–1522.

Mahowald, N., Albani, S., Kok, J. F., Engelstaeder, S., Scanza, R., Ward, D. S., and Flanner, M. G. (2014). The size distribution of desert dust aerosols and its impact on the Earth system. *Aeolian Research*, 15:53 – 71.

Marticorena, B. and Bergametti, G. (1995). Modeling the atmospheric dust cycle: 1. Design of a soil-derived dust emission scheme. *Journal of Geophysical Research: Atmospheres*, 100(D8):16415–16430.

Marticorena, B., Bergametti, G., Aumont, B., Callot, Y., N'Doumé, C., and Legrand, M. (1997). Modeling the atmospheric dust cycle: 2. Simulation of Saharan dust sources. *Journal of Geophysical Research: Atmospheres*, 102(D4):4387–4404.

Martiny, N. and Chiapello, I. (2013). Assessments for the impact of mineral dust on the meningitis incidence in West Africa. *Atmospheric Environment*, 70:245 – 253.

Menut, L., Pérez, C., Haustein, K., Bessagnet, B., Prigent, C., and Alfaro, S. (2013). Impact of surface roughness and soil texture on mineral dust emission fluxes modeling. *Journal of Geophysical Research: Atmospheres*, 118(12):6505–6520.

Menut, L., Schmechtig, C., and Marticorena, B. (2005). Sensitivity of the sandblasting flux calculations to the soil size distribution accuracy. *Journal of Atmospheric and Oceanic Technology*, 22(12):1875–1884.

Monahan, E. C., Spiel, D. E., and Davidson, K. L. (1986). *A Model of Marine Aerosol Generation Via Whitecaps and Wave Disruption*, pages 167–174. Springer Netherlands, Dordrecht.

Morman, S. A. and Plumlee, G. S. (2013). The role of airborne mineral dusts in human disease. *Aeolian Research*, 9:203–212.

Nabat, P., Solmon, F., Mallet, M., Kok, J. F., and Somot, S. (2012). Dust emission size distribution impact on aerosol budget and radiative forcing over the Mediterranean region: a regional climate model approach. *Atmospheric Chemistry and Physics*, 12(21):10545–10567.

Nichols, N. K. (2010). Mathematical concepts of data assimilation. In Lahoz, W., Khattatov, B., and Menard, R., editors, *Data Assimilation. Making Sense of Observations.*, pages 13–39. Springer-Verlag Berlin Heidelberg.

Nightingale, P. D., Malin, G., Law, C. S., Watson, A. J., Liss, P. S., Liddicoat, M. I., Boutin, J., and Upstill-Goddard, R. C. (2000). In situ evaluation of air-sea gas exchange parameterizations using novel conservative and volatile tracers. *Global Biogeochemical Cycles*, 14(1):373–387.

Olkin, I. (1981). Range restrictions for product–moment correlation matrices. *Psychometrika*, 46(4):469–472.

Pannekoucke, O., Berre, L., and Desroziers, G. (2008). Background–error correlation length–scale estimates and their sampling statistics. *Quarterly Journal of the Royal Meteorological Society*, 134(631):497–508.

Panofsky, R. A. (1949). Objective weather-map analysis. *Journal of Meteorology*, 6(6):386–392.

Pedregosa, F., Varoquaux, G., Gramfort, A., Michel, V., Thirion, B., Grisel, O., Blondel, M., Prettenhofer, P., Weiss, R., Dubourg, V., Vanderplas, J., Passos, A., Cournapeau, D., Brucher, M., Perrot, M., and Duchesnay, E. (2011). Scikit-learn: Machine learning in Python. *Journal of Machine Learning Research*, 12:2825–2830.

Pérez García-Pando, C., Stanton, M. C., Diggle, P. J., Trzaska, S., Miller, R. L., Perlwitz, J. P., Baldasano, J. M., Cuevas, E., Ceccato, P., Yaka, P., and Thomson, M. C. (2014). Soil dust aerosols and wind as predictors of seasonal meningitis incidence in Niger. *Environmental Health Perspectives*, 122:679–686.

Peyridieu, S., Chédin, A., Capelle, V., Tsamalis, C., Pierangelo, C., Armante, R., Crevoisier, C., Crépeau, L., Siméon, M., Ducos, F., and Scott, N. A. (2013). Characterisation of dust aerosols in the infrared from IASI and comparison with PARASOL, MODIS, MISR, CALIOP, and AERONET observations. *Atmospheric Chemistry and Physics*, 13(12):6065–6082.

Pilon, R., Grandpeix, J.-Y., and Heinrich, P. (2015). Representation of transport and scavenging of trace particles in the Emanuel moist convection scheme. *Quarterly Journal of the Royal Meteorological Society*, 141(689):1244–1258.

Pope, R. J., Marsham, J. H., Knippertz, P., Brooks, M. E., and Roberts, A. J. (2016). Identifying errors in dust models from data assimilation. *Geophysical Research Letters*, 43(17):9270–9279. 2016GL070621.

Qi, H. and Sun, D. (2006). A quadratically convergent newton method for computing the nearest correlation matrix. *SIAM Journal on Matrix Analysis and Applications*, 28(2):360–385.

Rabier, F. (2005). Overview of global data assimilation developments in numerical weather–prediction centres. *Quarterly Journal of the Royal Meteorological Society*, 131(613):3215–3233.

Redelsperger, J.-L., Thorncroft, C. D., Diedhiou, A., Lebel, T., Parker, D. J., and Polcher, J. (2006). African monsoon multidisciplinary analysis – An international research project and field campaign. *Bulletin of the American Meteorological Society*, 87(12):1739–1746.

Remer, L. A., Kaufman, Y. J., Tanré, D., Mattoo, S., Chu, D. A., Martins, J. V., Li, R.-R., Ichoku, C., Levy, R. C., Kleidman, R. G., Eck, T. F., Vermote, E., and Holben, B. N. (2005). The MODIS aerosol algorithm, products, and validation. *Journal of the Atmospheric Sciences*, 62(4):947–973.

Remer, L. A., Kleidman, R. G., Levy, R. C., Kaufman, Y. J., Tanré, D., Mattoo, S., Martins, J. V., Ichoku, C., Koren, I., Yu, H., and Holben, B. N. (2008). Global aerosol climatology from the MODIS satellite sensors. *Journal of Geophysical Research: Atmospheres*, 113(D14). D14S07.

Saha, S., Moorthi, S., Pan, H.-L., Wu, X., Wang, J., Nadiga, S., Tripp, P., Kistler, R., Woollen, J., Behringer, D., Liu, H., Stokes, D., Grumbine, R., Gayno, G., Wang, J., Hou, Y.-T., Chuang, H.-Y., Juang, H.-M. H., Sela, J., Iredell, M., Treadon, R., Kleist, D., Delst, P. V., Keyser, D., Derber, J., Ek, M., Meng, J., Wei, H., Yang, R., Lord, S., Dool, H. V. D., Kumar, A., Wang, W., Long, C., Chelliah, M., Xue, Y., Huang, B., Schemm, J.-K., Ebisuzaki, W., Lin, R., Xie, P., Chen, M., Zhou, S., Higgins, W., Zou, C.-Z., Liu, Q., Chen, Y., Han, Y., Cucurull, L., Reynolds, R. W., Rutledge, G., and Goldberg, M. (2010). The NCEP Climate Forecast System Reanalysis. *Bulletin of the American Meteorological Society*, 91(8):1015–1057.

Saide, P. E., Kim, J., Song, C. H., Choi, M., Cheng, Y., and Carmichael, G. R. (2014). Assimilation of next generation geostationary aerosol optical depth retrievals to improve air quality simulations. *Geophysical Research Letters*, 41(24):9188–9196. 2014GL062089.

Sayer, A. M., Hsu, N. C., Bettenhausen, C., and Jeong, M.-J. (2013). Validation and uncertainty estimates for MODIS collection 6 “Deep Blue” aerosol data. *Journal of Geophysical Research: Atmospheres*, 118(14):7864–7872.

Sayer, A. M., Hsu, N. C., Bettenhausen, C., Jeong, M.-J., and Meister, G. (2015). Effect of MODIS Terra radiometric calibration improvements on Collection 6 Deep Blue aerosol products: Validation and Terra/Aqua consistency. *Journal of Geophysical Research: Atmospheres*, 120(23):12,157–12,174. 2015JD023878.

Sayer, A. M., Munchak, L. A., Hsu, N. C., Levy, R. C., Bettenhausen, C., and Jeong, M.-J. (2014). MODIS Collection 6 aerosol products: Comparison between Aqua's e-Deep Blue, Dark Target, and "merged" data sets, and usage recommendations. *Journal of Geophysical Research: Atmospheres*, 119(24):13965–13989. 2014JD022453.

Schepanski, K., Tegen, I., Laurent, B., Heinold, B., and Macke, A. (2007). A new Saharan dust source activation frequency map derived from MSG–SEVIRI IR–channels. *Geophysical Research Letters*, 34(18). L18803.

Schepanski, K., Tegen, I., and Macke, A. (2012). Comparison of satellite based observations of Saharan dust source areas. *Remote Sensing of Environment*, 123:90–97.

Schulz, M., Balkanski, Y. J., Guelle, W., and Dulac, F. (1998). Role of aerosol size distribution and source location in a three-dimensional simulation of a Saharan dust episode tested against satellite-derived optical thickness. *Journal of Geophysical Research: Atmospheres*, 103(D9):10579–10592.

Schulz, M., Textor, C., Kinne, S., Balkanski, Y., Bauer, S., Berntsen, T., Berglen, T., Boucher, O., Dentener, F., Guibert, S., Isaksen, I. S. A., Iversen, T., Koch, D., Kirkevåg, A., Liu, X., Montanaro, V., Myhre, G., Penner, J. E., Pitari, G., Reddy, S., Seland, Ø., Stier, P., and Takemura, T. (2006). Radiative forcing by aerosols as derived from the AeroCom present-day and pre-industrial simulations. *Atmospheric Chemistry and Physics*, 6(12):5225–5246.

Schutgens, N., Nakata, M., and Nakajima, T. (2012). Estimating aerosol emissions by assimilating remote sensing observations into a global transport model. *Remote Sensing*, 4(11):3528–3543.

Seinfeld, J. H. and Pandis, S. N. (2012). *Atmospheric Chemistry and Physics: From Air Pollution to Climate Change*. John Wiley & Sons.

Shao, Y., Ishizuka, M., Mikami, M., and Leys, J. F. (2011). Parameterization of size-resolved dust emission and validation with measurements. *Journal of Geophysical Research: Atmospheres*, 116(D8). D08203.

Shao, Y. and Lu, H. (2000). A simple expression for wind erosion threshold friction velocity. *Journal of Geophysical Research: Atmospheres*, 105(D17):22437–22443.

Sow, M., Alfaro, S. C., and Rajot, J. L. (2011). Comparison of the size–resolved dust emission fluxes measured over a Sahelian source with the Dust Production Model (DPM) predictions. *Atmospheric Chemistry and Physics Discussions*, 11(4):11077–11107.

Talagrand, O. (1998). A posteriori evaluation and verification of analysis and assimilation algorithms. In *Workshop on Diagnosis of Data Assimilation Systems, 2–4 November 1998*, pages 17–28, Shinfield Park, Reading. ECMWF, ECMWF.

Tanré, D., Bréon, F. M., Deuzé, J. L., Dubovik, O., Ducos, F., François, P., Goloub, P., Herman, M., Lifermann, A., and Waquet, F. (2011). Remote sensing of aerosols by using polarized, directional and spectral measurements within the A–Train: the PARASOL mission. *Atmospheric Measurement Techniques*, 4(7):1383–1395.

Tegen, I., Schepanski, K., and Heinold, B. (2013). Comparing two years of Saharan dust source activation obtained by regional modelling and satellite observations. *Atmospheric Chemistry and Physics*, 13(5):2381–2390.

van der Werf, G. R., Randerson, J. T., Giglio, L., Collatz, G. J., Mu, M., Kasibhatla, P. S., Morton, D. C., DeFries, R. S., Jin, Y., and van Leeuwen, T. T. (2010). Global fire emissions and the contribution of deforestation, savanna, forest, agricultural, and peat fires (1997–2009). *Atmospheric Chemistry and Physics*, 10(23):11707–11735.

Wang, R., Balkanski, Y., Bopp, L., Aumont, O., Boucher, O., Ciais, P., Gehlen, M., Peñuelas, J., Ethé, C., Hauglustaine, D., Li, B., Liu, J., Zhou, F., and Tao, S. (2015). Influence of anthropogenic aerosol deposition on the relationship between oceanic productivity and warming. *Geophysical Research Letters*, 42(24):10,745–10,754. 2015GL066753.

Washington, R., Flamant, C., Parker, D., Marsham, J., Mc-Quaid, J., Brindley, H., Todd, M., Highwood, E., Ryder, C., Chaboureau, J., et al. (2012). Fennec–the Saharan climate system. *CLIVAR Exchanges*, 17(3):31–33.

Washington, R., Todd, M. C., Engelstaedter, S., Mbainayel, S., and Mitchell, F. (2006). Dust and the low-level circulation over the Bodélé Depression, Chad: Observations from BoDEx 2005. *Journal of Geophysical Research: Atmospheres*, 111(D3). D03201.

White, B. R. (1979). Soil transport by winds on Mars. *Journal of Geophysical Research: Solid Earth*, 84(B9):4643–4651.

Woodward, S. (2001). Modeling the atmospheric life cycle and radiative impact of mineral dust in the Hadley Centre climate model. *Journal of Geophysical Research: Atmospheres*, 106(D16):18155–18166.

Yu, H., Chin, M., Yuan, T., Bian, H., Remer, L. A., Prospero, J. M., Omar, A., Winker, D., Yang, Y., Zhang, Y., Zhang, Z., and Zhao, C. (2015). The fertilizing role of African dust in the Amazon rainforest: A first multiyear assessment based on data from Cloud-Aerosol Lidar and Infrared Pathfinder Satellite Observations. *Geophysical Research Letters*, 42(6):1984–1991. 2015GL063040.

Yumimoto, K. and Takemura, T. (2013). The SPRINTARS version 3.80/4D–Var data assimilation system: development and inversion experiments based on the observing system simulation experiment framework. *Geoscientific Model Development*, 6(6):2005–2022.

Yumimoto, K., Uno, I., Sugimoto, N., Shimizu, A., Liu, Z., and Winker, D. M. (2008). Adjoint inversion modeling of Asian dust emission using lidar observations. *Atmospheric Chemistry and Physics*, 8(11):2869–2884.

Zender, C. S., Bian, H., and Newman, D. (2003). Mineral Dust Entrainment and Deposition (DEAD) model: Description and 1990s dust climatology. *Journal of Geophysical Research: Atmospheres*, 108(D14). 4416.

Zhang, J., Campbell, J. R., Hyer, E. J., Reid, J. S., Westphal, D. L., and Johnson, R. S. (2014). Evaluating the impact of multisensor data assimilation on a global aerosol particle transport model. *Journal of Geophysical Research: Atmospheres*, 119(8):4674–4689. 2013JD020975.

Zhang, J. and Reid, J. S. (2006). MODIS aerosol product analysis for data assimilation: Assessment of over-ocean level 2 aerosol optical thickness retrievals. *Journal of Geophysical Research: Atmospheres*, 111(D22). D22207.

Zhang, K., Zhao, C., Wan, H., Qian, Y., Easter, R. C., Ghan, S. J., Sakaguchi, K., and Liu, X. (2016). Quantifying the impact of sub–grid surface wind variability on sea salt and dust emissions in CAM5. *Geoscientific Model Development*, 9(2):607–632.

Zhao, C., Chen, S., Leung, L. R., Qian, Y., Kok, J. F., Zaveri, R. A., and Huang, J. (2013). Uncertainty in modeling dust mass balance and radiative forcing from size parameterization. *Atmospheric Chemistry and Physics*, 13(21):10733–10753.

Zhu, C., Byrd, R. H., Lu, P., and Nocedal, J. (1997). Algorithm 778: L-BFGS-B: Fortran subroutines for large-scale bound-constrained optimization. *ACM Trans. Math. Softw.*, 23(4):550–560.

Jerónimo ESCRIBANO **9 mars 2017**

Sujet : Inversion régionale des sources de poussières désertiques

Résumé : Dans cette thèse, nous concevons et appliquons un système d'assimilation de données pour l'estimation des sources de poussières désertiques à l'échelle régionale. Nous assimilons des données d'épaisseur optique des aérosols à partir de produits satellitaires dans une configuration régionale d'un modèle de circulation générale, couplé à un modèle d'aérosol et à un module de production de poussières. Le vecteur de contrôle dans le système d'assimilation est composé des facteurs de correction pour les émissions obtenues par l'ébauche du module de production de poussières. Nous concentrons nos inversions sur l'Afrique du Nord et la péninsule arabique pour une période d'un an. Nous décrivons le module de production de poussières et le système d'assimilation. Les résultats de l'inversion et la validation par rapport à des mesures indépendantes sont ensuite présentés en détail. Nous poursuivons cette thèse en mettant l'accent sur la sensibilité des émissions de poussières au jeu de données d'observation. Pour cela, nous avons assimilé cinq produits différents d'épaisseur optique d'aérosols dans notre système d'assimilation de données. Nous avons identifié des erreurs systématiques dans le modèle et dans les observations, ainsi que les limites et les avantages de notre approche. Nous avons accordé une attention particulière à la définition des statistiques d'erreur et à la procédure numérique pour calculer les analyses. Nous proposons et mettons en oeuvre un schéma de correction de biais dans l'espace des observations, et nous évaluons sa performance.

Mots clés : inversion, poussières désertiques, assimilation de données, modèle atmosphérique LMDZ, aérosols, donnés satellitaires

Subject : Regional inversion of desert dust sources

Abstract : In this thesis we design and apply a data assimilation system for the estimation of mineral dust emission fluxes at the regional scale. We assimilate aerosol optical depth retrievals from satellite-borned instruments in a regional configuration of a general circulation model, coupled to an aerosol model and to a dust production module. The control variable in the assimilation system are correction factors for the prior emissions of the dust production module. We focus our inversions over North Africa and the Arabian Peninsula for a one-year period. We describe the dust production module and the assimilation system. The inversion results and the validation against independent measurements is presented in detail. We continue this thesis with a focus on the sensitivity of the inferred dust emissions with respect to the observational dataset assimilated. For this purpose, we have assimilated five different aerosol optical depth retrievals in our data assimilation system. We have identified systematic errors in the model, in the observations and limitations and advantages of our approach. We have given special attention to the definition of the error statistics and the numerical procedure to compute the analyses. We propose and implement a bias correction scheme in the observational space, and we evaluate its performance.

Keywords : inversion, desert dust, data assimilation, LMDZ atmospheric model, aerosols, satellite data